

The University of Nottingham

UNITED KINGDOM · CHINA · MALAYSIA

Inorganic Materials in Hollow Carbon Nanostructures

Ákos Botos, MSci

Thesis submitted to the University of Nottingham for the degree of Doctor of Philosophy

October 2015

Abstract

The interactions of metal-containing molecules and nanoparticles (NPs) with the interior of hollow graphitic carbon nanostructures (CNs) were investigated and their chemical transformations in the nanoscale channels of CNs appraised. The gas phase insertion of Group VI metal hexacarbonyl complexes ($M(CO)_6$, M=Cr, Mo, W) into CNs was successfully developed and optimised to provide good filling rates as confirmed by transition electron microscopy (TEM). Infrared (IR) and Raman spectroscopy demonstrated that Group VI $M(CO)_6$ complexes with greater polarisability exhibit stronger van der Waals interactions with the interior of single-walled carbon nanotubes (SWNTs). The synthesis of metal-based NPs inside graphitised carbon nanofibers (GNFs) by the *in situ* transformation of the encapsulated $M(CO)_6$ precursor molecules was successfully achieved and it was demonstrated that GNFs can act as a source of oxygen in these reactions. The nanotube filling methodology was applied for the multi-step synthesis of new inorganic materials inside CNs by the controlled reactions of $M(CO)_6$, I_2 and H_2S. This approach yielded unusual van der Waals hybrid materials such as "tube inside a tube" and other hybrid structures of MoS_2 and GNFs. In SWNTs, with significantly narrower diameters than GNFs or multi-walled carbon nanotubes (MWNTs), metal complexes form unique 1D arrays of octahedral

$[M_6I_{14}]^{2-}$ clusters with the nanotube acting as a nanocontainer and a poly-cation balancing the charge of the guest-clusters. The iodides of Mo and W were effectively converted into extremely thin MS_2 nanoribbons (NRs) within SWNTs, providing a new more efficient route to the hybrid inorganic nanostructures. In MWNTs, the $[Mo_6I^i_8I^a_2I^{a\text{-}a}_{4/2}]$ clusters are packed in a hexagonal pattern to optimise filling of the void, and when reacted with H_2S they provide a range of multi-layered MS_2NRs with their widths controlled by the internal diameter of the host nanotube.

Acknowledgements

I would like to express my gratitude to Prof. Andrei N. Khlobystov for his continued support and guidance during my PhD studies. I appreciate all his contributions of time, criticism, and funding to make my research experience productive and stimulating. His guidance and encouragement helped to improve my skills and become a better scientist.

I would like to thank Dr. Thomas W. Chamberlain for being a mentor during the course of my PhD. I would like to thank his quick and thorough corrections he provided during the production of this thesis and throughout my PhD studies.

I would like to thank all the help I have received from the members of the Electron Microscopy Group of Materials Science of the Ulm University (Ulm, Germany) with aberration corrected transmission electron microscopy and image simulation.

I would like to thank the help of Sebastian Osswald (Naval Postgraduate School, Monterey, CA) with some of the Raman spectroscopy measurements on metal hexacarbonyls in single-walled carbon nanotubes.

I would like to thank Dr. Alessandro Torre from our group and Dr. Nigel Neate (Advanced Materials Group, School of Engineering)

for helping me get started with powder X-ray measurements and data analysis.

I am very grateful for the help from the Nottingham Nanocarbon group members for their continuous support over the years.

In addition, I would like to thank all of the technical staff, particularly Mark Guyler and Clive Dixon without whom I could not complete my experimental work.

Finally, I would like to thank my wife Emese and my Family and all my Friends their constant love and support and that they believed in me.

Abbreviation list

2D	Two dimensional
4T	5,5'''-dimethyl-2,2':5',2'': 5'',2'''-quaterthiophene
AC-TEM	aberration corrected transmission electron microscopy
AD	Arc-discharge
ATR	Attenuated total reflectance
BN	Boron nitride
BNNT	Boron nitride nanotube
CDS	Chemical Database Service
CN	Hollow graphitic carbon nanostructures
CNF	Carbon nanofiber
CNT	Carbon nanotube (might include single-, duoble- and multiwalled carbon nanotubes)
$Co(II)(CpEt)_2$	Bis(ethylcyclopentadienyl) cobalt
$Co(II)Cp_2$	Cobaltocene
CVD	Chemical vapour deposition
DCTB	trans-2-[3-(4-tert-Butylphenyl)-2-methyl-2-propenylidene]malononitrile
DFT	Density functional theory
DGU	Density gradient ultracentrifugation
DOS	Density of states
DWNT	Double walled nanotube
EA-NT	Electric arch-discharge carbon nanotube
e-beam	Electron beam
EDX	Energy dispersive X-ray spectroscopy
EN	Electronegativity
F_4TCNQ	2,3,5,6-tetrafluoro-7,7,8,8-tetracyanoquinodimethane
$FeCp_2$	Ferrocene

FET	Field-effect transistors
GC-MS	Gas chromatography-mass spectrometry
GNF	Graphitised carbon nanofibre
HAADF STEM	High-angle annular dark-field scanning TEM
HF	Hartree-Fock theory
HF+D	Hartree-Fock theory with additional dispersion component
HiPCO-SWNTs	Single-walled carbon nanotubes made by the high pressure carbon monoxide process
HMM	Hexamethylmelamine
HOMO	Highest Occupied Molecular Orbital
HPW	Phosphotungstic acid ($H_3PW_{12}O_{40}$)
I@SWNT	Carbon nanotubes filled with iodine
ICP-AAS	Inductive-coupled plasma atomic absorption spectroscopy
IF	Inorganic fullerene
I_m^-	polyiodine ions (m=5, 4, 3)
I_n	Polyiodine molecules
IR	Infrared
LA	Laser ablation
LUMO	Lowest Unoccupied Molecular Orbital
M	Metal
M NP	Metal nanoparticle
$M(CO)_6$	Group VI metal hexacarbonyl M=Cr, Mo, W
$M(CO)_x$@SWNT	Nanotube endohedrally-functionalised with metal carbonyl
$M@C_n$	Endohedral fullerene
MADLI-ToF MS	Matrix-assisted laser desorption/ionization-time of flight mass spectrometry
MOCVD	Metal-organic chemical vapour deposition
MWNT	Multi-walled carbon nanotube
NEXAFS	Near edge X-ray absorption fine structure

NMR	Nuclear magnetic resonance
NP	Nanoparticle
NP@NT	Nanoparticle encapsulated in a nanotube
NR	Nanoribbon
NT	Nanotube
OLEDs	Transparent semiconductors for solar cells and displays
PTFE	Polytetrafluoroethylene
PXRD	Powder X-ray diffraction
RBM	Radial breathing mode
SWNT	Single-walled carbon nanotube
TCNQ	7,7,8,8-tetracyanoquinodimethane
TDAE	Tetrakis-(dimethylamino)-ethylene
TEM	Transmission electron microscopy
TGA	Thermogravimetric analysis
THF	Tetrahydrofuran
UV-Vis	Ultra violet-visible
XPS	X-ray photoelectron spectroscopy
XRD	X-ray diffraction
ZnDPP	Zn complex of diphenylporphyrin

Table of contents

Abstract **2**

Acknowledgements **4**

Abbreviation list **6**

Table of contents **9**

1 Introduction **16**

1.1 INTRODUCTION 16

1.2 STRUCTURE AND PROPERTIES OF HOLLOW GRAPHITIC NANOSTRUCTURES 17

1.2.1 Carbon nanotubes *19*

1.2.1.1 Structure of carbon nanotubes 19

1.2.1.2 Electronic and optical properties of carbon nanotubes 20

1.2.1.3 Chemical properties of carbon nanotubes 25

1.2.1.4 Carbon nanotubes as nano-reactors 26

1.2.2 Graphitised nanofibers *27*

1.3 HYBRID MATERIALS OF HOLLOW GRAPHITIC STRUCTURES 29

1.3.1 Filling methods of carbon nanotubes *30*

1.3.2 Filled carbon nanotubes *32*

1.3.2.1 Examples of inorganic materials encapsulated in carbon nanotubes and other materials used for nanotube doping 33

1.3.2.2 Examples of materials encapsulated in carbon nanotubes characterised by vibrational spectroscopy 37

1.3.2.3 Examples of strategies and filling methods for the encapsulation of metal containing molecules in carbon nanotubes 42

1.3.3 Formation of metal nanoparticles in wide hollow tubular carbon nanostructures *46*

1.3.3.1 Liquid phase chemistry 47

1.3.3.2 Incipient wetness technique 47

1.3.3.3 Encapsulation of preformed nanoparticles 48

1.4 INORGANIC NANOMATERIALS RELATED TO CARBON BASED NANOMATERIALS 50

1.4.1.1 Inorganic nanotubes formed using carbon nanotubes as templates 55

1.5 SUMMARY 57

1.6 AIM AND OBJECTIVES 58

1.7 REFERENCES 59

2 Investigation of the interactions of metal hexacarbonyl complex with carbon nanotubes by vibrational spectroscopy 72

2.1 INTRODUCTION 72

2.1.1 Fundamental properties of metal carbonyl complexes 75

2.1.1.1 Vibrational spectroscopy of metal hexacarbonyl complexes 76

2.2 ENCAPSULATION OF METAL HEXACARBONYL COMPLEXES IN SWNTS 79

2.2.1 Development of a general gas phase filling method of SWNTs with metal hexacarbonyl complexes 80

2.2.2 Optimisation of the preparation of $M(CO)_6$@SWNT samples using $W(CO)_6$ 82

2.2.2.1 Optimisation of the gas phase filling method using $W(CO)_6$ 82

2.2.2.2 Optimisation of the removal of the excess metal hexacarbonyl complexes from the outer surface of carbon nanotubes 89

2.2.3 Encapsulation of $Cr(CO)_6$ and $Mo(CO)_6$ in SWNTs 97

2.2.4 Qualitative analysis of the mechanism and energetics of the encapsulation of metal hexacarbonyls into SWNTs 100

2.2.5 Summary and process map of the synthesis of $M(CO)_6$@SWNTs 103

2.3 EXPLORATION OF THE HOST-GUEST INTERACTIONS IN $M(CO)_6$@SWNTS 105

2.3.1 Vibrational spectroscopy analysis of $M(CO)_6$@SWNTs 105

2.3.1.1 Infrared spectroscopy analysis of the CO stretching vibration in $M(CO)_6$ molecules encapsulated in SWNTs 105

2.3.1.2 Results of Raman spectroscopy analysis of $M(CO)_6$@SWNTs 110

2.3.2 Discussion of the vibrational spectra of $M(CO)_6$@SWNTs 111

2.3.2.1 Analysis of the carbonyl band shape in $M(CO)_6$@SWNTs 111

2.3.2.2 Determination of the nature of the host-guest interactions in $M(CO)_6$@SWNTs 114

2.3.2.3 Theoretical investigation of the IR spectra of $M(CO)_6$@SWNTs 116

2.3.2.4 Relationship between the magnitude of the IR shift of the CO stretching vibration and the physicochemical properties of the $M(CO)_6$ complexes 119

2.4 CONCLUDING REMARKS 127

2.5 EXPERIMENTAL SECTION 129

2.5.1 Filling single-walled carbon nanotubes 129

2.5.1.1 Opening single-walled carbon nanotubes by oxidation in air 129

2.5.1.2 Optimisation of the gas phase filling of $M(CO)_6$ in SWNTs 129

2.5.1.3 Optimised gas phase filling method of SWNTs with $M(CO)_6$ 130

2.5.2 Removal of excess metal hexacarbonyl complex from the outside of SWNTs ... 131

2.5.2.1 Removal of excess $M(CO)_6$ by dynamic vacuum 131

2.5.2.2 Removal of excess $M(CO)_6$ with organic solvent 131

2.5.3 Preparation of control samples for IR measurements 132

2.5.3.1 Preparation of $W(CO)_6$+SWNT control sample by mechanical mixing 132

2.5.3.2 Preparation of $W(CO)_6$/SWNT control sample by sublimation 132

2.5.3.3 Preparation of $W(CO)_6$/(C_{60}@SWNT) control sample by sublimation 132

2.5.4 Transmission Electron Microscopy and Energy-dispersive X-ray spectroscopy 133

2.5.5 Infrared spectroscopy 134

2.5.6 Raman scattering 134

2.5.7 Calculation of the average size and CO bond length of $M(CO)_6$ complexes 135

2.5.8 Theoretical investigation of the infrared spectra of $M(CO)_6$@SWNTs 135

2.6 REFERENCES 137

3 Controlled formation of metal nanoparticles inside graphitised carbon nanofibers ... 140

3.1 INTRODUCTION 140

3.2 SELECTION OF FILLING METHOD AND PRECURSOR MOLECULES 142

3.3 GAS PHASE ENCAPSULATION OF $M(CO)_6$ MOLECULES IN GNFS 144

3.4 FORMATION OF NANOPARTICLES FROM $M(CO)_6$ IN GNFS 146

3.4.1 Decomposition of $M(CO)_6$ in GNFs by the e-beam in TEM 146

3.4.2 Formation of nanoparticles from $M(CO)_6$ in GNFs by thermal decomposition 146

3.5 CHARACTERISATION OF THE PRODUCTS OF ENCAPSULATION AND THERMAL DECOMPOSITION OF $M(CO)_6$ MOLECULES IN GNFS 150

3.5.1 TEM analysis of $M(CO)_6$ encapsulated in GNFs 150

3.5.2 Structural and chemical properties of the materials formed via the thermal decomposition of $M(CO)_6$ molecules in GNFs 155

3.5.2.1 Chemical and structural properties of the materials formed *via* the thermal decomposition of $Cr(CO)_6$@GNFs 155
3.5.2.2 Chemical and structural properties of the materials formed *via* the thermal decomposition of $Mo(CO)_6$@GNFs 159
3.5.2.3 Chemical and structural properties of the materials formed *via* the thermal decomposition of $W(CO)_6$@GNFs 166
3.6 DISCUSSION 178
3.6.1 Behaviour of $M(CO)_6$ in GNFs under the e-beam of TEM 178
3.6.2 Comparing the structure and shape of products of the different thermal decomposition processes 179
3.6.3 Investigation of the metal oxide formation in GNFs 183
3.7 CONCLUDING REMARKS 189
3.8 EXPERIMENTAL SECTION 191
3.8.1 Materials 191
3.8.2 Gas phase filling of GNFs with $M(CO)_6$ 191
3.8.2.1 Heat treatment of GNFs in air prior to encapsulation 191
3.8.2.2 Encapsulation of $M(CO)_6$ into GNFs 191
3.8.3 Chemical transformation of $M(CO)_6$ encapsulated in GNFs into nanoparticles via thermal decomposition 192
3.8.3.1 Thermal decomposition of $M(CO)_6$@GNF under Ar atmosphere 192
3.8.3.2 Thermal decomposition of $M(CO)_6$@GNF under vacuum 192
3.8.3.3 Encapsulation and consecutive thermal decomposition of $M(CO)_6$ in GNFs under vacuum 193
3.8.3.4 Thermal decomposition of $M(CO)_6$@GNF in H_2/Ar flow 194
3.8.4 Transmission Electron Microscopy and Energy-dispersive X-ray spectroscopy 195
3.8.5 Powder X-ray diffraction measurements and calculations 196
3.9 REFERENCES 198

4 Synthesis of metal disulphide-graphitised carbon nanofiber hybrid nanomaterials ... 203

4.1 INTRODUCTION 203
4.2 METHODS FOR THE SYNTHESIS OF MoS_2 IN GNFS 204

4.2.1 Formation of MoS_2@GNFs from $Mo(CO)_6$@GNFs 206

4.2.2 Formation of MoS_2@GNFs from MoO_2@GNFs 206

4.2.3 Formation of MoS_2@GNFs from ($Mo(CO)_6$ and I_2)@GNFs and MoI_2@GNFs 207

4.2.3.1 Formation of MoS_2@GNFs from MoI_2@GNFs 207

4.2.3.2 Formation of MoS_2@GNFs from ($Mo(CO)_6$ and I_2)@GNFs 207

4.3 CHARACTERISATION OF THE MATERIALS FORMED BY REACTING METAL PRECURSORS ENCAPSULATED IN GNFS WITH H_2S 208

4.3.1 Characterisation of the material formed by reacting $Mo(CO)_6$@GNFs with H_2S 208

4.3.2 Characterisation of the material formed by reacting MoO_2@GNFs with H_2S . 213

4.3.2.1 Characterisation of MoO_2@GNFs 213

4.3.2.2 Characterisation of the material formed by reacting MoO_2@GNFs with H_2S 214

4.3.3 Characterisation of MoI_2@GNFs and the MoS_2@GNFs formed by the reaction of MoI_2@GNFs with H_2S 218

4.3.3.1 Characterisation of MoI_2@GNFs 218

4.3.3.2 Characterisation of the material formed by reacting MoI_2@GNFs with H_2S 221

4.3.4 Characterisation of ($Mo(CO)_6$ and I_2)@GNFs and the MoS_2@GNFs formed by reacting it with H_2S 223

4.3.4.1 Characterisation of ($Mo(CO)_6$ and I_2)@GNFs 223

4.3.4.2 Characterisation of the material formed by reacting ($Mo(CO)_6$ and I_2)@GNFs with H_2S 225

4.4 ANALYSIS OF THE MECHANISM OF MoS_2 FORMATION IN GNFS 229

4.4.1 Formation of MoS_2@GNFs from $Mo(CO)_6$@GNFs 229

4.4.2 Formation of MoS_2@GNFs from MoO_2@GNFs 230

4.4.3 Formation of MoS_2@GNFs from MoI_2@GNFs 232

4.4.4 Formation of MoS_2@GNFs from ($Mo(CO)_6$ and I_2)@GNFs 234

4.5 CONCLUDING REMARKS 238

4.6 EXPERIMENTAL SECTION 239

4.6.1 Materials 239

4.6.2 Gas phase filling of GNFs 239

4.6.2.1 Heat treatment of GNFs in air prior to encapsulation 240

4.6.2.2 Encapsulation of $Mo(CO)_6$ or $Mo(CO)_6$ and I_2 together into GNFs 240

4.6.2.3 Encapsulation of I_2 into $Mo(CO)_6$@GNFs 240

4.6.3 Chemical transformation of $Mo(CO)_6$ or $Mo(CO)_6$ and I_2 precursor molecules into MoO_2 or MoI_2 in GNFs 241

4.6.4 Reaction of the different precursors situated in GNFs with H_2S gas 243

4.6.5 Calcination of MoS_2@GNFs under an Ar atmosphere 244

4.6.6 Transmission Electron Microscopy and Energy-dispersive X-ray spectroscopy 244

4.6.7 Powder X-ray diffraction measurements and calculations 246

4.7 REFERENCES 247

5 Synthesis of inorganic nanomaterials inside carbon nanotubes 250

5.1 INTRODUCTION 250

5.2 METHODS OF INORGANIC NANOMATERIALS SYNTHESIS INSIDE CARBON NANOTUBES 253

5.3 CHARACTERISATION OF THE ENCAPSULATED MOLECULES AND PRODUCTS OF CHEMICAL REACTIONS PERFORMED INSIDE CNTS 255

5.3.1 Characterisation of the materials formed by the encapsulation and subsequent reaction of $M(CO)_6$ and I_2 in CNTs 256

5.3.1.1 Characterisation of the materials formed by reacting W(CO)6 and I2 precursors in SWNTs 256

5.3.1.2 Characterisation of the materials formed by reacting $Mo(CO)_6$ and I_2 in SWNTs 263

5.3.1.3 Characterisation of the material formed by the encapsulation of $Mo(CO)_6$ and I_2 in MWNTs 271

5.3.1.4 Characterisation of the materials formed by reacting $Mo(CO)_6$ and I_2 in MWNTs and further calcination of the product 273

5.3.2 Characterisation of the materials formed by reacting metal containing precursors encapsulated in CNTs with H_2S 279

5.3.2.1 Characterisation of the material formed by reacting $Mo(CO)_6$@SWNT with H_2S 279

5.3.2.2 Characterisation of the material formed by reacting Mo_6I_{14}@SWNT with H_2S 280

5.3.2.3 Characterisation of the materials formed by reacting W_6I_{14}@SWNT with H_2S 287

5.3.2.4 Characterisation of the material formed by reacting ($Mo(CO)_6$, I_2)@MWNT with H_2S 292

5.3.2.5 Characterisation of the material formed by reacting $Mo_6I^i_8I^a_2I^{a\text{-}a}_{4/2}$@MWNT with H_2S 293

5.4 DISCUSSION 296

5.4.1 Analysis of the mechanism of metal iodide formation in CNTs 296

5.4.2 Analysis of the mechanism of MS_2 formation in CNTs..... 298

5.4.2.1 Formation of MoS_2@SWNTs from $Mo(CO)_6$@SWNTs..... 298

5.4.2.2 Formation of MS_2@CNTs from M_6I_{14}@CNTs and ($M(CO)_6$, I_2)@CNTs..... 299

5.4.3 Analysis of the chemistry behind the formation of MS_2 (M=Mo, W) nanoribbons in SWNTs..... 302

5.4.4 Dynamic behaviour of M_6I_{14} clusters (M=Mo, W) in CNTs..... 305

5.5 CONCLUDING REMARKS 308

5.6 EXPERIMENTAL SECTION 309

5.6.1 Materials..... 309

5.6.2 Gas phase filling of CNTs..... 309

5.6.2.1 Opening CNTs by oxidation in air..... 310

5.6.2.2 Encapsulation of $M(CO)_6$ or $M(CO)_6$ and I_2 together into CNTs..... 310

5.6.3 Chemical transformation of M(CO)6 and I2 precursor molecules into M6I14 in CNTs 311

5.6.4 Reaction of the different precursors situated in CNTs with H_2S gas 314

5.6.5 Calcination under an Ar atmosphere..... 315

5.6.6 Transmission electron microscopy and energy-dispersive X-ray spectroscopy 315

5.6.7 Transmission Electron Microscopy image simulation..... 316

5.6.8 Raman spectroscopy 316

5.6.9 MADLI-ToF mass spectrometry..... 317

5.7 REFERENCES 318

6 CONCLUSIONS 322

6.1 REFERENCES 330

1 Introduction

1.1 Introduction

In recent years we have witnessed unexpected technological advances due to the development of new materials. Novel ceramics, polymers, metal alloys, bio- and hybrid materials have substantially improved our quality of life through enhanced, cheaper and more sustainable products and services, generating wealth and employment. From the medical to the information industry, these new materials have contributed to radical changes in our quality of life. It is certainly true to say that materials are shaping our society as it was stated in the report of the European Commission in 2001.[1]

Since then hybrid materials have become even more important, therefore they are at the forefront of both applied and fundamental research. Key current challenges are to find building units suitable for a particular hybrid nanomaterial and to combine them together in a controlled bottom-up assembly to achieve the desired physicochemical properties. However, first the fundamental interactions and their effect on the physicochemical properties of nanomaterials have to be systematically studied at the atomic scale.

Therefore, the main motivation of this work is in furthering the understanding of how confinement on the nanoscale alters the

properties of matter by non-covalent interactions thus allowing more intelligent design of functional materials in the future.

Particularly this study is dedicated to probe the interactions of metal containing molecules and nanoparticles (NP) with the interior of hollow graphitic structures, and to investigate the effect of confinement on the products of chemical reactions performed in the nanoscale channels of the hollow graphitic materials.

1.2 Structure and properties of hollow graphitic nanostructures

Although hollow graphitic structures were synthesised in the early 20th century, good quality hollow carbon fibers have only been produced since the 1960's.[2] Hollow carbon structures, however did not become an exciting scientific topic until the discovery of fullerenes in 1985 by Kroto *et al.* and the mass production of them in 1990 by Krätschmer.[3,4]

A year later in 1991 "helical microtubules of graphitic carbon", nowadays known as multi-walled carbon nanotubes (MWNTs) were observed experimentally by Iijima, using transmission electron microscopy (TEM).[5] Later on it transpired that similar structures were observed earlier by others and although those results did not receive much attention before, there is a debate about who should be given the credit for the discovery of carbon nanotubes (CNT).[6] In the same year atomically thin single-walled carbon nanotubes (SWNTs) were discovered simultaneously by Iijima and Bethune.[7,8]

The newest member of the nanocarbon family, the mother of all graphitic structures, is graphene, which is a single layer of sp^2 type carbon atoms ordered in a two dimensional (2D) hexagonal lattice (Figure 1-1 a).[9] The closest material to graphene one might say is graphite which can be constructed theoretically by stacking graphene layers on top of each other forming a 3D structure held together by non-covalent van der Waals interactions (Figure 1-1 d).

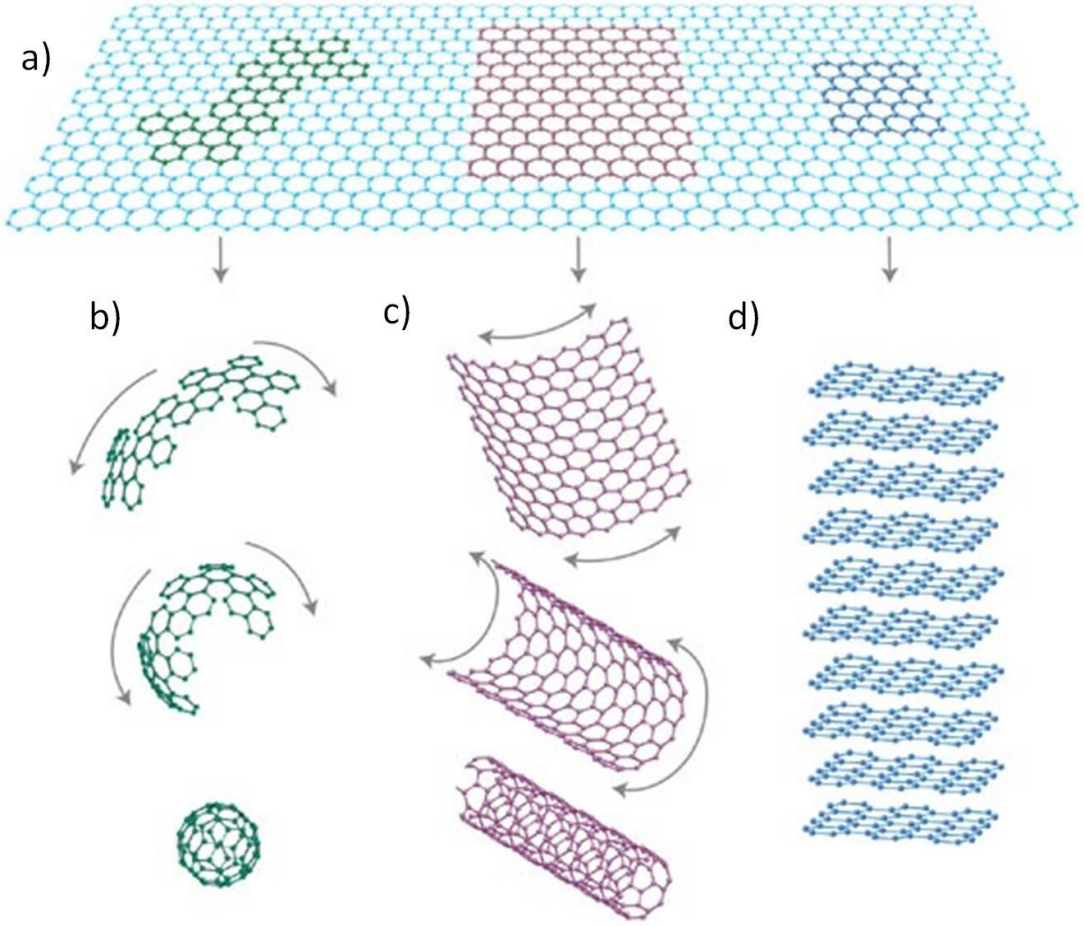


Figure 1-1. The mother of all graphitic forms, Graphene, a), is a 2D building material for carbon materials of all other dimensionalities. Theoretically it can be wrapped up into quasi-0D buckyballs, b), rolled into quasi-1D nanotubes, c), or stacked into 3D graphite, d).[10]

Importantly, despite their wide morphological variety hollow graphitic structures such as quasi-0D fullerenes (Figure 1-1 b) and

quasi-1D CNTs (Figure 1-1 c) can be theoretically related to graphene as they consist solely of sp^2 type carbon atoms.[10] Moreover, recently (2010) the *in situ* formation of C_{60} from a graphene flake under the influence of the electron beam (e-beam) of a transmission electron microscope was demonstrated by Khlobystov *et al.*[11]

1.2.1 Carbon nanotubes

Since their discovery CNTs have received a significant amount of attention in the fields of physics, chemistry and material science due to their remarkable physicochemical properties. They are good candidates for several microelectronic applications *e.g.* transparent semiconductors for solar cells and displays (OLEDs), field-effect transistors (FET) and quantum data storage.[12] They are also suggested to be used in next generation energy storage devices such as batteries and supercapacitors.[13,14,15,16]

1.2.1.1 Structure of carbon nanotubes

Single-walled carbon nanotubes can be synthesised by electric arc-discharge (AD), chemical vapour deposition (CVD) or laser ablation (LA) resulting in a mixture of semiconducting and metallic SWNTs with diverse diameter and chirality (*n*,*m*) distributions and unavoidable impurities including amorphous carbon and residual metal catalysts.

Theoretically the cylinder of a CNT can be made from a graphene sheet by rolling it up along a so-called chiral, or roll-up

vector C_h ($C_h = n*a_1 + m*a_2$), where a_i are the primitive lattice vectors of the graphene sheet and *n, m* are integers (Figure 1-2 a). SWNTs can be divided into three categories based on their chiral vector (*n,m*) resulting in three different arrangement of carbon atoms, namely zigzag (*n,0*), armchair (*n,n*) and chiral (*n,m*) where $n \neq m$ and $m \neq 0$ (Figure 1-2 b).

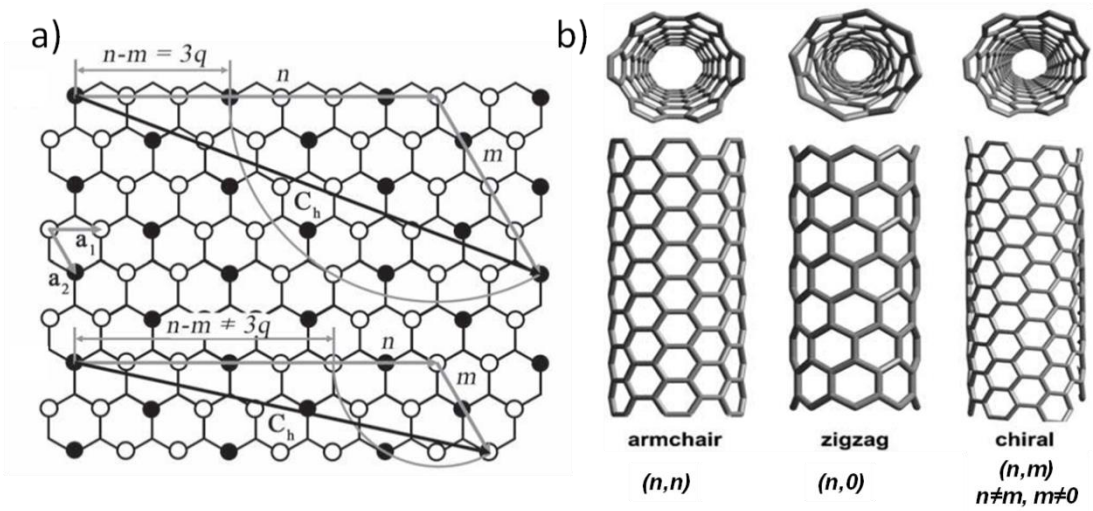


Figure 1-2. a) Theoretical rolling up of a graphene sheet along different chirality vectors. Black arrows represent the chiral or roll-up vector C_h that is a linear combination of the lattice vectors a_1 and a_2, with coefficients *n* and *m* ($C_h = na_1 + ma_2$). The grey arrows indicate the components na_1 and ma_2, q is an integer b) Chiral, armchair and zigzag SWNT models.[17,18]

Multi-walled carbon nanotubes (MWNT) can be viewed as coaxially oriented SWNTs of different diameters separated by the van der Waals distance typical for graphitic materials (~0.34 nm). The average inner diameter of MWNTs (10-50 nm) is larger than the maximum diameter of SWNTs.

1.2.1.2 Electronic and optical properties of carbon nanotubes

The chirality of carbon nanotubes defines their physical, optical and chemical properties including their diameter, electric

conductance, density, reactivity, *etc*. The diameter of a carbon nanotube (d_{NT}) can be determined by using Equation 1-1 where *n* and *m* are the components of the chiral vector (*n,m*) and a_0=0.246 nm is the length of the base vector of the graphene lattice.

Equation 1-1 $$d_{\mathrm{NT}} = \sqrt{n^2 + m^2 + nm} \cdot {}^{a_0}/_{\pi} \ \mathrm{nm}$$

The electronic structure of carbon nanotubes is unique as they possess the characteristics of both bulk semiconductors and discrete molecules due to their nanoscale diameter but macroscopic length, meaning that they have continuous valence and conductance bands (below and above the Fermi level) and discrete energy levels called van Hove singularities where the density of states (DOS) is very high (Figure 1-3).

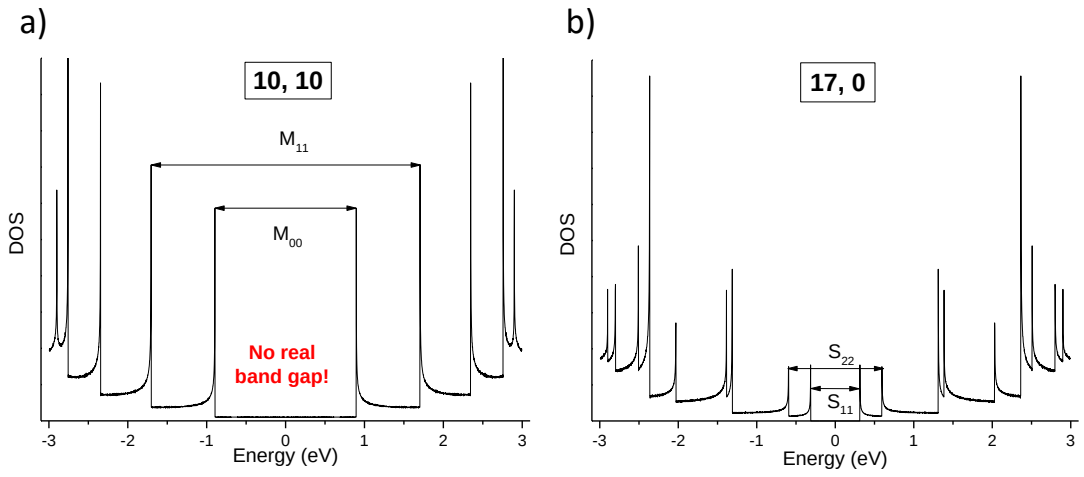


Figure 1-3. Density Of States plot of a) a metallic 10,10 armchair SWNT, and b) a semiconductor 17,0 zigzag SWNT with a band gap of ~0.6 eV.

In the case of semiconducting SWNTs the size of the band gap (0-1 eV) is inversely proportional to d_{NT},[19,20] while in the case of metallic SWNTs there is a pseudo gap induced by the curvature of

the nanotubes, where the DOS is very small but not zero. The electronic properties of carbon nanotubes strongly depend on their chirality, if the value (*n*-*m*)/3 is an integer the SWNT will be metallic otherwise it will be semiconducting.[21]

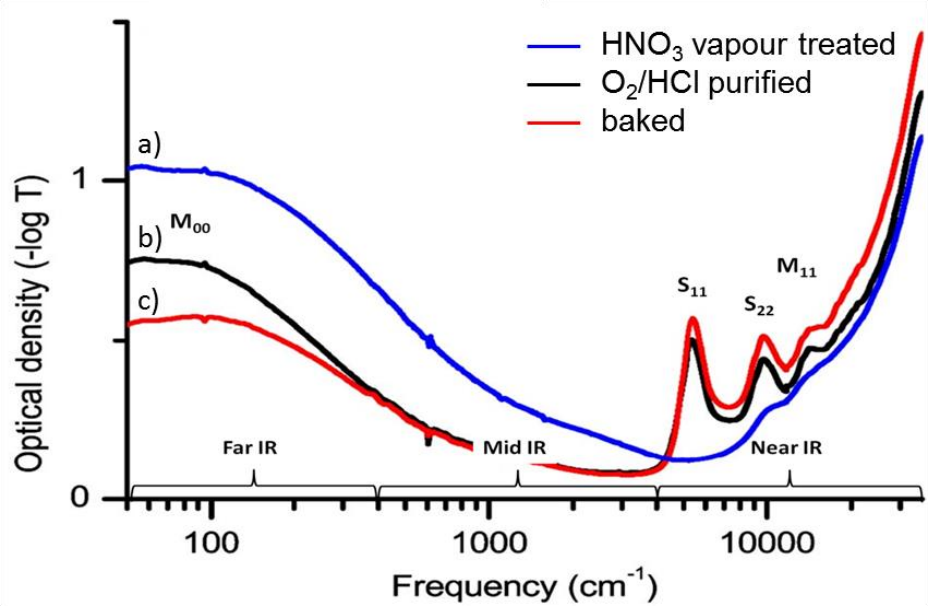


Figure 1-4. Wide-range IR spectrum of a) SWNTs treated with nitric acid vapour at room temperature overnight (blue), b) pristine O_2/HCl purified SWNTs (black), c) purified and baked SWNTs (400 °C, vacuum) (red).[22]

Carbon nanotubes strongly adsorb light if the energy of the radiation matches the energy difference of given van Hove singularities *e.g.* S_{11} (Figure 1-3, Figure 1-4), therefore infrared (IR) and Raman spectroscopy are widely used to assess their optical properties.[22] The energy of the transitions between the corresponding van Hove singularities (M_{00} in far IR; S_{11}, S_{22}, M_{11} in near IR) are unique to CNTs of a particular structure, therefore they provide an opportunity to identify the chirality (*n*,*m*) of SWNTs.[21] Moreover, as demonstrated in Figure 1-4, SWNTs only have a limited absorption in the mid IR region of the optical

spectrum (400-3000 cm^{-1}).

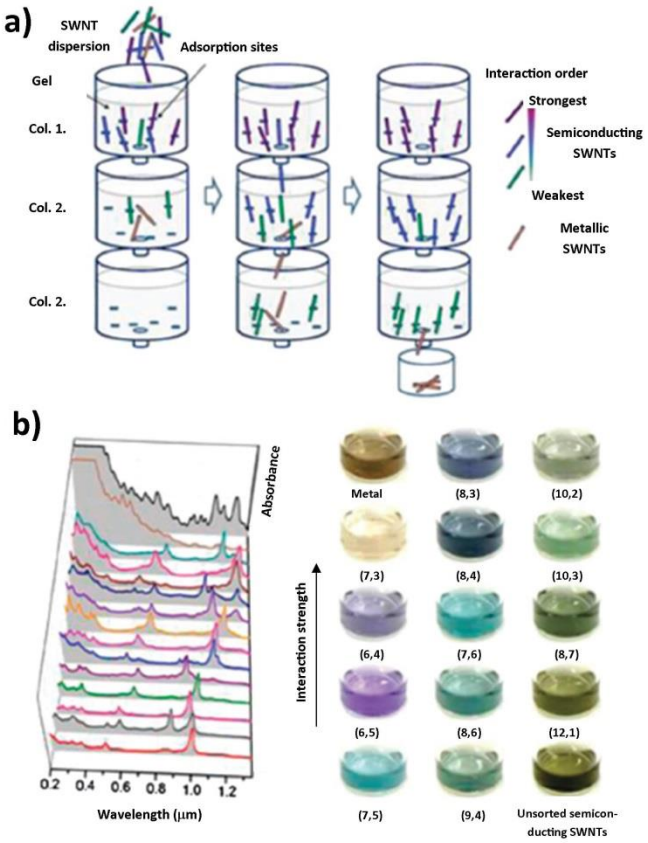


Figure 1-5. a) Schematic diagram of the single-surfactant multicolumn gel chromatography approach to separating SWNTs. b) Optical absorption spectra (left) and photographs (right) of 13 separated (*n*,*m*) semiconducting species together with those of metallic and pristine SWNT mixtures.[23,24]

Although typically SWNT samples are polydisperse and appear black due to the coexistence of different chirality (*n*,*m*) nanotubes which adsorb light across the whole visible spectrum, after separation *via* gel column chromatography, density gradient ultracentrifugation (DGU) or dielectrophoresis they appear colourful (Figure 1-5).[23,24]

All allotropic forms of carbon are Raman active but the positions, relative intensities and width of the bands are different.[25,26] The two most important bands are the low frequency resonant A_{1g} radial breathing mode (RBM) (<200 cm^{-1}) and a

strong band associated with the E_{2g} C-C stretching vibrations of graphite (1500-1700 cm^{-1}) called a tangential G band (Figure 1-6).[27,28]

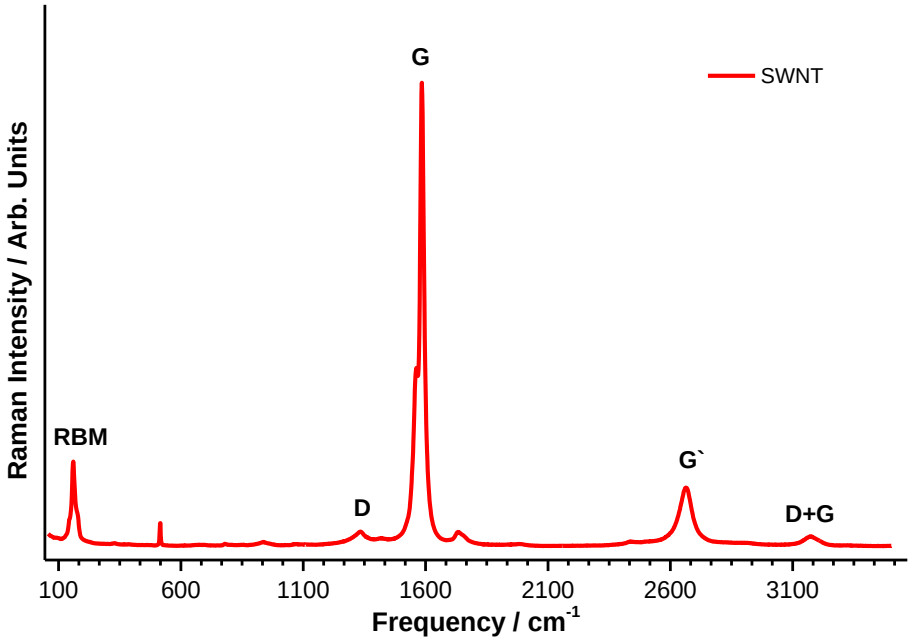


Figure 1-6. Typical Raman spectrum of SWNTs (red) recorded at Nottingham Nanotechnology and Nanoscience Centre as a CNT film dispersed on the surface of a Si chip using 514 nm excitation wavelength. The spectrum shows the low frequency resonant A_{1g} *i.e.* RBM, the D band attributed to the disorder of the hexagonal sp^2 C lattice, the most intense G band associated with the E_{2g} C-C stretching vibrations, the G`, G* or 2D band which is the overtone of the D band and lastly the combination band of D and G bands.

The frequency of the RBM is inversely proportional to d_{NT}, but is not directly related to the chirality of the SWNTs.[29,30,31] The D band around 1300 cm^{-1}, on the high frequency side of the G band, is attributed to disorder within the hexagonal sp^2 C lattice such as pentagons, vacancies (missing C atoms) and sp^3 C atoms. The overtone of this vibration appears as a relatively strong band (G`, G* or 2D band) around 2500 cm^{-1}. In addition, there is a combination band of the D and the G band between (2700-3000 cm^{-1}).

Based on Raman spectroscopy semiconducting and metallic nanotubes can be distinguished as for semiconducting SWNTs the G band is relatively sharp and the intensity of G^+ and G^- is different whilst for metallic SWNTs the G band is broad and the intensity of G^+ and G^- is similar (Figure 1-7).[32,33,34]

The effect of internal modification of CNTs on their Raman spectra will be discussed below (Section 1.3).

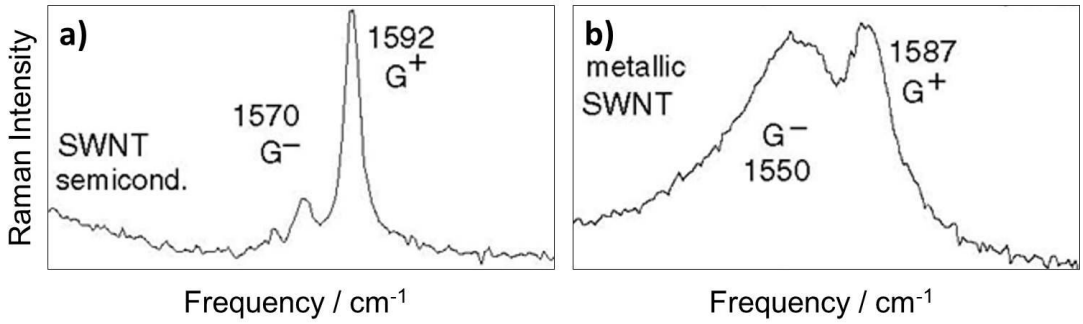


Figure 1-7. Images are showing the profile of the G band in the case of a) semiconducting and b) metallic SWNTs.[32] N.B. The relative intensity of G^+ and G^- is different in the case of a) semiconducting and b) metallic SWNTs.

1.2.1.3 Chemical properties of carbon nanotubes

From a chemist`s point of view CNTs are a family of molecules which are less reactive than the structurally related fullerenes. The sp^2 network of the nanotube sidewalls is relatively chemically inert and its reactivity has an inverse relationship with the diameter of the nanotube.[35] Carbon nanotubes are stable up to 350-700 °C (depending on purity and concentration of structural defects) in air and even higher temperatures (~2500 °C) in vacuum or inert atmosphere.[36] Although the highly curved endcaps containing pentagons, and the vacancies within the hexagonal sidewalls are chemically reactive, they represent a tiny portion of the nanotube

structure. Therefore, acid treatment of CNTs is frequently used to introduce defects in their hexagonal sidewalls prior to covalent sidewall functionalisation.[37] In addition to covalent functionalisation non-covalent interactions, such as van der Waals or π-π stacking, can also be used for the external modification of CNTs.[38,39]

1.2.1.4 Carbon nanotubes as nano-reactors

Importantly, as the interior of CNTs is even less reactive these atomically thin nanostructures can be used as nano test tubes or reaction vessels to study the properties of delicate species within a protected environment *e.g.* with spectroscopy or TEM.[40,41]

Moreover, due to the chemically stable network of sp^2 hybridised C atoms, the effect of confinement can be investigated on a wide range of chemical reactions within nanotubes, in contrast to other nano/micro-scale materials that have been developed in the past few decades such as zeolites, cyclodextrins, crown ethers, cucurbituril, calixarene.[42,43,44] For example, it was shown recently that the regioselectivity and kinetics of aromatic halogenation reactions are drastically affected due to the confinement of reactant molecules inside SWNTs.[45]

The complex interplay of the interactions potentially present within CNT based hybrid systems is summarised in Table 1-1.[46]

Table 1-1. Summary of the possible effects of carbon nano-reactors on chemical reactions.[46]

Interactions between Carbon Nanotube and Catalyst	Interactions between Carbon Nanotube and Reactants	Interactions between Carbon Nanotube and Products
Enhanced stability of catalyst inside nanotube	Attractive interactions between nanotube interior and reactant molecules leading to higher local concentration and effective pressure inside nano-reactors	Restriction of reaction space inside nanotube favouring formation of one product (*e.g.* linear isomer) over another (*e.g.* branched isomer)
Electron transfer between catalyst and interior surface of nanotube altering catalytic activity	Alignment of reactant molecules within nanotube facilitating reaction	Efficient transport of product molecules from nano-reactor to bulk phase
Chemical reactions between metal catalyst and nanotube interior leading to transformations of CNT sidewall	Van der Waals or electron transfer interactions between reactants and nanotube interior lowering activation energy	

1.2.2 Graphitised nanofibers

Graphitised carbon nanofibers (GNFs) are defined as a type of turbostratic graphitic structures. GNFs are closely related to CNTs as they both consist of sp^2 C layer(s). Similarly to CNTs, GNFs have high chemical resistance, high surface area, extraordinary mechanical strength and electrical conductivity. Hollow graphitic materials have been successfully utilised to produce light yet remarkably strong composite materials for use in aviation and Formula 1.[47]

The inner diameter of graphitised nanofibers (20-500 nm) is larger than the maximum diameter of CNTs (0.4-50 nm).[27] The

morphology of GNFs is very different in comparison to CNTs as they consist of perpendicularly or obliquely stacked graphite layers separated by ~0.34 nm, which might be encased into coaxial graphitic tube.[48]

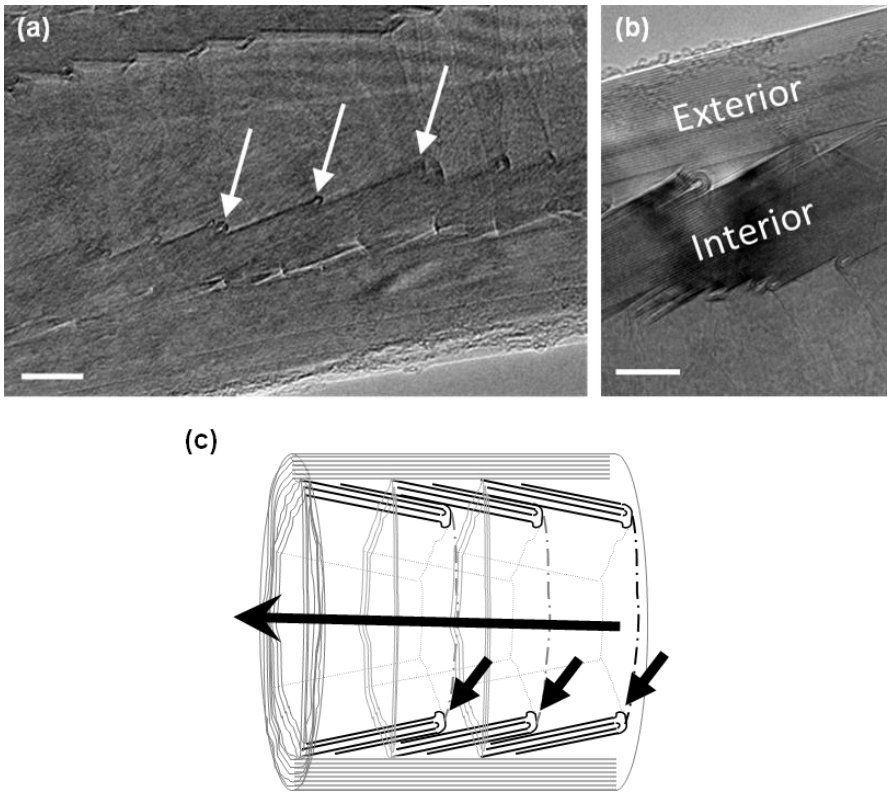


Figure 1-8. TEM micrograph of a) a graphitised carbon nanofiber with arrows pointing towards the step-edges, b) the exterior and the interior of GNF (scale bars are 10 nm), c) schematic representation of the GNF.

The obliquely stacked graphitic layers create a unique structural motif (Figure 1-8) referred as step-edges and consequently a terraced inner surface in contrast to the atomically smooth inner surface of carbon nanotubes.[49] At the step-edges of the GNFs the graphene sheets are extremely curved and the resulting strain makes the C atoms reactive resulting in -COOH, =O, -OH *etc*. groups bonded to the defects of the sp^2 C network. These functional groups may alter the physicochemical properties of GNFs

such as chemical reactivity, mass transport, hydrophobicity, electrical capacitance, *etc.* The GNFs used in our experiments (PR-24 GNF from Pyrograf®) have a "cup-stack" structure with outer diameter of 80-100 nm, inner diameter 30-40 nm and lengths of a few to 100 μm (Figure 1-8).

1.3 Hybrid materials of hollow graphitic structures

Due to the empty space inside both NTs and GNFs various materials can be inserted into hollow graphitic structures, since the encapsulation of C_{60} into SWNTs (C_{60}@SWNT) by Luzzi *et al.* was reported,[50] a substantial amount of research was carried out on the encapsulation of a whole variety of guest species within CNTs; and the understanding of the capacity of nanotubes to confine materials has been significantly advanced.[51,52,53,54]

It was demonstrated that as a result of the encapsulation the physical and chemical properties of the encapsulated materials may be altered in comparison to their bulk properties due to the interactions with the host material and the nanoscale confinement. Additionally the shape of host CNTs and their physicochemical properties such as band gap, type and concentration of charge carriers can also be affected as a result of the introduction of guest-molecules.[55] For example TEM revealed how C_{60} molecules within carbon nanotubes adopt a variety of packing arrays depending on the diameter of the carbon nanotube vessel, different to their packing in the face-centred cubic crystal lattice in C_{60}

crystal (Figure 1-9).[51]

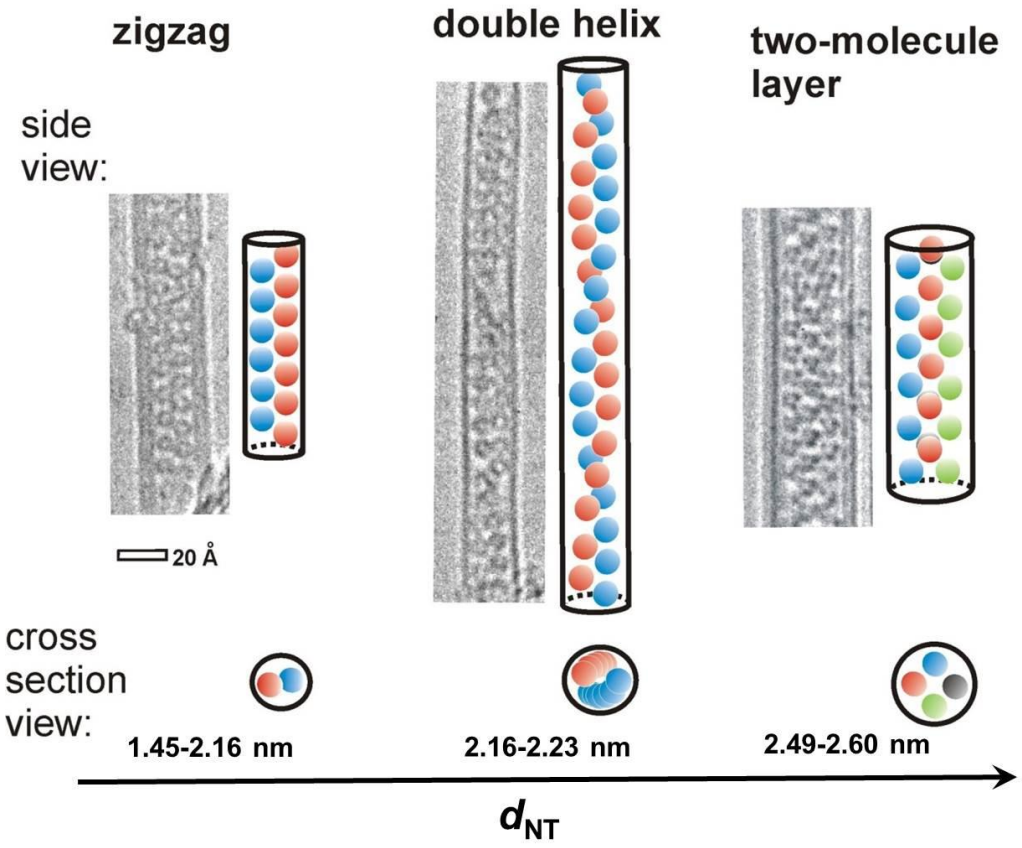


Figure 1-9. An example of the effect of molecular confinement: The packing arrangement of C_{60} inside nanotubes depends on the internal diameter of the nanotube container.[51]

The topic of encapsulation materials in SWNTs and MWNTs has been systematically reviewed by Monthioux,[56,57] Khlobystov,[51,58] and Chamberlain *et al.*[59] A few examples of CNTs filled with molecular or ionic compounds, relevant to this thesis, have been selected from the literature and are summarised in Section 1.3.2 after the discussion of the existing encapsulation methods.

1.3.1 Filling methods of carbon nanotubes

Several methodologies have been developed and refined over time enabling CNTs to be filled with a wide range of different materials such as elements, inorganic and organic compounds. In

general these can be classified into three main groups: gas phase filling, capillary filling with molten material and filling from the solution of the guest material.

By definition, gas phase filling can only be utilised when the guest-compound is stable in the gas phase. During this procedure the material is vaporised and combined with previously opened CNTs, allowing the guest-molecules and the empty nanotubes to become intimately mixed. Although this method provides high filling ratios it cannot be utilised with heat sensitive compounds.

The second method is based on capillary forces and can be used to insert those materials into CNTs which melt at relatively low temperatures but do not vaporise or sublime. Importantly the surface tension of the molten material has to be below 200 N/m to wet the internal channels of the CNTs.[60] This technique has been used mostly to encapsulate ionic compounds (See Section 1.3.2.1). The usage of this method is limited to heat tolerant compounds similarly to a gas phase filling. It also has to be mentioned that the guest-compound always fills the whole cross section of the container and blocks its internal channel.

Finally the method using the solution of the guest-compound has been developed to incorporate delicate compounds into CNTs which cannot be sublimed nor melted. This method involves the immersion of CNTs into the solution of the guest-compound. The most important criteria of successful encapsulation is that the

interaction between the guest-molecules and the CNT must be larger than both the solvent-guest and solvent-nanotube interactions, see Figure 1-10.[61]

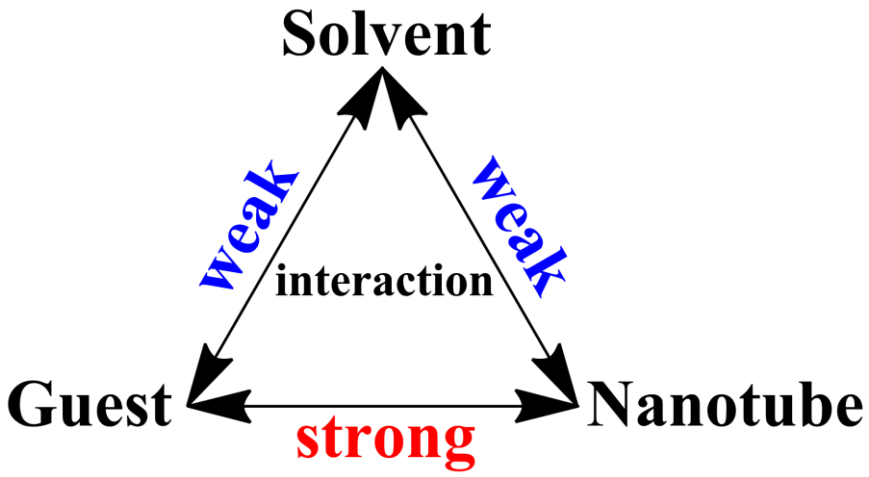


Figure 1-10. Diagrammatic representation of the key principle of encapsulation of molecules from solution phase into carbon nanotubes. The interaction between the guest-compound and the host carbon nanotube must be greater than the interactions between guest-compound and the solvent and solvent with the nanoutbe.[61]

Although the mechanism of nanotube filling from solutions is still not fully understood, in the case of C_{60}, molecular clusters were found to play an important role in the encapsulation process.[52] In general, these methods are using a saturated solution of the guest-compound to reach as high filling ratio as possible despite the large excess of the solvent molecules.

1.3.2 Filled carbon nanotubes

In the following sections examples of filled modified CNTs relevant to the thesis are summarised.

The first set of examples was selected to showcase inorganic compounds which were encapsulated into CNTs.

The second set of examples was compiled to showcase studies in which vibrational spectroscopy (preferably IR) was used to analyse the molecules which were encapsulated into CNTs.

The third set of examples was selected to showcase the different strategies and filling methods which were used to deliver metal (M) atoms into CNTs in a controlled fashion.

Moreover, the consequences of the host-guest interaction are discussed in all three sets of examples.

1.3.2.1 Examples of inorganic materials encapsulated in carbon nanotubes and other materials used for nanotube doping

Selenium has been inserted into CNTs using gas phase filling.[62] The structure of encapsulated Se is partly ordered (in the form of trigonal chains) and partly amorphous based on X-ray diffraction (XRD), however no TEM data was reported. Sulphur, tellurium and selenium have also been inserted into SWNTs by capillary filling.[63] Raman spectroscopy of these materials indicated a change in the shape and the frequency of the radial breathing mode of the CNTs towards higher wavenumbers (blueshift) (Figure 1-11). The shape of the G band did not alter significantly although its frequency was found to be slightly blueshifted as well (~3 cm^{-1}). The study attributes the shift of RBM to charge transfer from the SWNTs to the electron accepting chalcogens, as the size of the shift increases with increasing electronegativity/electron affinity of the guest-compounds (Te<Se<S).[63] Recently conducting linear chains

of sulphur was synthesised in CNTs, however Raman spectroscopy indicated negligible charge transfer.[64]

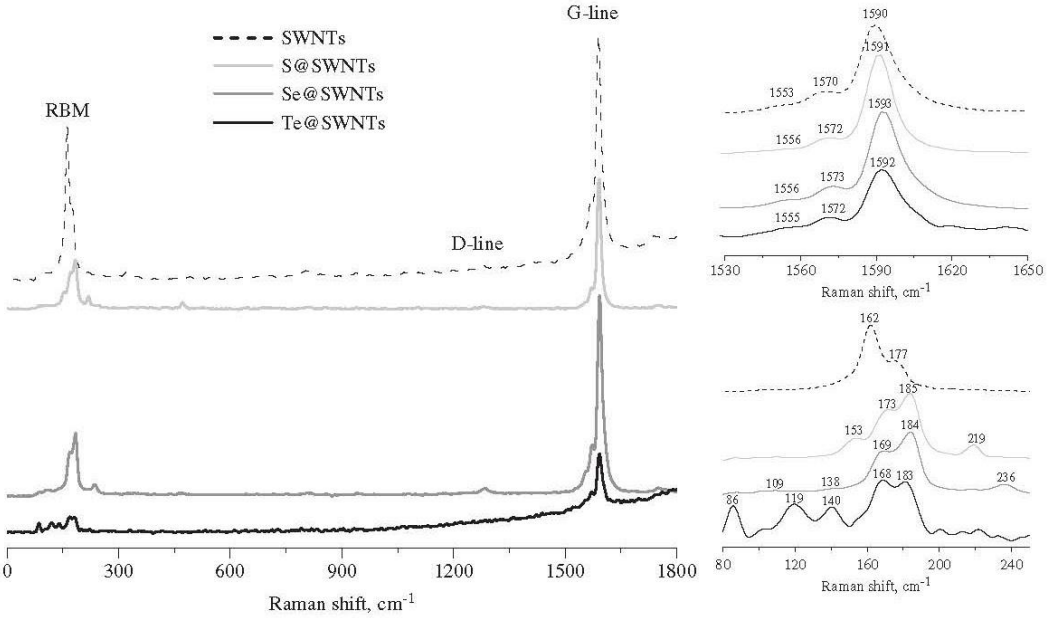


Figure 1-11. Image shows the Raman spectra of SWNTs and chalcogens (S, Se, Te) encapsulated in SWNTs (left), RBMs (bottom inset) and G band (top inset) of these spectra which were recorded using 1064 nm excitation wavelength.[63]

Metal chalcogenides such as HgTe,[65] SnTe,[66] Bi_2Te_3 and GaSe,[67] were encapsulated into CNTs. In the case of GaSe@SWNT a blueshift of the G band was observed in Raman spectroscopy and was interpreted as an indication of charge transfer from the nanotube to the 1D GaSe crystal.[67] In contrast, no charge transfer was observed in the case of SnTe and Bi_2Te_3 encapsulated in CNTs.[66,67]

Atomic chains of iodine were observed during TEM analysis of carbon nanotubes filled with iodine (I@SWNT) by gas phase filling (Figure 1-12).[68] Their structure was found to be strongly dependent on the diameter of the CNT due to confinement as has been observed previously to C_{60}.[51] In SWNTs with d_{NT}>1.5 nm a

crystalline phase identical to that of bulk iodine was observed, however in narrower SWNTs atomic chains of iodine were observed, which resulted in elliptical distortion of the SWNTs due to repulsive forces between iodine chains (Figure 1-12).

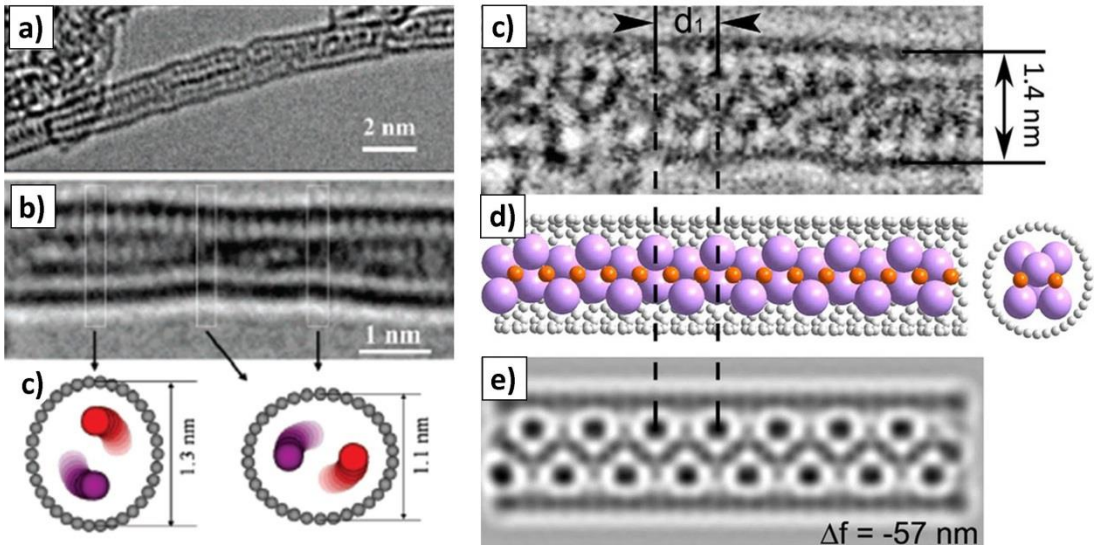


Figure 1-12. The elliptical distortion of SWNT induced by the repulsive force between atomic chains of iodine. a) Diameter variation from 1.10±0.05 nm to 1.30±0.05 nm of a SWNT encapsulating a double iodine chain. b) Repulsive interactions lead to the elliptical distortion of the SWNT.[68] c) TEM image, d) structural model, and e) TEM image simulation results for a AgI one-dimensional nanocrystal within a 1.34 nm SWNT channel. Large atoms correspond to the iodine.[69]

This illustrates clearly that while CNTs are rigid enough to impose confinement on guest species, the CNTs are flexible enough to be able to adapt their shape to the guest structure.[68] In I@SWNT Raman spectroscopy showed an blueshift of the G band which can be attributed to charge transfer to the polyiodine molecules (I_n) from the π electron system of the CNTs resulting in partial charge separation and the contraction of the C-C bonds.[70,71] Similar blueshifts (9 and 12 cm^{-1}) were observed in the case of the D and G* bands, respectively.

Metal halides such as AgX (Figure 1-12 c-e),[69] CuX,[72,73,74] and

CdX_2 [75] (X=Cl, Br, I) were encapsulated in CNTs *via* capillary filling using the corresponding molten salts. Based on X-ray photoelectron spectroscopy (XPS), Near Edge X-ray Absorption Fine Structure (NEXAFS), optical absorption and Raman spectroscopy it was concluded that charge is transferred from the CNTs to the encapsulated metal halide [69,74,75] Other metal halides, such as SnF_2 have been encapsulated from the molten phase and charge transfer from the SWNT to the guest-compound has also been observed.[76] The encapsulation of lanthanum iodide (LaI_3) led to an unexpected LaI_2 stoichiometry in CNTs as a result of the steric confinement imposed by the nanotube.[77] It was proposed that electronic interactions between the CNT and LaI_2 have a stabilising effect on the structure of the salt with unusual oxidation state of lanthanum.

It has been demonstrated that organic molecules such as 7,7,8,8-tetracyanoquinodimethane (TCNQ), 2,3,5,6-tetrafluoro-7,7,8,8-tetracyanoquinodimethane (F_4TCNQ), and tetrakis-(dimethylamino)-ethylene (TDAE) (see Figure 1-13) can also be used to efficiently produce p- and n-doped CNTs due to the electron transfer between the host nanotube and guest organic molecules.[78]

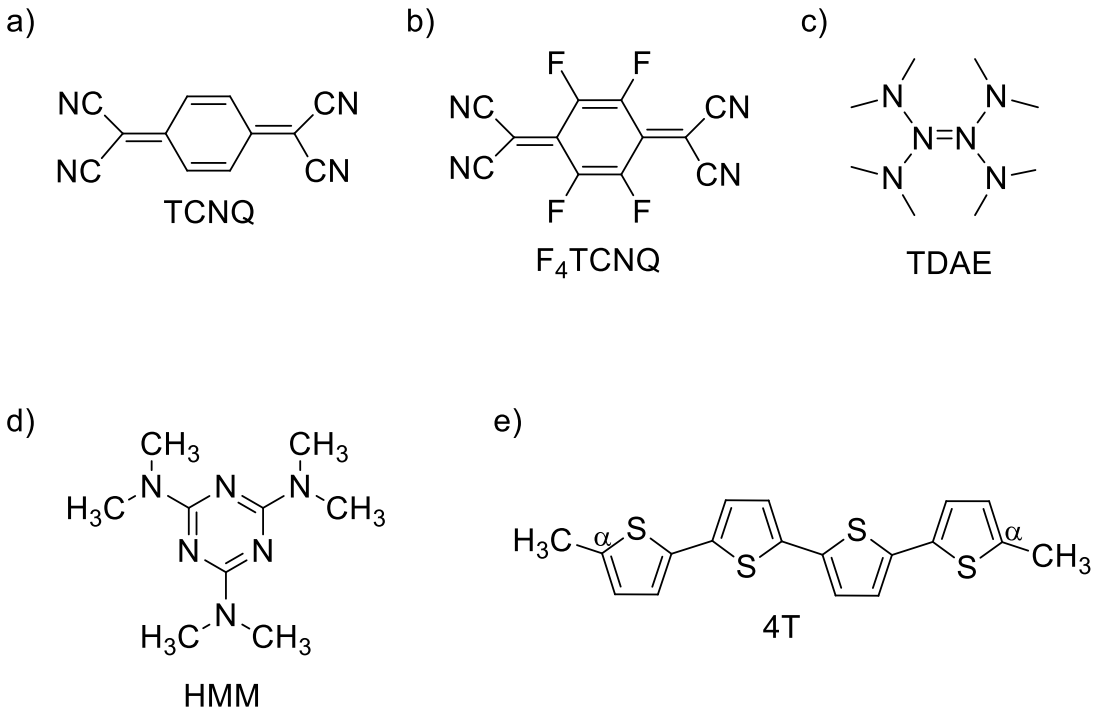


Figure 1-13. Examples of organic molecules inserted in carbon nanotubes: a) 7,7,8,8-tetracyanoquinodimethane (TCNQ),[78] b) 2,3,5,6-tetrafluoro-7,7,8,8-tetracyanoquinodimethane (F_4TCNQ),[78] c) tetrakis(dimethylamino)ethylene (TDAE),[78] d) hexamethylmelamine (HMM),[79] e) 5,5'''-dimethyl-2,2':5',2'':5'',2'''-quaterthiophene (4T).[80]

1.3.2.2 Examples of materials encapsulated in carbon nanotubes characterised by vibrational spectroscopy

5,5'''-dimethyl-2,2':5',2'':5'',2'''-quaterthiophene (4T, Figure 1-13) has been inserted into CNTs.[80] In the IR spectra of 4T, the bands at 1513 and 1445 cm^{-1} are associated with the anti-symmetric and symmetric C=C stretching modes (Figure 1-14). The absorption band at 1279 cm^{-1} corresponds to anti-symmetric in-plane C–H bending. The doublet at 1217 and 1166 cm^{-1} arises from the inter-ring C–C stretching vibration. The band at 1198 cm^{-1} can be related to anti-symmetric stretching of the two-end C_α–CH_3 bonds. Peaks at 1066 and 1042 cm^{-1} correspond to in plane C–H bending. The multiplet of bands at 899 and 843 cm^{-1} arise from the

symmetric and anti-symmetric C-S stretching modes. The absorption bands at 795 and 787 cm^{-1} are assigned to the out-of-plane C-H bending vibrations. The weak band at 644 cm^{-1} is associated with an in-plane ring deformation mode. The IR study of 4T@SWNT suggests that there is a charge transfer from the 4T molecules to the nanotubes.

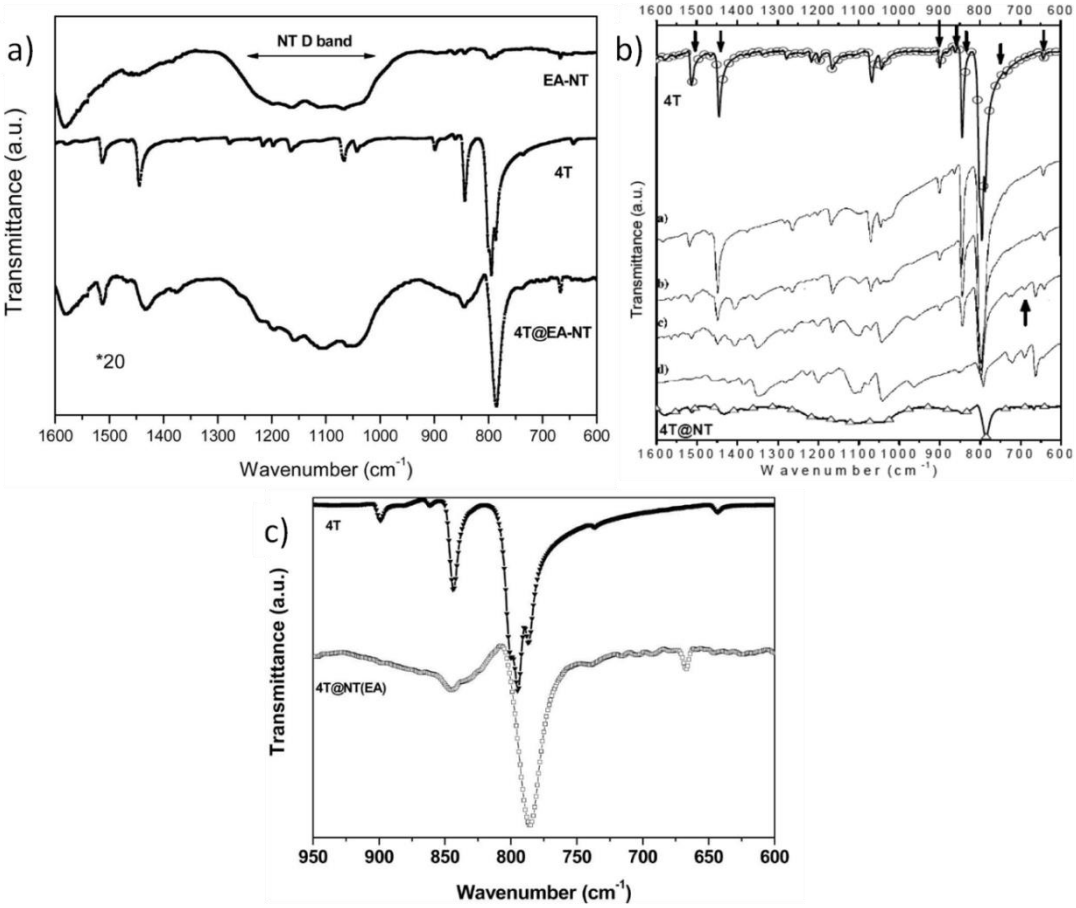


Figure 1-14. a) IR spectra of pristine electric arc-discharge carbon nanotube (EA-NT, top curve), pristine 4T (middle curve), and 4T@NT (bottom curve). The spectra are vertically translated for clarity, and the intensity of the 4T@NT spectrum is multiplied by 20. b) Infrared transmittance spectra of raw 4T (open circles, top) and 4T inserted NTs (triangles, bottom) together with iodine-doped 4T (gray lines) from ref. 39 in original paper (spectra a, b, c, d correspond respectively to pristine (a) and time doping (td) of 7, 30 min and td>1 h). The spectra are vertically translated for clarity. Arrows indicate the IR peaks of 4T mainly affected by the encapsulation process. c) Infrared spectra of raw 4T (full triangles) and 4T@NT (open squares). The spectra are vertically translated for clarity.[80]

The most intense peak around 800 cm^{-1} peak redshifts and

becomes broad which shows good agreement with what has been found previously for iodine doped 4T (Figure 1-14).

Hexamethylmelamine (HMM, Figure 1-13), a molecule similar in size to C_{60}, was encapsulated into CNTs and IR spectroscopy was successfully used to identify the presence of the encapsulated species (Figure 1-15).[79]

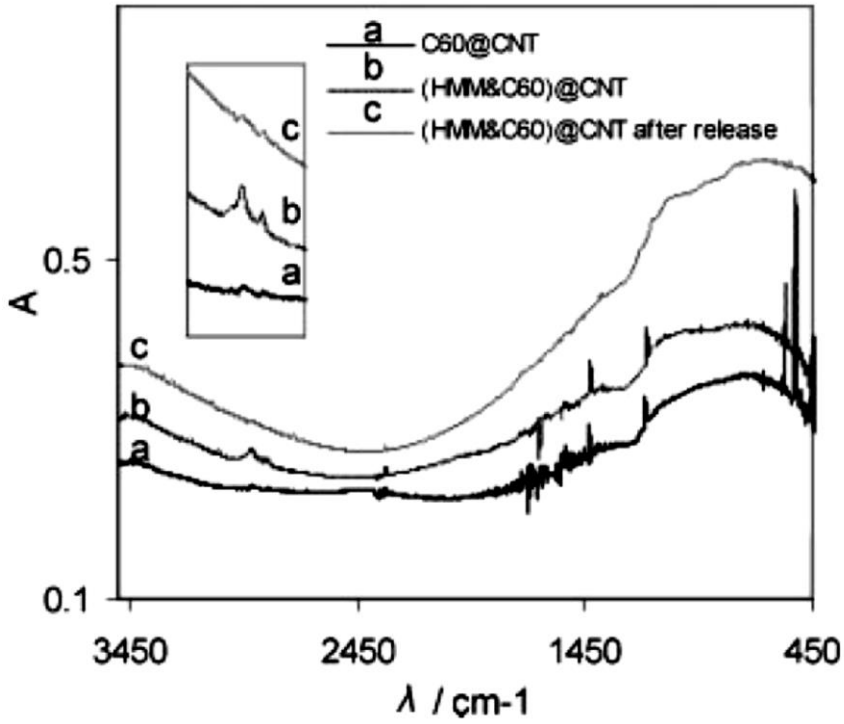


Figure 1-15. IR spectra of a) a C_{60}@CNT control, b) (HMM&C_{60})@CNT sample before and c) after release of HMM. The peak around 2900 cm^{-1} was used to verify the existence of hexamethylmelamine (HMM).[79]

Phosphotungstic acid ($H_3PW_{12}O_{40}$, Figure 1-16 a) was encapsulated into MWNTs as demonstrated by TEM (Figure 1-16 b, c) and Raman spectroscopy (Figure 1-17).[81] In the Raman spectra of $H_3PW_{12}O_{40}$@MWNT the bands at 1007 (ν_{P-O}), 903 (ν_{W-O-W}) and 238 (not assigned) cm^{-1} remain unshifted. However, the terminal $\nu_{W=O}$ band was redshifted from 998 to 992 cm^{-1} and its intensity increased relative to the ν_{P-O} band (Figure 1-17). These results

indicate strong interactions between the MWNT and terminal W=O groups.

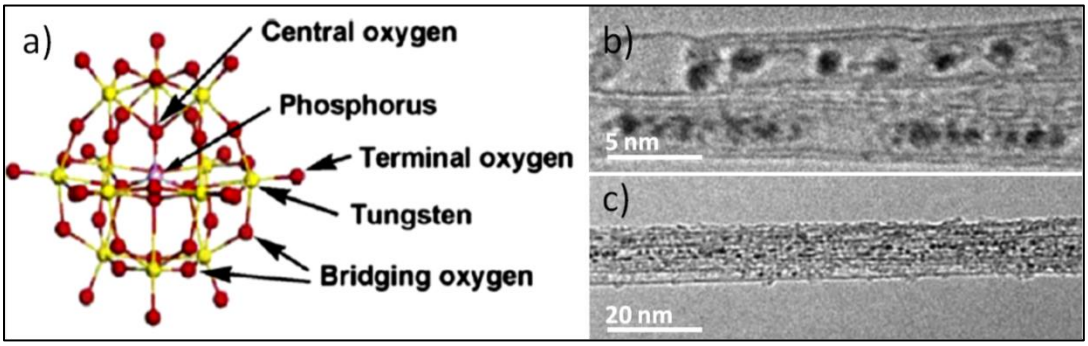


Figure 1-16. a) Model of phosphotungstic acid ($H_3PW_{12}O_{40}$). TEM images of CNTs filled with phosphotungstic acid molecules showing b) metal based material inside individual nanotubes and c) a bundle of filled SWNTs.[81]

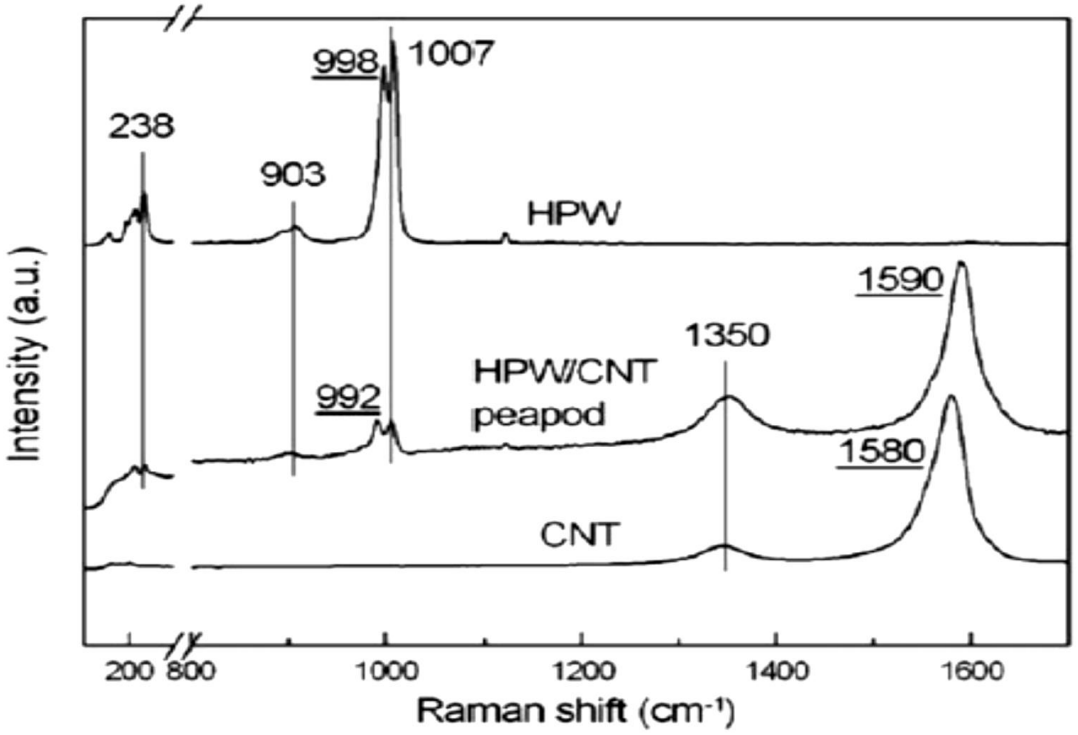


Figure 1-17. Raman spectra of pure phosphotungstic acid ($H_3PW_{12}O_{40}$, HPW) (top), CNTs boiled with HNO_3 (bottom), and their complex peapods.[81]

Adamantane was encapsulated in nanotubes with different diameters and characterised by IR, Raman, and solid state NMR spectroscopies.[82] In the IR spectra (Figure 1-18), the C-H vibration of adamantane is redshifted by 11 cm^{-1} due to van der Waals interactions between the guest and the nanotube. IR spectroscopy

has also been used to monitor the release of molecules from the larger nanotubes at elevated temperature (100 °C, 1 h).

The cube-shaped molecule octasiloxane ($Si_8H_8O_{12}$), with eight terminal H atoms, has been inserted into NTs using supercritical CO_2.[83] As a result of encapsulation, the absorption band of the Si-H stretching vibration in the resultant $Si_8H_8O_{12}$@SWNT system is broadened and redshifted by approximately 15 cm^{-1} from its original position, 2277 cm^{-1}. This can be explained by considering the van der Waals interactions between the H atoms and the interior of the CNTs. Such interactions polarise the Si-H bond, elongating it and making it weaker. The broadening of the peak is attributed to the different local environments experienced by the Si-H bonds within the NT.

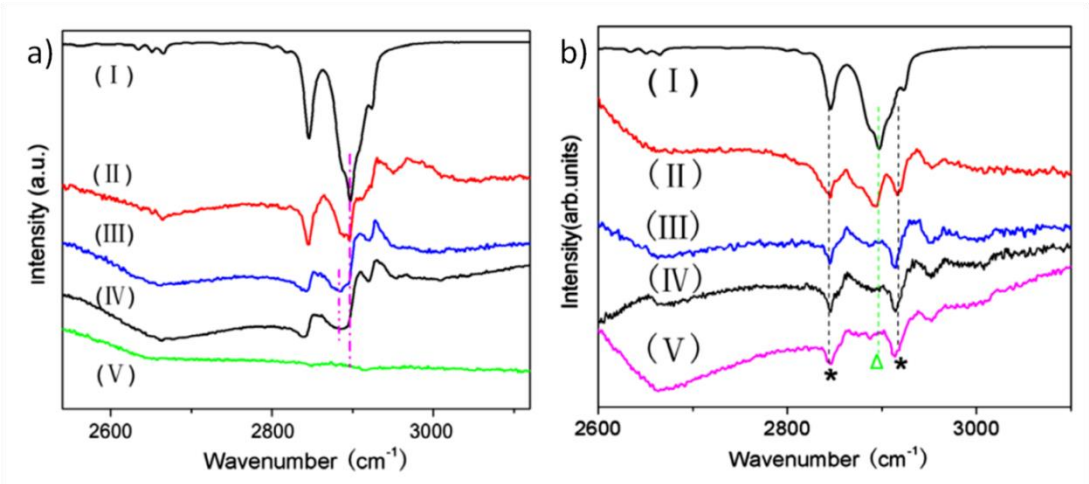


Figure 1-18. a) IR spectra of crystalline adamantane, (I), adamantane treated HP-SWNTs, (II), filled MWNTs, (III), filled arc-discharge (AD) SWNTs, (IV), and empty SWNTs, (V), made by the High Pressure Carbon Monoxide process (HiPCO-SWNTs). b) IR spectra of as-prepared adamantane–SWNTs mixture, (I), and adamantane@NT samples after heating at 100 °C for 1 h: filled AD-SWNT, (II), filled MWNT, (III), adamantane–SWNTs mixture, (IV), and adamantane treated HiPCO-SWNTs, (V). The position marked with a triangle shows the position of the band assigned to adamantane and the two peaks marked with an asterisk are from new C–H bonds on the nanotube surfaces due to reaction with moisture or adamantane.[82]

1.3.2.3 Examples of strategies and filling methods for the encapsulation of metal containing molecules in carbon nanotubes

The encapsulation of metal containing molecules in CNTs is important as the resulting hybrid nanomaterials may have interesting physicochemical properties. Even more importantly metal containing molecules encapsulated in CNTs provide a great opportunity to increase the understanding of how metals catalyse the growth of CNTs *via* studying metal-carbon (nanotube) interactions on the atomic scale.[84]

As metals typically have extremely high melting/boiling point their encapsulation into CNTs challenging, however, successful methodologies have been developed which can be used to transport metals into CNTs as discussed in the following section.

1.3.2.3.1 Organometallic molecules

Organometallic molecules are ideal precursors for the incorporation of metals in CNTs as many of them are able to sublime without decomposition. In addition, after their encapsulation organometallic molecules can be easily transformed into metal NPs (M NPs) by thermal decomposition, reduction with H_2, e-beam irradiation in TEM or UV light.[85]

Ferrocene ($FeCp_2$)[86,87] and other metallocenes such as $Ru(II)Cp_2$, $Cr(II)Cp_2$ (16 VE *i.e.* valence electrons), $V(II)Cp_2$ (17 VE) as well as tungstenocene-dihydride[88] were encapsulated in

CNTs from the gas phase and in the case of $FeCp_2$ from the molten phase as well. The presence of metals inside the CNTs was confirmed by TEM and energy-dispersive X-ray spectroscopy (EDX). Importantly, the IR absorption of the C-H stretching vibration of the Cp ring in $FeCp_2$ was redshifted from 3095 cm^{-1} to 2920 cm^{-1}, whilst the C-C vibration of the CNTs was blueshifted by 10 cm^{-1} indicating electron transfer from the $FeCp_2$ molecules to the CNT (n-doping).[89]

Similar effects have been observed in the case of encapsulation of the Zn complex of diphenylporphyrin (ZnDPP) in SWNTs.[90] The absorption peak measured by photo-luminescence was redshifted from 3.02 eV/24358 cm^{-1} to 2.88 eV/23229 cm^{-1} due to distortion of the DPP molecule in the CNTs.

Cobaltocene ($Co(II)Cp_2$) and bis(ethylcyclopentadienyl) cobalt ($Co(II)(CpEt)_2$) were encapsulated into SWNTs and as a result of charge transfer from $Co(II)Cp_2$ or $Co(II)(CpEt)_2$ to the CNTs (n-doping) the oxidation state of the Co(II) changed to Co(III) determined by UV-vis absorption spectroscopy.[91]

1.3.2.3.2 Fullerenes as carriers of metals into carbon nanotubes

Three different approaches have been taken to utilise the very strong van der Waals interaction between fullerenes and CNTs to encapsulate d- or f-block metals into CNTs (Figure 1-19, Figure 1-20).[92,93]

First endohedral metallofullerenes ($M@C_n$) were used to transfer

a metal atom or small metal clusters (M=Ce, La, La_2, Gd, Sc_2, Sm) in their inner cavity into CNTs (Figure 1-19, Figure 1-20 a).[84]

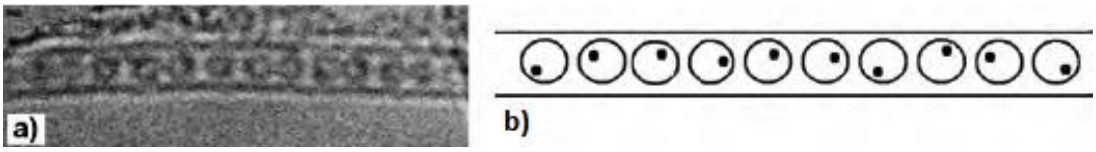


Figure 1-19. a) TEM image of ($Ce@C_{82}$)@SWNT and b) corresponding schematic representation.[84]

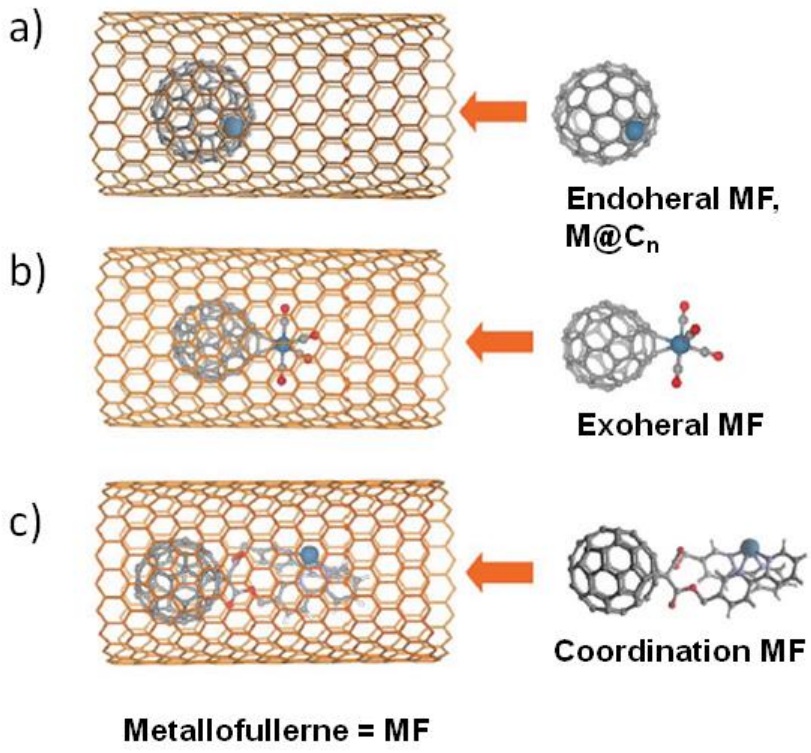


Figure 1-20. Fullerenes as carriers of metals into carbon nanotubes: a) endohedral metallofullerene, b) exohedral metallofullerene, c) coordination metallofullerene.[46]

However, the preparation of metallofullerenes requires special equipment and after purification the typical overall yield is less than 1%. In addition, as the metal atom is located inside the fullerene it is not accessible for electronic interactions and cannot take place in chemical reactions inside the nanotubes. Therefore to liberate the M atoms the fullerene cage has to be broken up by heating ($M@C_n$)@SWNTs at 1300-1400 °C. Moreover the type of

metals which can be encapsulated in the fullerene cage is usually limited to the Group III elements.[94]

The second approach is utilising exohedral metallofullerenes such as $Os_3(CO)_{11}(\eta^2\text{-}C_{60})$, $Os_3(CO)_9(\mu^3\text{-}\eta^2, \eta^2, \eta^2\text{-}C_{60})$ (Figure 1-21)[94] and $Re(\mu^5\text{-}C_{60}H_5)(CO)_3$,[95] which are organometallic complexes in which the fullerene cage ligates the metal atoms *via* C-M π-bonding (Figure 1-20 b). As exohedral metallofullerenes are not stable at the temperature (400-600 °C) required for the gas phase filling of C_{60} they were inserted into CNTs using a solution based filling method developed earlier.[52]

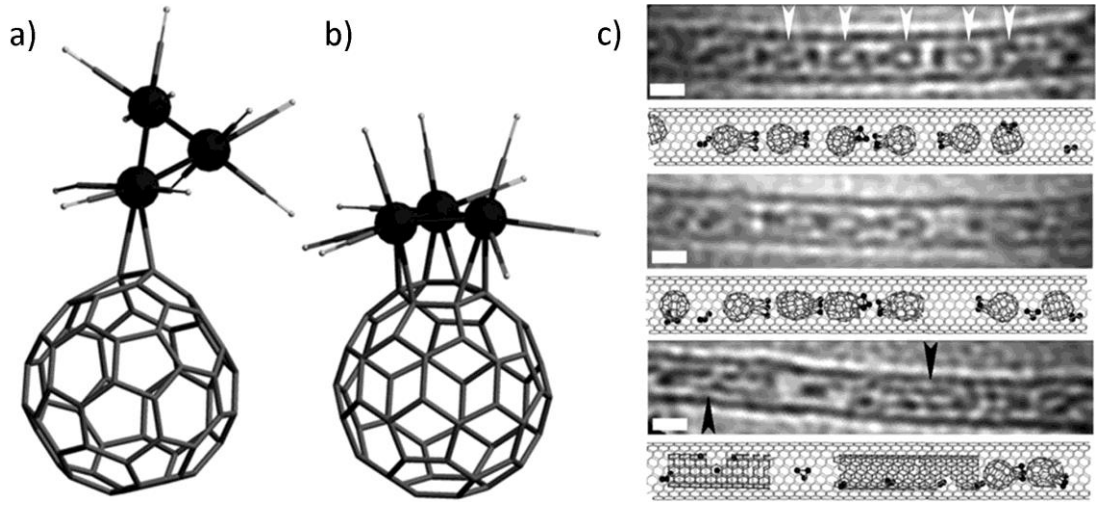


Figure 1-21. Structural diagrams of a) $Os_3(CO)_{11}(\eta^2\text{-}C_{60})$, b) $Os_3(CO)_9(\mu^3\text{-}\eta^2, \eta^2, \eta^2\text{-}C_{60})$ exohedral fullerenes and c) time-sequence of HRTEM images and structural diagrams of the evolution of exohedral metallofullerene b) in SWNT. White arrows indicate the positions of five intact metallofullerene molecules with M atoms to the side of each C_{60} cage (top image), and black arrows indicate segments of internal carbon nanotube formed through decomposition of b).[94]

In comparison to $(M@C_n)@SWNT$ in exohedral metallofullerenes the transition metal is readily accessible for interactions and reactions, consequently the TEM investigation of exohedral metallofullerenes encapsulated in CNTs requires moderate e-beam

current density. Such accessibility of the M atom(s) of exohedral metallofullerenes makes them valuable for the study of metal-carbon interactions and bonding in CNTs (Figure 1-21 c).

Unfortunately this methodology is typically limited to late transition metals which can form stable exohedral metallofullerenes.

In the third approach a fullerene functionalised with two double-chelating groups was designed to broaden the range of metals that can be inserted into CNTs in a controlled fashion (Figure 1-20 c).[96] In order to be able to accommodate M cations of different ionic radii and coordination numbers the double-chelating groups are attached to the fullerene cage *via* flexible methylene ester groups (–CH_2–OC(O)–) thereby allowing the variation of the disposition and distance between the two 2,2'-bipyridyl units. This methodology may allow the encapsulation of various M such as Cu, Ni, Co in CNTs.[97]

1.3.3 Formation of metal nanoparticles in wide hollow tubular carbon nanostructures

The formation hybrid nanomaterials based on discrete M-based NPs encased into wide hollow tubular carbon nanostructures *i.e.* carbon fibers and MWNTs is a field of growing interest. There are two methods used for the formation of discrete NPs in wide hollow carbon nanostructures including liquid phase chemistry, and incipient wetness technique. However, controlling

the size, shape and distribution of the NPs formed *in situ* is challenging. Therefore, the insertion of preformed NPs in hollow tubular carbon nanostructures has become widely used.

1.3.3.1 Liquid phase chemistry

As hollow tubular carbon nanostructures are inherently relatively inert and hydrophobic they have to be treated in order to make their surface capable to host the NPs. Jiang *et al.* successfully produced Au NPs with uniform size and shape in MWNTs using a novel liquid phase chemistry procedure.[98] First basic functional groups were introduced on the inner surface of the nanotubes *via* heating in NH_3, which then made the adsorption of citric acid possible. The last step of the procedure is the *in situ* reduction of $HAuCl_4$ to provide Au NPs inside the CNTs.

1.3.3.2 Incipient wetness technique

Endo *et al.* synthesised hybrid materials of GNF and individual Pt NPs by immersing the nanofibers into a solution of hexachloroplatinic acid (H_2PtCl_6).[99] After the solvent was removed by evaporation the sample was heated in H_2 atmosphere to form Pt NPs (Figure 1-22). Depending on the surface morphology of the GNFs, the authors managed to deposit NPs exclusively either on the surface, by using pristine GNFs, or on the interior of the GNFs, by using GNFs with pyrolytic (amorphous-like) carbon layers on their surface (Figure 1-22). If a shortened version of the GNFs was used it led to the formation of material in which NPs were

deposited on both the surface and interior of the GNFs.

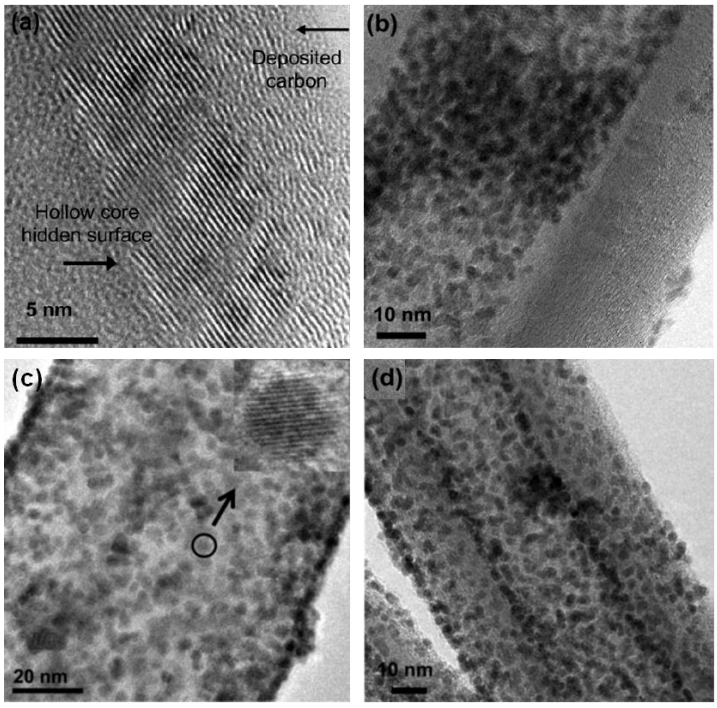


Figure 1-22. TEM images are showing: a) a duplex structure carbon nanofiber b) Pt NPs located exclusively inside a GNF, c) Pt NPs located exclusively on the surface of a GNF and d) Pt NPs located on the surface and inside shortened GNFs.[99]

1.3.3.3 Encapsulation of preformed nanoparticles

Serp *et al.* for the first time incorporated preformed PtRu NPs stabilised with 4-(3-phenylpropyl)pyridine in GNFs (Figure 1-23).[100] The M NPs were suspended in tetrahydrofuran which can easily penetrate into GNFs and deposit the M NPs in there due to its low surface tension (26 mN/m). Dodecanethiol-stabilised preformed gold NPs were incorporated into GNFs using a mixture of n-pentane and CO_2 in supercritical conditions (4000 psi, 40°C) by La Torre *et al.* to study their growth mechanism.[101]

In addition, magnetic Mn_3O_4 NPs have been inserted into two types of carbon nanofibers and it was found that the arrangement of the Mn_3O_4 NPs is determined by the internal structure of the

host nanofiber (Figure 1-24).[102]

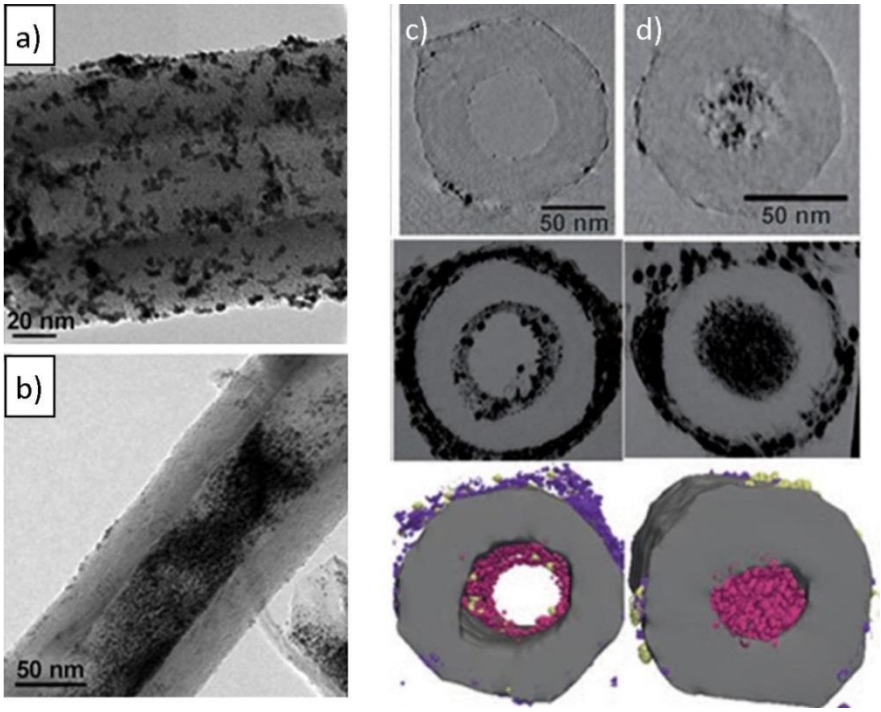


Figure 1-23. 2D TEM images are showing: a) PtRu NPs located on both the inside and outside of GNF, b) PtRu NPs located inside GNF. 3D TEM images are showing: c) PtRu NPs located on both the inside and outside of GNF, d) PtRu NPs located inside GNF.[100]

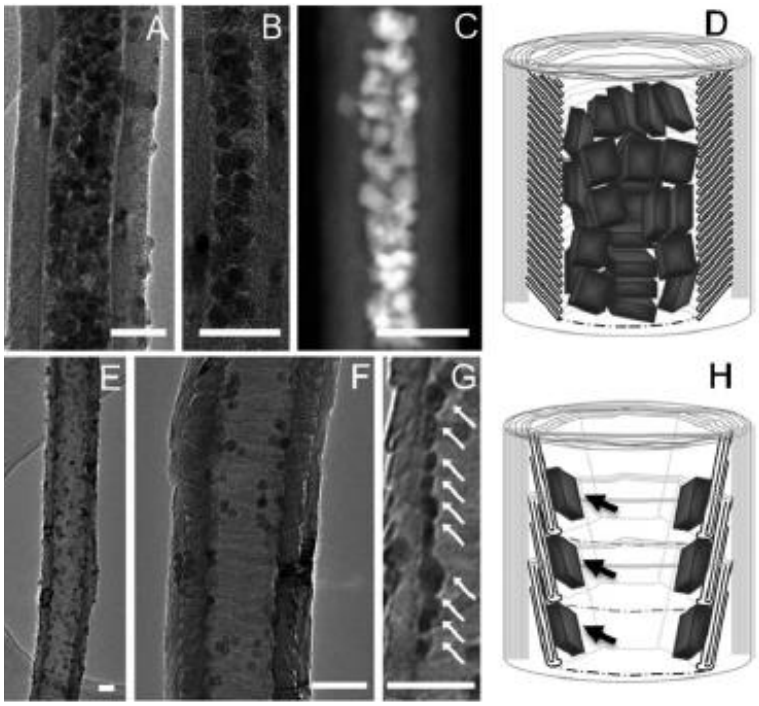


Figure 1-24. TEM images of Mn_3O_4@CNF a)–c) and Mn_3O_4@GNF e)–g). Dense packing of NPs in Mn_3O_4@CNF, as revealed by bright field TEM a)-b) and high-angle annular dark-field scanning TEM (HAADF STEM) C). Bright-field TEM images of Mn_3O_4 "nanobricks" adsorbed on the step-edges of GNF e)–g). The scale bars are 40 nm. Schematic diagrams illustrating Mn_3O_4 NP densely packed in a GNF d) and sparsely distributed within a GNF through anchoring to the graphitic step-edges h).[102]

1.4 Inorganic nanomaterials related to carbon based nanomaterials

In addition to fullerenes and CNTs other materials, which possess a weakly bonded layered structure in their bulk form, may form low-dimensional nanostructures with spherical or cylindrical shapes. The driving force behind the formation of curved nanostructures is the saturation of dangling bonds that can be found on the edges of the layers. These curved nanostructures are considered to be the thermodynamically preferred phase if the crystallites do not exceed a critical size (~100 nm).[103,104] In the bulk, above the critical crystallite size the van der Waals interactions between the layers are strong enough to prevent their curling, despite the presence of dangling bonds on the edges of the layers.[103,104] Consequently, in order to overcome the activation barrier *i.e.* the interlayer van der Waals interaction during the rolling up of the 2D layers even in the case of a few-layer thick material high reaction temperatures (>800 °C) or large activation energy is required.[104,105]

The first family of layered inorganic nanomaterials based on metal dichalcogenides in a form of concentric closed-shell structures was discovered by Tenne and coworkers.[106,107,108] In metal dichalcogenides the metal atoms typically are from Group IV-VII (M=Mo, W, Nb, Re, Ni, V) while the chalcogen atom may be S, Se, Te. The coordination of M in metal dichalcogenides

depends on which group M is from. Group IV, V and VII metal atoms prefer octahedral coordination geometry, while group VI metals *i.e.* Mo and W typically favour a trigonal-prismatic coordination, which is directly related to their semiconducting properties.[105]

MoS_2 and WS_2 were found to be ideal to synthesise inorganic onion-like structures, fullerenes (IF)[109] and nanotubes[106] as a single sheet of these compounds has a honeycomb structure that is similar to graphene. However, in contrast to the atomically thin graphene each MS_2 sheet consists of a single layer of M atoms sandwiched by two layers of S atoms (Figure 1-25).

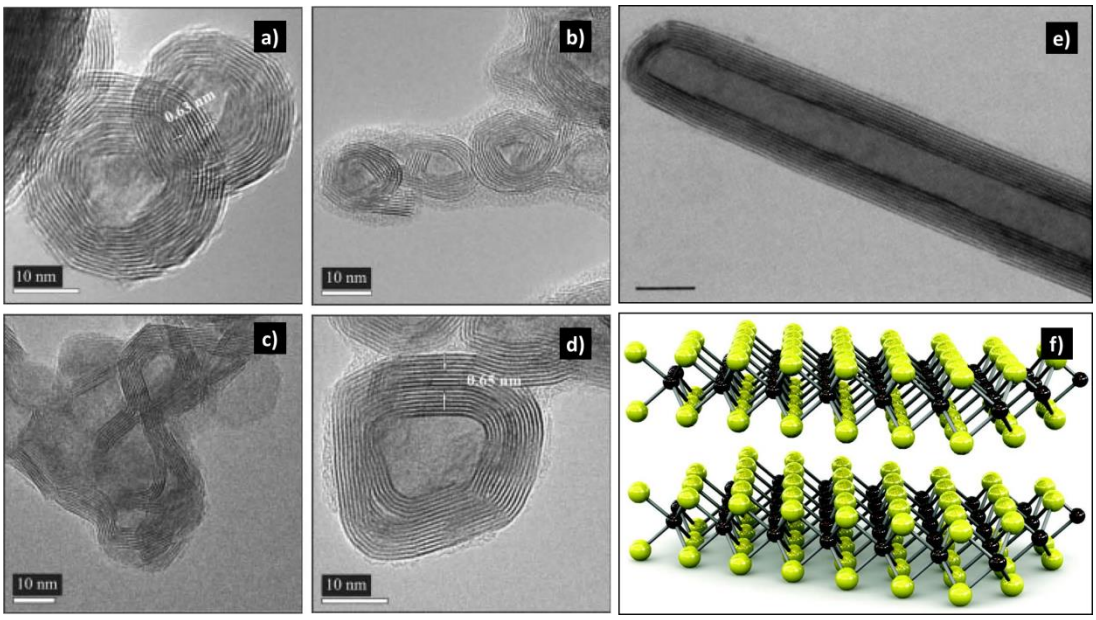


Figure 1-25. Images a)-d) are showing IF made of MoS_2,[109] e) shows a multi-walled MoS_2 nanotube[106] and f) depicts two layers of MoS_2 layers *i.e.* the lattices of Mo atoms are separated by 0.65 nm in which black atoms are Mo and yellow atoms are S.[110]

It is well known that spherical objects cannot be constructed from hexagonal rings exclusively, therefore, the formation of IF requires deviations from the ideal crystal structure of bulk MS_2. It

was proposed that triangular (Figure 1-26 a) or rhombohedral point defects (Figure 1-26 b) in the MS_2 lattice can result in curved layers similarly to those obtained by pentagonal or heptagonal rings in the case of graphene sheets.[107,111] The metal chalcogenide sheets in curved MoS_2 and WS_2 structures *i.e.* the lattices of Mo atoms are separated by 0.62-0.7 nm depending on how bent the sheets are.[109]

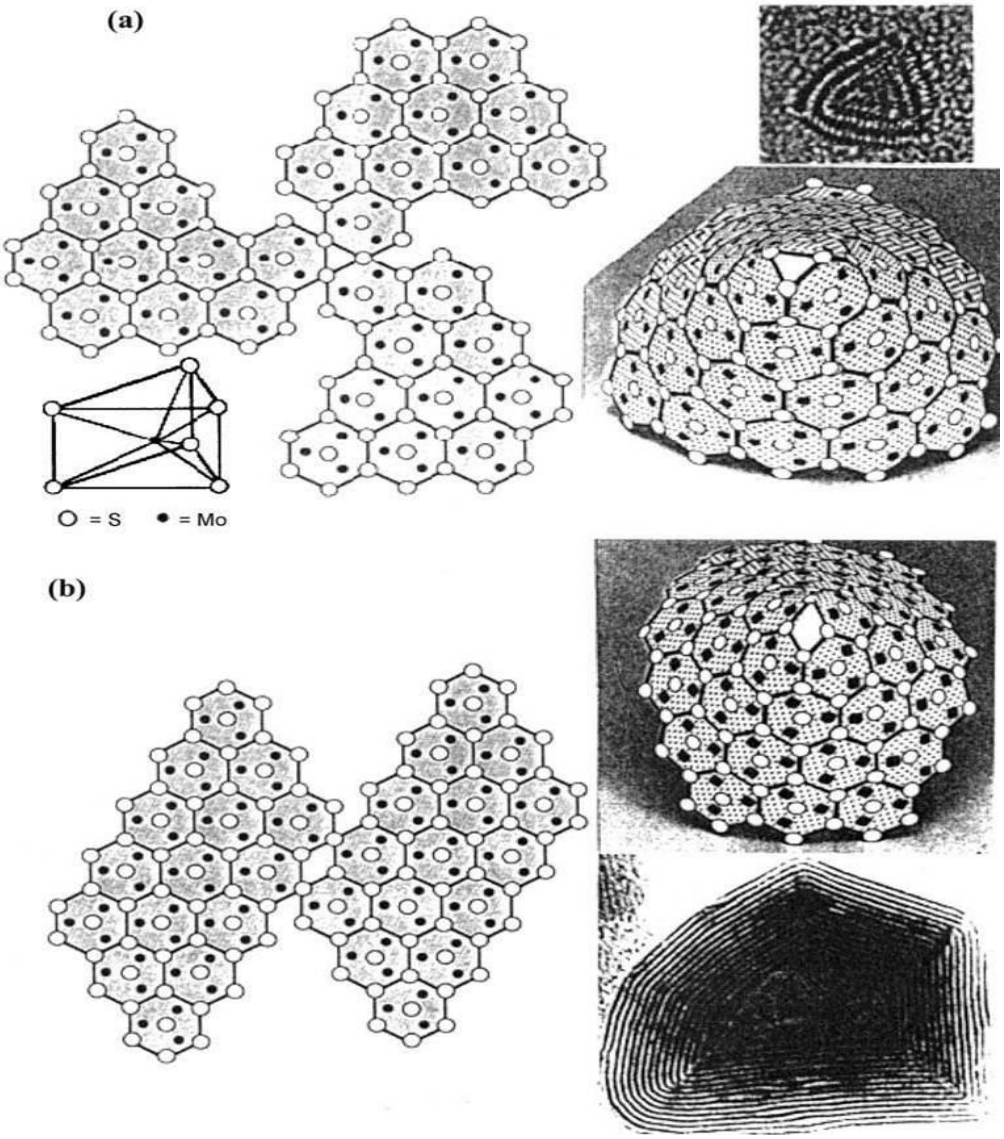


Figure 1-26. Illustration of various point defects which exists in the vertices of IF MoS_2: a) a triangular point defect, b) a rhombohedral point defect. Insets show IF structures that are likely to contain such point defects.[107,111]

The successful synthesis of metal dichalcogenides nanostructures sparked the growth an entire field of quasi-1D and 2D inorganic nanostructures such as inorganic-fullerenes and nanotubes based on layered materials.

Several of these inorganic nanostructures are inorganic nanotubes built from layered metal oxides.[111] These nanotubes and nanofibers can be synthesised directly or by using a template *via* sol–gel, hydro/solvothermal or electrochemical methods.[112,113] The most well-known examples are V_2O_5,[114] TiO_2,[113] (Figure 1-27) SiO_2,[115] Al_2O_3.[116]

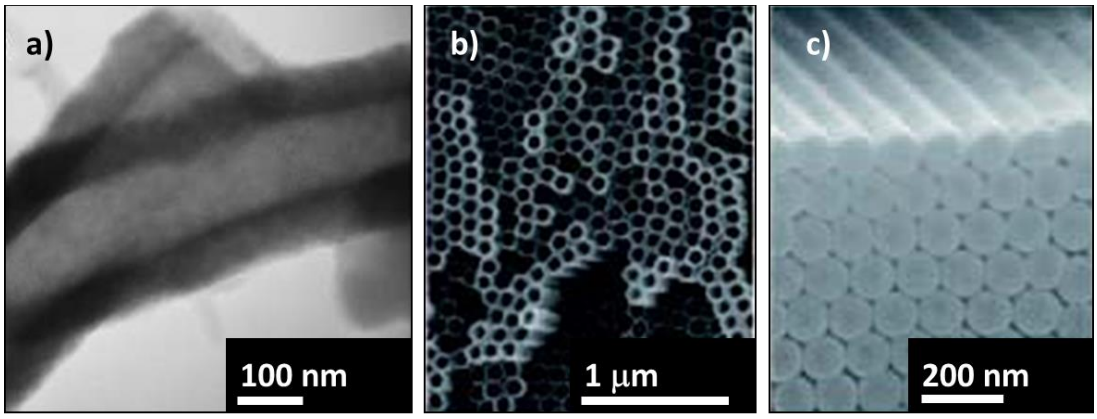


Figure 1-27. Image a) shows TEM micrograph of V_2O_5 nanotubes synthesised *via* template-based electrodeposition.[114] b)-c) are showing scanning electron microscope images of highly ordered TiO_2 nanotubes prepared by electrochemical anodisation.[113]

Another well-known family of inorganic nanostructures are made of boron nitride (BN). Boron nitride is remarkable as α-BN has a hexagonal graphite-like structure (Figure 1-28 a) in which each C-C pair is replaced by a B-N pair (Figure 1-28 b).[117,118] Despite the high similarity the layers are stacked differently in bulk α-BN crystal in comparison to graphite. In graphite the hexagonal layers *i.e.* A and B are shifted in respect to each other consequently a

series of C atoms found in layer B are located beneath the middle of a hexagon found in layer A (Figure 1-28 a), whereas the hexagonal layers of the BN (A and B) are located perfectly on top of each other and a N atom can be found beneath each B atom (Figure 1-28 b).

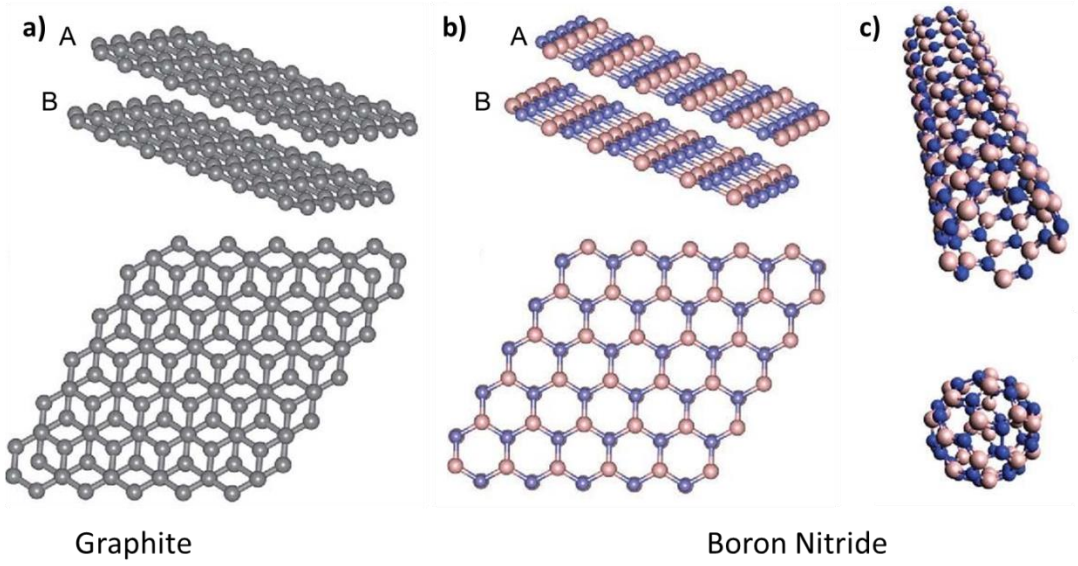


Figure 1-28. Structural diagrams a) shows the structure and AB stacking sequence of hexagonal graphite, while b) shows the structure and stacking sequence of α-BN in which B atoms are located on top of N atoms. Image c) shows 1D BN nanotube and 0D BN fullerene.[117]

Since B and N are the two nearest neighbours of C in the first row of the periodic table graphene and BN are isoelectronic, therefore BN is ideal material to form nanotubes or to dope CNTs.[119,120] Multi-walled BN nanotubes (BNNT) were synthesised for the first time using plasma assisted arc-discharge method similar that was used during the synthesis of C_{60} by Zettl and co-workers.[121] Growth of BNNTs is still challenging although numerous different methods such as laser ablation, substitution reactions from CNTs, ball-milling, chemical vapour deposition (CVD), have

been developed over the years.[122]

The physicochemical properties of BNNTs are very similar to CNTs *i.e.* they are mechanically robust and resist oxidation up to ~1000 °C. However, the electronic properties of BNNTs differ from CNTs as they have a large band gap (~6 eV) which is independent from their diameter and chirality, while SWNTs typically have a 0-1 eV band gap which strongly depends on their diameters and chiralities.[123,20]

1.4.1.1 Inorganic nanotubes formed using carbon nanotubes as templates

The first example of a nanotube inside nanotube system was DWNTs synthesised by the thermal decomposition of C_{60},[124] although DWNTs and MWNTs can be directly produced by other methods. The smallest diameter SWNT was produced in a similar way *via* thermal decomposition of $FeCp_2$ encapsulated in SWNTs.[125]

The templating capability of CNTs was utilised in several synthesis of various inorganic nanotubes with the inorganic nanotubes forming either on the surface of the CNT or inside the CNTs.

Carbon nanotubes were successfully applied as templates to grow MoS_2,[126,127] WS_2 (Figure 1-29)[128] and NbS_2 nanotubes on their surface by first coating CNTs with the oxide of the metals which were converted into MS_2 in a $H_2S/H_2/N_2$ atmosphere at elevated temperatures.[111]

Metal oxide nanotubes such as SiO_2, Al_2O_3, MoO_3, V_2O_5 and ZrO_2 were also prepared on the outer surface of CNTs.[129,111] In the latter case the inner CNTs were removed to provide freestanding ZrO_2 inorganic nanotubes (Figure 1-29).[130]

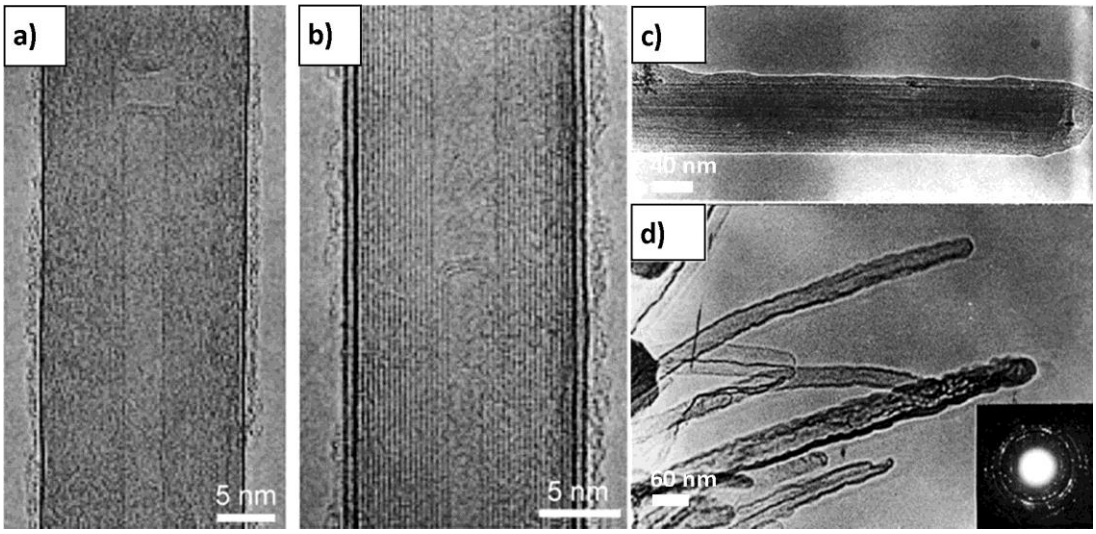


Figure 1-29. TEM images of a CNT coated with a) a single layer and b) a double layer of WS_2,[128] c) with ZrO_2 and d) hollow ZrO_2 nanotubes after removal of the CNT template.[130]

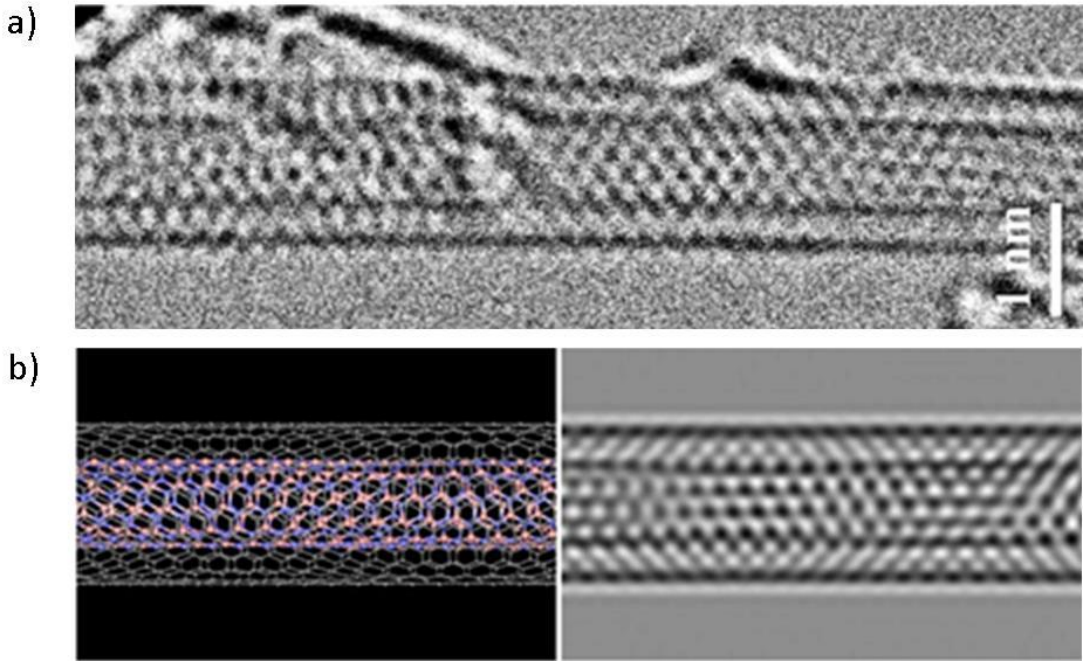


Figure 1-30. a) High magnification TEM image of BNNT@SWNT (d_{SWNT}=1.45 nm, d_{BNNT}=0.80 nm) and b) structural model and simulated TEM image of (7,5)BNNT encapsulated in (12,10)SWNT.[131]

Similarly to metal sulphides and oxides BN nanotubes were

grown using CNTs as templates. SWNTs were first filled with precursor molecules (ammonia borane) containing B as well as N, then the material was heated at high temperature to produce BNNT@SWNT (Figure 1-30).[131]

1.5 Summary

In summary, due to the empty space inside them various materials can be inserted into both CNTs and GNFs by applying the most suitable filling method from those which were described in Section 1.3.1. As it was discussed above the interaction between the host *i.e.* CNTs or GNFs and the encapsulated material can alter the physical and chemical properties of the hybrid nanomaterial which can lead to unique and potentially useful physicochemical properties. Currently the biggest challenges are to find suitable building units for the synthesis of hybrid nanomaterials with particular physicochemical properties and to combine them together in a controlled bottom-up assembly to achieve the desired properties. Therefore, in order to aid the selection of the right building units which if combined in a controlled fashion will provide hybrid nanomaterials with tailored physicochemical properties, first the fundamental interactions and their effect on the physicochemical properties of hybrid nanomaterials need to be systematically studied at the atomic scale.

1.6 Aim and Objectives

Building on the achievements of the field demonstrated in Section 1.3 the aim of this work is in furthering the understanding of how confinement on the nanoscale alters the properties of matter by covalent and non-covalent interactions to pave the design and synthesis of novel hybrid nanomaterials in the future.

Particularly, this study is dedicated to probe the interactions of metal containing molecules, nanoparticles (NP) and nanostructures with the interior of hollow graphitic structures, and to investigate the effect of confinement on the products of chemical reactions performed in the nanoscale channels of the hollow graphitic materials. Therefore, the main objectives of the research project were:

- the preparation of hybrid nanostructures based on metal containing molecules and hollow graphitic structures,

- the probing of interactions of metal containing molecules and nanoparticles (NP) with the interior of hollow graphitic structures,

- the investigation of the confinement effects on the products of chemical reactions performed in the nanoscale channels of the hollow graphitic materials.

1.7 References

1. Europien Comission, *Future Needs & Challenges for Materials and Nanotechnology Research*, Brussels, 2001.
2. L. Radushkevich and V. Lukyanovich, *Zurn Fis. Chim*, 1952, **26**, 88–95.
3. H. W. Kroto, J. R. Heath, S. C. O'Brien, R. F. Curl, and R. E. Smalley, *Nature*, 1985, **318**, 162–163.
4. W. Krätschmer, L. D. Lamb, K. Fostiropoulos, and D. R. Huffman, *Nature*, 1990, **347**, 354–358.
5. S. Iijima, *Nature*, 1991, **354**, 56–58.
6. M. Monthioux and V. Kuznetsov, *Carbon N. Y.*, 2006, **44**, 1621–1623.
7. S. Iijima and T. Ichihashi, *Nature*, 1993, **363**, 603–605.
8. D. S. Bethune, C. H. Klang, M. S. de Vries, G. Gorman, R. Savoy, J. Vazquez, and R. Beyers, *Nature*, 1993, **363**, 605–607.
9. K. S. Novoselov, A. K. Geim, S. V Morozov, D. Jiang, Y. Zhang, S. V Dubonos, I. V Grigorieva, and A. A. Firsov, *Science*, 2004, **306**, 666–669.
10. A. K. Geim and K. S. Novoselov, *Nat. Mater.*, 2007, **6**, 183–191.
11. A. Chuvilin, U. Kaiser, E. Bichoutskaia, N. A. Besley, and A. N. Khlobystov, *Nat. Chem.*, 2010, **2**, 450–453.

12. C. Wang, K. Takei, T. Takahashi, and A. Javey, *Chem. Soc. Rev.*, 2013, **42**, 2592–609.
13. T. Hasobe, S. Fukuzumi, and P. V Kamat, *J. Phys. Chem. B*, 2006, **110**, 25477–25484.
14. S. Tans, A. Verschueren, and C. Dekker, *Nature*, 1998, **393**, 49–52.
15. D. Yu, K. Goh, H. Wang, L. Wei, W. Jiang, Q. Zhang, L. Dai, and Y. Chen, *Nat. Nanotechnol.*, 2014, **9**, 555–562.
16. H. Sun, X. You, J. Deng, X. Chen, Z. Yang, J. Ren, and H. Peng, *Adv. Mater.*, 2014, **26**, 2868–2873.
17. E. Joselevich, *Chemphyschem*, 2004, **5**, 619–624.
18. P. Castrucci, M. Scarselli, M. De Crescenzi, M. A. El Khakani, and F. Rosei, *Nanoscale*, 2010, **2**, 1611–1625.
19. S. Niyogi, M. A. Hamon, H. Hu, B. Zhao, P. Bhowmik, R. Sen, M. E. Itkis, and R. C. Haddon, *Acc. Chem. Res.*, 2002, **35**, 1105–1113.
20. R. Saito, M. Fujita, G. Dresselhaus, and M. S. Dresselhaus, *Appl. Phys. Lett.*, 1992, **60**.
21. R. Satio, G. Dresselhaus, and M. S. Dresselhaus, *Physical properties of carbon nanotubes*, Imperial College, London, 1998.
22. K. Kamarás, Á. Pekker, B. Botka, H. Hu, S. Niyogi, M. E. Itkis, and R. C. Haddon, *Phys. Status Solidi B*, 2010, **247**, 2754–2757.

23. H. Liu, D. Nishide, T. Tanaka, and H. Kataura, *Nat. Commun.*, 2011, **2:309**, 1–8.

24. S. A. Hodge, M. K. Bayazit, K. S. Coleman, and M. S. P. Shaffer, *Chem. Soc. Rev.*, 2012, **41**, 4409–4429.

25. S. Arepalli, P. Nikolaev, O. Gorelik, V. G. Hadjiev, W. Holmes, B. Files, and L. Yowell, *Carbon N. Y.*, 2004, **42**, 1783–1791.

26. A. Ferrari and J. Robertson, *Phys. Rev. B*, 2000, **61**, 14095–14107.

27. M. Burghard, *Surf. Sci. Rep.*, 2005, **58**, 1–109.

28. A. A. Mamedov, N. A. Kotov, M. Prato, D. M. Guldi, J. P. Wicksted, and A. Hirsch, *Nat. Mater.*, 2002, **1**, 190–194.

29. A. Jorio, M. A. Pimenta, A. G. S. Filho, R. Saito, G. Dresselhaus, and M. S. Dresselhaus, *New J. Phys.*, 2003, **5**, 139.1–139.7.

30. R. A. Jishi, L. Venkataraman, M. S. Dresselhaus, and G. Dresselhaus, *Chem. Phys. Lett.*, 1993, **209**, 77–82.

31. J. Kürti, G. Kresse, and H. Kuzmany, *Phys. Rev. B*, 1998, **58**, R8869–R8872.

32. M. S. Dresselhaus, G. Dresselhaus, A. Jorio, A. G. Souza Filho, and R. Saito, *Carbon N. Y.*, 2002, **40**, 2043–2061.

33. M. Pimenta, A. Marucci, S. Empedocles, M. Bawendi, E. Hanlon, A. Rao, P. Eklund, R. Smalley, G. Dresselhaus, and M. Dresselhaus, *Phys. Rev. B*, 1998, **58**, R16016–R16019.

34. A. Jorio, A. Souza Filho, G. Dresselhaus, M. Dresselhaus, A. Swan, M. Ünlü, B. Goldberg, M. Pimenta, J. Hafner, C. Lieber, and R. Saito, *Phys. Rev. B*, 2002, **65**, 155412–1–155412–9.

35. D. Tasis, N. Tagmatarchis, A. Bianco, and M. Prato, *Chem. Rev.*, 2006, **106**, 1105–1136.

36. E. T. Thostenson, C. Li, and T. W. Chou, *Compos. Sci. Technol.*, 2005, 65, 491–516.

37. P. Singh, S. Campidelli, S. Giordani, D. Bonifazi, A. Bianco, and M. Prato, *Chem. Soc. Rev.*, 2009, **38**, 2214–2230.

38. C. Romero-Nieto, R. García, M. Á. Herranz, C. Ehli, M. Ruppert, A. Hirsch, D. M. Guldi, and N. Martín, *J. Am. Chem. Soc.*, 2012, **134**, 9183–9192.

39. J. Zhao, J. P. Lu, J. Han, and C.-K. Yang, *Appl. Phys. Lett.*, 2003, **82**, 3746–3748.

40. D. Nishide, H. Dohi, T. Wakabayashi, E. Nishibori, S. Aoyagi, M. Ishida, S. Kikuchi, R. Kitaura, T. Sugai, and M. Sakata, *Chem. Phys. Lett.*, 2006, **428**, 356–360.

41. L. Moura, L. Malard, M. Carneiro, P. Venezuela, R. Capaz, D. Nishide, Y. Achiba, H. Shinohara, and M. Pimenta, *Phys. Rev. B*, 2009, **80**, 161401–1–161401–4.

42. U. H. Brinker and J. L. Mieusset, Eds., *Molecular Encapsulation: Organic Reactions in Constrained Systems*, New York, 2010.

43. D. A. Britz, A. N. Khlobystov, K. Porfyrakis, A. Ardavan, and G. A. D. Briggs, *Chem. Commun.*, 2005, 37–39.

44. H. Shiozawa, T. Pichler, A. Grüneis, R. Pfeiffer, H. Kuzmany, Z. Liu, K. Suenaga, and H. Kataura, *Adv. Mater.*, 2008, **20**, 1443–1449.

45. S. A. Miners, G. A. Rance, and A. N. Khlobystov, *Chem. Commun. (Camb).*, 2013, **49**, 5586–5588.

46. A. N. Khlobystov, *ACS Nano*, 2011, **5**, 9306–9312.

47. Http://www.formula1-dictionary.net/carbon-carbon.html, .

48. M. Endo, Y. a. Kim, T. Hayashi, Y. Fukai, K. Oshida, M. Terrones, T. Yanagisawa, S. Higaki, and M. S. Dresselhaus, *Appl. Phys. Lett.*, 2002, **80**, 1267–1269.

49. S.-H. Kim, P. B. Kelly, and A. J. Clifford, *Anal. Chem.*, 2008, **80**, 7661–7669.

50. B. W. Smith, M. Monthioux, and D. E. Luzzi, *Chem. Phys. Lett.*, 1999, **315**, 31–36.

51. A. N. Khlobystov, D. A. Britz, and G. A. D. Briggs, *Acc. Chem. Res.*, 2005, **38**, 901–909.

52. T. W. Chamberlain, A. M. Popov, A. A. Knizhnik, G. E. Samoilov, and A. N. Khlobystov, *ACS Nano*, 2010, **4**, 5203–5210.

53. D. A. Britz and A. N. Khlobystov, *Chem. Soc. Rev.*, 2006, **35**, 637–659.

54. A. N. Khlobystov, D. A. Britz, J. Wang, S. A. O'Neil, M. Poliakoff, and G. A. D. Briggs, *J. Mater. Chem.*, 2004, **14**, 2852–2857.

55. H. Shiozawa, T. Pichler, C. Kramberger, A. Grüneis, M. Knupfer, B. Büchner, V. Zólyomi, J. Koltai, J. Kürti, D. Batchelor, and H. Kataura, *Phys. Rev. B*, 2008, **77**, 3–6.

56. M. Monthioux, *Carbon N. Y.*, 2002, **40**, 1809–1823.

57. M. Monthioux and E. Flahaut, *Mater. Sci. Eng. C*, 2007, **27**, 1096–1101.

58. A. N. Khlobystov, in *Chemistry of Carbon Nanotubes*, eds. V. A. Basiuk and E. V. Basiuk, 1st edn., 2008, pp. 87–109.

59. T. W. Chamberlain, M. del C. Gimenez-Lopez, and A. N. Khlobystov, *Carbon Nanotub.*, 2010, 349–384.

60. D. Mattia and Y. Gogotsi, *Microfluid. Nanofluidics*, 2008, **5**, 289–305.

61. M. Yudasaka, *Chem. Phys. Lett.*, 2003, **380**, 42–46.

62. J. Chancolon, F. Archaimbault, S. Bonnamy, a Traverse, L. Olivi, and G. Vlaic, *J. Non. Cryst. Solids*, 2006, **352**, 99–108.

63. M. Chernysheva, E. Kiseleva, N. Verbitskii, A. A. Eliseev, a Lukashin, Y. Tretyakov, S. Savilov, N. Kiselev, O. Zhigalina, and a Kumskov, *Phys. E Low-dimensional Syst. Nanostructures*, 2008, **40**, 2283–2288.

64. T. Fujimori, A. Morelos-Gómez, Z. Zhu, H. Muramatsu, R. Futamura, K. Urita, M. Terrones, T. Hayashi, M. Endo, S. Young Hong, Y. Chul Choi, D. Tománek, and K. Kaneko, *Nat. Commun.*, 2013, **4**, 2162–2170.

65. R. Carter, J. Sloan, A. Kirkland, R. Meyer, P. Lindan, G. Lin, M. Green, A. Vlandas, J. Hutchison, and J. Harding, *Phys. Rev. Lett.*, 2006, **96**, 215501–1–215501–4.

66. L. V. Yashina, A. A. Eliseev, M. V. Kharlamova, A. A. Volykhov, A. V. Egorov, S. V. Savilov, A. V. Lukashin, R. Püttner, and A. I. Belogorokhov, *J. Phys. Chem. C*, 2011, **115**, 3578–3586.

67. M. V. Kharlamova, L. V. Yashina, and A. V. Lukashin, *Appl. Phys. A*, 2013, **112**, 297–304.

68. L. Guan, K. Suenaga, Z. Shi, Z. Gu, and S. Iijima, *Nano Lett.*, 2007, **7**, 1532–1535.

69. A. A. Eliseev, L. V. Yashina, M. M. Brzhezinskaya, M. V. Chernysheva, M. V. Kharlamova, N. I. Verbitsky, A. V. Lukashin, N. A. Kiselev, A. S. Kumskov, and R. M. Zakalyuhin, *Carbon N. Y.*, 2010, **48**, 2708–2721.

70. L. Grigorian, K. Williams, S. Fang, G. Sumanasekera, A. Loper, E. Dickey, S. Pennycook, and P. Eklund, *Phys. Rev. Lett.*, 1998, **80**, 5560–5563.

71. H. Song, Y. Ishii, A. Al-Zubaidi, T. Sakai, and S. Kawasaki, *Phys. Chem. Chem. Phys.*, 2013, **15**, 5767–5770.

72. M. V. Chernysheva, A. A. Eliseev, A. V. Lukashin, Y. D. Tretyakov, S. V. Savilov, N. A. Kiselev, O. M. Zhigalina, A. S. Kumskov, A. V. Krestinin, and J. L. Hutchison, *Phys. E Low-dimensional Syst. Nanostructures*, 2007, **37**, 62–65.

73. N. Kiselev, R. Zakalyukin, O. Zhigalina, N. Grobert, A. Kumskov, Y. V. Grigoriev, M. Chernysheva, A. A. Eliseev, A. Krestinin, Y. D. Tretyakov, and others, *J. Microsc.*, 2008, **232**, 335–342.

74. A. A. Eliseev, L. V. Yashina, N. I. Verbitskiy, M. M. Brzhezinskaya, M. V. Kharlamova, M. V. Chernysheva, A. V. Lukashin, N. A. Kiselev, A. S. Kumskov, B. Freitag, A. V. Generalov, A. S. Vinogradov, Y. V. Zubavichus, E. Kleimenov, and M. Nachtegaal, *Carbon N. Y.*, 2012, **50**, 4021–4039.

75. M. V. Kharlamova, L. V. Yashina, and A. V. Lukashin, *J. Mater. Sci.*, 2013, **48**, 8412–8419.

76. R. Zakalyukin, B. Mavrin, L. Demyanets, and N. Kiselev, *Carbon N. Y.*, 2008, **46**, 1574–1578.

77. S. Friedrichs, U. Falke, and M. L. H. Green, *Chem. Phys. Chem.*, 2005, **6**, 300–305.

78. T. Takenobu, T. Takano, M. Shiraishi, Y. Murakami, M. Ata, H. Kataura, Y. Achiba, and Y. Iwasa, *October*, 2003, **2**, 683–688.

79. Y. Ren and G. Pastorin, *Adv. Mater.*, 2008, **20**, 2031–2036.

80. L. Alvarez, Y. Almadori, R. Arenal, R. Babaa, T. Michel, R. Le Parc, J. Bantignies, B. Jousselme, S. Palacin, P. Hermet, and others, *J. Phys. Chem. C*, 2011, 11898–11905.

81. B. Fei, H. Lu, W. Chen, and J. Xin, *Carbon N. Y.*, 2006, **44**, 2261–2264.

82. M. Yao, P. Stenmark, E. Abou-Hamad, F. Nitze, J. Qin, C. Goze-Bac, and T. Wagberg, *Carbon N. Y.*, 2010, **49**, 1159–1166.

83. J. Wang, M. K. Kuimova, M. Poliakoff, G. A. D. Briggs, and A. N. Khlobystov, *Angew. Chem. Int. Ed. Engl.*, 2006, **45**, 5188–5191.

84. A. N. Khlobystov, K. Porfyrakis, M. Kanai, D. a Britz, A. Ardavan, H. Shinohara, T. J. S. Dennis, and G. A. D. Briggs, *Angew. Chem. Int. Ed. Engl.*, 2004, **43**, 1386–1389.

85. J. Sloan, J. Hammer, M. Zwiefka-Sibley, and M. L. H. Green, *Chem. Commun.*, 1998, **1**, 347–348.

86. H. Shiozawa, T. Pichler, R. Pfeiffer, H. Kuzmany, and H. Kataura, *Phys. Status Solidi B*, 2007, **244**, 4102–4105.

87. H. Shiozawa, C. E. Giusca, S. R. P. Silva, H. Kataura, and T. Pichler, *Phys. Status Solidi B*, 2008, **245**, 1983–1985.

88. N. Nemes, F. Stercel, J. Fischer, and D. E. Luzzi, *Mat. Res. Soc. Symp. Proc.*, 2001, **706**, Z.7.8.1–Z.7.8.6.

89. L. Guan, Z. Shi, M. Li, and Z. Gu, *Carbon N. Y.*, 2005, **43**, 2780–2785.

90. H. Kataura, Y. Maniwa, M. Abe, A. Fujiwara, K. Kikuchi, T. Kodama, H. Imahori, Y. Misaki, S. Suzuki, and Y. Achiba, *Appl. Phys. A Mater. Sci. Process.*, 2002, **74**, 349–354.

91. L.-J. Li, A. N. Khlobystov, J. G. Wiltshire, G. A. D. Briggs, and R. J. J. Nicholas, *Nat. Mater.*, 2005, **4**, 481–485.

92. L. Girifalco and M. Hodak, *Phys. Rev. B*, 2002, **65**, 1–5.

93. H. Ulbricht, G. Moos, and T. Hertel, *Phys. Rev. Lett.*, 2003, **90**, 7–10.

94. T. W. Chamberlain, N. R. Champness, M. Schröder, and A. N. Khlobystov, *Chem. Eur. J.*, 2011, **17**, 668–674.

95. T. W. Chamberlain, J. C. Meyer, J. Biskupek, J. Leschner, A. Santana, N. A. Besley, E. Bichoutskaia, U. Kaiser, and A. N. Khlobystov, *Nat. Chem.*, 2011, **3**, 732–737.

96. J. Fan, T. W. Chamberlain, Y. Wang, S. Yang, A. J. Blake, M. Schröder, and A. N. Khlobystov, *Chem. Commun. (Camb).*, 2011, **47**, 5696–5698.

97. M. a. Lebedeva, T. W. Chamberlain, E. S. Davies, D. Mancel, B. E. Thomas, M. Suyetin, E. Bichoutskaia, M. Schröder, and A. N. Khlobystov, *Chem. - A Eur. J.*, 2013, **19**, 11999–12008.

98. L. Jiang and L. Gao, *Carbon N. Y.*, 2003, **41**, 2923–2929.

99. M. Endo, Y. A. Kim, M. Ezaka, K. Osada, T. Yanagisawa, T. Hayashi, M. Terrones, and M. S. Dresselhaus, *Nano Lett.*, 2003, **3**, 723–726.

100. E. Castillejos, P.-J. Debouttière, L. Roiban, A. Solhy, V. Martinez, Y. Kihn, O. Ersen, K. Philippot, B. Chaudret, and P. Serp, *Angew. Chem. Int. Ed. Engl.*, 2009, **48**, 2529–2533.
101. A. La Torre, M. D. C. Gimenez-Lopez, M. W. Fay, G. A. Rance, W. A. Solomonsz, T. W. Chamberlain, P. D. Brown, and A. N. Khlobystov, *ACS Nano*, 2012, **6**, 2000–2007.
102. M. D. C. Gimenez-Lopez, A. La Torre, M. W. Fay, P. D. Brown, and A. N. Khlobystov, *Angew. Chem. Int. Ed. Engl.*, 2013, **52**, 2051–2054.
103. W. Tremel, *Angew. Chemie - Int. Ed.*, 1999, 38, 2175–2179.
104. R. Tenne, *Adv. Mater.*, 1995, **7**, 965–995.
105. N. Zink, J. Pansiot, J. Kieffe, H. A. Therse, M. Panthöfer, F. Rocker, U. Kolb, and W. Tremel, *Chem. Mater.*, 2007, **19**, 6391–6400.
106. R. Tenne, L. Margulis, M. Genut, and G. Hodes, *Nature*, 1992, 360, 444–446.
107. L. Margulis, G. Salitra, R. Tenne, and M. Talianker, *Nature*, 1993, **365**, 113–114.
108. Y. Feldman, E. Wasserman, D. J. Srolovitz, and R. Tenne, *Science*, 1995, **267**, 222–225.
109. J. Etzkorn, H. a. Therese, F. Rocker, N. Zink, U. Kolb, and W. Tremel, *Adv. Mater.*, 2005, **17**, 2372–2375.
110. B. Radisavljevic, A. Radenovic, J. Brivio, V. Giacometti, and A. Kis, *Nat. Nanotechnol.*, 2011, **6**, 147–50.

111. C. N. R. Rao and M. Nath, *Dalt. Trans.*, 2003, 1–24.

112. M. Lee, T. Kim, C. Bae, H. Shin, and J. Kim, *Jom*, 2010, 62, 44–49.

113. P. Roy, S. Berger, and P. Schmuki, *Angew. Chemie - Int. Ed.*, 2011, 50, 2904–2939.

114. Y. Wang, K. Takahashi, H. Shang, and G. Cao, *J. Phys. Chem. B*, 2005, 109, 3085–3088.

115. L. Wang, S. Tomura, F. Ohashi, M. Maeda, M. Suzuki, and K. Inukai, *J. Mater. Chem.*, 2001, **11**, 1465–1468.

116. J. Hwang, B. Min, J. S. Lee, K. Keem, K. Cho, M.-Y. Sung, M.-S. Lee, and S. Kim, *Adv. Mater.*, 2004, **16**, 422–425.

117. N. G. Chopra, R. J. Luyken, K. Cherrey, V. H. Crespi, M. L. Cohen, S. G. Louie, and A. Zettl, *Science*, 1995, **269**, 966–967.

118. A. L. Tiano, C. Park, J. W. Lee, H. H. Luong, L. J. Gibbons, S.-H. Chu, S. Applin, P. Gnoffo, S. Lowther, H. J. Kim, P. M. Danehy, J. a. Inman, S. B. Jones, J. H. Kang, G. Sauti, S. a. Thibeault, V. Yamakov, K. E. Wise, J. Su, and C. C. Fay, *Proc. SPIE*, 2014, **9060**, 906006–906019.

119. T. Oku, *Synthesis, Atomic Structures and Properties of Boron Nitride Nanotubes*, 2013.

120. D. Golberg, Y. Bando, W. Han, K. Kurashima, and T. Sato, 1999, 337–342.

121. N. G. Chopra, R. J. Luyken, K. Cherrey, V. H. Crespi, M. L. Cohen, S. G. Louie, and a Zettl, *Science (80-.).*, 1995, 269, 966–967.

122. J. Wang, C. H. Lee, Y. Bando, D. Golberg, and Y. K. Yap, *Carbon N. Y.*, 2009, 23–45.

123. A. Rubio, J. L. Corkill, and M. L. Cohen, *Phys. Rev. B*, 1994, **49**, 5081–5084.

124. S. Bandow, M. Takizawa, K. Hirahara, M. Yudasaka, and S. Iijima, *Chem. Phys. Lett.*, 2001, **337**, 48–54.

125. L. Guan, K. Suenaga, and S. Iijima, *Nano Lett.*, 2008, **8**, 459–462.

126. Q. Wang and J. Li, *J. Phys. Chem. C*, 2007, **111**, 1675–1682.

127. C. Lu, W.-W. Liu, H. Li, and B. K. Tay, *Chem. Commun. (Camb).*, 2014, 3338–3340.

128. R. L. D. Whitby, W. K. Hsu, C. B. Boothroyd, P. K. Fearon, H. W. Kroto, and D. R. M. Walton, *ChemPhysChem*, 2001, **2**, 620–623.

129. B. C. Satishkumar, A. Govindaraj, M. Nath, and C. N. R. Rao, *J. Mater. Chem.*, 2000, **10**, 2115–2119.

130. C. N. R. Rao, B. C. Satishkumar, and A. Govindaraj, *Chem. Commun.*, 1997, **2**, 1581–1582.

131. R. Nakanishi, R. Kitaura, J. H. Warner, Y. Yamamoto, S. Arai, Y. Miyata, and H. Shinohara, *Sci. Rep.*, 2013, **3**, 1385.1–1385.6.

2 Investigation of the interactions of metal hexacarbonyl complex with carbon nanotubes by vibrational spectroscopy

2.1 Introduction

The aim of this study is to gain an understanding of the fundamental interactions between the interior of single-walled carbon nanotubes (SWNTs) and the molecules located inside their one-dimensional channel. To be able to tackle this challenge a number of key objectives have to be determined. The most important milestones are 1) the identification of suitable guest-molecules; 2) finding the correct method of their insertion into carbon nanotubes and most importantly 3) determining a suitable analytical technique to analyse the resultant materials.

The ideal analysis technique would be transmission electron microscopy (TEM) which provides extremely valuable real time information in direct space about the atomic structure of hybrid nanomaterials such as C_{60}@SWNT. TEM image series can help to understand the dynamics of the interactions and processes present in materials such as the rotational motion of (Ce@C_{82})@ SWNTs.[1]

However, currently the analysis of host-guest interactions by TEM is limited, as most molecules quickly decompose in the microscope due to knock-on damage caused by the electron beam (e-beam). It is expected that faster acquisition times and lower

acceleration voltages will enable researchers to collect high quality data on delicate molecular nanomaterials in the near future. However, regardless of future developments in TEM, any analysis will always be limited to microscopic portions of the material. Therefore, to bypass this difficulty and to be able to harness the desired information about delicate systems on a macroscopic scale less invasive alternative analytical techniques have to be utilised.

In chemistry, the properties of materials are most commonly probed by spectroscopic techniques. Among the numerous types of available spectroscopic methods, vibrational spectroscopy provides essential information about the strength of chemical bonds and the symmetry of molecules. Although single-walled carbon nanotubes have strong resonant Raman active vibrations, they are not particularly infrared (IR) active apart from a C=C vibration which occurs around 1600 cm^{-1}. Consequently, if the guest-molecules were to posses IR active vibrations, upon nanotube encapsulation these vibrations could be used as internal probes to assess the nature and strength of the host-guest interactions by IR spectroscopy.

Another important parameter that has to be taken into account is the size and shape of the guest-molecules, as it has to be commensurate with the internal cavity of the host SWNTs. The size of an ideal guest-molecule (d_{guest}) can be estimated by Equation 2-1, which is 0.8 nm in case of SWNTs of a diameter

(d_{NT}) 1.4 nm, typical for nanotubes prepared in an electric arc-discharge.

Equation 2-0 $$d_{guest} = d_{NT} - 0.6\text{nm}$$

After considering all of the above outlined criteria, transition metal carbonyl complexes were selected as guest-molecules for the following reasons.

Firstly, their vibrational properties make them ideal candidates to act as internal IR probes, as the C=O stretching vibrations (ν_{CO}) of metal carbonyl complexes have a very intense IR response and their frequencies are extremely sensitive to the molecular environment.[2]

In addition, the IR spectra of group VI metal hexacarbonyl complexes ($M(CO)_6$, M=Cr, Mo, W) only contain one ν_{CO} band, which may simplify the interpretation of the IR spectrum of the $M(CO)_6$-SWNT host-guest systems.

Secondly, the van der Waals diameter of $M(CO)_6$ molecules is approximately a 0.77 nm diameter which is very close to the ideal guest-molecule size (0.8 nm) for 1.4 nm SWNTs (Equation 2-0).

Thirdly, metal carbonyl complexes are used to produce metal coatings by chemical vapour deposition (CVD), as they sublime readily without decomposition and are thermodynamically stable (Table 2-1).[3] Therefore, it is possible for them to be encapsulated into carbon nanotubes using a gas phase filling method.

Table 2-1. Dissociation energies of the metal carbon (M-C) bond for ($M(CO)_6$, M=Cr, Mo, W).[3]

$D_{(M-C)}$/kJ mol^{-1}		
$Cr(CO)_6$	$Mo(CO)_6$	$W(CO)_6$
113.04	150.72	175.85

Finally, the metal centre of $M(CO)_6$ molecules can be used to determine whether the encapsulation process was successful by transmission electron microscopy, since the metal atoms will produce a relatively high contrast in TEM due to their high atomic number, *Z*. In addition, all three metals can be easily identified by the characteristic X-ray photons that the metal atoms emit in the electron beam of TEM, so that successful insertion of the molecules into nanotubes can be confirmed by energy dispersive X-ray spectroscopy (EDX).

2.1.1 Fundamental properties of metal carbonyl complexes

Metal carbonyl complexes are defined as molecules with at least one central metal atom surrounded by coordinated carbon monoxide ligands *i.e.* $M_x(CO)_y$ (homoleptic/binary carbonyls). However, not only homoleptic but also heteroleptic carbonyls are well known such as $M_x(CO)_yL_n$, where L is a non-carbonyl ligand, *e.g.* acetonitrile, arenes, cyclopentadienyl or triphenylphosphine groups.

In metal carbonyl complexes the CO ligands simultaneously act as σ-donors and π-acceptors, therefore the metal carbon bond can be considered to be a synergic bond (Figure 2-1).[4] Due to its

multiple character the M-C bond is often shorter than 1.8 Å.

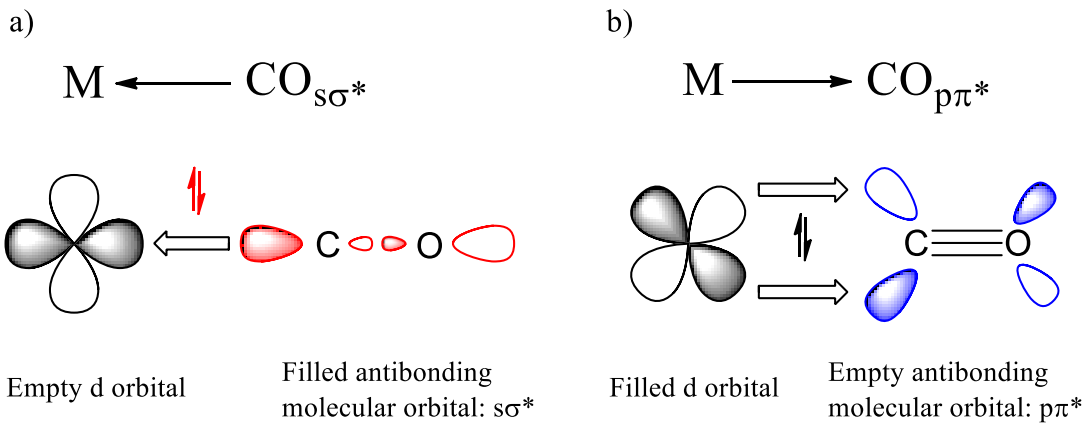


Figure 2-1. The metal-carbonyl bond consists of both a) σ-donor (red) and b) π-acceptor (blue) behaviour of CO ligand.

2.1.1.1 Vibrational spectroscopy of metal hexacarbonyl complexes

The most widely used characterisation technique for analysing metal hexacarbonyl complexes is IR spectroscopy as the characteristic CO stretching vibrations can provide useful information about the symmetry, charge and bonding of the CO group. The frequency of the CO stretching vibration (ν_{CO}) in free CO molecules is 2143 cm^{-1}.[5] Importantly, in metal carbonyl complexes this frequency is lowered indicating a weaker C=O bond as a result of the electron transfer from antibonding CO orbitals to M during the synergic bonding (Figure 2-1).

In the case of an $M(CO)_6$ molecule 33 fundamental vibrational modes are expected. In reality however, the high octahedral symmetry (O_h) of the molecule results in a six-fold degenerate CO stretching mode, which has a totally symmetric A_{1g}, a doubly degenerate forbidden E_g and a triply degenerate allowed T_{1u} mode

(Figure 2-2).[6] From these modes only the T_{1u} is IR active in the 2125-1850 cm^{-1} range while the A_{1g} and E_g are Raman active.[7,8]

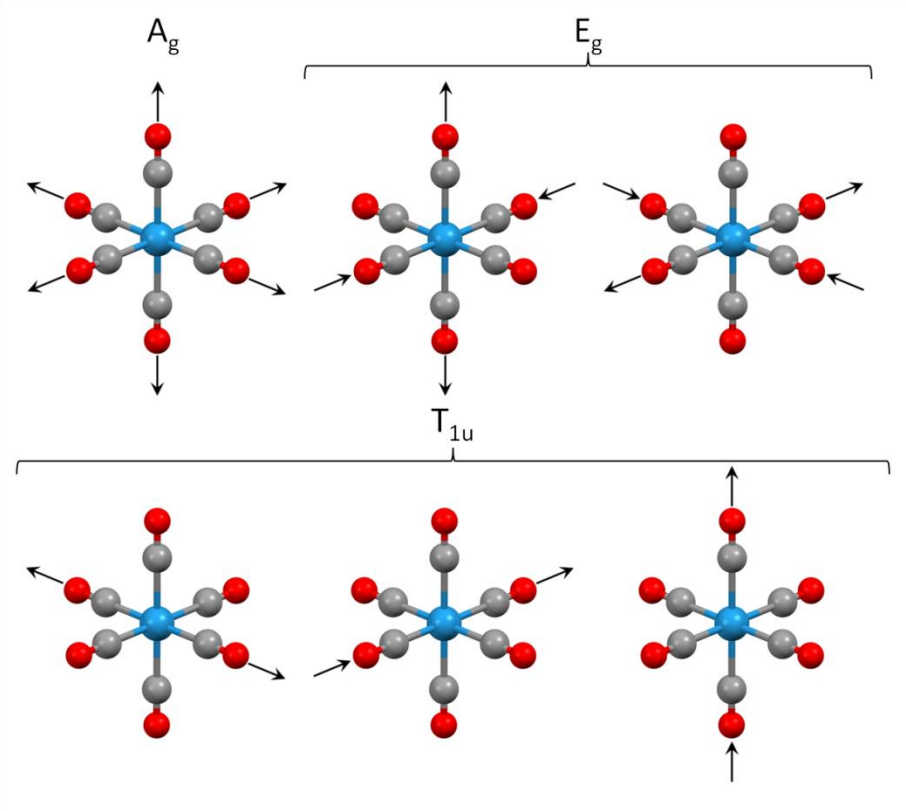


Figure 2-2. CO stretching modes of $M(CO)_6$ molecules, of which only the triply degenerate T_{1u} mode is IR active. However, the A_{1g} and E_g modes are Raman active. The arrows indicate the direction of the O atom`s movement.

If $M(CO)_6$ molecules are isolated, *i.e.* in the gas phase or dilute solutions, the triply degenerate T_{1u} carbonyl stretching vibration appears as a single IR band with a shoulder at higher frequency due to ^{13}C isotopic effects, see (Figure 2-3, Figure 2-4 a).[8]

However, in condensed matter such as KBr disc (Figure 2-4 b), cryogenic matrices[9] and zeolites[2] the ν_{CO} IR band reveals a fine structure as the energies of the T_{1u} mode`s vibrations are no longer degenerate due to the lower symmetry of the environment of the molecules.[10] Other IR active vibrational modes of $M(CO)_6$ complexes appear at lower energies; W-C-O bending appears at

480-580 cm^{-1}; W-C stretching appears at 370-430 cm^{-1} and C-W-C bending appears at 80-120 cm^{-1}.[9]

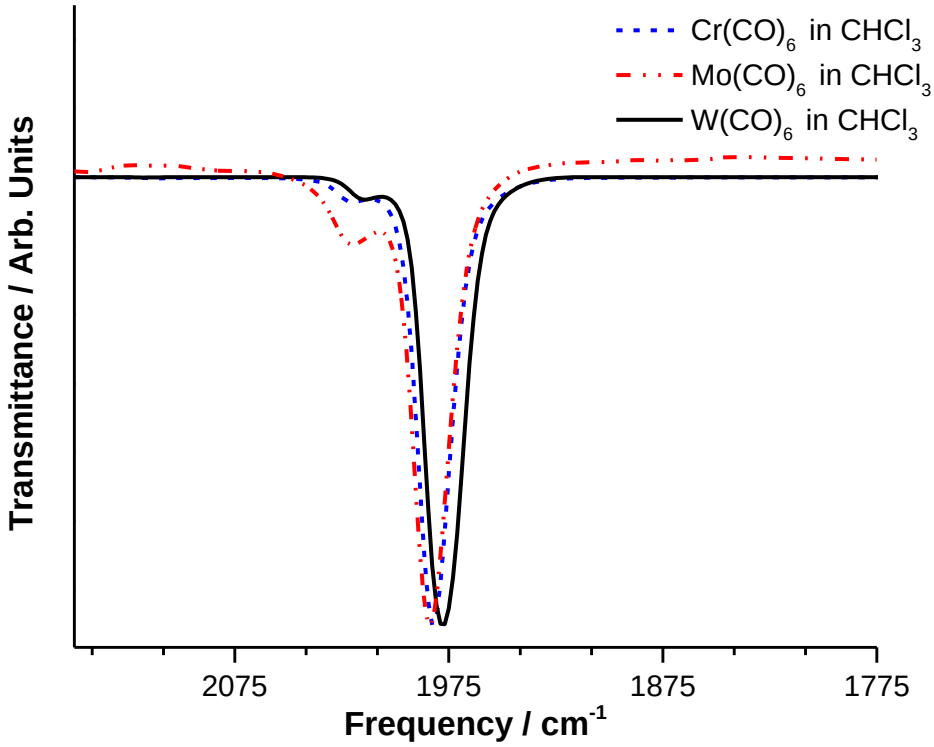


Figure 2-3. Transmission IR spectra of $Cr(CO)_6$ 1982 cm^{-1} (blue dotted), $Mo(CO)_6$ 1984 cm^{-1} (red dashed), and $W(CO)_6$ 1978 cm^{-1} (black solid) recorded in chloroform. The bands correspond to the T_{1u} CO stretching vibration.

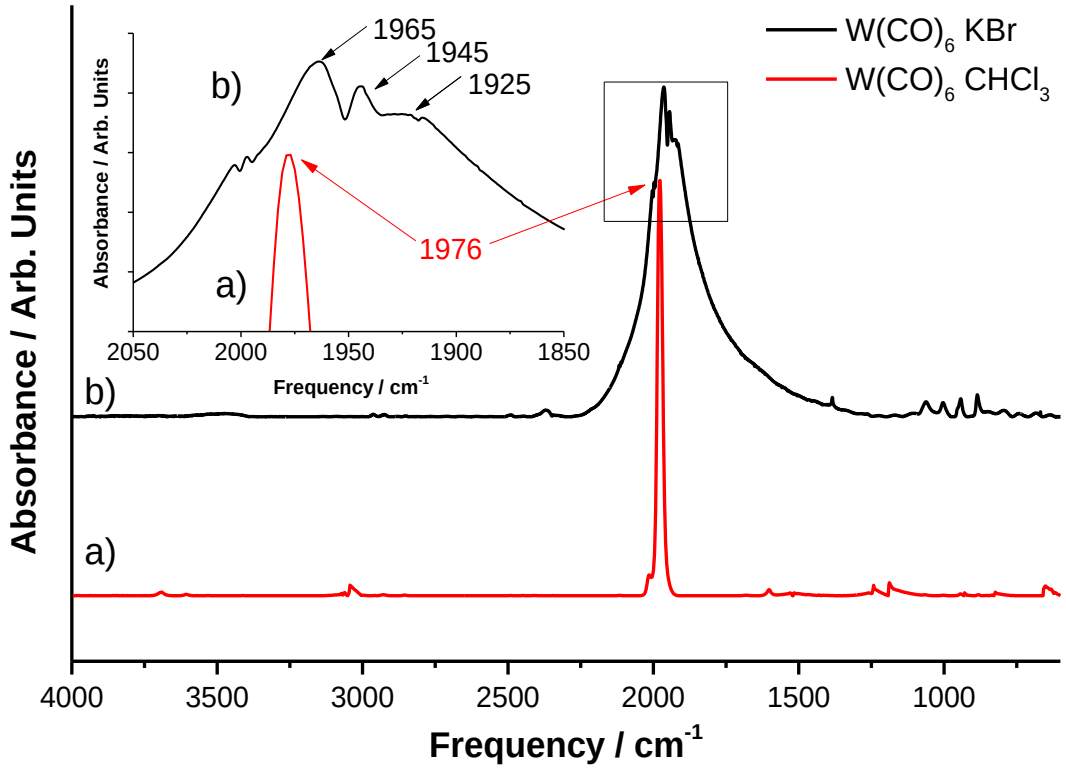


Figure 2-4. IR spectra of $W(CO)_6$ recorded in a) $CHCl_3$ (red) and b) KBr disc (black) showing the difference in the shape of the ν_{CO} band depending on the method of sample preparation. The inset shows expanded selected areas of the spectra.

2.2 Encapsulation of metal hexacarbonyl complexes in SWNTs

In this section a general encapsulation method of group VI metal hexacarbonyl complexes ($M(CO)_6$, M=Cr, Mo, W) is discussed. As metal hexacarbonyl complexes sublime readily under vacuum without noticeable decomposition, gas phase filling was utilised to incorporate them into carbon nanotubes.

First, to establish a reliable filling method the encapsulation procedure was optimised using $W(CO)_6$ then extended to the lighter Cr and Mo analogues.

Secondly, Kazachkin *et al.* showed that the IR signals of molecular species encapsulated in SWNTs are significantly

suppressed due to dielectric screening effects caused by the SWNTs.[11] Therefore, it is essential to ensure that all $M(CO)_6$ molecules are located within the carbon nanotubes, *i.e.* there is no $M(CO)_6$ left on the outside of the nanotubes as otherwise they would dominate the overall IR spectrum. Since during the filling of carbon nanotubes from the gas phase unwanted adsorption of guest species on the surface of carbon nanotubes is also likely to take place, a variety of techniques were tested. These included exposing $M(CO)_6$@SWNT samples to dynamic vacuum and several solution based washing methods to selectively remove any surface adsorbed molecules from the nanotubes.

2.2.1 Development of a general gas phase filling method of SWNTs with metal hexacarbonyl complexes

In order to provide access for the guest-molecules to the interior of single-walled carbon nanotubes the nanotubes have to open. The established treatment involves heating carbon nanotubes in air above their oxidation temperature (300-600 °C).[12] In order to determine the precise oxidation temperature of the individual types of carbon nanotubes thermogravimetric analysis (TGA) can be used. During the thermal treatment the end caps of the carbon nanotubes and some of the amorphous carbon content present in the material is oxidised. Moreover, all adsorbed substances (mainly water) are removed from the internal channels

of the carbon nanotubes. The opened nanotubes are then either immediately mixed with the guest-compounds or stored in a furnace below their oxidation temperature (c.a. 300 °C) until required, to prevent the re-adsorption of water.

The opened nanotubes and an excess of solid metal hexacarbonyl are then combined and sealed in a Pyrex glass vessel (l=10 cm, *d*=10 mm) under vacuum (10^{-6} mbar) using a custom built vacuum system (Figure 2-5). As metal hexacarbonyl complexes are very volatile at such low pressures, the tip of the Pyrex glass tube is immersed into a cooling bath during evacuation to prevent the loss of the metal carbonyl complex *via* sublimation into the vacuum system.

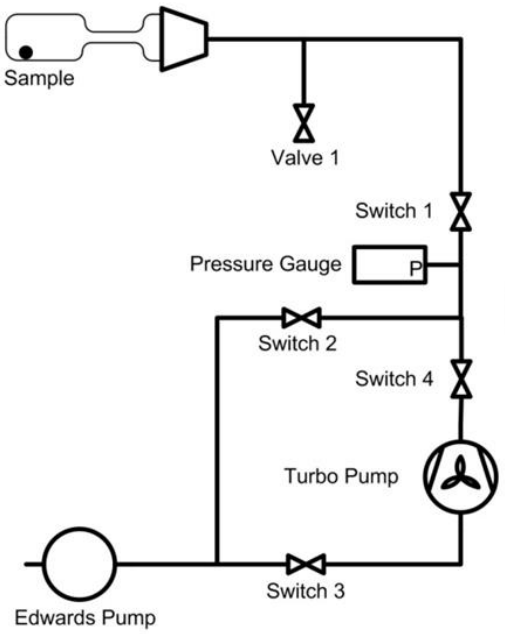


Figure 2-5. Experimental setup of the vacuum system used for insertion of metal carbonyl complexes into nanotubes.

The sealed Pyrex glass ampoule is then transferred into a

furnace, which is preheated above the sublimation temperature of the metal hexacarbonyl complex (between 100-150 °C) and this constant temperature is maintained for several days (Figure 2-6). The glass ampoule is then taken out of the furnace and cooled down prior to opening. The sample is collected in a glass vial and stored in a freezer to avoid desorption of the metal complex from the nanotubes.

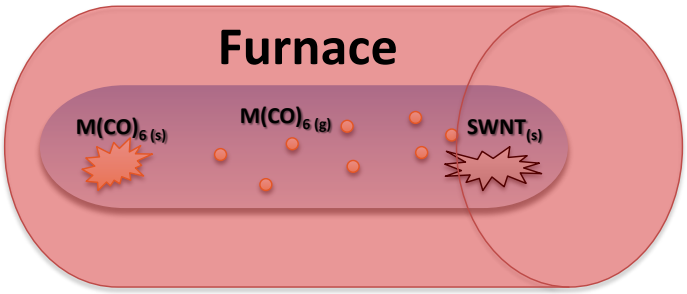


Figure 2-6. Schematic representation showing the experimental setup of gas phase filling: The Pyrex glass tube (blue) contains the guest-molecules $M(CO)_xL_y$ (left side) and SWNTs (right side) in the furnace (red).

2.2.2 Optimisation of the preparation of $M(CO)_6$@SWNT samples using $W(CO)_6$

The main objectives of the optimisation of the sample preparation were firstly to maximise the filling rate, *i.e.* the number of encapsulated metal hexacarbonyl molecules per carbon nanotube and secondly to develop a method for the removal of all $M(CO)_6$ molecules adsorbed on the surface of SWNTs prior to IR investigations.

2.2.2.1 Optimisation of the gas phase filling method using $W(CO)_6$

Tungsten hexacarbonyl was chosen as a test molecule to

optimise the filling procedure, as this allows the evaluation of the filling rate *via* TEM as W has the greatest contrast in the TEM among group VI metals due to its high atomic number (Z_W=74> Z_{Mo}=42> Z_{Cr}=24).

All test experiments were based on the general gas phase filling method described above (Section 2.2.1). However, the reaction temperature, reaction time and the cooling rate were systematically varied to study their effect on the overall filling rate (Table 2-2).

The first set of experiments focused on the determination of the optimal reaction temperature, therefore two identical mixtures of $W(CO)_6$ and pre-treated SWNTs were heated at 100 °C and 150 °C for the same length of time (1 day) see Reaction 2–1 and Reaction 2–3 (Table 2-2 and Table 2-8 in Section 2.5.1.3).

Table 2-2. Summary of the physical parameters of test experiments that were performed to optimise the gas phase filling method using $W(CO)_6$.

Experiment	Metal	Temp./°C	Time/days	Cooling method
Reaction **2–1**	W	100	1	Ice-water
Reaction **2–2**	W	100	7	Ice-water
Reaction **2–3**	W	150	1	Ice-water
Reaction **2–4**	W	150	3	Ice-water
Reaction **2–5**	W	150	3	Temp. gradient 1 °C/min

Secondly, the effect of reaction time on the filling rate was investigated by performing pairs of reactions at temperatures of 100 °C and 150 °C for different periods of time, see Reaction 2–1,

Reaction 2–2 and Reaction 2–3, Reaction 2–4, respectively (Table 2-2 and Table 2-8 in Section 2.5.1.3).

The last experiment was designed to test how the cooling rate of the reaction affects the number of encapsulated molecules. Therefore, two identical glass ampoules containing the same amount of $W(CO)_6$ and SWNT reaction mixture were heated in parallel in a box furnace for three days. After the ampoules were taken out from the box furnace, one of them was cooled by applying a cooling rate of 1 °C/min in a tube furnace until the sample reached 25 °C (Reaction 2–5), while the other one was immersed in an ice-water bath for 5 minutes to rapidly cool the sample to 0 °C (Reaction 2–4) (Table 2-2 and Table 2-8 in Section 2.5.1.3).

2.2.2.1.1 Evaluation of the gas phase filling test reactions by TEM and IR analysis

The qualitative filling rates of the SWNTs were evaluated by TEM imaging several areas in each sample. During TEM investigation analysis of the material formed in Reaction 2–1 (heated at 100 °C for 1 day), exclusively empty carbon nanotubes were observed (Figure 2-7 a, b). Moreover, IR spectroscopy did not confirm the presence of $W(CO)_6$ in the material *i.e.* inside or on SWNTs, as no peak was observed in the CO stretching region of the IR spectrum (Figure 2-9 a).

In contrast, during TEM analysis of the material formed in Reaction 2–3 (heated at 150 °C for 1 day) the *in situ* formation of nanoparticles (NP) were observed as a result of decomposition of encapsulated $W(CO)_6$ molecules due to the knock on damage caused by the e-beam (Figure 2-7 c, d). EDX analysis also confirmed the presence of tungsten in the nanotubes (Figure 2-8).

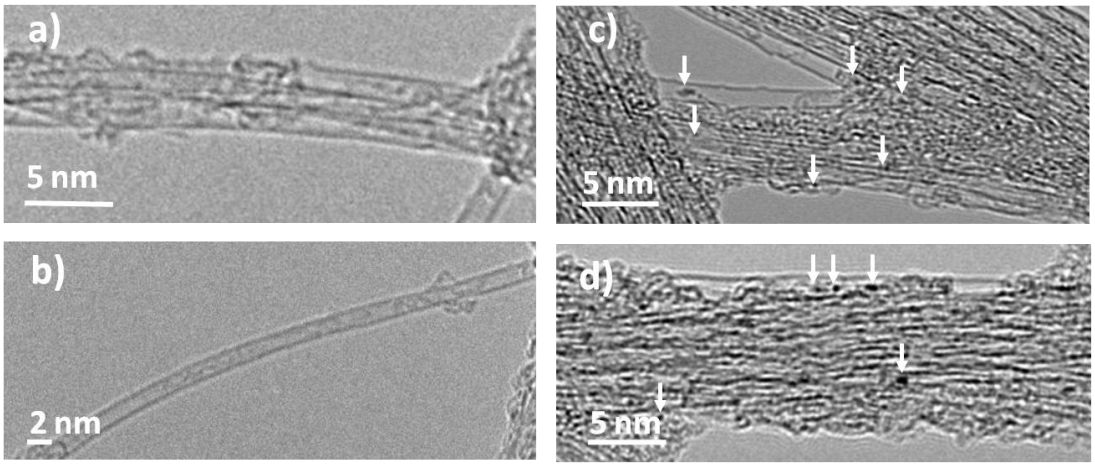


Figure 2-7. TEM images of the material formed a)-b) in Reaction 2–1 (heated at 100 °C for 1 day) showing empty SWNTs and c)-d) in Reaction 2–3 (heated at 150 °C for 1 day). The arrows indicate W nanoparticles formed by the decomposition of $W(CO)_6$ within the SWNTs during TEM imaging.

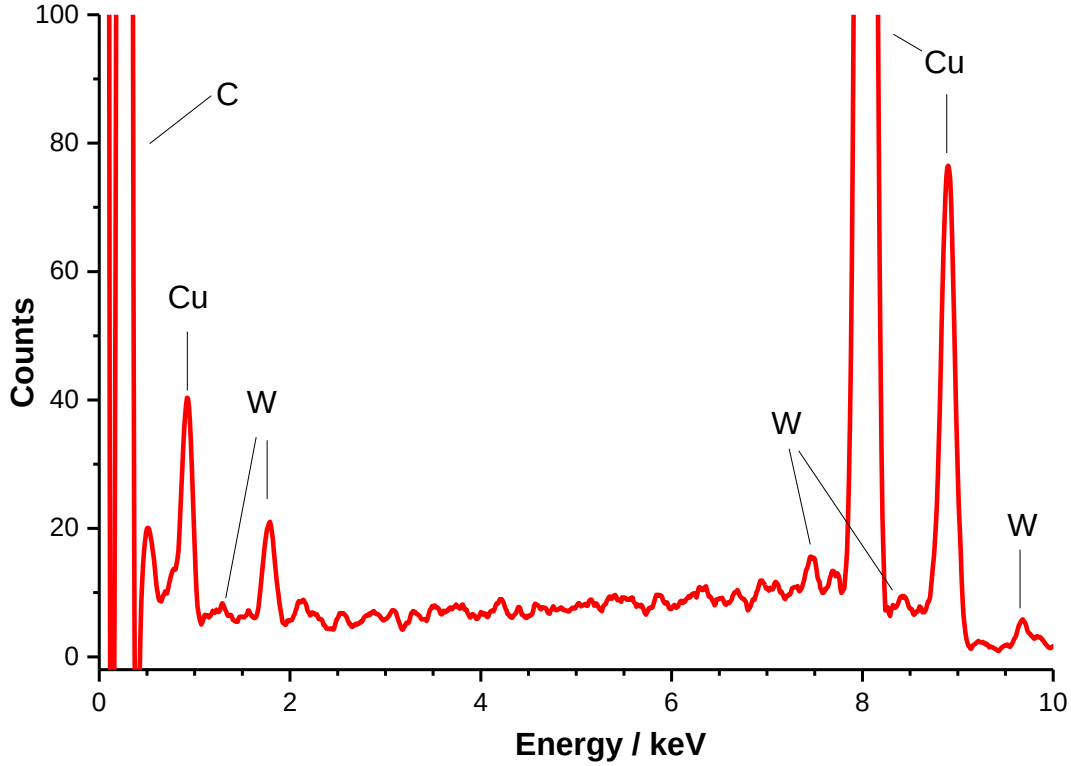


Figure 2-8. EDX spectrum of a bundle of nanotubes filled in Reaction 2–3 ($W(CO)_6$, 150 °C for 1 day) confirming the presence of W inside nanotubes. The copper (Cu) peaks are due to the copper grid of the TEM specimen holder.

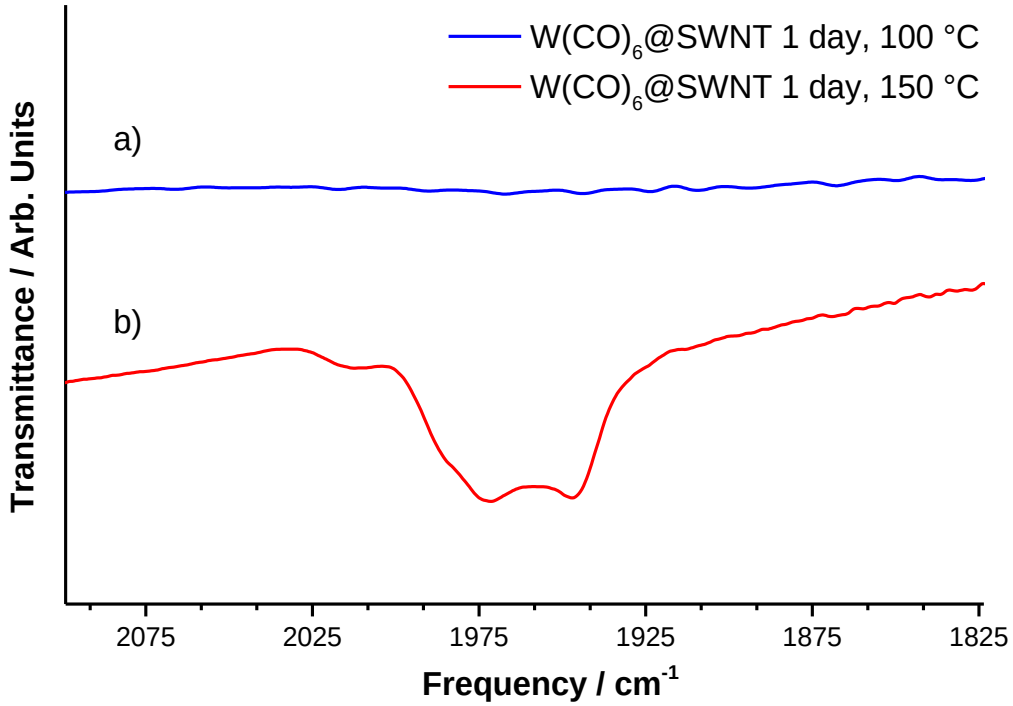


Figure 2-9. CO stretch areas of transmission IR spectra of the materials a) in which no W was and b) in which W NPs were observed in SWNTs by TEM prepared in Reaction 2–1 (100 °C, 1 day) and Reaction 2–3 (150 °C, 1 day), respectively. The IR spectra were recorded as KBr discs.

Moreover, in the IR spectrum of the material formed in Reaction 2–3 a broad band was observed in the ν_{CO} region (Figure 2-9 b) indicating the presence of $W(CO)_6$ in the sample.

Furthermore, TEM analysis of the material synthesised in Reaction 2–2 (heated at 100 °C for 7 days) showed that no $W(CO)_6$ was encapsulated in SWNTs at 100 °C regardless of the duration of the experiment (Figure 2-10 a, b).

Similarly, the increased duration of Reaction 2–4 (heated at 150 °C for 3 days) only had a minor improvement on the number of encapsulated $W(CO)_6$ molecules in SWNTs (Figure 2-10 c).

In the IR spectrum of the material an unresolved band was observed in the CO stretching region identical to those observed in the material formed in Reaction 2–3 (heated at 150 °C for 1 day) (Figure 2-9 b).

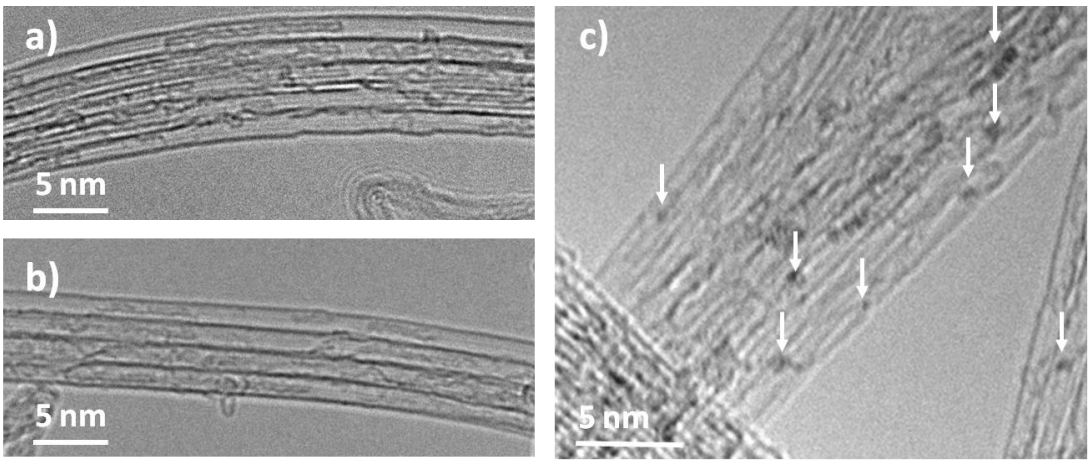


Figure 2-10. TEM images a) and b) showing the absence of W NPs in the material formed in Reaction 2–2 (heated at 100 °C for 7 days) and c) their presence in the material formed in Reaction 2–4 (heated at 150 °C for 3 days). The arrows indicate W NPs formed as a result of the decomposition of $W(CO)_6$ within the SWNTs under the electron beam.

In contrast, during TEM investigation of the material formed in Reaction 2–5 (heated at 150 °C for 3 days) in which the material

was cooled down slowly instead of using rapid ice-water bath cooling, only one W NP was found within the SWNTs in the entire sample (Figure 2-11). Moreover, IR spectroscopy was not able to detect the presence of $W(CO)_6$ in the material.

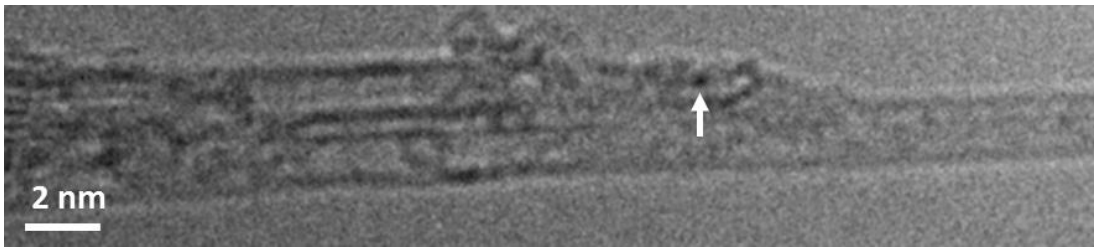


Figure 2-11. TEM image of the material formed in Reaction 2–5 (heated at 150 °C for 3 days), where the sample was cooled by 1 °C/min to room temperature (25 °C). The arrow points towards the only W NP observed in the sample. All other nanotubes were found to be empty.

In summary, the performed test reactions showed that the key physicochemical parameters of the filling method are the reaction temperature and the cooling rate (Table 2-3).

Table 2-3. Summary of the results and the conditions of test experiments that were performed to optimise the gas phase filling method using $W(CO)_6$.

Experiment	M	T / °C	t / day	Cooling	Filling
Reaction 2–1	W	100	1	Ice-water	No
Reaction 2–2	W	100	7	Ice-water	No
Reaction 2–3	W	150	1	Ice-water	Yes
Reaction 2–4	W	150	3	Ice-water	Yes
Reaction 2–5	W	150	3	1 °C/min	No

Therefore, to guarantee the optimal filling rate of nanotubes, all gas phase filling reactions were performed using the highest temperature that the guest-molecule could tolerate (*e.g.* 150 °C for $W(CO)_6$) and for 3 days. The material was then cooled down as

quickly as possible with an ice-water bath to trap the guest-molecules inside the SWNTs. A detailed discussion of these findings is included in Section 2.2.4.

2.2.2.2 Optimisation of the removal of the excess metal hexacarbonyl complexes from the outer surface of carbon nanotubes

As mentioned above the infrared signal of the encapsulated species is significantly suppressed due to dielectric screening effects caused by the nanotube, especially in comparison to the molecules adsorbed on the surface of SWNTs. Thus if the IR signal of the molecules within SWNTs is to be observed it is essential to remove the surface adsorbed molecules.[11]

The selective removal of surface adsorbed molecules relies on the fact that the interaction between molecules and the outer surface of carbon nanotubes is weaker than the interaction between encapsulated molecules and the inner surface of SWNTs.[13]

It has been reported previously that surface adsorbed molecules have a slightly higher vapour pressure than molecules encapsulated inside the nanotubes.[14–16] Therefore, dynamic vacuum was utilised in order to remove the surface adsorbed molecules from a $W(CO)_6$@SWNT sample (Section 2.5.2.1).

Alternatively, it is also possible to selectively dissolve the molecules from the outer surface of nanotubes by washing the material with an appropriate solvent (Section 2.5.2.2). During the washing procedures $W(CO)_6$@SWNT samples were mixed with

tetrahydrofuran (THF) in a glass vial using either magnetic stirring, an ultrasonic bath or a titanium sonic probe to ensure efficient mixing of the solvent and the solid material prior to filtration as described in Section 2.5.2.2.1, 2.5.2.2.2 and 2.5.2.2.3 respectively.

2.2.2.2.1 Preparation of control samples with $M(CO)_6$ complexes on the outer surface of SWNTs

Infrared spectroscopy was utilised to evaluate how effectively the excess of the metal hexacarbonyl complexes was removed from the outer surface of carbon nanotubes. To aid the evaluation control samples were formulated to replicate the IR spectrum of $W(CO)_6$ molecules adsorbed on the surface of SWNTs by selective deposition of $M(CO)_6$ molecules on the surface of SWNTs. The technical details of sample preparation and characterisation can be found in Section 2.5.3 and 2.5.5, respectively.

The first control sample was made by grinding pristine SWNTs and $W(CO)_6$ together in an agate mortar. As the SWNTs were not heated in air prior to use the majority of their cavity was not accessible for the $W(CO)_6$ molecules. As the majority of the SWNTs were unopened, therefore their cavity was not accessible for the $W(CO)_6$ molecules, the ν_{CO} band observed in the IR spectrum of the sample should correspond to molecules located solely on the outer surface of nanotubes. This control sample is labelled $W(CO)_6$+SWNT (Section 2.5.3.1).

The second control sample was synthesised using an altered gas phase filling procedure also using pristine *i.e.* untreated SWNTs to assess the effect of heating on the adsorption of $M(CO)_6$ complexes. As the nanotubes were kept in their pristine state, no detectable encapsulation is expected to have occurred. This control sample is labelled $W(CO)_6$/SWNT (Section 2.5.3.2).

The third control sample was prepared by paying extra attention to mimicking the entire procedure of the optimised gas phase filling method including the heating of SWNTs in air but still minimising the chance of unwanted encapsulation. Therefore, first the cavity of pre-treated SWNTs was completely filled with C_{60} molecules to form the extremely stable and well-known C_{60}@SWNT. After the excess of C_{60} molecules was removed from the surface of carbon nanotubes with CS_2, the washed C_{60}@SWNT was exposed to $W(CO)_6$ vapour under conditions identical to the optimised gas phase filling method. This procedure should exclusively result in the deposition of $W(CO)_6$ molecules on the surface of SWNTs, since their cavity has been already occupied by C_{60} molecules. This control sample is labelled $W(CO)_6$/(C_{60}@SWNT) (Section 2.5.3.3).

2.2.2.2.1.1Analysis of the control samples via infrared spectroscopy

In the IR spectrum of $W(CO)_6$+SWNT (Figure 2-12 b) a broad peak was observed at 1960 cm^{-1} with three features separated equally by 12 cm^{-1}. The shape of the ν_{CO} band observed in the IR spectrum of $W(CO)_6$+SWNT and unwashed $W(CO)_6$@SWNT

(Figure 2-12 g) are similar, although they are not completely identical. However, similarly to $W(CO)_6$+SWNT, equidistant separation (20 cm^{-1}) of the features in the ν_{CO} band was observed in the spectrum of $W(CO)_6$ measured as a KBr disc (Figure 2-12 e), although the relative intensity and overall shape of the band were different. This similarity suggests that the ν_{CO} band observed in the IR spectrum of $W(CO)_6$+SWNT might correspond to a dispersion of $W(CO)_6$ molecules in KBr, which have been easily removed from the surface of SWNTs during the preparation of the KBr disc. Based on these observations the interpretation of IR spectrum of $W(CO)_6$+SWNT is inconclusive because of the uncertain location of $W(CO)_6$ molecules. Therefore, $W(CO)_6$+SWNT cannot be used as a control sample to represent the IR spectrum of $W(CO)_6$ molecules adsorbed on the surface of SWNTs.

During IR measurements of $W(CO)_6$/SWNT (Figure 2-12 c) an asymmetric, low intensity band (60 times weaker than in other $W(CO)_6$@SWNT samples) was observed in the terminal CO stretching region. Since the shape of the band was qualitatively different in comparison to ν_{CO} IR bands which were previously observed in $W(CO)_6$@SWNT samples, $W(CO)_6$/SWNT was investigated by TEM. The TEM analysis of the material revealed that a small amount of $W(CO)_6$ was able to enter into the carbon nanotubes during the gas phase filling, although the SWNTs were not opened in air prior to the exposure of $W(CO)_6$ vapour

(not shown). Consequently, $W(CO)_6$/SWNT is not suitable to represent the IR spectrum of $W(CO)_6$ complexes adsorbed on the surface of SWNTs.

In the IR spectrum of the $W(CO)_6$/(C_{60}@SWNT) control sample (Figure 2-12 f) an asymmetric, unresolved band was observed in the terminal CO stretching region, which has two features. The overall shape of the ν_{CO} IR band was found to be identical to the one observed in the IR spectrum of the unwashed $W(CO)_6$@SWNT (Figure 2-12 g). This suggests that the gas phase deposition of $W(CO)_6$ on C_{60}@SWNT exclusively resulted in $W(CO)_6$ on SWNTs surfaces and their encapsulation in SWNTs was successfully prohibited by C_{60}. Therefore, $W(CO)_6$/(C_{60}@SWNT) can be used as a good reference material to represent the IR spectrum of $W(CO)_6$ molecules adsorbed on the surface of SWNTs and help the evaluation of the various techniques for the removal of non-encapsulated molecules from $M(CO)_6$@SWNT samples.

Moreover, these results reinforce the importance of the removal of surface adsorbed $M(CO)_6$ molecules from nanotube samples and suggest that they dominate the IR spectra of the previously prepared $M(CO)_6$@SWNTs in agreement with Kazachkin *et al.*[11]

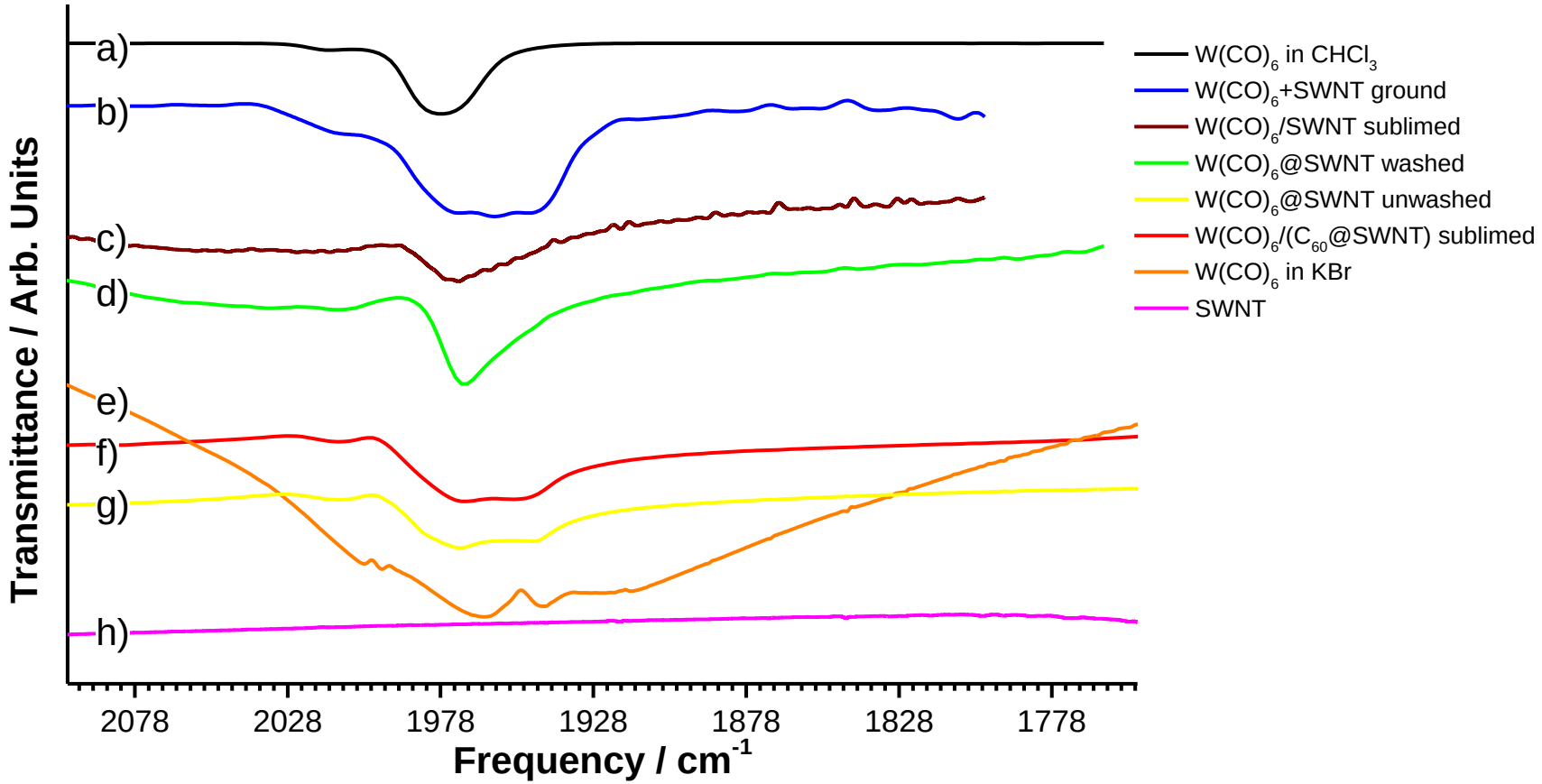


Figure 2-12. Transmission IR spectra of $W(CO)_6$ in a) $CHCl_3$ solution and e) in KBr disc and $W(CO)_6$ on SWNT control samples recorded as KBr discs: b) $W(CO)_6$+SWNT *i.e.* $W(CO)_6$ mechanically ground together with SWNTs, c) $W(CO)_6$/SWNT *i.e.* $W(CO)_6$ deposited from gas phase onto un-opened SWNTs, f) $W(CO)_6/(C_{60}$@SWNT) *i.e.* $W(CO)_6$ deposited from gas phase on SWNTs filled with C_{60}, d) washed and g) unwashed $W(CO)_6$@SWNT and h) blank SWNT.

2.2.2.2.2 Evaluation of the effectiveness of the removal of excess metal hexacarbonyl complexes from the outer surface of SWNTs

To determine which of the above described (Section 2.2.2.2) cleaning techniques was the most effective, the processed $W(CO)_6$@SWNT samples were investigated by IR spectroscopy and/or TEM.

After the previously synthesised $W(CO)_6$@SWNT was exposed to low vacuum (10^{-3} mbar) TEM analysis showed the formation of large, dark clusters on the surface of the SWNT bundles (Figure 2-13 a). Based on *in situ* EDX measurement these clusters consist of W, indicating that $W(CO)_6$ was not completely removed from the surface of nanotubes by this method. In contrast, a higher vacuum (10^{-6} mbar) seemed to be more effective as no W clusters were found on the SWNTs during TEM analysis. In addition, no noticeable decrease was observed in the amount of encapsulated molecules (Figure 2-13 b).

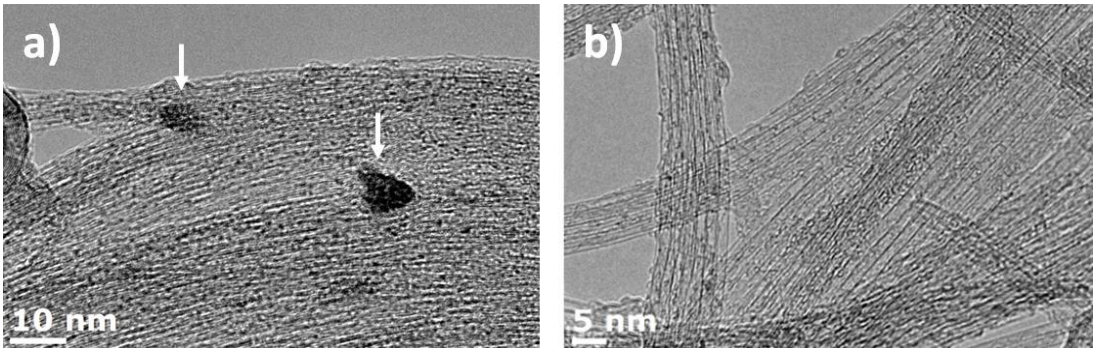


Figure 2-13. TEM images of $W(CO)_6$@SWNTs bundles after they were subjected to dynamic vacuum. a) In case of low vacuum (10^{-3} mbar) a large amount of $W(CO)_6$ remain on the surface of nanotubes. b) The application of high vacuum (10^{-6} mbar) resulted in the removal of $W(CO)_6$ from the surface of SWNT bundles based on TEM results as no W NP formation was observed outside of the nanotubes.

However, IR spectroscopy suggested that $W(CO)_6$ is still present

on the surface of the SWNTs, even after exposure to 10^{-6} mbar (Figure 2-14 c, d), as the shape of the observed IR band is identical to that found in the spectrum of the $W(CO)_6/(C_{60}@SWNT)$ control sample (Figure 2-12 f).

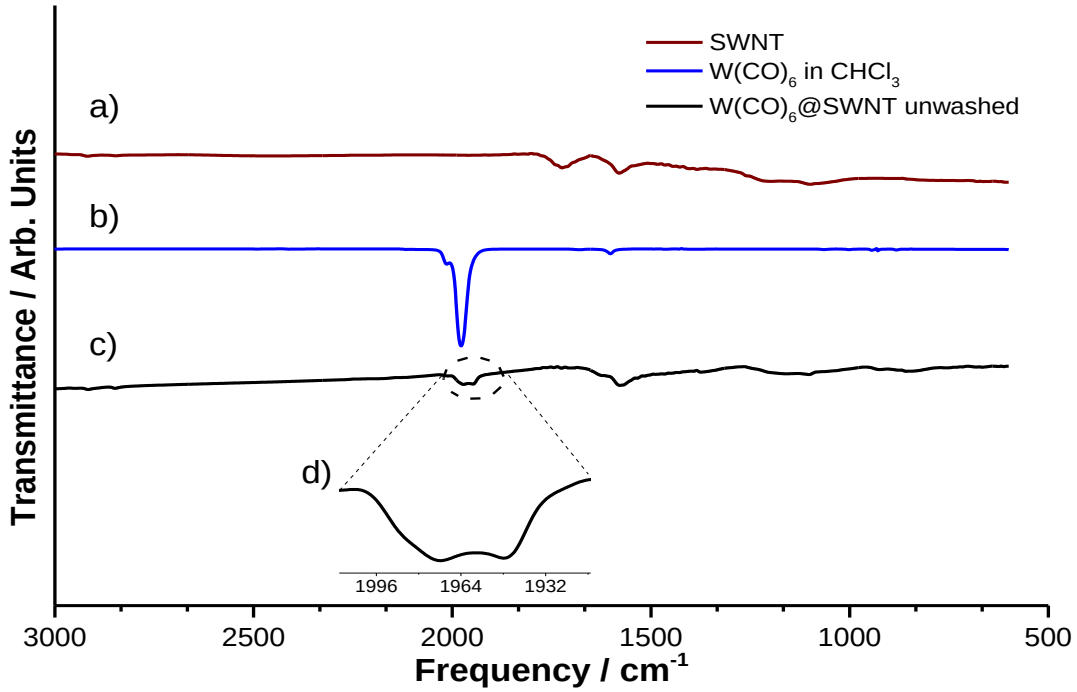


Figure 2-14. Transmission IR spectra of a) SWNT, b) $W(CO)_6$ in $CHCl_3$, c) unwashed $W(CO)_6$@SWNT and d) the magnification of the CO stretching vibration region recorded as KBr discs if not stated otherwise.

In the IR spectra of the samples which were either stirred (Section 2.5.2.2.1) or dispersed using an ultrasonic bath (Section 2.5.2.2.2) in THF to remove the excess $W(CO)_6$, a broad band with two features was observed which are similar to the $W(CO)_6/(C_{60}@SWNT)$ control sample (Figure 2-12 f). Therefore, $W(CO)_6$ must have been still present on the surface of SWNTs after these treatments.

In contrast, in the IR spectrum of the $W(CO)_6$@SWNT sample dispersed in THF using the titanium ultrasonic probe

(Section 2.5.2.2.3), an asymmetric band with one minimum has been observed at 1970 cm^{-1} (Figure 2-24 c). As this peak was retained after repeating the procedure, it was assigned to the $W(CO)_6$ molecules situated in the internal channels of the SWNTs.

In summary, neither dynamic vacuum nor solvent based gentle cleaning methods were able to remove $W(CO)_6$ from the surface of the carbon nanotubes. Therefore, in the future $M(CO)_6$@SWNT samples have to be dispersed in THF by a titanium ultrasonic probe prior to filtration to provide clean $M(CO)_6$@SWNTs for IR measurements.

2.2.3 Encapsulation of $Cr(CO)_6$ and $Mo(CO)_6$ in SWNTs

The encapsulation of lighter $M(CO)_6$ (M=Cr, Mo) into carbon nanotubes is based on the gas phase filling method optimised using $W(CO)_6$, but the reaction temperature has to be decreased to 120 °C to prevent decomposition of the molecules.

TEM analysis of the materials synthesised in Reaction 2–6 ($Cr(CO)_6$, heated at 120 °C for 3 days) and in Reaction 2–7 ($Mo(CO)_6$, heated at 120 °C for 3 days) revealed that nanoparticles were formed in SWNTs (Figure 2-15) as a result of *in situ* decomposition of encapsulated $M(CO)_6$ molecules by the electron beam of TEM, in an identical fashion to $W(CO)_6$@SWNT. EDX analysis of the materials confirmed that the nanoparticles consist of Cr (Figure 2-16) in the case of $Cr(CO)_6$@SWNT and Mo (Figure 2-17) in the case of $Mo(CO)_6$@SWNT.

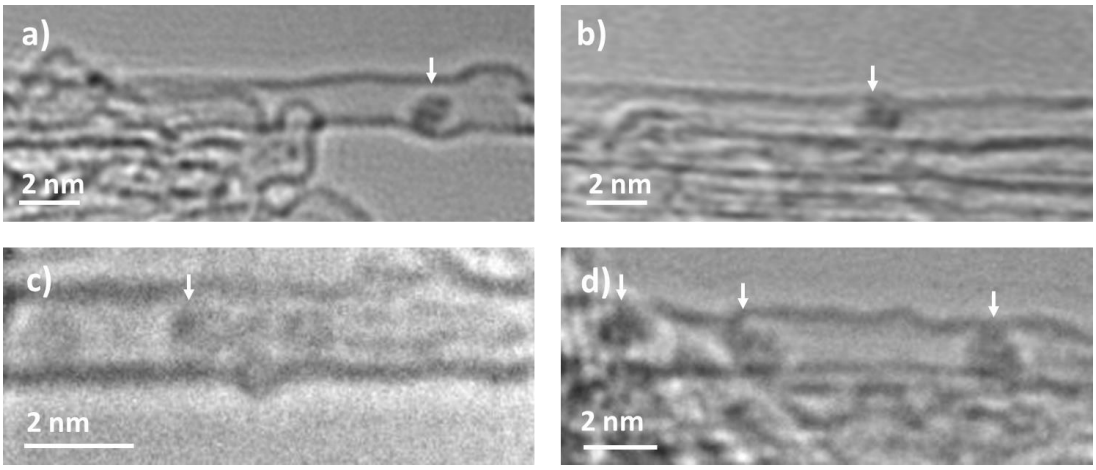


Figure 2-15. TEM micrographs of $Cr(CO)_6$ and $Mo(CO)_6$ encapsulated in SWNTs in Reaction 2–6 and Reaction 2–7, respectively. a) The sidewall of the SWNT deformed due to interacting with an *in situ* formed Cr NP. b) A Cr NP formed inside a SWNT. In images c) and d) examples Mo NPs inside SWNTs are shown. The arrows highlight the metallic nanoparticles in all images.

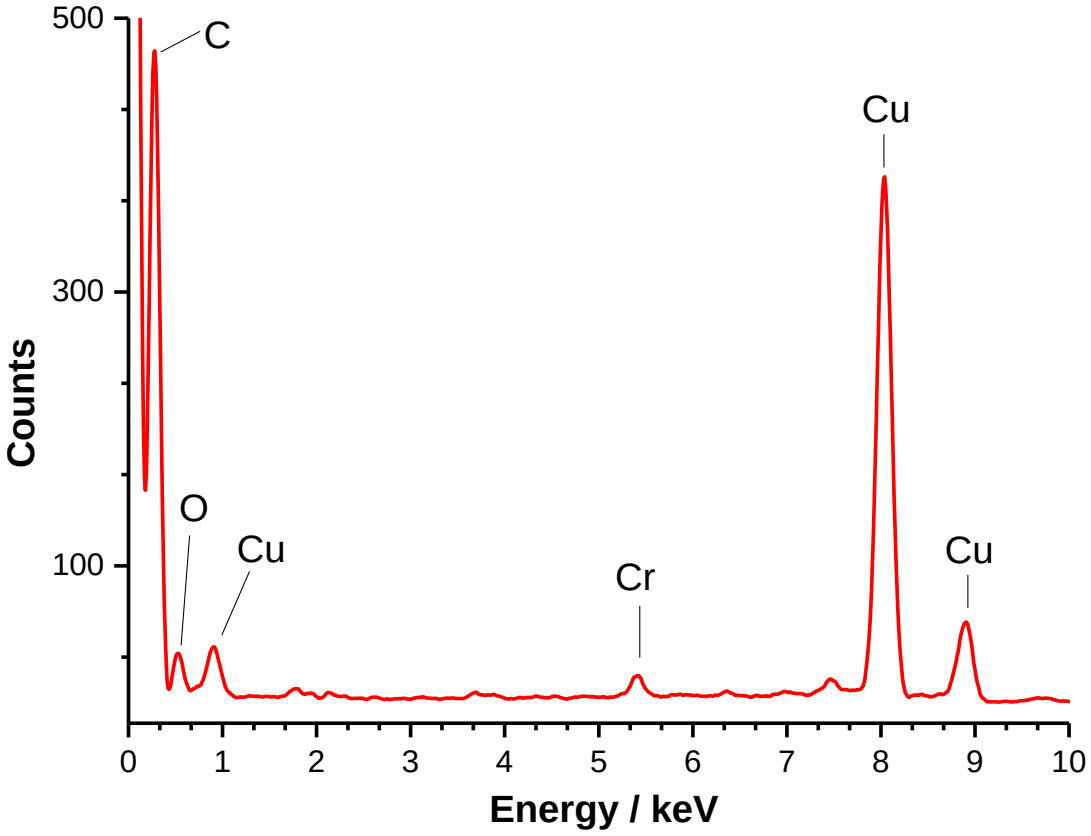


Figure 2-16. EDX spectrum of Cr NPs@SWNT recorded during TEM analysis confirming the presence of Cr in the material formed in Reaction 2–6 ($Cr(CO)_6$, heated at 120 °C for 3 days). The Cu peaks are due to the copper grid of the TEM specimen holder.

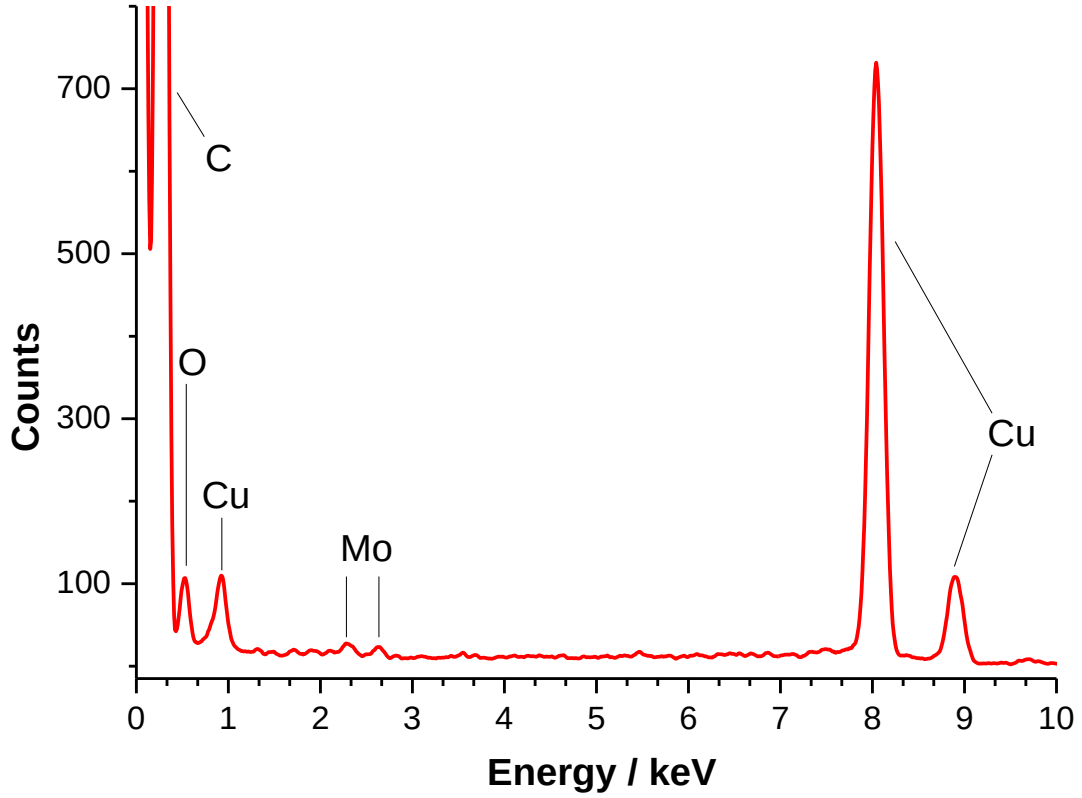


Figure 2-17. EDX spectrum of Mo NPs@SWNT recorded during TEM analysis confirming the presence of Mo in the material formed in Reaction 2–7 ($Mo(CO)_6$, heated at 120 °C for 3 days). The Cu peaks are due to the copper grid of the TEM specimen holder.

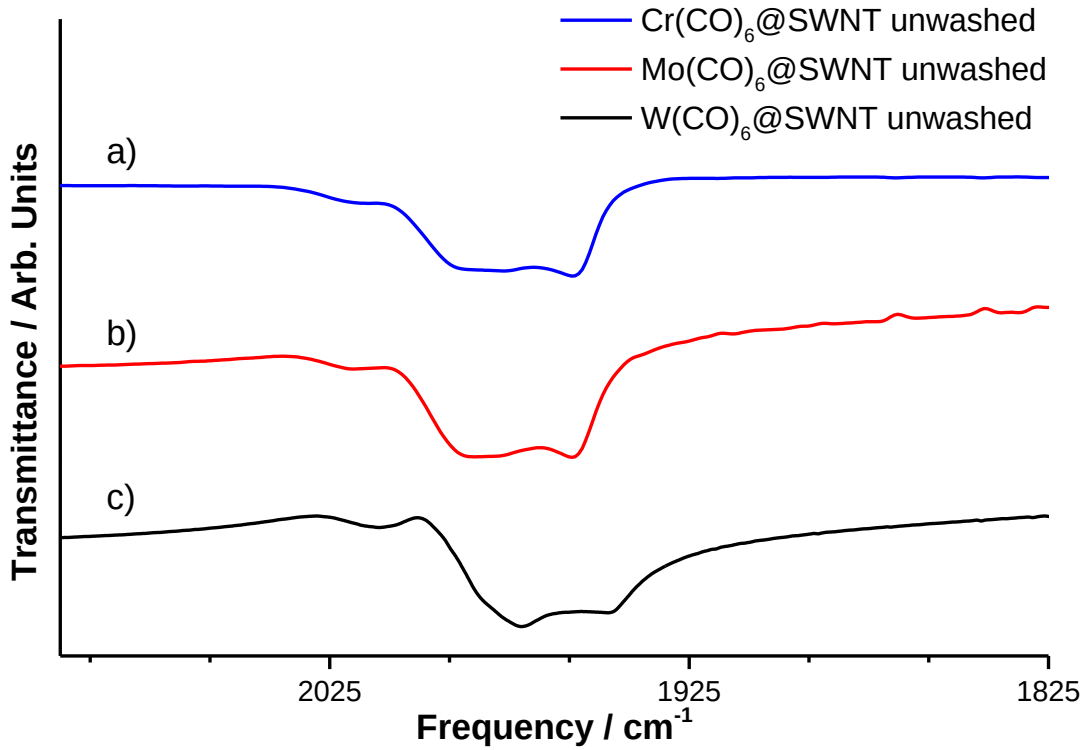


Figure 2-18. Transmission IR spectra of unwashed samples of a) $Cr(CO)_6$@SWNTs, b) $Mo(CO)_6$@SWNTs and c) $W(CO)_6$@SWNTs recorded as KBr discs.

In addition, IR analysis of unwashed $Cr(CO)_6$ and $Mo(CO)_6$ in

SWNT samples showed a new broad band in the CO stretching region of the IR spectra confirming the presence of the guest species in the materials (Figure 2-18 a and b). Moreover, the shape of the ν_{CO} IR bands were found to be similar in all $M(CO)_6$@SWNTs including the one observed in $W(CO)_6$@SWNT (Figure 2-18 c).

2.2.4 Qualitative analysis of the mechanism and energetics of the encapsulation of metal hexacarbonyls into SWNTs

In this section the mechanism and energetics of gas phase encapsulation of $M(CO)_6$ into single-walled carbon nanotubes is discussed. To aid the understanding of the encapsulation process the findings from the $M(CO)_6$ filling reactions are compared to previously published work for the gas phase insertion of C_{60} into carbon nanotubes. The filling of SWNTs with C_{60} from the gas phase was investigated by variable temperature high-resolution transmission electron microscopy[17] as well as theoretically.[18,19] It was found that prior to their encapsulation C_{60} molecules adsorb on the surfaces of the carbon nanotubes, then above a certain temperature they become mobile and are able to move along and enter into the nanotubes through their open ends or sidewall defects. However, the pre-adsorbed guest-molecules have to overcome an energy barrier (0.3 eV/C_{60}), before entering into the SWNT (Figure 2-19) and becoming stabilised (3 eV/C_{60} in SWNTs with the optimum internal diameter).[19,13] It should be pointed out

that the energy of the host-guest interaction is significantly higher than the cohesive energy in the 3D face centred cubic crystal of C_{60} (~2 eV/C_{60}), therefore the formation of C_{60}@SWNT is thermodynamically highly favourable and irreversible.[13] The reason of this remarkably strong interaction is the perfect geometrical fit of the convex C_{60} molecules and the concave interior of SWNTs.

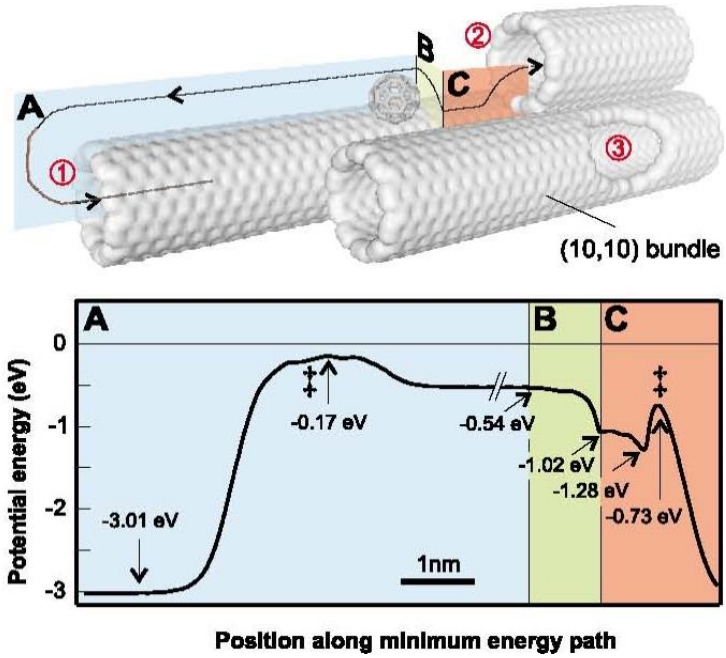


Figure 2-19. Cut through of the three-dimensional potential energy surface of a small (10,10) SWNT bundle. Spontaneous encapsulation along all relevant reaction paths is prevented by lip barriers (LBs) due to the lower C_{60} coordination at the rim of SWNTs. Calculations show that encapsulation is most efficient *via* the head-on approach along the reaction path labelled (C).Transition states are marked by a double dagger (‡).[13]

Theoretical calculations also imply that the alternative ballistic encapsulation mechanism based on the concept that SWNTs are filled by C_{60} molecules striking their entry points from the gas phase is less likely, since it could not result in such high filling rates after such a short reaction time, *e.g.* 98% after 12 hours, observed in C_{60}@SWNT samples by TEM analysis.[17, 18]

In summary, these results suggest that the filling rate is mainly

determined by the reaction time in the case of ballistic encapsulation and by the reaction temperature in case of encapsulation of pre-adsorbed molecules. Moreover, in ideal diameter (10,10) SWNTs (1.36 nm) the encapsulation of C_{60} is thermodynamically favourable and irreversible.[13]

The results of the $M(CO)_6$ encapsulation test reactions (Section 2.2.2.1) showed that the filling rate is mainly affected by the reaction temperature but not influenced by the reaction time. These observations strongly suggest that the encapsulation of $M(CO)_6$ molecules into SWNTs follows the above described pre-adsorption mechanism similarly to C_{60}.

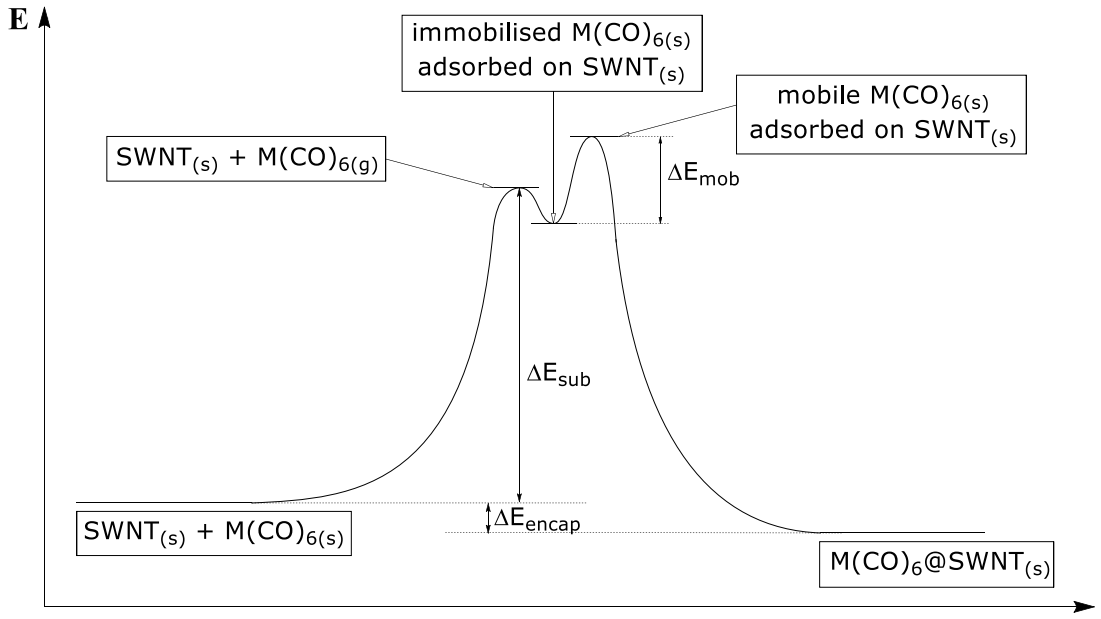


Figure 2-20. Schematic representation of the proposed encapsulation process of $M(CO)_6$ in SWNTs. ΔE_{sub} is the energy required for the sublimation of $M(CO)_6$ molecules. ΔE_{mob} is the energy required to mobilise the surface adsorbed $M(CO)_6$ molecules prior they enter into the nanotubes. ΔE_{encap} is the energy difference between the cohesive energy of bulk and $M(CO)_6$ encapsulated in SWNT.

However, it is important to point out that that the cohesive energy in bulk $M(CO)_6$ and in $M(CO)_6$@SWNTs must be very close

to each other as the $M(CO)_6$ and SWNT reaction mixture needs to be quenched by ice-water to entrap molecules in $M(CO)_6$@SWNT (Figure 2-20). This means that the energy gained due to encapsulation (ΔE_{encap}) *i.e.* the energy difference between a $M(CO)_6$ molecule located in a bulk $M(CO)_6$ crystal and same molecule encapsulated in SWNTs is close to zero, and the encapsulation of $M(CO)_6$ in some SWNTs may not be thermodynamically favoured and irreversible.

2.2.5 Summary and process map of the synthesis of $M(CO)_6$@SWNTs

In summary, the gas phase encapsulation of $M(CO)_6$ molecules in SWNTs has been optimised by performing a series of test experiments with $W(CO)_6$ as a test molecule, which showed that the cooling rate and the reaction temperature are the key physicochemical parameters of the filling method. Moreover, these results suggest that the encapsulation of $M(CO)_6$ in SWNTs may not be thermodynamically favoured and irreversible.

The optimised gas phase filling method was then successfully utilised to encapsulate $M(CO)_6$ (M=Cr, Mo, W) in SWNTs and confirmed by TEM, EDX and IR analysis.

In addition, since IR investigation of $M(CO)_6$@SWNTs requires samples with no $M(CO)_6$ molecules adsorbed on the surface of SWNTs several cleaning procedures were tested. Based on the analysis of the effectiveness of the removal of excess $M(CO)_6$

complexes a thorough cleaning procedure has been established, which relies on the treatment of the materials with a titanium ultrasonic probe in organic solvent prior to filtration.

The process of the sample preparation from synthesis to cleaning and the analysis of the materials is summarised in Figure 2-21.

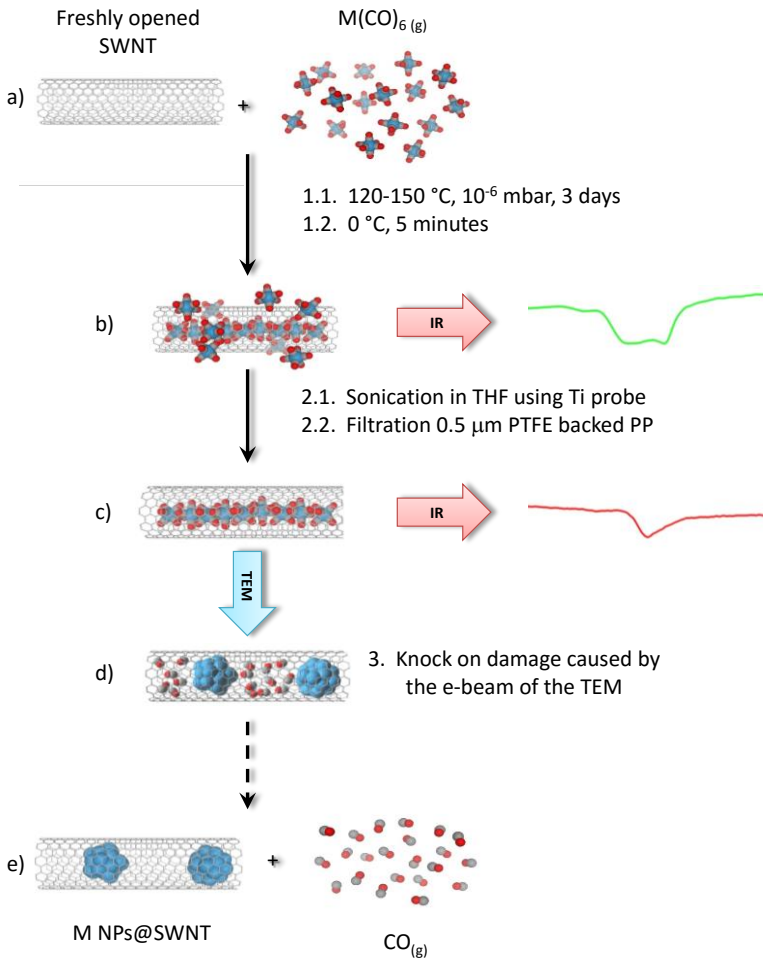


Figure 2-21. The process map is showing the preparation of $M(CO)_6$@SWNTs by gas phase filling and the analysis of the materials. a) Freshly opened SWNTs and $M(CO)_6$ are sealed in a Pyrex glass vessel under vacuum (10^{-6} mbar) and heated at 120-150 °C for 3 days then cooled down to 0 °C as described in Section 2.5.1.3 to result in unwashed $M(CO)_6$@SWNT where some molecules are adsorbed on SWNT surfaces and some encapsulated. b) The sample is then washed with THF according to the procedure presented in Section 2.5.2.2.3 to give washed $M(CO)_6$@SWNT, c), which is analysed by IR spectroscopy as described in Section 2.5.5. This data was used to study the host-guest interaction in $M(CO)_6$@SWNT systems as discussed in Section 2.3. M NPs@SWNT, d) is formed by the decomposition of $M(CO)_6$ in SWNTs during TEM analysis due to the knock-on damage of the e-beam and then finally CO gas escapes the nanotube, e).

2.3 Exploration of the host-guest interactions in $M(CO)_6$@SWNTs

In this section the CO stretching region of the IR spectra of $M(CO)_6$@SWNTs (M= Cr, Mo, W) is investigated experimentally and by theoretical calculations in order to gain an understanding of the fundamental interactions between carbon nanotubes and encapsulated $M(CO)_6$ molecules.

The results of these investigations are analysed to understand the behaviour of the $M(CO)_6$ molecules inside SWNTs and determine the nature of the host-guest interaction.

The details of sample preparation including the synthesis, post-synthesis processing and vibrational spectroscopy measurements of $M(CO)_6$@SWNT are described in Section 2.5.

2.3.1 Vibrational spectroscopy analysis of $M(CO)_6$@SWNTs

2.3.1.1 Infrared spectroscopy analysis of the CO stretching vibration in $M(CO)_6$ molecules encapsulated in SWNTs

The IR spectra of $M(CO)_6$@SWNTs were recorded (as described in Section 2.5.5) after the cleaning procedure and compared to the IR spectra of the corresponding $M(CO)_6$ recorded in chloroform solution and to gas phase data published previously.[20] To ensure the integrity of the study the IR spectra were also recorded directly after the encapsulation, *i.e.* unwashed samples.

IR spectra of $Cr(CO)_6$@SWNT formed in Reaction 2–6 were examined first. In the IR spectrum of unwashed $Cr(CO)_6$@SWNT a

wide band with local minima at 1982 and 1957 cm^{-1} was observed (Figure 2-22 b). In contrast, in the IR spectrum of washed $Cr(CO)_6$@SWNT sample an asymmetric broad band was observed with a single minimum at 1979 cm^{-1} (Figure 2-22 c). This band is redshifted by 3 cm^{-1} in comparison to the ν_{CO} frequency (1982 cm^{-1}) of $Cr(CO)_6$ recorded in chloroform solution (Figure 2-22 a).

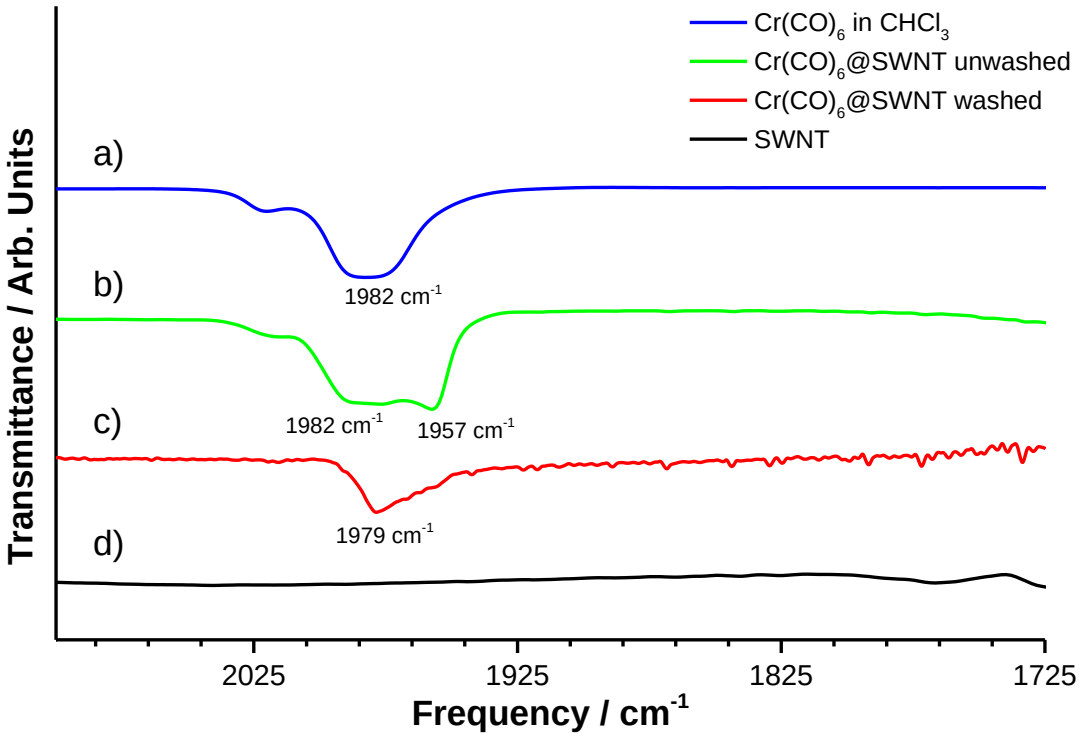


Figure 2-22. Transmission IR spectra of a) $Cr(CO)_6$ in $CHCl_3$, b) unwashed $Cr(CO)_6$@SWNT, c) $Cr(CO)_6$@SWNT washed with THF using an ultrasonic probe and d) SWNTs recorded as KBr discs in ambient conditions with Bruker Tensor 27 spectrometer.

The second series of IR measurements were performed on a set of $Mo(CO)_6$ samples. In the spectrum of unwashed $Mo(CO)_6$@SWNT formed in Reaction 2–7 a wide band was observed, which has two features at 1984 and 1958 cm^{-1} (Figure 2-23 b). In contrast, the asymmetric ν_{CO} band

found in the IR spectrum of washed $Mo(CO)_6$@SWNT had a single minimum at 1978 cm^{-1} (Figure 2-23 c), which corresponds to a 6 cm^{-1} redshift compared to the ν_{CO} frequency of $Mo(CO)_6$ acquired in chloroform solution (1984 cm^{-1}) (Figure 2-23 a).

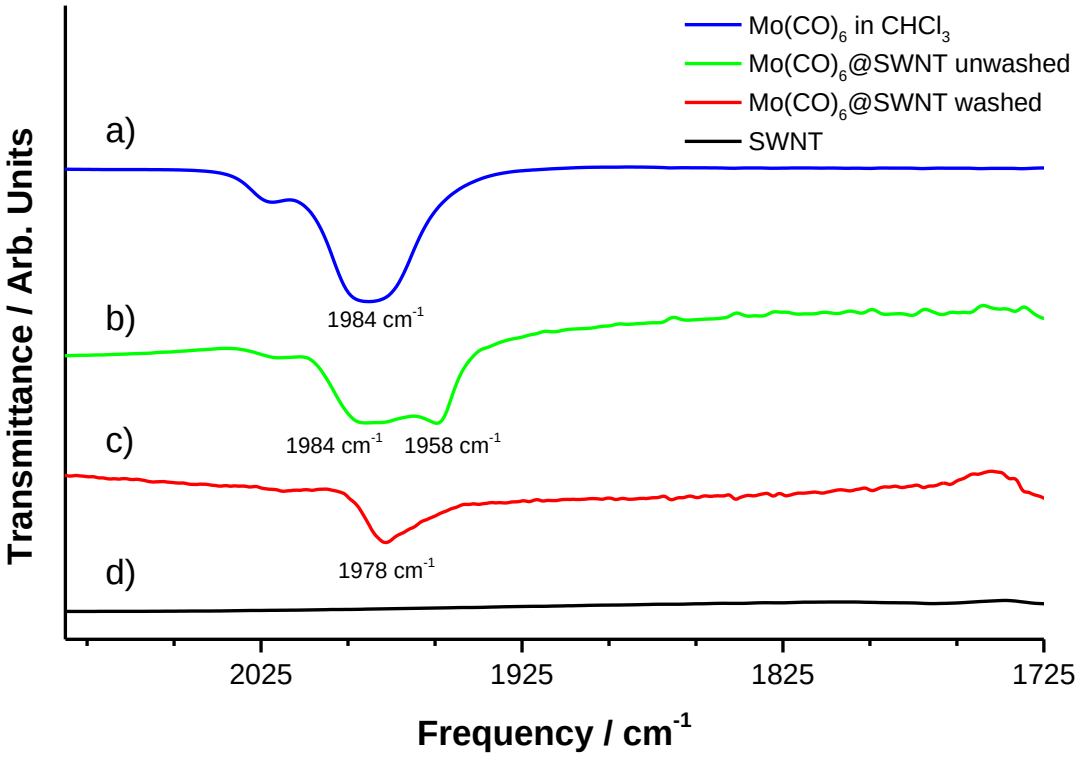


Figure 2-23. Transmission IR spectra of a) $Mo(CO)_6$ in $CHCl_3$, b) unwashed $Mo(CO)_6$@SWNT, c) $Mo(CO)_6$@SWNT washed with THF using an ultrasonic probe and d) SWNT recorded as KBr discs in ambient conditions with Bruker Tensor 27 spectrometer.

Lastly the series of $W(CO)_6$@SWNT samples were investigated by IR spectroscopy. In the IR spectrum of the unwashed material formed in Reaction 2–4 an unresolved band was observed (Figure 2-24 b), which has two features at 1972 and 1948 cm^{-1}. However, in the IR spectrum of washed $W(CO)_6$@SWNT only a broad asymmetric band was found at 1970 cm^{-1} (Figure 2-24 c), which corresponds to a 8 cm^{-1} redshift compared to the IR spectrum of $W(CO)_6$ (1978 cm^{-1}) recorded in chloroform solution (Figure

2-24 a).

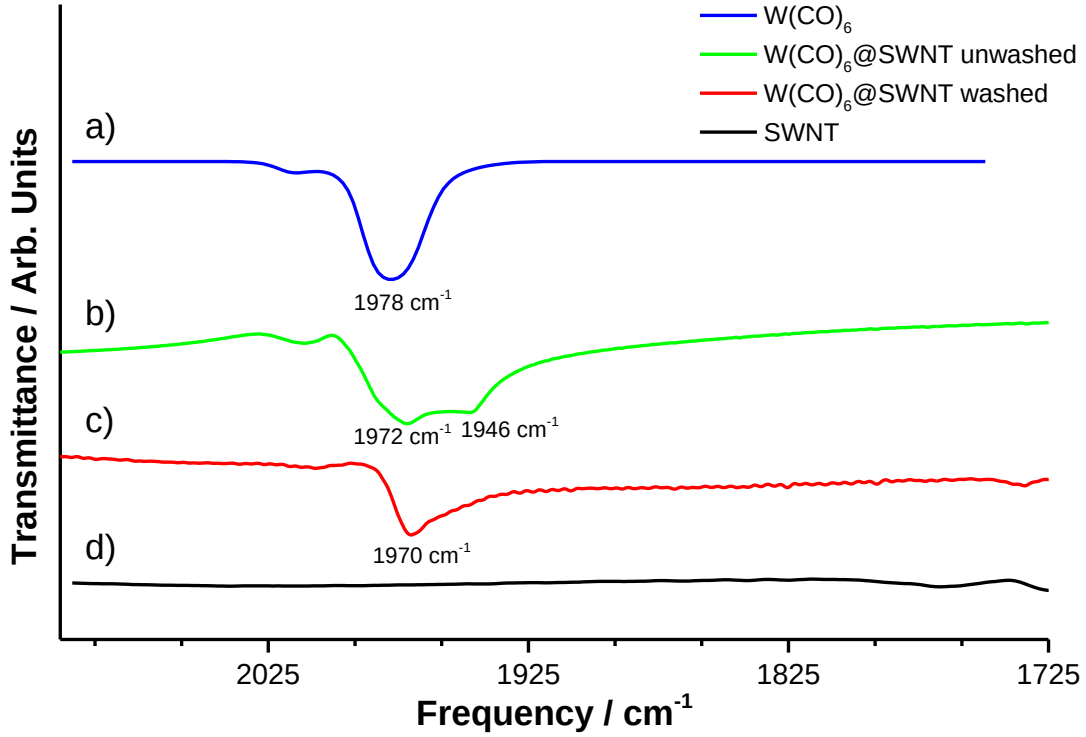


Figure 2-24. Transmission IR spectra of a) $W(CO)_6$ in $CHCl_3$, b) unwashed $W(CO)_6$@SWNT, c) $W(CO)_6$@SWNT washed with THF using an ultrasonic probe and d) SWNT recorded as KBr discs in ambient conditions with Bruker Tensor 27 spectrometer.

The transmission IR spectrum of washed $M(CO)_6$@SWNT samples were also recorded under vacuum as KBr discs using a Bruker IFS66v spectrometer (Figure 2-25) in order to verify the data shown above. The ν_{CO} frequencies detected with the Bruker IFS66v spectrometer were found to be consistent in case of all three $M(CO)_6$@SWNT samples with the results of the measurements performed with the Bruker Tensor 27 spectrometer (Table 2-4).

IR analysis for all three washed $M(CO)_6$SWNT samples showed that the ν_{CO} vibration has been affected upon encapsulation and is slightly redshifted in comparison to the values recorded in

chloroform solution of $M(CO)_6$ and significantly redshifted as compared to metal carbonyls in the gas phase (Table 2-4).[20]

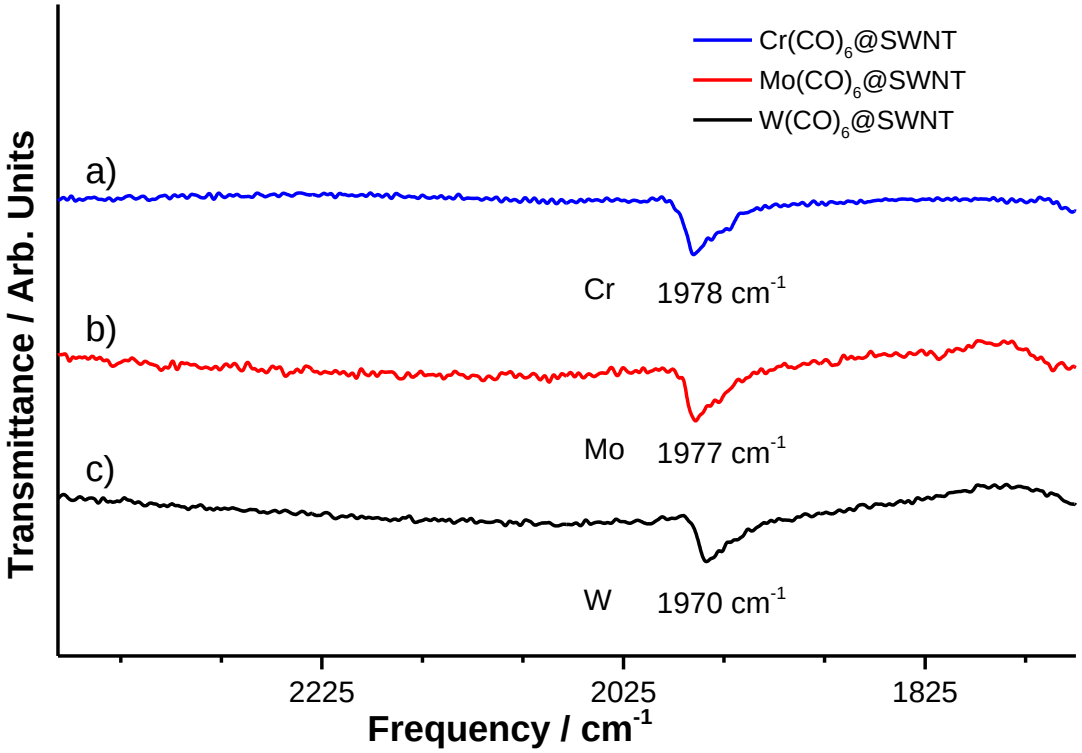


Figure 2-25. Transmission IR spectra of a) $Cr(CO)_6$@SWNT, b) $Mo(CO)_6$@SWNT, c) $W(CO)_6$@SWNT recorded as KBr discs under vacuum with a Bruker IFS66v spectrometer.

Table 2-4. Summary of ν_{CO} of $M(CO)_6$. Gas phase values were taken from the literature.[20] The IR spectra of $M(CO)_6$ in $CHCl_3$, unwashed and washed $M(CO)_6$SWNT in KBr were measured using a Bruker Tensor 27 spectrometer. In addition, the IR spectra of clean $M(CO)_6$SWNT samples in KBr were recorded using a Bruker IFS66v spectrometer.

	ν_{CO} / cm^{-1}									
	$M(CO)_6$		$M(CO)_6$@SWNT				Shift for $M(CO)_6$@SWNT			
					Washed		Tensor27		IFS66v	
	Gas phase[20]	$CHCl_3$	Unwashed		Tensor27	IFS66v	vs Gas	vs $CHCl_3$	vs Gas	vs $CHCl_3$
$Cr(CO)_6$	2000	***1982***	1982	1957	**1979**	*1978*	-21	**-3**	-22	*-4*
$Mo(CO)_6$	2004	***1984***	1984	1958	**1978**	*1977*	-26	**-6**	-27	*-7*
$W(CO)_6$	1998	***1978***	1972	1946	**1970**	*1970*	-27	**-8**	-28	*-8*

2.3.1.2 Results of Raman spectroscopy analysis of $M(CO)_6$@SWNTs

In a complementary fashion to IR spectroscopy, pristine SWNT and $W(CO)_6$@SWNT were investigated by Raman spectroscopy using 514 and 785 nm excitation wavelengths. In the recorded spectra of $W(CO)_6$@SWNT no significant change was observed in the G mode or the radial breathing mode (RBM) of the SWNTs as a result of encapsulation (Figure 2-26) which suggests that no measurable charge transfer occurred between the SWNTs and $M(CO)_6$ molecules.

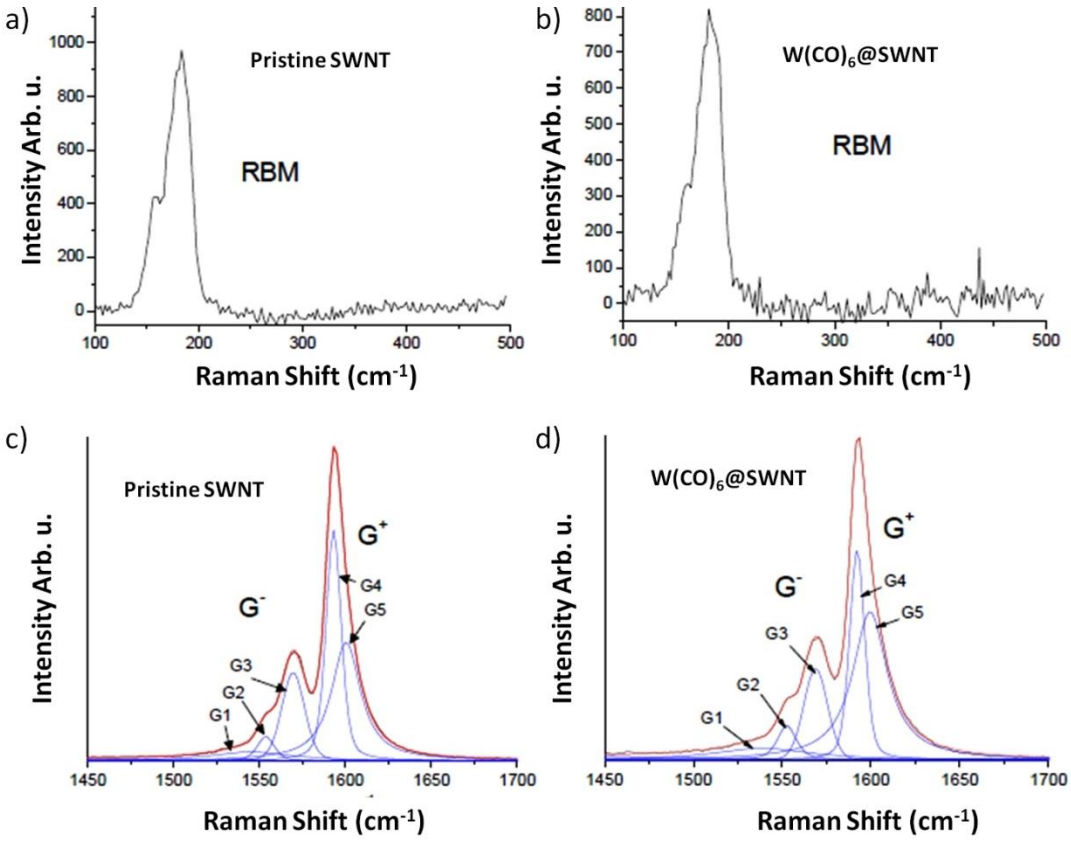


Figure 2-26. Raman spectra of the RBM of a) pristine SWNTs, b) $W(CO)_6$@SWNT and the G mode of c) pristine SWNTs, d) $W(CO)_6$@SWNT recorded using 514 nm excitation wavelength as described in Section 2.5.6. No significant change were observed in the shape or frequency of the G and RBM bands as a result of the encapsulation of $W(CO)_6$ in SWNTs.

2.3.2 Discussion of the vibrational spectra of $M(CO)_6$@SWNTs

2.3.2.1 Analysis of the carbonyl band shape in $M(CO)_6$@SWNTs

In contrast to the well-defined IR band observed in the case of isolated $M(CO)_6$ molecules in chloroform or in the gas phase, the IR spectra of $M(CO)_6$@SWNTs were found to be more complex. Deviations in the ν_{CO} band shape may be the result of the $M(CO)_6$ molecules being situated in anisotropic environments within the SWNTs as was also observed in the IR spectra of $M(CO)_6$ recorded in KBr (Figure 2-4) and earlier in cryogenic matrices and zeolites.[2,9] Under such circumstances the energy levels of the T_{1u} vibrational modes are not degenerate, therefore the frequency of the IR bands will be detuned resulting in a complex spectrum.

To explain the shape of the ν_{CO} band observed in $M(CO)_6$@SWNTs two models were constructed considering configurations of $M(CO)_6$ which would result in an asymmetric environment around the $M(CO)_6$ molecules in the SWNTs.

In the first model the asymmetric shape of the ν_{CO} band is considered to be a consequence of the inherent polydispersity of SWNT samples, *i.e.* as the sample contains SWNTs with various diameters (1.4±0.1 nm) and chirality, so that $M(CO)_6$ molecules would be located off axis in larger diameter SWNTs. Therefore, the C=O bond in the CO groups pointing towards the void of the nanotube would be affected to a lesser extent by the host-guest interactions, than those facing towards the sidewall of the SWNT

resulting in an anisotropic, orientation-dependent variation in the strength of the host-guest interaction (Figure 2-27). This would lead to a redshift that is smaller than in the case of an "ideal" diameter (d_{NT}~1.4 nm) SWNT and that is inversely proportional to the diameter of the host SWNT. In addition, the anisotropic strength of the interaction would lead to the energy levels of the T_{1u} vibrational mode becoming perturbed and would result in the broadening of the ν_{CO} IR band. Moreover, SWNTs with larger diameters than the ideal 1.4 nm might also affect the ν_{CO} IR band *via* influencing the filling rate of SWNTs as they are easier to fill meaning that they will contain more guest-molecules and contribute to the IR spectrum to a greater extent than ideal or smaller diameter SWNTs.

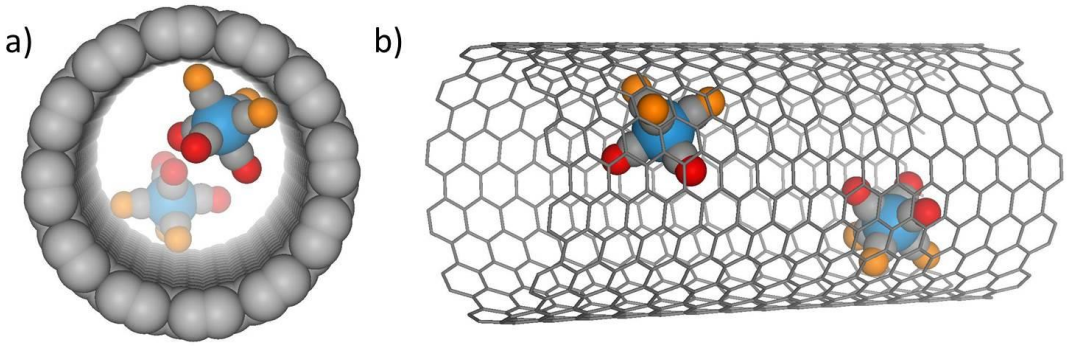


Figure 2-27. a) Space-filled model of $M(CO)_6$ molecules in a (12,12)SWNT (d_{NT}=1.63 nm). The orange O atoms indicate CO groups pointing towards the sidewall of the SWNTs and thus more involved in host-guest interactions. b) Side view of the same $M(CO)_6$@(12,12) SWNT structure.

Overall, the diameter distribution of SWNTs may result in broadening the ν_{CO} band that has higher intensity at higher wave numbers due to the higher number of molecules encapsulated into wider SWNTs.

The second model involves only "ideal" diameter (d_{NT}~1.4 nm) SWNTs in which the $M(CO)_6$ molecules may have a specific arrangement, in which four of the CO groups (equatorial) are perpendicular and the two axial CO groups (axial) are parallel to the principal axis/sidewall of the carbon nanotube (Figure 2-28). In this case, the equatorial CO groups would interact more strongly with the sidewall and therefore experience greater host-guest interactions, leading to differences in energy levels and vibrational frequencies of the equatorial and axial carbonyl groups, and resulting in the split of the T_{1u} IR band.

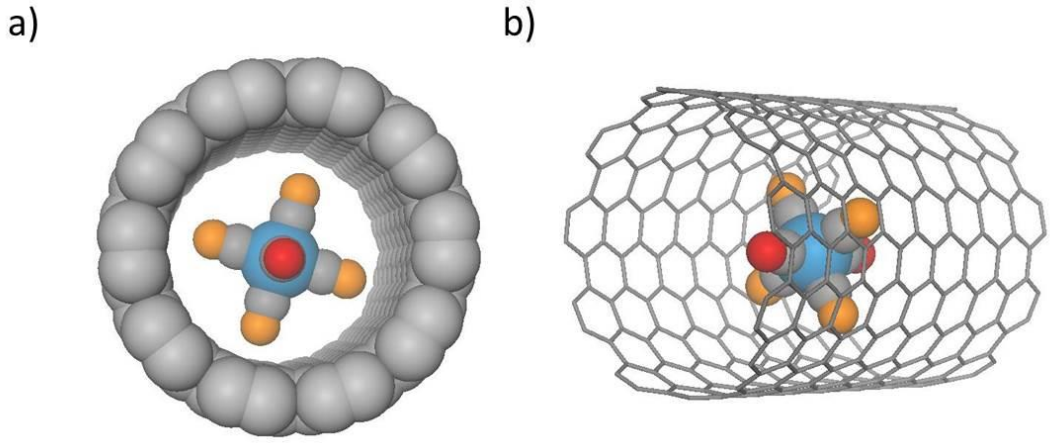


Figure 2-28. a) Space-filled model of a $M(CO)_6$ molecule in a (10,10) SWNT (d_{NT}=1.37 nm). Four CO groups (equatorial, orange O atoms) are perpendicular, two (axial, red O atoms) are parallel to the sidewall of SWNT. b) Side view of $M(CO)_6$@ SWNT(10,10) structure.

Comparison of the band shapes expected in the case of the two proposed models to the experimentally observed IR spectrum of $M(CO)_6$@SWNT samples leads to an important ascertainment. The single ν_{CO} absorption band observed in the IR spectra of $M(CO)_6$@SWNTs suggests that the $M(CO)_6$ molecules are not

packed in any specific way relative to the principal axis of the nanotube in SWNTs, rather they form a mobile, gas-like 1D array, *i.e.* they appear to be equivalent to each other on the timescale of the IR measurements. Consequently, the asymmetric shape of the ν_{CO} band *i.e.* maximum intensity at high wave numbers (see Figure 2-25) in the IR spectrum of $M(CO)_6$@SWNTs must be the result of the effects caused by the polydispersity of the SWNT sample *i.e.* the anisotropic strength of the an der Waals interaction and higher filling rate of larger diameter SWNTs.

2.3.2.2 Determination of the nature of the host-guest interactions in $M(CO)_6$@SWNTs

In this section the information obtained *via* vibrational spectroscopy is analysed to elucidate the nature of the host-guest interaction in $M(CO)_6$@SWNT systems. When introducing species inside carbon nanotubes three different interactions can occur: 1) ubiquitous dispersive interactions, (*i.e.* van der Waals interactions), 2) charge transfer interactions and 3) elastic strain caused by the encapsulation of large molecules which distort the nanotube structure. All of these interactions may affect the SWNTs resulting in a change of their vibrational spectra, introduced in Chapter I.

Mechanical strain in the carbon nanotubes caused by the encapsulated guest-molecules usually results in the upshift of the RBM due to the stress on the carbon framework.[21]

In contrast, van der Waals interactions between the guest-molecules and the host SWNTs have been reported previously to cause a downshift of the RBM by approx. 3 cm^{-1}, explained by softening of the C–C bonds of the SWNTs.[22]

Charge transfer to and from SWNTs causes the down or upshift of the G band, respectively, as it alters the C–C bonds and the electronic structure of the SWNTs.[23]

Raman spectroscopy showed that the encapsulation of $M(CO)_6$ molecules in SWNTs did not result in the shift of the G mode in any direction (Figure 2-26 c, d), implying that there is no charge transfer between the host SWNTs and the guest-molecules.

However, as no perturbation of the RBM was observed (Figure 2-26 a, b) only moderate van der Waals interactions may be present between the sidewall of SWNTs and the $M(CO)_6$ molecules.

In addition, IR measurements revealed that the ν_{CO} IR band is redshifted by 3-8 cm^{-1} in $M(CO)_6$@SWNTs. This shift is likely to be caused by the polarisation of the CO bond due to van der Waals interactions between the interior of the SWNTs and the $M(CO)_6$ molecules. The magnitude and direction of these shifts are in good agreement with the ones previously observed in the IR spectrum of octasiloxane ($Si_8H_8O_{12}$) (redshift of 15 cm^{-1})[24] and adamantane ($C_{10}H_{16}$) in SWNTs (redshift of 11 cm^{-1}),[25] where the redshift of the IR bands was attributed to the van der Waals interaction between

the guest-molecules and the nanotube upon encapsulation.

2.3.2.3 Theoretical investigation of the IR spectra of $M(CO)_6$@SWNTs

The effect of encapsulation on the IR spectra of $M(CO)_6$ molecules inside SWNTs was also investigated by a theoretical approach as described in Section 2.5.8. The calculations focused on the CO stretching mode of the molecules as these vibrational modes are essentially decoupled from the rest of the vibrational modes and, more importantly, they were the subject of the experimental IR study described in Section 2.3.1.1.

Prior to calculating the IR spectrum of $M(CO)_6$@SWNTs systems, their structures were optimised using a section of (10,10)SWNT consisting of 200 carbon atoms terminated with hydrogen atoms (Figure 2-29).

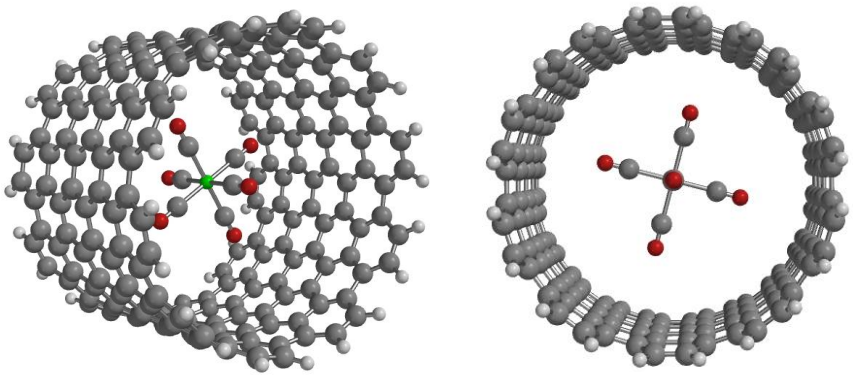


Figure 2-29. Optimised structure of $M(CO)_6$@SWNT where the (10,10)SWNT section consists of 200 carbon atoms terminated with hydrogen atoms.

It was found that the $M(CO)_6$ molecules align themselves in the SWNTs such that four CO groups (equatorial) are perpendicular and the remaining two CO groups (axial) are parallel to the

principal axis/sidewall of the carbon nanotube as proposed previously (Page 113, Figure 2-28). Moreover, the O_h symmetry of $M(CO)_6$ is distorted as a result of encapsulation resulting in longer M-C bonds in case of the equatorial CO groups. This effect is even greater (+0.003-0.01 Å) when dispersion is taken into account (Table 2-5). Therefore, the A_{1g} and E_g modes, which are not observed in the spectra of the free molecule, may became IR active, although their intensity is predicted to be negligible by the calculations.

Table 2-5. Calculated change of the equatorial M-C bond lengths in $M(CO)_6$ molecules due to the encapsulation in SWNTs. The calculations were performed by LANL2DZ+6-31G*+STO-3G and LANL2DZ+6-31G*+STO-3G basis sets in case of HF and HF+D, respectively.

Molecule	M-C bond length/Å	
	HF	HF+D
$Cr(CO)_6$	+0.003	+0.013
$Mo(CO)_6$	+0.002	+0.009
$W(CO)_6$	+0.002	+0.005

Table 2-6. Calculated charge of the $M(CO)_6$ molecules encapsulated in SWNTs as calculated by Mülliken population. The calculations were performed with the LANL2DZ+6-31G*+STO-3G basis sets.

Molecule	Charge of $M(CO)_6$ / e^-	
	HF	HF+D
$Cr(CO)_6$	-0.057	-0.058
$Mo(CO)_6$	-0.051	-0.052
$W(CO)_6$	-0.040	-0.040

Hartree-Fock (HF) calculations showed a small redshift of ν_{CO} in $M(CO)_6$@SWNTs in the range 2.7-4.5 cm^{-1} compared to the calculated gas phase values (Table 2-7), which is attributed to a

small amount of charge transfer from SWNT to $M(CO)_6$ (Table 2-6). In contrast with this result experimental observations do not indicate charge transfer in $M(CO)_6$@SWNT systems, as only a minor change was observed in the shape of the RBM and G mode by Raman spectroscopy (Figure 2-26 on Page 110).

Table 2-7. Computed shifts of the ν_{CO} vibrational modes in $M(CO)_6$@SWNTs given by HF and HF+D calculations using LANL2DZ+6-31G*+STO-3G and LANL2DZ+6-31G*+STO-3G basis sets, respectively.

	$\Delta\nu_{CO}$ / cm^{-1}					
$M(CO)_6$@SWNT	T_{1u}		E_g		A_{1g}	
	HF	HF+D	HF	HF+D	HF	HF+D
$Cr(CO)_6$	-3.3 -3.5 -3.9	-5.0 -5.0 -6.2	-2.2 -2.6	-4.0 -4.5	-1.1	-4.2
$Mo(CO)_6$	-2.7 -2.9 -3.0	-5.3 -6.3 -6.9	-0.6 -0.9	-3.3 -4.4	+0.3	-4.6
$W(CO)_6$	-3.3 -4.4 -4.5	-5.2 -8.1 -8.5	-1.4 -1.6	-3.4 -5.1	-0.4	-4.9

As the LUMO of $M(CO)_6$ (Figure 2-30) has antibonding character any occupation of this orbital would result in the weakening of the CO bond and in the redshift of the CO stretching frequency. However, the amount of redshift predicted by HF theory increases from Mo to W (Mo<Cr<W) in contrast to the experimentally observed Cr<Mo<W order. Importantly, the inclusion of dispersion in the model (HF+D) increases the redshift of ν_{CO} in $M(CO)_6$@SWNTs (Table 2-7), moreover it also alters the order of the magnitude of the shift to $Cr(CO)_6$<$Mo(CO)_6$<$W(CO)_6$, which is in agreement with the experimentally measured order. However,

the amount of ν_{CO} shift is underestimated which may be resolved by running density functional theory (DFT) calculations in the future.

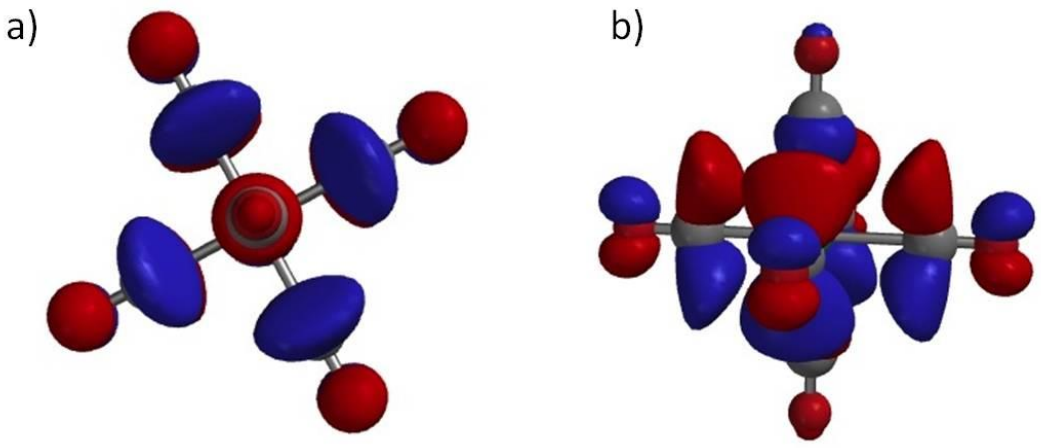


Figure 2-30. LUMO of a $M(CO)_6$ molecule showing its antibonding character a) from axial and b) equatorial viewpoints.

2.3.2.4 Relationship between the magnitude of the IR shift of the CO stretching vibration and the physicochemical properties of the $M(CO)_6$ complexes

The fact that the magnitude of the redshift of the ν_{CO} IR band in $M(CO)_6$@SWNTs increases from $Cr(CO)_6$ to $W(CO)_6$ (Table 2-4 on Page 109) suggests that the strength of the host-guest interactions is directly influenced by the physicochemical properties of the $M(CO)_6$ molecules increasing from $Cr(CO)_6$ to $W(CO)_6$. In order to find out which molecular properties of $M(CO)_6$ are responsible for the gradual increase in the strength of the host-guest interactions a selection of them, such as size, CO bond length or polarisability, were plotted versus the redshift of the ν_{CO} IR band.

Initially the relationship between the size of the $M(CO)_6$

molecules and the IR shift was investigated, as in systems confined on the nanoscale a small difference in size can significantly influence the physicochemical properties of the system. The physical size of the $M(CO)_6$ molecules was calculated using single crystal X-ray diffraction (XRD) data as described in Section 2.5.7.

As it can be seen in Figure 2-31 there are only small differences in the size of $M(CO)_6$ complexes. The largest ($Mo(CO)_6$) is only 0.37 Å larger than the smallest ($Cr(CO)_6$) and there is only 0.02 Å difference between the size of $Mo(CO)_6$ and $W(CO)_6$ complexes. Nevertheless, even such a small difference (0.37 Å) in size may be responsible for the gradually increasing redshift of the ν_{CO} IR band, since it is approximately 11% of the van der Waals distance (3.3 Å) that separates the oxygen atoms of the hexacarbonyl complexes and the inner surface of the SWNTs (typical diameter = 14 Å/1.4 nm).

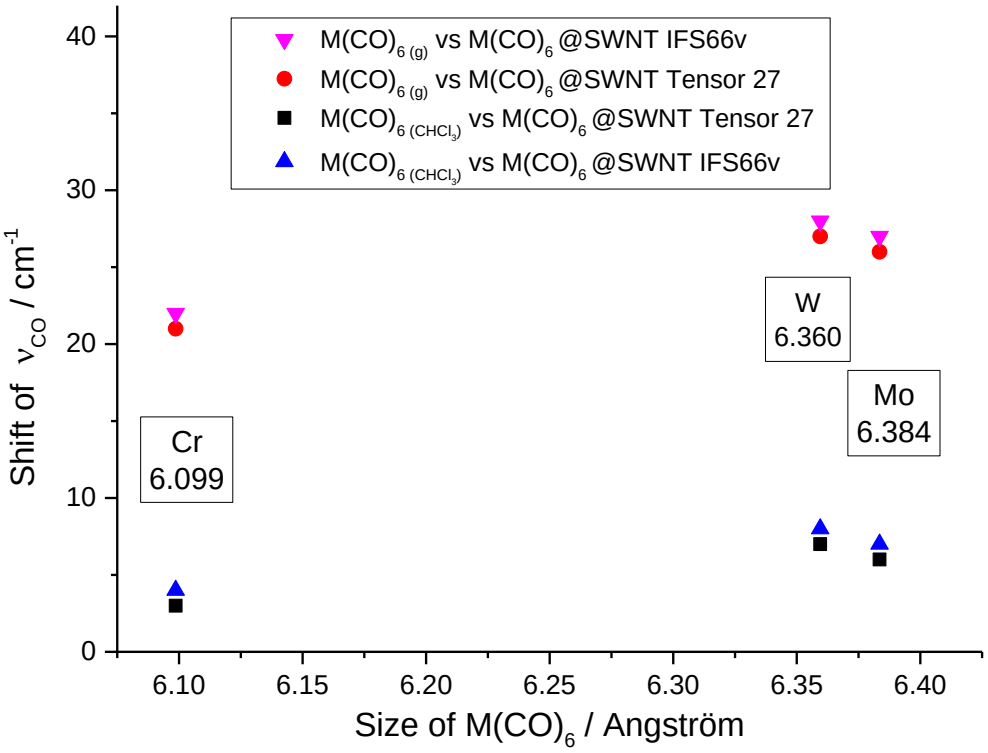


Figure 2-31. Correlation between the size of $M(CO)_6$ molecules and the shift of ν_{CO} in $M(CO)_6$@SWNTs (M=Cr, Mo, W). The shift of ν_{CO} was calculated by comparing the gas phase and $CHCl_3$ solution values of $M(CO)_6$ molecules to the values measured in case of $M(CO)_6$@SWNTs with Bruker Tensor 27 and IFS66v spectrometers as KBr discs.

However, it is clear from Figure 2-31 that the size distribution of $M(CO)_6$ molecules (Mo>W>Cr) does not correlate with the observed trend of the ν_{CO} shift (W>Mo>Cr). Consequently, it can be concluded that the shift of ν_{CO} IR band and the host-guest interactions are not dramatically influenced by the size of $M(CO)_6$ molecules in $M(CO)_6$@SWNTs systems.

The second parameter to be investigated was the variation of the CO bond length in $M(CO)_6$ molecules versus the redshift of the ν_{CO} IR band, since its length is influenced by the van der Waals interaction and has an intimate relationship with the CO bond strength and consequently with the frequency of the CO stretching vibration. The CO bond lengths were also measured using single

crystal XRD data as described in Section 2.5.7.

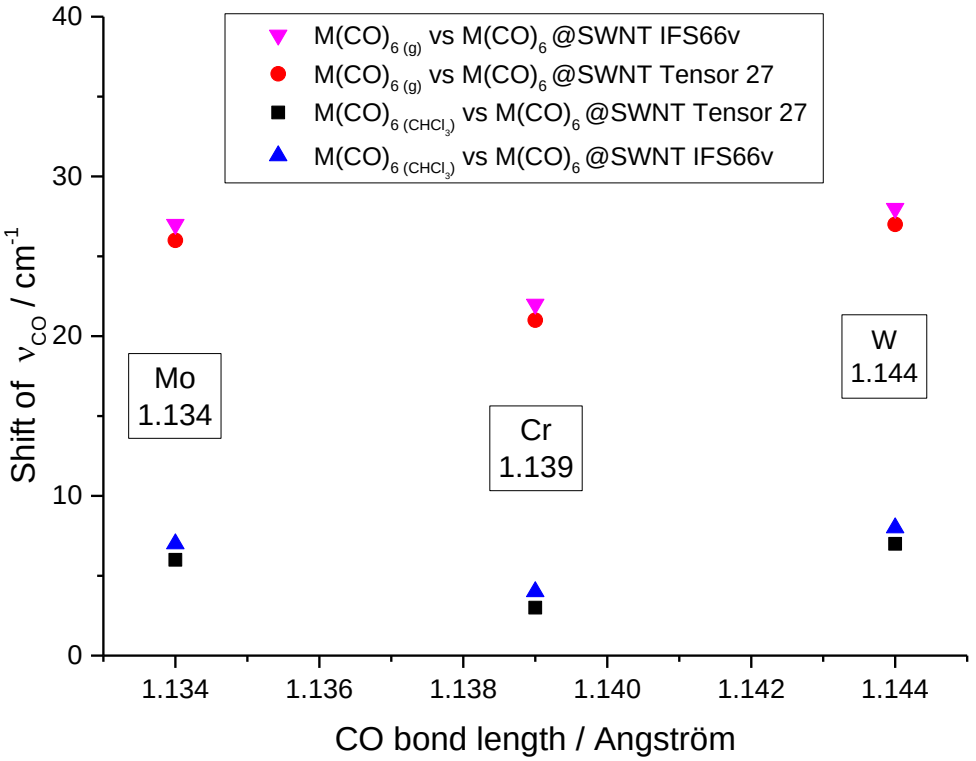


Figure 2-32. Length of the CO bond versus the shift of ν_{CO} in $M(CO)_6$@SWNTs (M=Cr, Mo, W). The shift of ν_{CO} was calculated by comparing the gas phase and $CHCl_3$ solution values of $M(CO)_6$ molecules to the values measured in case of $M(CO)_6$@SWNTs with Bruker Tensor 27 and IFS66v spectrometers as KBr discs.

The average CO bond lengths were plotted versus the shift of the ν_{CO} IR band (Figure 2-32), revealing that the bond length increases in the order of Mo<W<Cr in contrast to the redshift of ν_{CO} band (Cr<Mo<W). This suggests that the change of the CO bond length due to the host-guest interaction does not depend on the original bond length of the guest.

The strength of van der Waals interactions is known to depend on the dipole moment and polarisability of the interacting molecules.[20] However, in the case of $M(CO)_6$@SWNTs systems the SWNT is constant while the $M(CO)_6$ complex (M=Cr, Mo, W) varies. Therefore, to analyse the nexus between the encapsulated $M(CO)_6$

molecules and SWNTs the shift of the ν_{CO} IR band was plotted versus the polarisability of the $M(CO)_6$ molecules and their subunits *i.e.* the metal centre and the CO ligands, which were extracted from a study by G. Nagrajan.[26]

First, the polarisability of the CO bond was compared to the redshift of ν_{CO} (Figure 2-33) and it was found to increase from Mo to Cr (Mo<W<Cr) which differs from the order of the IR shift (Cr<Mo<W). This means that the polarisability of the CO bond is not the defining parameter which controls the van der Waals interactions in these systems.

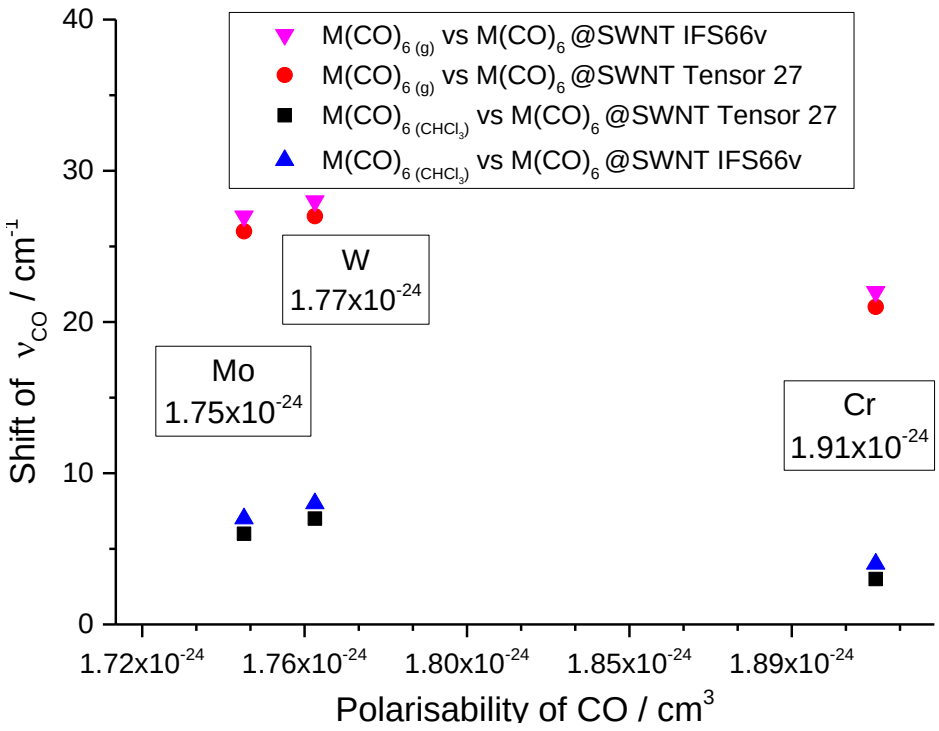


Figure 2-33. Correlation between the polarisability of the CO bond and the shift of ν_{CO} in $M(CO)_6$@SWNTs (M=Cr, Mo, W). The shift of ν_{CO} was calculated by comparing the gas phase and $CHCl_3$ solution values of $M(CO)_6$ molecules to the values measured in case of $M(CO)_6$@SWNTs with Bruker Tensor 27 and IFS66v spectrometers as KBr discs.

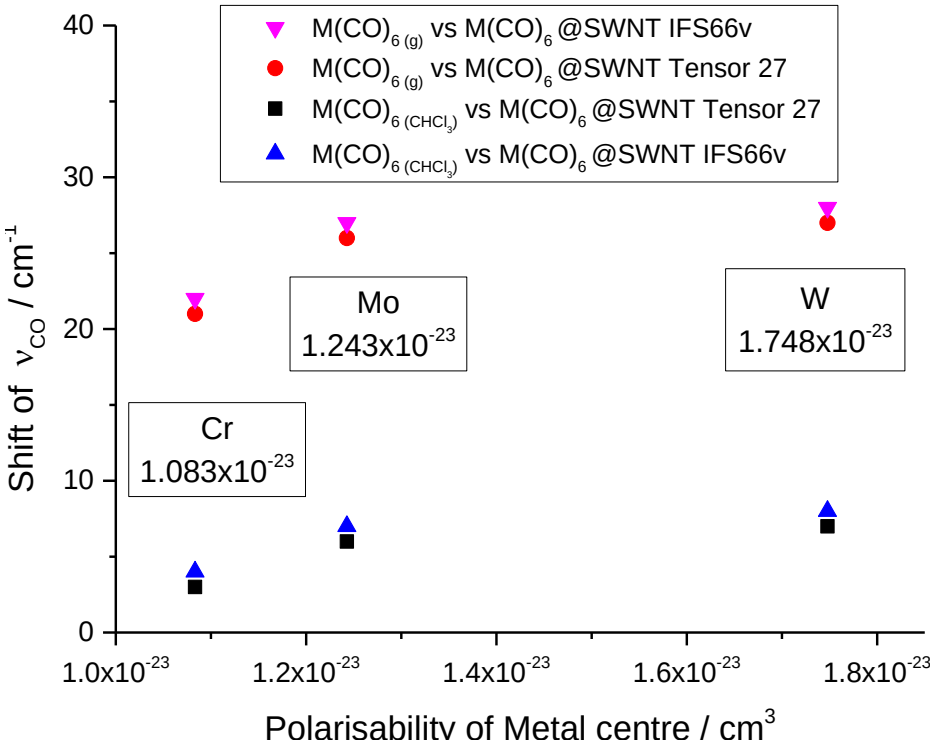


Figure 2-34. Correlation between the polarisability of metal centre and the shift of ν_{CO} in $M(CO)_6$@SWNTs (M=Cr, Mo, W). The shift of ν_{CO} was calculated by comparing the gas phase and $CHCl_3$ solution values of $M(CO)_6$ molecules to the values measured in case of $M(CO)_6$@SWNTs with Bruker Tensor 27 and IFS66v spectrometers as KBr discs.

The polarisability of the metal centres does increase down Group VI (Cr<Mo<W) despite the effects of the lanthanide contraction. Therefore, it follows the same trend as the shift of ν_{CO} IR band (Cr<Mo<W) (Figure 2-34), suggesting that the nature of the metal centre is a significant factor in the strength of the host-guest interaction in the $M(CO)_6$@SWNTs.

The influence of the electronegativity (EN) of the individual metal centre of $M(CO)_6$ complexes on the redshift of the ν_{CO} IR band was also analysed, as it is has a close relationship with their polarisability.

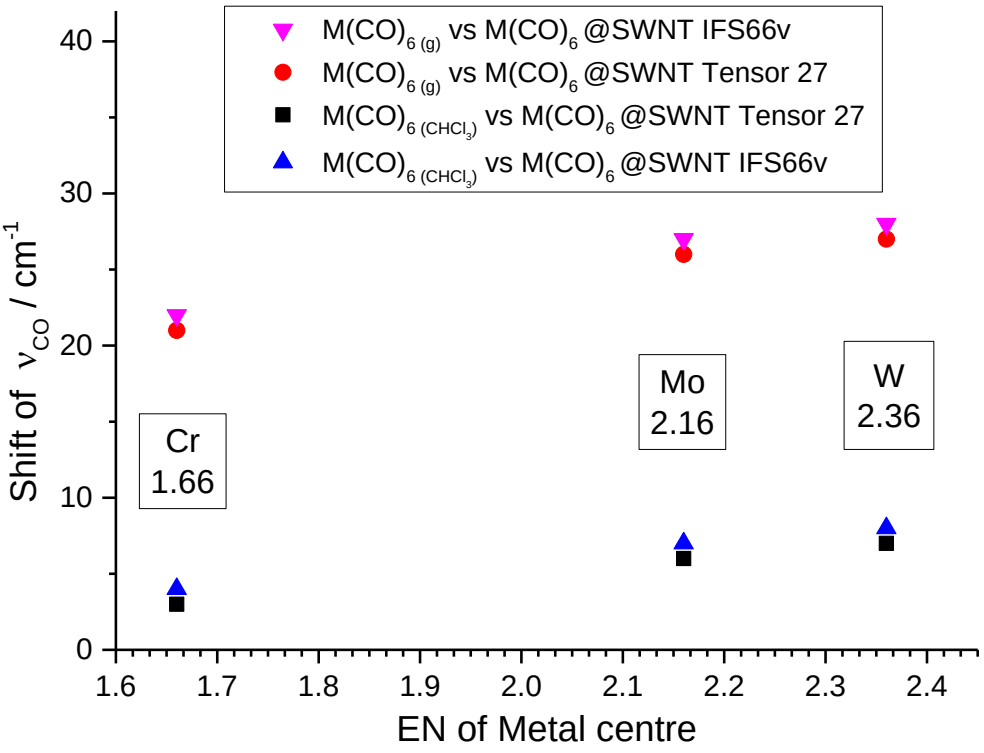


Figure 2-35. Correlation between the electronegativity of the metal centre and the shift of ν_{CO} in $M(CO)_6$@SWNTs (M=Cr, Mo, W). The shift of ν_{CO} was calculated by comparing the gas phase and $CHCl_3$ solution values of $M(CO)_6$ molecules to the values measured in case of $M(CO)_6$@SWNTs with Bruker Tensor 27 and IFS66v spectrometers as KBr discs.

As expected, it was found that the EN of the metal centres increases down the group in the same way as the IR shift of the ν_{CO} band and importantly there is a correlation between them (Figure 2-35).

Finally, the relationship between the redshift of the ν_{CO} IR band and the polarisability of the entire $M(CO)_6$ molecule was investigated. The overall polarisability of $M(CO)_6$ was found to increase in the same order, Cr<Mo<W, as the shift of the ν_{CO} band, which demonstrates that the metal centres have a greater contribution to the overall polarisability than the CO groups. Moreover, the correlation between the polarisability of the $M(CO)_6$ molecules and the redshift of the ν_{CO} band also exists,

see Figure 2-36.

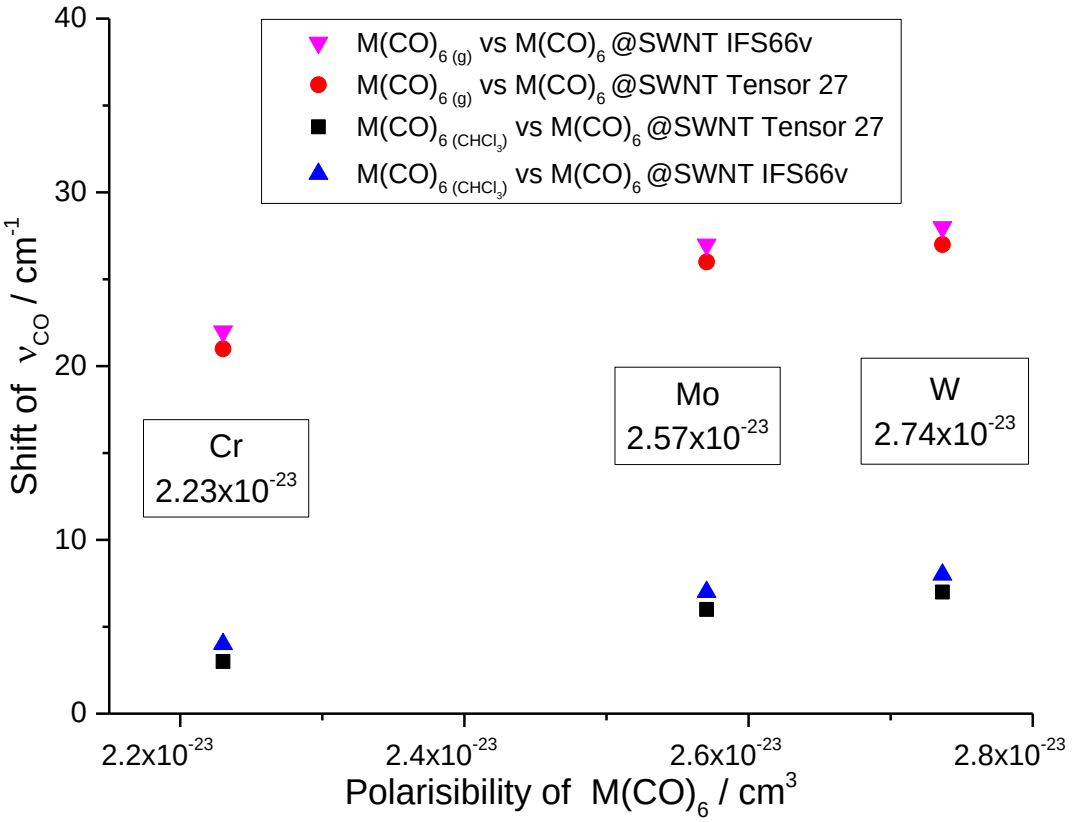


Figure 2-36. Correlation between the polarisability of $M(CO)_6$ molecule and the shift of ν_{CO} in $M(CO)_6$@SWNTs (M=Cr, Mo, W). The shift of ν_{CO} was calculated by comparing the gas phase and $CHCl_3$ solution values of $M(CO)_6$ molecules to the values measured in case of $M(CO)_6$@SWNTs with Bruker Tensor 27 and IFS66v spectrometers as KBr discs.

In conclusion, the strength of the van der Waals interactions between $M(CO)_6$ molecules and SWNTs and consequently the magnitude of the redshift of the ν_{CO} IR band depends on the electronegativity and polarisability of the metal centre and on the overall polarisability of the $M(CO)_6$ complexes. This result demonstrates that host-guest interactions are stronger if the bonds of the guest-molecules are already inherently polarised, and can be more readily polarisable by their environment *i.e.* by the host SWNTs.

2.4 Concluding remarks

In this study the host-guest interactions between single-walled carbon nanotubes and encapsulated Group VI (Cr, Mo and W) hexacarbonyl complexes were investigated.

First, the gas phase insertion of metal hexacarbonyl complexes into SWNTs was optimised to provide the highest filling rate possible in order to maximise the IR response of the encapsulated $M(CO)_6$ molecules. Test reactions showed that the reaction temperature has to be above a certain threshold (~120 °C) and the reaction mixture has to be quenched rapidly at the end of the reaction in order to entrap the $M(CO)_6$ molecules in SWNTs.

Based on these observations it was found that the encapsulation of metal hexacarbonyl complexes happens *via* a pre-adsorption mechanism similar to C_{60}, however the energy gained due to encapsulation is expected to be close to zero and the encapsulation of $M(CO)_6$ molecules in SWNTs is neither significantly thermodynamically favoured nor irreversible.

TEM analysis of the as-synthesised $M(CO)_6$@SWNTs confirmed the presence of metal hexacarbonyl complexes inside as well as on the surface of carbon nanotubes. As surface adsorbed molecules can mask the IR response of the encapsulated ones, a cleaning procedure was developed for their removal.

Vibrational spectroscopy investigations showed that no charge transfer takes place in $M(CO)_6$@SWNT systems, as no significant

change was observed in the shape of the RBM and G mode of SWNTs by Raman spectroscopy. In contrast HF calculations, including an additional dispersion component (HF+D), predicted electron transfer from the SWNTs to the $M(CO)_6$ molecules resulting in a partial negative charge on M centre (Table 2-6).

Analysis of $M(CO)_6$@SWNT systems by IR spectroscopy revealed the redshift of the ν_{CO} IR band, which is attributed to van der Waals host-guest interactions in agreement with the earlier published observations.[24,25] Importantly, the shift of the CO stretching vibrations was found to increase from $Cr(CO)_6$ to $W(CO)_6$ (Cr<Mo<W) both experimentally and theoretically.

The shape of the ν_{CO} IR band observed in washed $M(CO)_6$@SWNTs is a result of the effects caused by the inherent polydispersity of SWNTs and the mobility of $M(CO)_6$ molecules inside the nanotubes.

Investigation of the relationship between the increasing redshift of the ν_{CO} IR band and various physicochemical properties of $M(CO)_6$ complexes revealed that the strength of the van der Waals interactions between SWNTs and $M(CO)_6$ complexes depends on the electronegativity and polarisability of the metal centre as well as on the overall polarisability of the $M(CO)_6$ molecules.

To conclude, in metal hexacarbonyl and SWNT based host-guest systems the greater the overall polarisability of the guest-molecule the greater the van der Waals interactions between the host

nanotube and the guest-molecules, and the bigger the redshift of the ν_{CO} IR band.

2.5 Experimental section

Arc-discharge SWNTs (HELIX, d_{NT}=1.4 nm, purity 90%) were purchased from Helix Material Solutions. $Cr(CO)_6$ (purity≥98%) was obtained from Sigma-Aldrich and $Mo(CO)_6$ and $W(CO)_6$ complexes (purity≥98 and 99%, respectively) were purchased from Acros Organics. All materials were used without further purification.

2.5.1 Filling single-walled carbon nanotubes

2.5.1.1 Opening single-walled carbon nanotubes by oxidation in air

To provide access for the guest species to their interior, carbon nanotubes were heated in air at 380 °C for 20 minutes to open their closed ends and remove any adsorbed water.

2.5.1.2 Optimisation of the gas phase filling of $M(CO)_6$ in SWNTs

Freshly opened carbon nanotubes (5 mg, 0.42 mmol) were mixed with a large excess of $W(CO)_6$ (10 mg, 0.028 mmol) and the resultant mixture was sealed in a custom made Pyrex glass vessel (diameter=10 mm, length=10 cm) under vacuum (10^{-6} mbar) using a vacuum system (Page 81, Figure 2-5). The sealed glass vessel was placed in a preheated box furnace (1-7 days, T=100-150 °C) (Table 2-8). Prior to opening, the Pyrex glass vessel was taken out from the furnace and cooled, either by

immersing it into an ice-water bath for 5 minutes or by applying a temperature gradient (1 °C/min) in a tube furnace until the temperature reached 25 °C.

2.5.1.3 Optimised gas phase filling method of SWNTs with $M(CO)_6$

Pre-treated carbon nanotubes (5 mg, 0.42 mmol) were mixed with a large excess of $M(CO)_6$ (10 mg) and the resultant mixture was sealed in a Pyrex glass vessel (d=10 mm, l=10 cm) under high vacuum (10^{-6} mbar). The sealed vessel was placed in a preheated box furnace (T=120 or 150 °C) for 3 days (See Table 2-8). Prior to opening, the Pyrex glass vessel was taken out from the furnace and cooled down to 0 °C by immersing it into an ice-water bath for 5 minutes. After opening the Pyrex glass vessel the samples were transferred into a glass vial and stored in the freezer at **-**15 °C until further treatment.

Table 2-8. Summary of the conditions of test experiments that were performed to optimise the gas phase filling of $M(CO)_6$ (M=Cr, Mo, W) in SWNTs. Optimal conditions are indicated in bold.

Experiment	M	$m_{M(CO)_6}$ / mg	$n_{M(CO)_6}$ / mmol	m_{SWNT} / mg	T / °C	t / day	Cooling	Filling
Reaction **2–1**	W	10	0.028	5	100	1	Ice-water	No
Reaction **2–2**	W	10	0.028	5	100	7	Ice-water	No
Reaction **2–3**	W	10	0.028	5	150	1	Ice-water	Yes
Reaction **2–4**	**W**	10	0.028	5	**150**	**3**	**Ice-water**	**Yes**
Reaction **2–5**	W	10	0.028	5	150	3	1 °C/min	No
Reaction **2–6**	**Cr**	10	0.045	5	**120**	**3**	**Ice-water**	**Yes**
Reaction **2–7**	**Mo**	10	0.038	5	**120**	**3**	**Ice-water**	**Yes**

2.5.2 Removal of excess metal hexacarbonyl complex from the outside of SWNTs

2.5.2.1 Removal of excess $M(CO)_6$ by dynamic vacuum

Dynamic vacuum (10^{-3} or 10^{-6} mbar) was applied for 1 hour at room temperature to $M(CO)_6$@SWNT samples (5 mg) which were placed in a Pyrex glass tube.

2.5.2.2 Removal of excess $M(CO)_6$ with organic solvent

$M(CO)_6$@SWNT samples were suspended in THF using a variety of different methods, see below. The resultant suspensions were then filtered (polytetrafluoroethylene (PTFE) backed polypropylene filter membrane, 0.5 μm) and rinsed with further THF (100 mL).

2.5.2.2.1 Removal of excess $M(CO)_6$ by stirring in organic solvent

The $M(CO)_6$@SWNT sample (5 mg) was suspended in THF (15 mL) using magnetic stirring (500 rpm) for 3 hours, the solid was then collected by filtration (Section 2.5.2.2).

2.5.2.2.2 Removal of excess $M(CO)_6$ using an ultrasonic bath

The $M(CO)_6$@SWNT sample (5 mg) was suspended in THF (15 mL) using an ultrasonic bath (Langford Sonomatic 375, 40 kHz, 150 W) for 45 minutes, then the solid was collected by filtration (Section 2.5.2.2).

2.5.2.2.3 Removal of excess $M(CO)_6$ by using ultrasonic probe

The $M(CO)_6$@SWNT sample (5 mg) was suspended in THF (50 mL) using an ultrasonic probe (Sonics Vibra Cell CPX 130,

20 kHz, 130 W; titanium tip CV18) applying the following parameters: power 75%, pulse: On, 3 sec/Off, 2 sec. During the process, the flask was immersed into an ice-water bath to dissipate the generated heat. The solid was then collected by filtration (Section 2.5.2.2).

2.5.3 Preparation of control samples for IR measurements

2.5.3.1 Preparation of $W(CO)_6$+SWNT control sample by mechanical mixing

$W(CO)_6$ (1 mg, 0.004 mmol) and as received SWNT (0.5 mg), *i.e.* not pre-treated in air, were mixed by grounding them together in an agate mortar for 5 minutes.

2.5.3.2 Preparation of $W(CO)_6$/SWNT control sample by sublimation

$W(CO)_6$ (8 mg, 0.023 mmol) was added to as received carbon nanotubes (4 mg), then the sample was prepared following the procedure and conditions described in section 2.5.1.3.

2.5.3.3 Preparation of $W(CO)_6$/(C_{60}@SWNT) control sample by sublimation

Freshly opened carbon nanotubes (6 mg) and C_{60} (22 mg, 0.030 mmol) were combined and the resultant mixture was sealed in a Pyrex glass vessel under vacuum (10^{-6} mbar). The sealed vessel was placed in a preheated tube furnace (600 °C) for 4 days. The sample was then opened and washed extensively with CS_2 (100 mL) using an ultrasonic bath (75 minutes) to remove any

residual C_{60}. The solid material (C_{60}@SWNT) was separated by filtration (PTFE backed polypropylene filter membrane, 0.5 μm) and rinsed with additional CS_2 (100 mL). The washing procedure was repeated by dispersing the sample in CS_2 (100 mL) using an ultrasonic bath (30 minutes) and the solid material was separated by filtration and the collected sample was dried overnight. The dry C_{60}@SWNT (4 mg) was combined with $W(CO)_6$ (9 mg, 0.026 mmol and the resultant mixture was sealed in a Pyrex glass vessel under vacuum (10^{-6} mbar). The sealed vessel was placed in a preheated box furnace (150 °C) for 3 days. Prior to opening, the Pyrex glass vessel was taken out from the furnace and immersed into an ice-water bath to cool down for 5 minutes. After opening the Pyrex glass vessel the sample was transferred into a glass vial and stored in the freezer.

2.5.4 Transmission Electron Microscopy and Energy-dispersive X-ray spectroscopy

TEM micrographs and EDX spectra were acquired with an emission gun JEOL 2100F microscope at 100 kV accelerating voltage. Prior to investigation, the carbon nanotube samples (~0.5 mg) were dispersed in isopropyl alcohol (2 mL) using an ultrasonic bath (~15 min). Subsequently, a few drops were drop-casted onto a copper TEM grid coated with lacy carbon film (Agar Scientific) to support the carbon nanotubes.

2.5.5 Infrared spectroscopy

The IR spectra of freestanding $M(CO)_6$ molecules were recorded in $CHCl_3$ solution and/or as a KBr disc in transmission configuration. The spectra of $M(CO)_6$-SWNT samples were recorded as KBr discs (~0.1 mg SWNT/$M(CO)_6$@SWNT and 300 mg KBr). After homogenisation in an agate mortar KBr discs were pressed at 10 tons for 2 minutes. The press was evacuated prior to (in Nottingham) or during (in Budapest) pressurisation.

Infrared spectroscopy was performed in ambient conditions on a Bruker Tensor 27 spectrometer in the range 400-4000 cm^{-1} with 1 cm^{-1} resolution, using 16 forward-backward scans and a 6 mm spot size (Nottingham, UK).

Additionally the IR spectrum of washed $M(CO)_6$@SWNT were recorded on a Bruker IFS66v spectrometer under vacuum (10^{-6} mbar) in the range 400-4000 cm^{-1} with 1 cm^{-1} resolution, using 128 forward-backward scans and a 4 mm spot size at the Wigner Research Centre for Physics of the Hungarian Academy of Sciences (Budapest, Hungary).

2.5.6 Raman scattering

Raman measurements of $M(CO)_6$@SWNTs were performed at room temperature using a Renishaw inVia Raman Microspectrometer (514 and 785 nm excitation wavelengths) at the Naval Postgraduate School (NPS, Monterey, CA, USA).

2.5.7 Calculation of the average size and CO bond length of $M(CO)_6$ complexes

The 3D models of the $M(CO)_6$ molecules are based on the single crystal XRD data provided by the Chemical Database Service at Daresbury (CDS).

The physical size of the $M(CO)_6$ molecules were calculated by averaging the distances, which were measured between the three pairs of O atoms located at the opposite vertices of the octahedron.

The average CO bond lengths were calculated by measuring all the individual CO bond lengths of the $M(CO)_6$ structure, then their average was taken.

2.5.8 Theoretical investigation of the infrared spectra of $M(CO)_6$@SWNTs

The theoretical calculations were performed by Dr. Nick Besley (School of Chemistry, University of Nottingham).

The vibrational frequencies of the CO stretching vibrations of $M(CO)_6$ molecules in the gas phase were calculated using Hartree-Fock (HF) theory with the LANL2DZ basis set for the metal centres and the 6-31G* basis set for the carbon and oxygen atoms. Frequencies were also computed with HF theory incorporating an empirical dispersion correction of the form (HF+D):

$$E_{disp} = -s_6 \sum_{A}^{N} \sum_{B<A}^{N} \frac{C_6^{AB}}{R_{AB}^6} f_{dmp}(R_{AB})$$

Equation 2-1 ,

where N is the number of atoms in the system, C_6^{AB} is the dispersion coefficient for atom pair AB, s_6 is a scaling factor and R_{AB} is the distance between atoms A and B. A damping function $f_{dmp}(R_{AB})$ is also included to avoid double counting of electron correlation effects and the near-singularities as $R_{AB} \rightarrow 0$. Harmonic frequencies computed with HF theory are known to be systematically too high, therefore the calculated frequecies are scaled by a factor of 0.8953 which is appropriate for HF/6-31G*.[27]

Prior to calculating the IR spectrum of $M(CO)_6$@SWNTs systems, their structures were optimised using a section of (10,10)SWNT consisting of 200 carbon atoms terminated with hydrogen atoms (Figure 2-29 on page 116). The STO-3G basis set was used for the atoms of the nanotube. The vibrational frequencies of $M(CO)_6$ located within the SWNT were computed with a partial Hessian approach wherein the Hessian matrix is computed for the degrees of freedom $M(CO)_6$ only.

2.6 References

1. A. N. Khlobystov, K. Porfyrakis, M. Kanai, D. a Britz, A. Ardavan, H. Shinohara, T. J. S. Dennis, and G. A. D. Briggs, *Angew. Chem. Int. Ed. Engl.*, 2004, **43**, 1386–1389.

2. Y. Okamoto, A. Maezawa, H. Kane, I. Mitsushima, and T. Imanaka, *J. Chem. Soc. Faraday Trans. 1*, 1988, **84**, 851–863.

3. K. Andras and S. Laszlo, *Chemistry of Organometallic compounds*, Budapest, 2001.

4. M. Kaushik, A. Singh, and M. Kumar, *Eur. J. Chem.*, 2012, **3**, 367–394.

5. H. Abe and K. M. T. Yamada, *Struct. Chem.*, 2003, **14**, 211–215.

6. S. L. Shufler, H. W. Sternberg, and R. Friedel, *J. Am. Chem. Soc.*, 1956, **78**, 2687–2688.

7. M. R. Afiz, R. J. H. Clark, and N. R. D'Urso, *J. Chem. Soc. Dalt. Trans.*, 1977, **3**, 250–254.

8. L. H. Jones, R. S. McDowell, and M. Goldblatt, *Inorg. Chem.*, 1969, **8**, 2349–2363.

9. M. Broquier, C. Crépin, H. Dubost, and J.-P. Galaup, *Chem. Phys.*, 2007, **341**, 207–217.

10. U. A. Jayasooriya, *J. Chem. Soc. Faraday Trans.*, 1994, **90**, 1265–1269.

11. D. V Kazachkin, Y. Nishimura, H. A. Witek, S. Irle, and E. Borguet, *J. Am. Chem. Soc.*, 2011, **133**, 8191–8198.

12. J. Sloan and M. Monthioux, in *Carbon Meta-Nanotubes: Synthesis, Properties and Applications*, ed. M. Monthioux, John Wiley & Sons, Ltd, Chichester, UK, 2011, pp. 225 –271.

13. H. Ulbricht, G. Moos, and T. Hertel, *Phys. Rev. Lett.*, 2003, **90**, 7–10.

14. V. V. Chaban and O. V. Prezhdo, *ACS Nano*, 2011, **5**, 5647–5655.

15. V. V. Chaban, V. V. Prezhdo, and O. V. Prezhdo, *ACS Nano*, 2012, **6**, 2766–2773.

16. K. Koga, G. T. Gao, H. Tanaka, and X. C. Zeng, *Nature*, 2001, **412**, 802–805.

17. B. W. Smith and D. E. Luzzi, *Chem. Phys. Lett.*, 2000, **321**, 169–174.

18. S. Berber, Y.-K. Kwon, and D. Tománek, *Phys. Rev. Lett.*, 2002, **88**, 185502–1–185502–4.

19. H. Ulbricht and T. Hertel, *J. Phys. Chem. B*, 2003, **107**, 14185–14190.

20. R. J. H. Clark and B. Crociani, *Inorganica Chim. Acta*, 1967, **1**, 12–16.

21. S. Bandow, M. Takizawa, H. Kato, T. Okazaki, H. Shinohara, and S. Iijima, *Chem. Phys. Lett.*, 2001, **347**, 23–28.

22. A. N. Khlobystov, R. Scipioni, D. Nguyen-Manh, D. A. Britz, D. G. Pettifor, G. A. D. Briggs, S. G. Lyapin, A. Ardavan, and R. J. Nicholas, *Appl. Phys. Lett.*, 2004, **84**, 792.

23. D. A. Britz and A. N. Khlobystov, *Chem. Soc. Rev.*, 2006, **35**, 637–659.

24. J. Wang, M. K. Kuimova, M. Poliakoff, G. A. D. Briggs, and A. N. Khlobystov, *Angew. Chem. Int. Ed. Engl.*, 2006, **45**, 5188–5191.

25. M. Yao, P. Stenmark, E. Abou-Hamad, F. Nitze, J. Qin, C. Goze-Bac, and T. Wagberg, *Carbon N. Y.*, 2010, **49**, 1159–1166.

26. G. Nagarajan, *Bull. des Sociétés Chim. Belges*, 1981, **90**, 1077–1092.

27. A. P. Scott and L. Radom, *J. Phys. Chem.*, 1996, **100**, 16502–16513.

3 Controlled formation of metal nanoparticles inside graphitised carbon nanofibers

3.1 Introduction

Understanding the formation of hybrid nanomaterials based on hollow graphitic carbon structures and metal-containing inorganic compounds is important, since they can be used as functional nanomaterials in next generation energy harnessing and storage devices such as solar cells, batteries and supercapacitors.[1–5] Moreover, their chemical properties are also the focus of research as it has been demonstrated that hollow graphitic carbon structures can effectively change the selectivity of chemical reactions due to the unique reaction environment in which the reactants are confined.[5,6] For example, the regioselectivity of hydrosilylation reactions have been altered dramatically by performing them inside graphitised carbon nanofibers (GNF) using an embedded Rh nanoparticle (NP) catalyst where the encapsulated Rh NPs are adsorbed on the step-edges of the GNFs as showed by transmission electron microscopy (TEM) (Figure 3-1).[7] The change in regioselectivity is attributed to π–π interactions between the reactant molecules and the step-edges of the GNF in close proximity to the Rh catalyst. The site-specific adsorption of NPs such as Pt,[8] Cu[9] and Au[10] on the step-edges of GNFs has also been observed, suggesting that this is a general

phenomenon, which may be driven by the maximisation of non-covalent interactions.

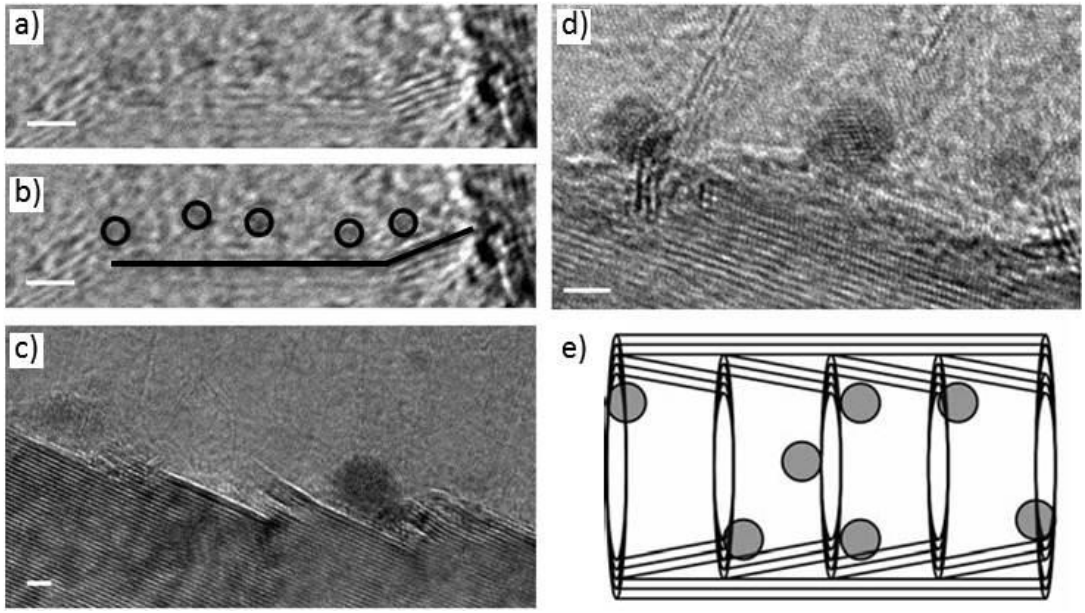


Figure 3-1. a)-b) TEM micrographs of Rh NPs situated on the step-edge of a GNF (top view). c)-d) Side view of thermally enlarged Rh NPs at the step-edge of GNF. e) Cartoon of Rh NPs (grey spheres) adsorbed at the step-edge of GNF. Scale bars are 2 nm.[7]

Although, M NP@GNFs have remarkable physicochemical properties their production is limited to a relatively small number of metals including Rh,[7] Pt,[8] Cu,[9] Ag,[9] and Au.[10] This is because M NP@GNFs are typically made by the capillary encapsulation of freestanding M NPs dispersed in water or organic solvents,[11] and the synthesis of NPs of certain metals is challenging due to oxidation, agglomeration *etc.* of the NPs. Therefore, to increase the variety of different M NPs supported on the inner surface of GNFs alternative strategies have to be developed. A promising strategy, previously utilised to make M NPs@SWNT is the encapsulation of reactive precursor molecules in GNFs which are subsequently transformed into NPs by thermal treatment.[12]

Consequently, the goal of this study is the synthesis of metal based nanoparticles inside GNFs by *in situ* transformation of encapsulated metal containing precursor molecules. This will result in the expansion of the rapidly growing field of hybrid nanomaterials based on hollow graphitic carbon structures.

3.2 Selection of filling method and precursor molecules

The main challenges during forming M NPs inside GNFs are the selection of appropriate; precursor molecules, filling methods and conditions to initiate the transformation of the encapsulated precursors into M NPs.

Since GNFs, though wider, are closely related to carbon nanotubes (CNTs), established filling methods such as gas phase filling, capillary filling with molten material or with the solution of a guest material can be conveniently adopted.[13]

During selection of the most appropriate filling method it has to be considered that the most important goal of the encapsulation is the exclusive deposition of the precursor molecules inside the channel of the GNFs. The different filling methods may provide structurally or chemically different composites of the GNFs and the precursor molecules, which could influence the subsequent formation of NPs in an undesired manner.

Using a solution of precursor molecules would inherently lead to the unwanted encapsulation of solvent molecules as well as the desired precursor, which may perturb any subsequent

transformation into NPs.

The encapsulation of molten precursor material *via* capillary filling would result in the saturation of GNFs and blocking their internal channel as shown in case of carbon nanotubes, which could prohibit the transport of reactants and products during the chemical transformation of the precursor molecules.[14]

Fortunately, these unwanted effects can be bypassed and the precursor molecules can be deposited on the inner surface of the GNFs without blocking their internal channels using gas phase filling.

The transformation of encapsulated precursor molecules into NPs can be initiated by various kinds of external stimuli such as heat, light, microwaves *etc*.[15,16] Moreover, to influence the properties of the final product the transformations may be performed in different environments such as vacuum, inert or reactive gas atmospheres. The resultant material of the transformation performed inside the GNFs may be extracted prior to analysis,[7] however, more frequently the composite of the product and GNFs is characterised *in situ* by TEM, powder X-ray diffraction (PXRD), *etc*.[10]

In summary, an ideal precursor molecule should: 1) contain the desired metal atom(s), 2) sublime readily without decomposition and 3) be easily converted into NPs by external stimuli.

Based on the above described criteria, metal hexacarbonyl

complexes ($M(CO)_6$, M=Cr, Mo, W) were chosen as precursor molecules, as metal carbonyls have been successfully inserted into carbon nanotubes from the gas phase and transformed into M NPs (M=W, Os, Re) by thermal decomposition or the knock-on damage of the e-beam, as it was shown by TEM and EDX spectroscopy (Figure 3-2).[12,17]

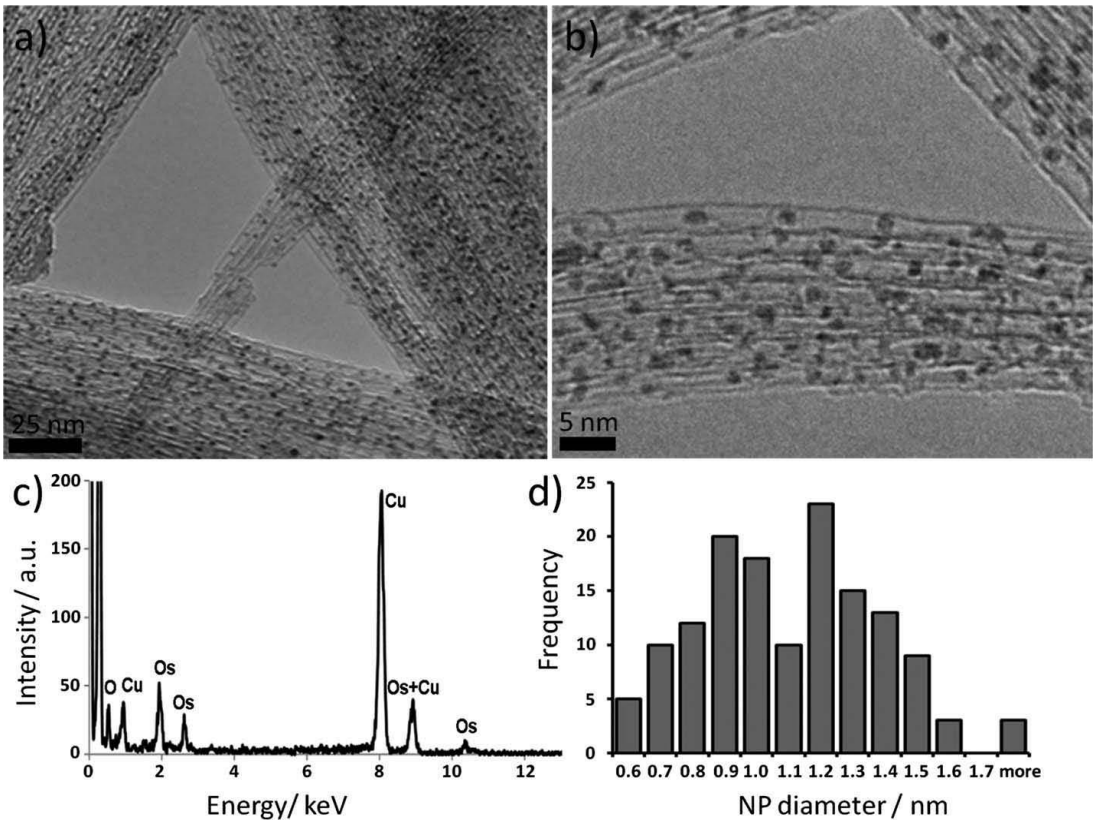


Figure 3-2. a)–b) TEM images of Os NPs@SWNT generated by thermal decomposition of $Os_3(CO)_{12}$@SWNT. c) EDX spectrum of an Os NPs@SWNT bundle (~80 nanotubes) confirming the presence of Os within the nanotubes. The Cu peaks are due to the TEM specimen grid. d) A histogram showing the size distribution of Os NPs generated by e-beam irradiation (100 keV) of $Os_3(CO)_{12}$@SWNT.[12]

3.3 Gas phase encapsulation of $M(CO)_6$ molecules in GNFs

The type of filling procedure and its physicochemical parameters *i.e.* reaction temperature and time of the gas phase encapsulation of $M(CO)_6$ molecules (M=Cr, Mo, W) in GNFs are based on their

optimised encapsulation into carbon nanotubes which is described in Chapter II, Section 2.5.1.3).[12,18]

Even though the ends of graphitised carbon nanofibers are always open, in contrast to carbon nanotubes, they have to be pre-treated by heating them at high temperature (500 °C) to remove adsorbed water from their internal channels.[10] In order to prevent the readsorption of water pre-treated GNFs were immediately combined with the guest-compounds in a glass vessel and sealed under high vacuum (10^{-6} mbar). As the guest-compounds may be volatile at such low pressure the glass tube is cooled during evacuation. The sealed glass ampoule is transferred into a furnace which is preheated above the sublimation temperature of the guest species and heated at constant temperature for several days. Then the glass vessel is removed from the furnace into an ice-water bath to rapidly cool it down to 0 °C to ensure effective entrapment of guest-molecules inside GNF, see Table 3-1 and Section 3.8.

Table 3-1. Parameters of the gas phase encapsulation of $M(CO)_6$ into GNFs.

Experiment	Precursor molecule	Atmosphere, pressure / bar	Reaction temp. / °C	Reaction time / days
3–1	$Cr(CO)_6$	Vacuum, 10^{-9}	120	5
3–2	$Mo(CO)_6$	Vacuum, 10^{-9}	120	3
3–3	$W(CO)_6$	Vacuum, 10^{-9}	150	3

3.4 Formation of nanoparticles from $M(CO)_6$ in GNFs

3.4.1 Decomposition of $M(CO)_6$ in GNFs by the e-beam in TEM

The formation of NPs from the $M(CO)_6$ molecules encapsulated in GNFs was attempted using e-beam radiation (200 kV) in TEM, as this method was demonstrated to be successful in the case of $Os_3(CO)_{12}$@SWNT and $M(CO)_6$@SWNT (Figure 3-2 and Chapter II).[12] Therefore, to study the effect of morphologically different interior of the GNF on the *in situ* formation of NPs from $M(CO)_6$ the as-formed $M(CO)_6$@GNF materials were analysed by TEM as described in Section 3.8.4.

3.4.2 Formation of nanoparticles from $M(CO)_6$ in GNFs by thermal decomposition

The chemical transformation of the precursors into NPs can be performed by heating $M(CO)_6$@GNF above the decomposition temperature (~200 °C) of the $M(CO)_6$ molecules as shown earlier.[12] The formation of NPs in GNFs from $M(CO)_6$ by thermal decomposition were performed using different reaction procedures in different environments to study the influence of the GNF and reaction conditions on the resultant material (Figure 3-3).

To remove any reactive contaminants such as O_2 and H_2O the glass ampoule was evacuated (10^{-6} mbar) and consecutively filled with Ar repeatedly several times prior to sealing.

In the first type of experiment $M(CO)_6$@GNF, formed as described in Section 3.3 and 3.8.2, was sealed in a glass ampoule

under Ar atmosphere and placed into a furnace preheated above the decomposition temperature of the metal complex to promote the formation of NPs for a time specified in Table 3-2 and in Section 3.8.3.1 and Figure 3-3.

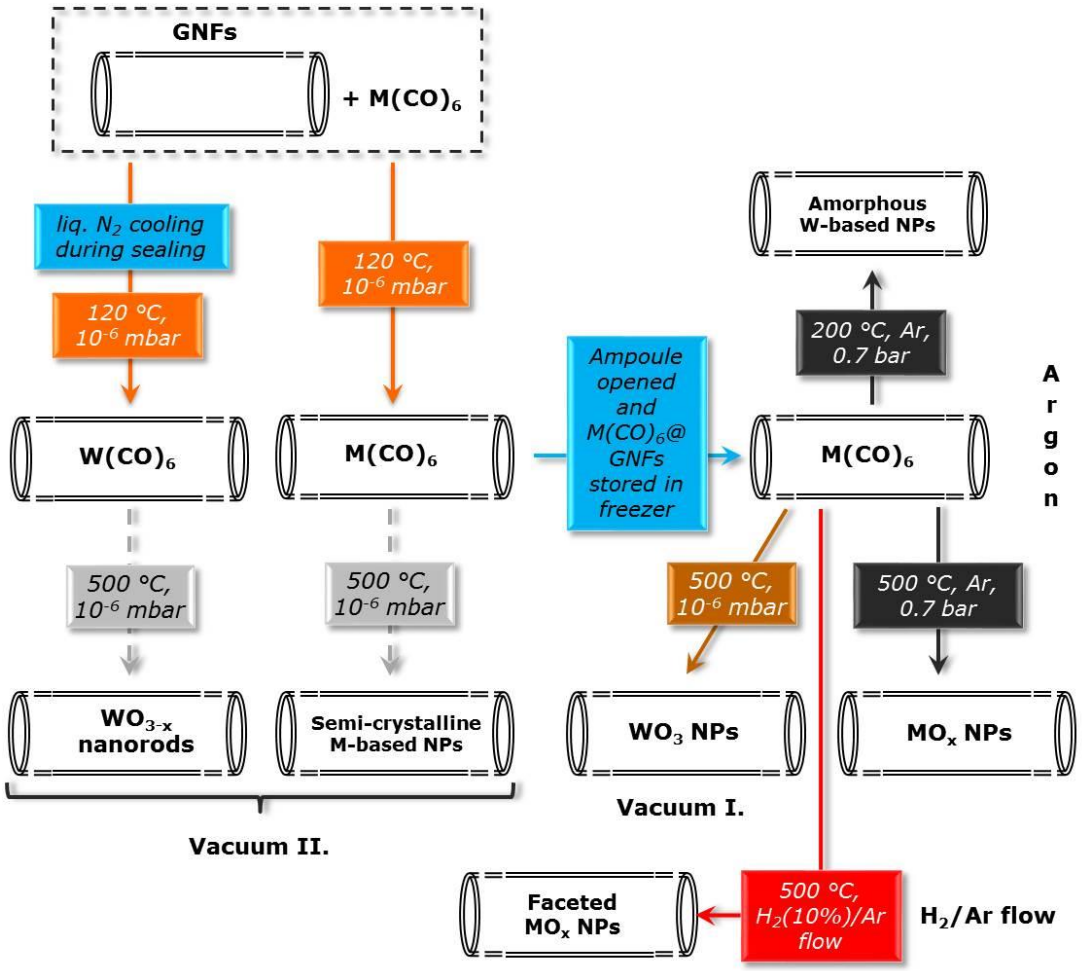


Figure 3-3. Diagram summarising the various synthetic methods utilised to form M NPs@GNFs. The orange boxes and arrows represent the encapsulation conditions used to insert precursor molecules into GNFs, while the blue boxes represent cooling conditions. The light grey, brown and black boxes and arrows represent the thermal decomposition of $M(CO)_6$@GNFs sealed in a glass ampule according to Section 3.8.3.3 (Vacuum II.), 3.8.3.2 (Vacuum I.) and 3.8.3.1 (Argon), respectively, while the red box and arrow represent the thermal decomposition of $M(CO)_6$@GNFs under H_2(10%)/Ar gas flow as described in Section 3.8.3.4.

In the second type of experiment the decomposition of $M(CO)_6$@GNFs, synthesised according to Section 3.3 and 3.8.2, was performed under vacuum. In similar fashion to the first type of

experiment the material was sealed in a glass ampoule; however, this time under vacuum, then it was placed into a preheated furnace to initiate the formation of NPs, see Table 3-2 and Section 3.8.3.2 and Figure 3-3.

Table 3-2. Parameters of the thermal decomposition of $M(CO)_6$@GNFs under Ar and vacuum.

Experiment	Starting material	Atmosphere, pressure / bar	Reaction temp. / °C	Reaction time / h
3–4	$Cr(CO)_6$@GNF	Argon, 0.7	500	1
3–5	$Mo(CO)_6$@GNF	Argon, 0.7	500	1
3–6	$W(CO)_6$@GNF	Argon, 0.7	200	72
3–7	$W(CO)_6$@GNF	Argon, 0.7	500	1
3–8	$W(CO)_6$@GNF	Vacuum, 10^{-9}	500	1

In the third type of experiment, in order to eliminate the contact of $M(CO)_6$@GNF with the environment, the encapsulation of $M(CO)_6$ molecules in GNFs and their subsequent decomposition were executed within the same glass ampoule in two consecutive steps under vacuum, see Table 3-3 and Section 3.8.3.3 and Figure 3-3.

In the fourth type of experiment, to gain more information about the possible effect of the environment on the transformation of $M(CO)_6$ into NPs in GNFs, the procedure described above in the third type of experiment was followed, however to trap any H_2O present the glass ampoule was cooled with liquid N_2 during evacuation, see Table 3-3 and Section 3.8.3.3 and Figure 3-3.

Table 3-3. Parameters of the encapsulation and consecutive thermal decomposition of $M(CO)_6$ in GNFs under vacuum.

Experiment	Starting materials	Atmosphere, pressure / bar	Reaction temp. / °C		Reaction time	
			Encap.	Decomp.	Encap. / day	Decomp. / h
3–9	$Cr(CO)_6$+ GNF	Vacuum, 10^{-9}	120	500	3	1
3–10	$Mo(CO)_6$+ GNF	Vacuum, 10^{-9}	120	500	3	1
3–11	$W(CO)_6$+ GNF	Vacuum, 10^{-9}	150	500	3	1
3–12	$W(CO)_6$+ GNF	Vacuum, 10^{-9} (liq. N_2 cooling)	150	500	3	1

In the fifth type of experiment the thermal decomposition of $M(CO)_6$@GNF, prepared as described in Section 3.3 and 3.8.2, was performed in a stream of H_2(10%)/Ar gas using a tube furnace. Prior to the heating stage, the whole system including the reaction tube containing the $M(CO)_6$@GNF was extensively flushed with H_2(10%)/Ar gas to remove any reactive contaminants that may be present *i.e.* H_2O and O_2. The temperature of the furnace was controlled by a temperature program see Table 3-4, Section 3.8.3.4 and Figure 3-3.

Table 3-4. Parameters of the thermal decomposition of $M(CO)_6$@GNFs under H_2(10%)/Ar gas flow.

Experiment	Starting material	Atmosphere	Reaction temp. / °C	Temp. ramp / °C min^{-1}		Dwell time / h
				Up	Down	
3–13	$Mo(CO)_6$@GNF	H_2(10%)/Ar	500	50	10	1
3–14	$W(CO)_6$@GNF	H_2(10%)/Ar	500	50	10	1

3.5 Characterisation of the products of encapsulation and thermal decomposition of $M(CO)_6$ molecules in GNFs

The materials formed *via* the gas phase encapsulation of $M(CO)_6$ in GNFs (M=Cr, Mo, W) were analysed by TEM and EDX to ensure the presence of the precursor molecules in the GNFs and to study the behaviour of $M(CO)_6$ in GNF under e-beam radiation. Moreover, the materials formed by thermal decomposition of $M(CO)_6$@GNFs were also analysed by TEM and PXRD to investigate the morphology and crystal structure of the objects formed within the GNFs.

3.5.1 TEM analysis of $M(CO)_6$ encapsulated in GNFs

During the TEM investigation of $Cr(CO)_6$@GNFs, formed in Experiment 3–1, the formation of small NPs (2-7 nm) were clearly observed at the step-edges of the GNFs (indicated with arrows) as a result of the decomposition of $Cr(CO)_6$ induced by the e-beam (Figure 3-4). EDX of $Cr(CO)_6$@GNFs recorded during the TEM analysis showed characteristic peaks of Cr at 0.5, 5.4 and 5.9 keV confirming the presence of Cr within the *in situ* formed NPs (Figure 3-5).

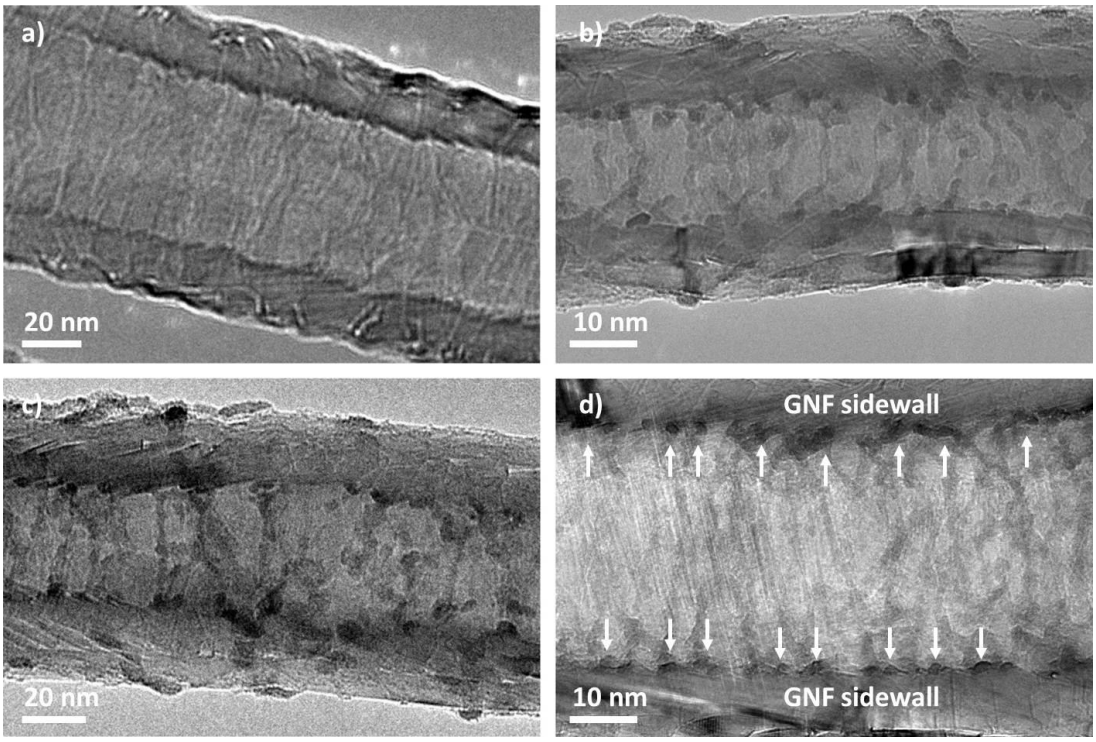


Figure 3-4. TEM images showing a) an empty GNF for reference and b)-d) Cr-based NPs formed *in situ* as a result of the decomposition of $Cr(CO)_6$ under the e-beam during the analysis of $Cr(CO)_6$@GNFs formed in Experiment 3–1. The arrows indicate NPs formed at the step-edges of the GNFs.

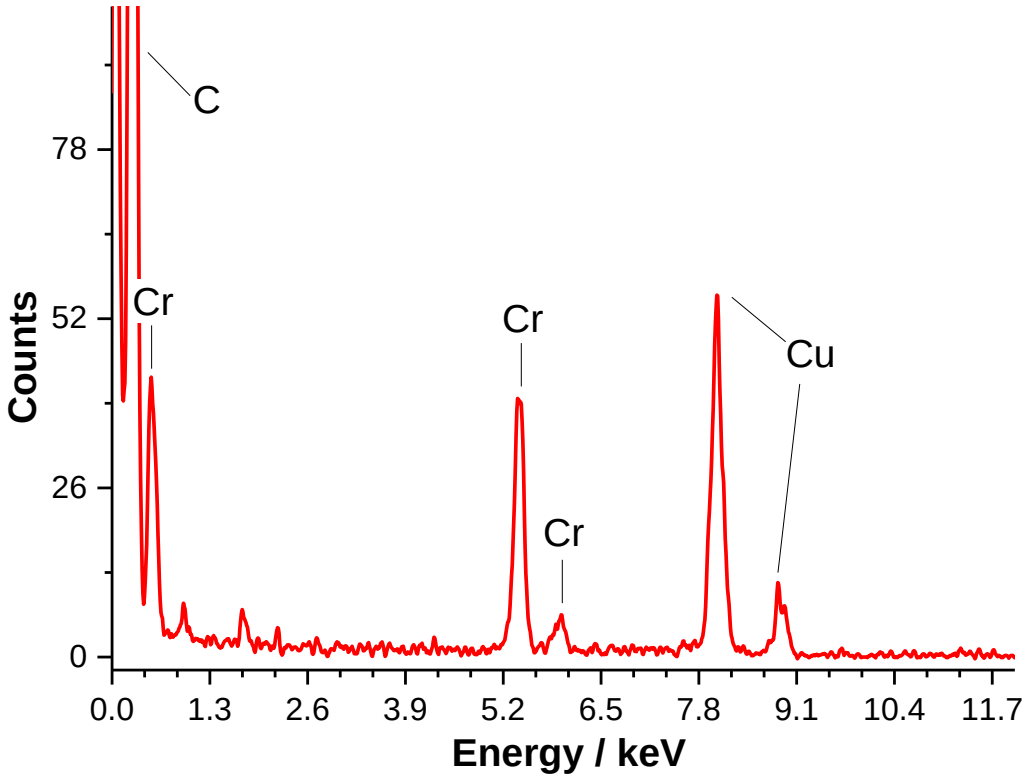


Figure 3-5. EDX spectrum of the NPs formed *in situ* as a result of the decomposition of $Cr(CO)_6$ under the e-beam during the analysis of $Cr(CO)_6$@GNFs formed in Experiment 3–1.

Characteristic peaks of Cr can be identified at 0.5, 5.4 and 5.9 keV. Cu peaks are due to the specimen holder.

TEM analysis of $Mo(CO)_6$@GNF, formed in Experiment 3–2, showed Mo-based NPs (2-5 nm) at the step-edges of GNFs. These NPs appear to be aggregates of smaller NPs (~0.5 nm) (Figure 3-6). On the plateaus, *i.e.* between the step-edges of GNFs large areas (5-30 nm) covered with irregularly shaped aggregates made of ~0.5 nm NPs

EDX spectroscopy of $Mo(CO)_6$@GNF confirmed the presence of Mo within the NPs which were formed during the TEM analysis, with characteristic peaks identified at 2.3 and 17.5 keV (Figure 3-7).

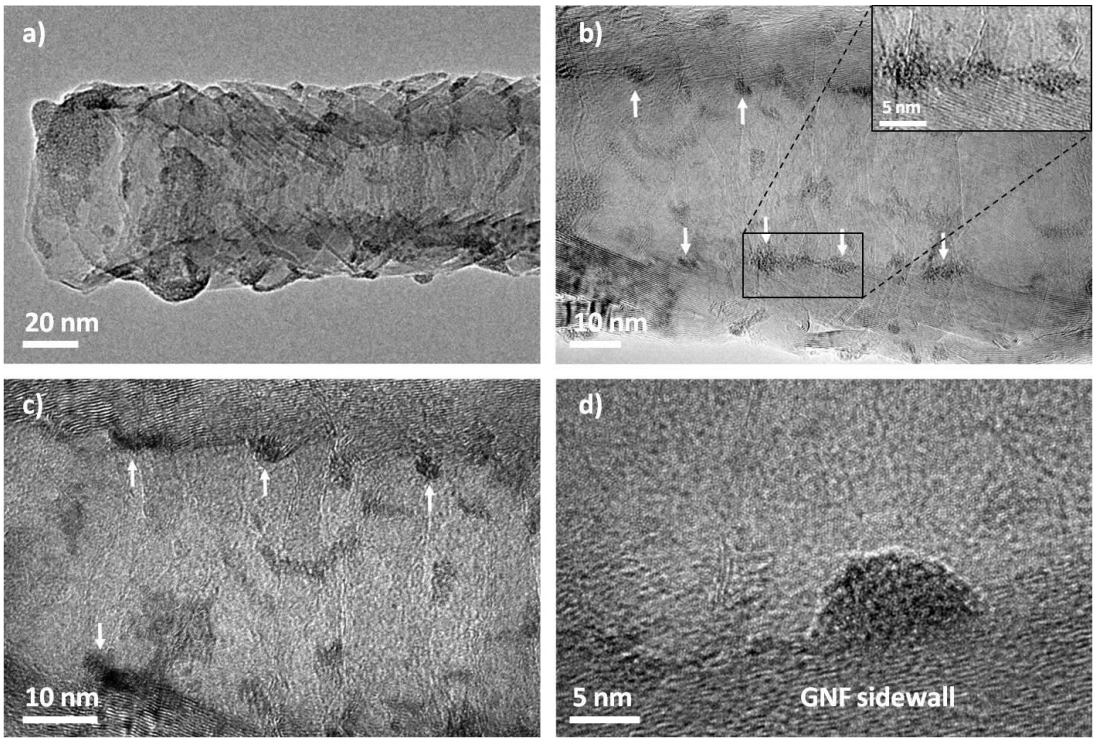


Figure 3-6. TEM images of $Mo(CO)_6$@GNFs formed in Experiment 3–2 showing the Mo-based NPs formed by the decomposition of $Mo(CO)_6$ due to e-beam damage. Image a) shows NPs at the tip of a GNF while b) and c) show NPs at the step-edges of GNFs and d) shows a high magnification image of a Mo NP.

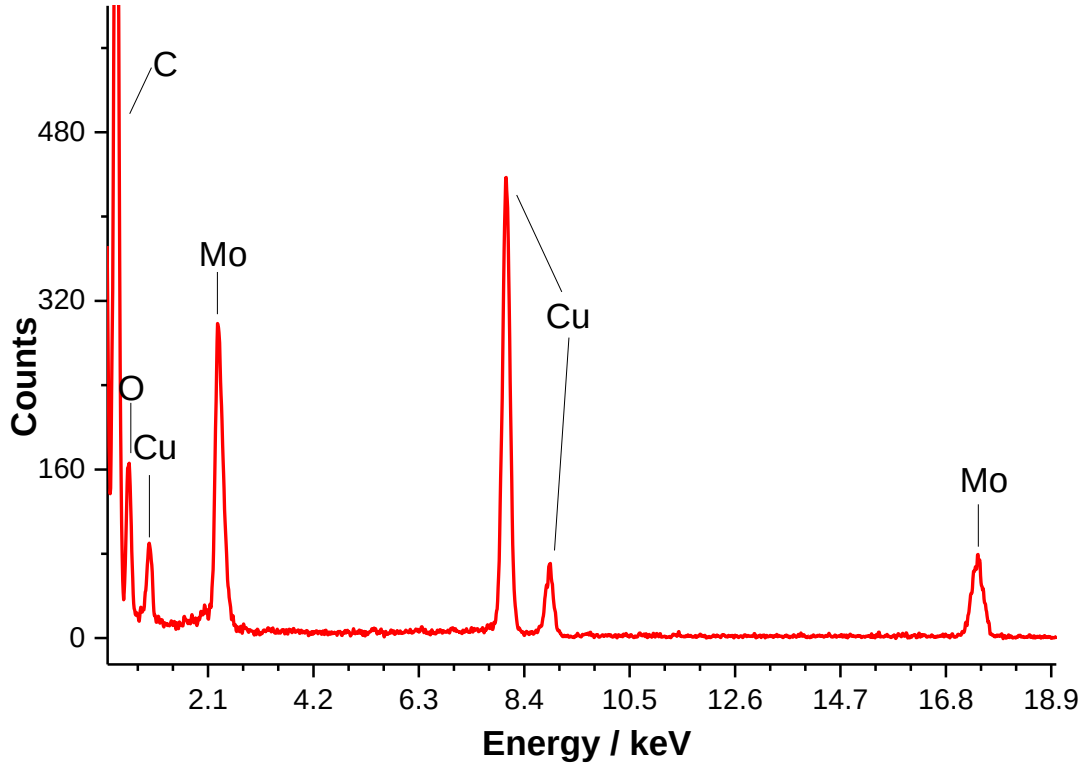


Figure 3-7. EDX spectrum of the NPs formed *in situ* as a result of the decomposition of $Mo(CO)_6$ under the e-beam during the analysis of $Mo(CO)_6$@GNFs formed in Experiment 3–2. Characteristic peaks of Mo were identified at 2.3 and 17.5 keV. Cu peaks are due to the specimen holder.

During TEM analysis of the $W(CO)_6$@GNF, formed in Experiment 3–3, large NPs (10-20 nm) were observed at the step-edges of the GNFs which were formed by the *in situ* decomposition of $W(CO)_6$ (Figure 3-8). These larger NPs consist of smaller NPs (~0.6 nm) packed loosely together (Figure 3-8 c) which occasionally cover a whole plateau step-edge of the GNF (Figure 3-8 d).

EDX spectroscopy of $W(CO)_6$@GNF showed the characteristic peaks of W at 1.4, 1.8, 8.4 and 9.6 keV indicating that the NPs in GNFs contain W metal (Figure 3-9).

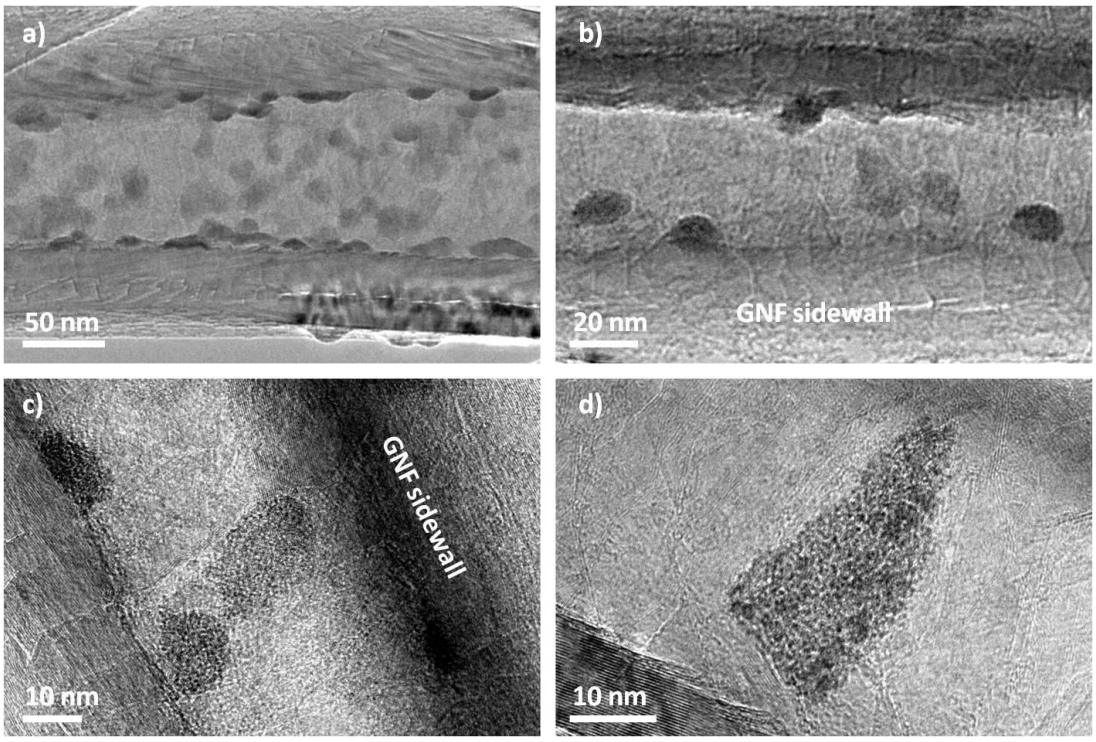


Figure 3-8. TEM images of $W(CO)_6$@GNFs, formed in Experiment 3–3, showing a) and b) W-based NPs formed at the step-edges of the GNFs by the decomposition of $W(CO)_6$ due to e-beam damage. Images c) and d) show that the NPs are built up from small W-based NPs which in some cases extend across a plateau of the GNF`s step-edge.

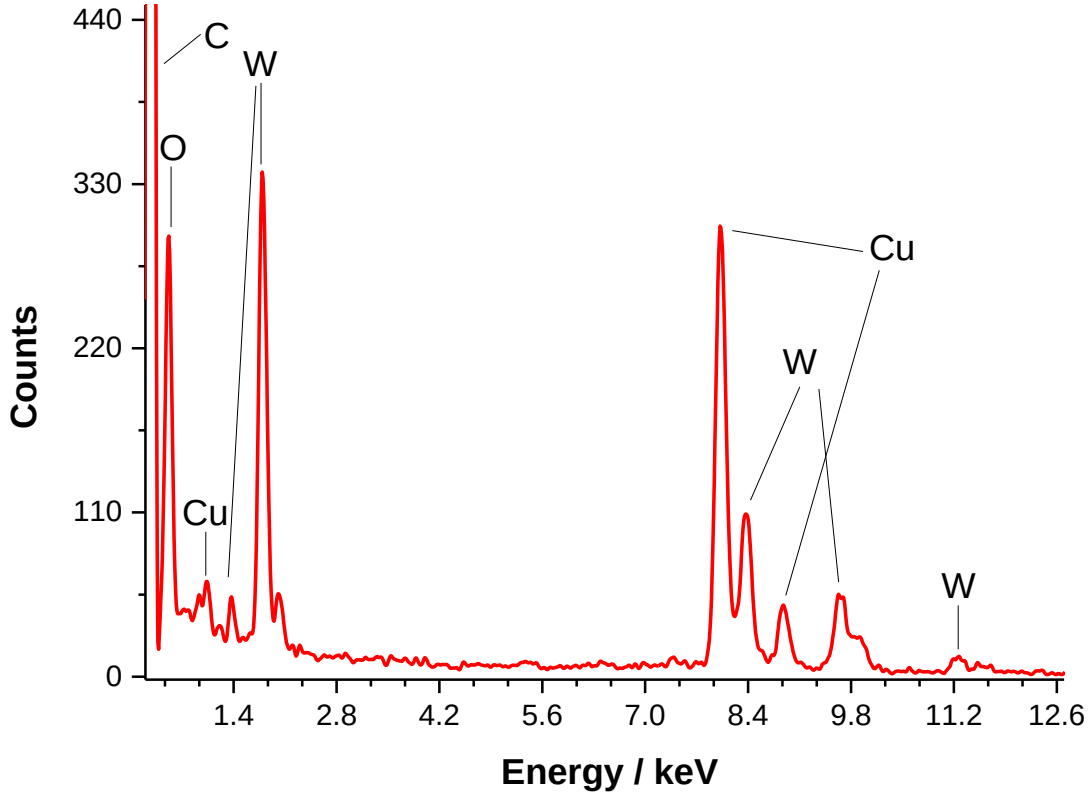


Figure 3-9. EDX spectrum a of the NPs formed *in situ* as a result of the decomposition of $W(CO)_6$ under the e-beam during the analysis of $W(CO)_6$@GNFs formed in Experiment 3–3. Characteristic peaks of W were identified at 1.4, 1.8, 8.4 and 9.6 keV.

In summary, TEM and EDX spectroscopy analysis of $M(CO)_6$@GNF samples, which were made by gas phase filling, confirmed the presence of the $M(CO)_6$ (M=Cr, Mo, W) precursor molecules in GNFs, therefore these materials can be used to study the formation of NPs by thermal decomposition in GNFs.

In addition, it was observed that under the e-beam the decomposition of the $M(CO)_6$ molecules lead to the formation of extremely small M NPs (~0.5 nm) which aggregated into larger NPs (2-5 nm Cr, Mo and 10-20 nm W) with no particular structure or internal order at the step-edges of the GNFs.

3.5.2 Structural and chemical properties of the materials formed *via* the thermal decomposition of $M(CO)_6$ molecules in GNFs

3.5.2.1 Chemical and structural properties of the materials formed *via* the thermal decomposition of $Cr(CO)_6$@GNFs

Based on TEM investigation, performed according to Section 3.8.4, the thermal decomposition of $Cr(CO)_6$@GNF under Ar atmosphere (Experiment 3–4) led to the formation of small NPs (3-5 nm) mostly located at the step-edges of GNFs, highlighted with arrows in Figure 3-10 c and d.

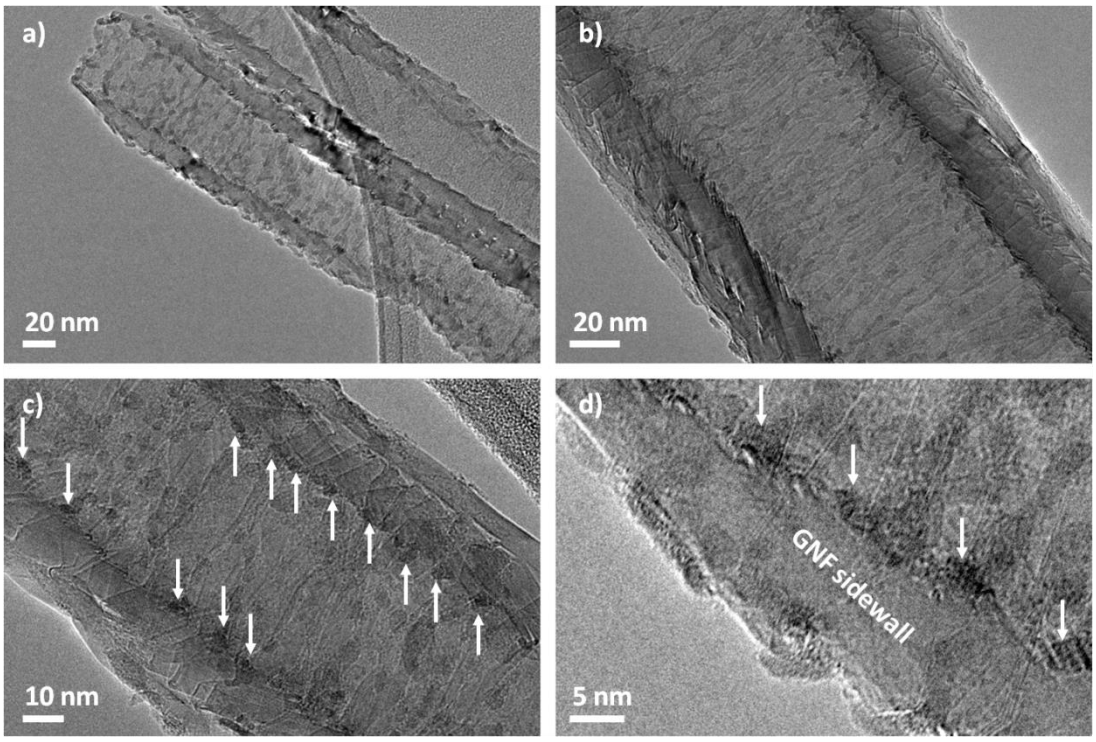


Figure 3-10. TEM images showing Cr-based NPs formed by the thermal decomposition of $Cr(CO)_6$@GNF under Ar atmosphere (Experiment 3–4). In images c) and d) the arrows indicate NPs located at the step-edges of GNFs.

The chemical composition of the NPs cannot be identified by TEM imaging as no clear crystal planes are observed; therefore the composite material was studied by PXRD as described in Section 3.8.5. In the diffraction pattern of the material in addition to the peaks of the GNFs two new peaks were observed at 2θ= 33.8° and 36.4° which are assigned to the NPs formed by the decomposition of $Cr(CO)_6$ (Figure 3-11). Comparison of the measured powder diffraction pattern with the calculated powder diffraction patterns of metallic Cr[19] and Cr_2O_3[20] showed that the peaks at 33.8° and 36.4° belong to the 104 and 2-10 crystallographic planes of Cr_2O_3. Therefore, thermal decomposition of $Cr(CO)_6$ in GNFs led to the formation of Cr_2O_3 NPs in GNF.

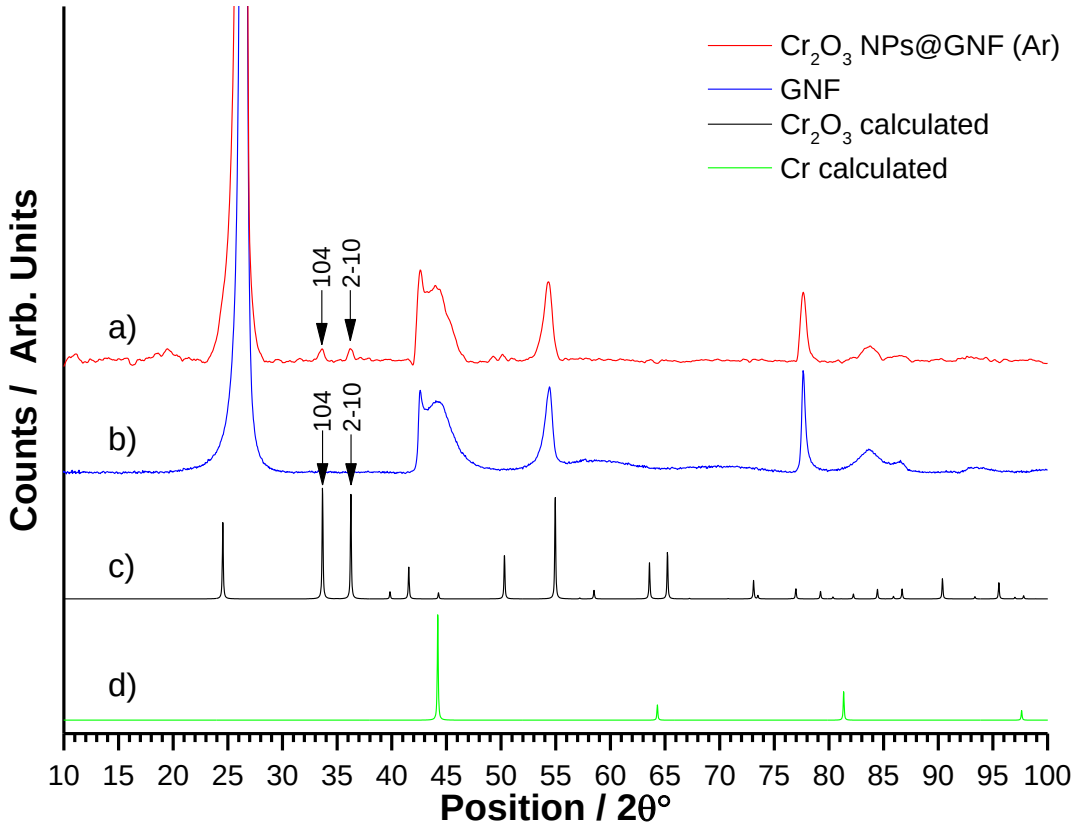


Figure 3-11. PXRD patterns of a) Cr_2O_3 NPs formed by the thermal decomposition of $Cr(CO)_6$@GNF under Ar (Experiment 3–4) and b) GNFs. Calculated powder XRD patterns of c) Cr_2O_3[20] and d) metallic Cr[19] are shown to allow comparison with the experimental patterns (λ=1.5432 Å).

TEM investigation of the material formed by the encapsulation and consecutive thermal decomposition of $Cr(CO)_6$ in GNF under vacuum (Experiment 3–9) showed the presence of small (2-5 nm) spherical NPs in GNFs in addition to some large NPs (~40x60 nm) which span across the internal channel of the GNFs (Figure 3-12). The small NPs are located on the step-edges of the GNFs, however, no crystallographic lattice is identifiable in the TEM images *i.e.* the NPs appear to be amorphous.

During EDX spectroscopy of the material characteristic peaks of Cr were observed at 0.5 and 5.4 keV confirming its presence in the NPs formed in GNFs (Figure 3-13).

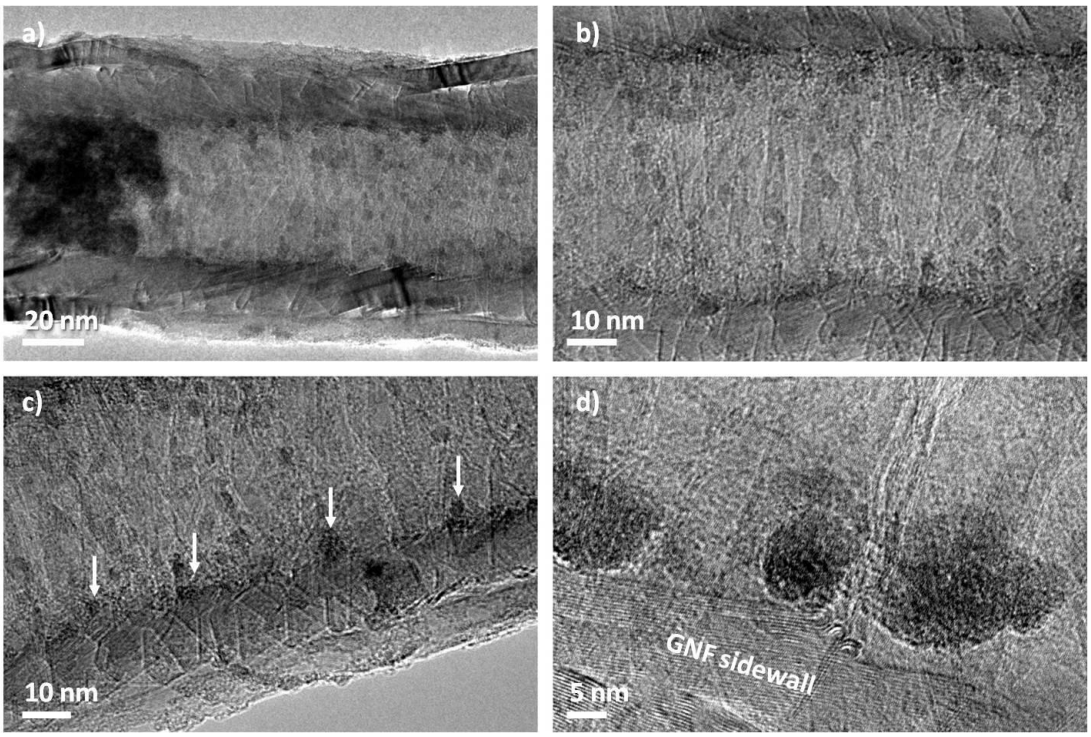


Figure 3-12. TEM images showing a) a large Cr-based NP partially blocking the internal channel of the GNF, b)-c) small NPs (2-5 nm) and d) larger NPs (15 nm) located at the step-edges of the GNFs formed by the encapsulation and consecutive thermal decomposition of $Cr(CO)_6$ in GNF under vacuum (Experiment 3–9).

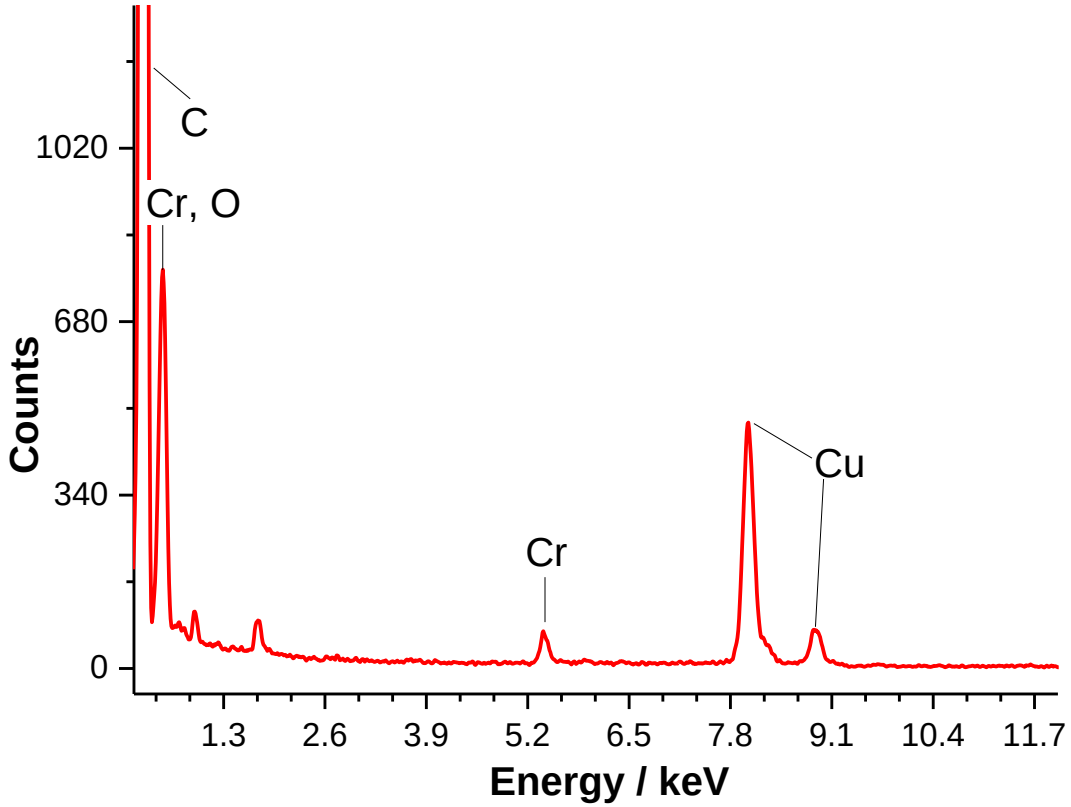


Figure 3-13. EDX spectrum of Cr-based NPs formed by the encapsulation and consecutive thermal decomposition of $Cr(CO)_6$ in GNF under vacuum (Experiment 3–9). Characteristic peaks of Cr were identified at 0.5 and 5.4 keV. Cu peaks are due to the specimen holder.

The material was investigated by PXRD to aid the identification of the NPs structure and chemical composition, however no new peaks were observed in addition to the peaks corresponding to the graphitic layers of the GNFs (Figure 3-14 a).

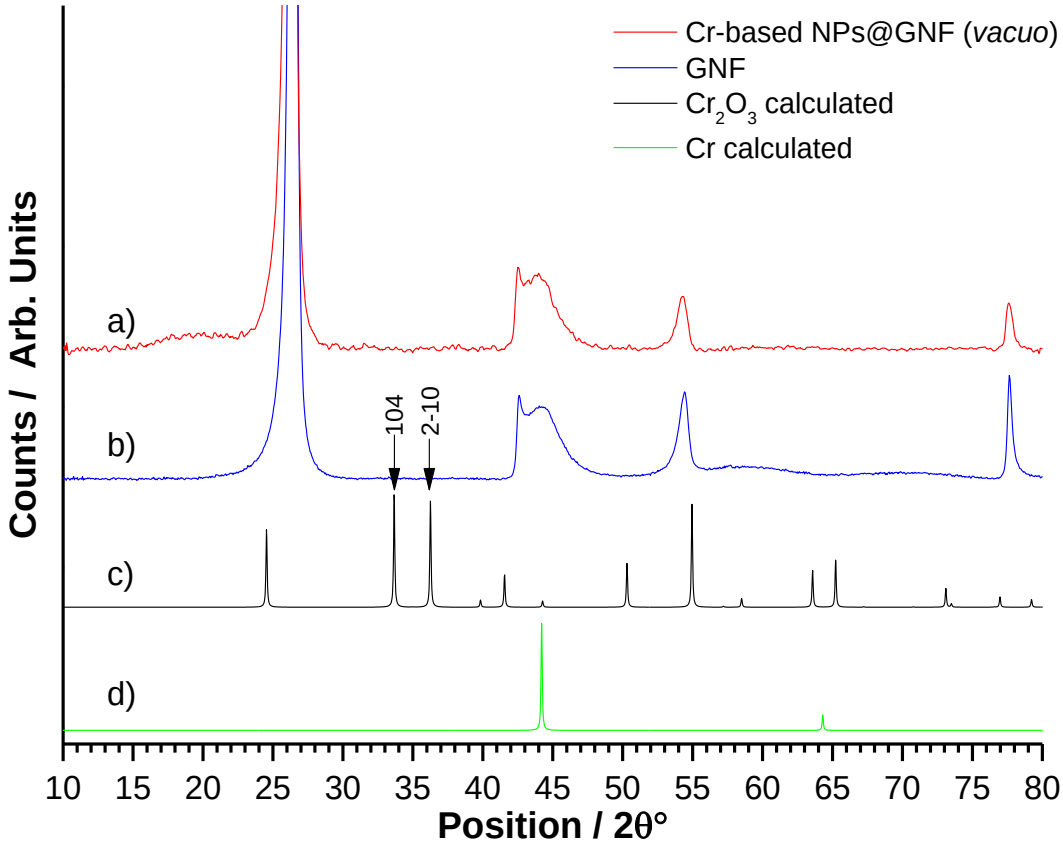


Figure 3-14. PXRD patterns of a) Cr-based NPs formed by the encapsulation and consecutive thermal decomposition of $Cr(CO)_6$ in GNF under vacuum (Experiment 3–9) and b) GNF. Calculated PXRD patterns of c) Cr_2O_3[20] and d) metallic Cr[19] are shown to allow comparison with experimental patterns (λ=1.5432 Å).

3.5.2.2 Chemical and structural properties of the materials formed *via* the thermal decomposition of $Mo(CO)_6$@GNFs

TEM investigation of the material formed by thermal decomposition of $Mo(CO)_6$@GNFs under Ar atmosphere (Experiment 3–5) showed the formation of Mo-based NPs (12-15 nm) with crystalline structure (Figure 3-15). Despite their large size the NPs grew on the step-edges of the GNFs. To identify

the structure and chemical composition of the NPs the distance between their crystallographic lattices was measured and found to be 0.35 nm. The presence of Mo in the NPs was confirmed by the characteristic peaks observed at 2.3 and 17.5 keV in EDX (Figure 3-16).

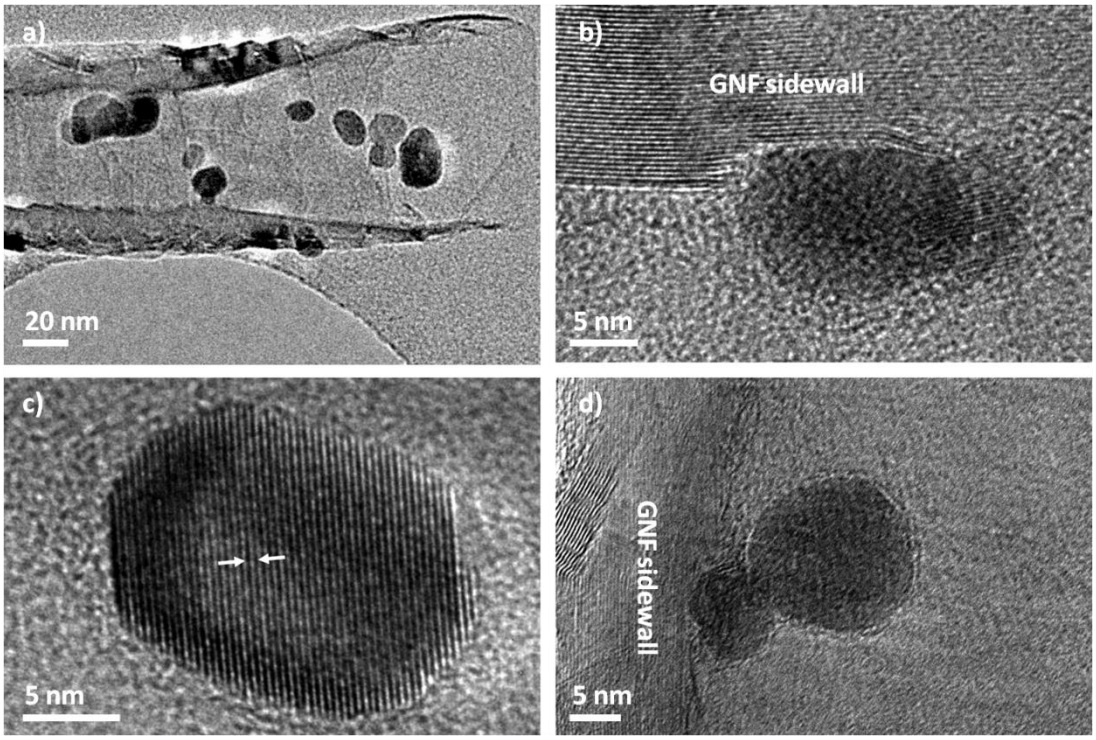


Figure 3-15. TEM images showing Mo-based NPs formed by the thermal decomposition of $Mo(CO)_6$@GNF under Ar atmosphere (Experiment 3–5): a) NPs at the end of a GNF, b) and d) NPs grown on the step-edge of the GNF, c) high magnification micrograph showing a Mo-based NP where arrows indicate the distance (0.35 nm) between the crystallographic lattice planes of the formed NPs.

In order to confirm the chemical composition of the NPs the composite material was investigated by PXRD. In the diffraction pattern of the material a new peak was observed at approximately $2\theta=37°$ in addition to a peak at 53.0° which appears as a shoulder on the peak of the GNFs (Figure 3-17 a).

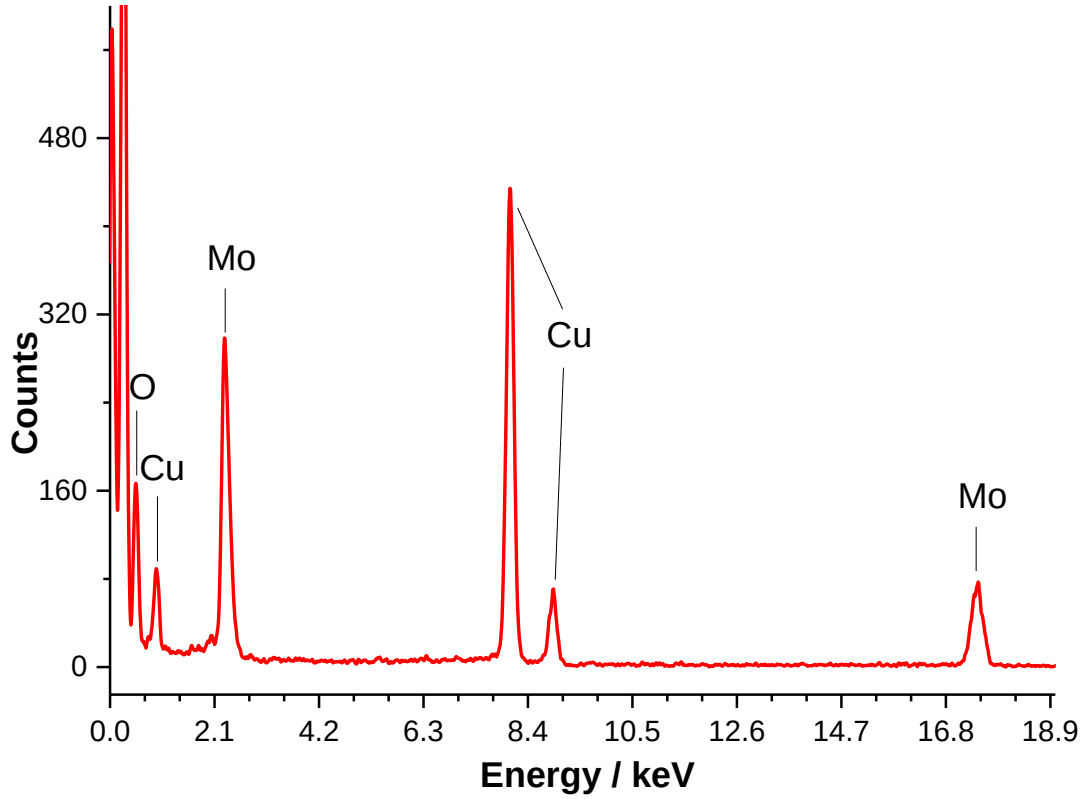


Figure 3-16. EDX spectrum of Mo-based NPs formed by the thermal decomposition of $Mo(CO)_6$@GNFs under Ar atmosphere (Experiment 3–5). Characteristic peaks of Mo were identified at 2.3 and 17.5 keV. Cu peaks are due to the specimen holder.

Based on comparison with the calculated PXRD patterns of MoO_2[21] (Figure 3-17 c) and metallic Mo[22] (Figure 3-17 d) the overlapping peaks centred at ~37° and ~54° correspond to the 20-2, 11-2, 020, 002, 200, 111 and to the 21-3, 22-2, 022, 220, 112, 211, crystallographic planes of MoO_2, respectively, whilst no peaks of metallic Mo were identified. Moreover, the *d* spacing (0.34 nm) belonging to the most intensive diffraction peak of MoO_2 ((Figure 3-17 c, 26.0°) and to the 011 crystallographic plane matches with the *d* spacing (0.35 nm) measured in TEM images (Figure 3-15 c) which confirms that the thermal decomposition of $Mo(CO)_6$@GNFs at 500 °C (Ar) led to the formation of MoO_2 NPs.

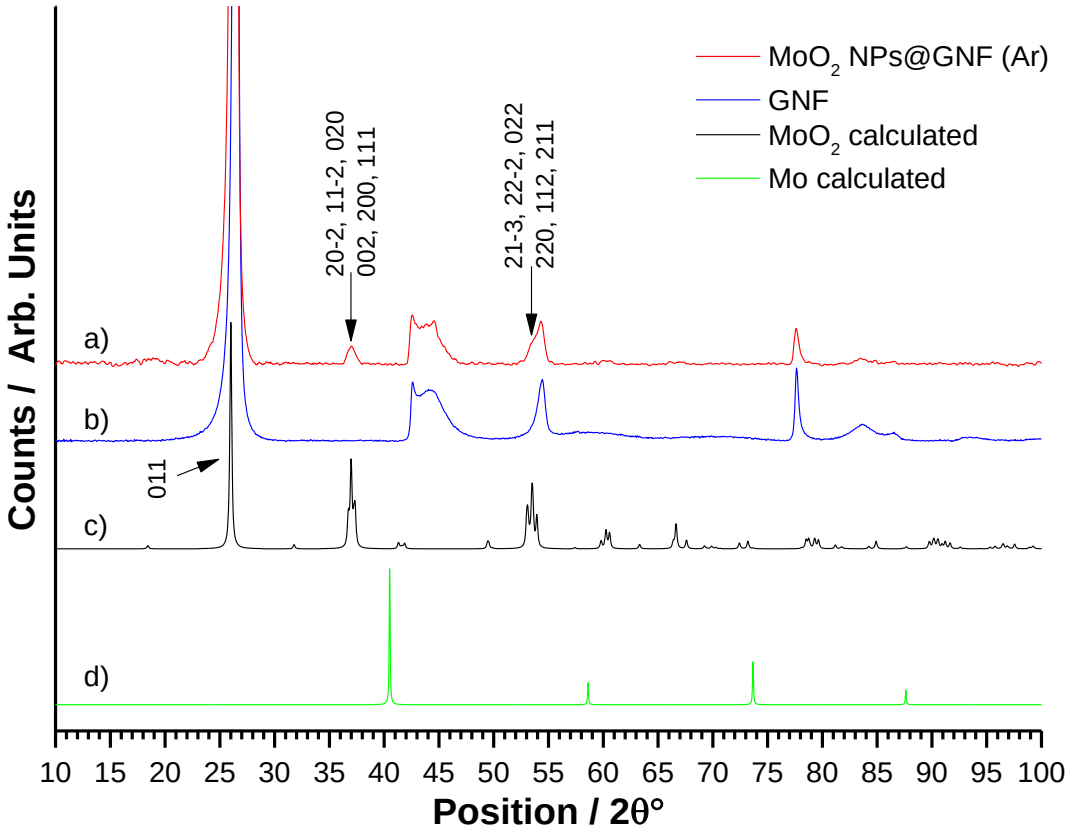


Figure 3-17. PXRD patterns of a) MoO_2 NPs formed by the thermal decomposition of $Mo(CO)_6$@GNF under Ar (Experiment 3–5) and b) GNF. Calculated PXRD patterns of c) MoO_2[21] and d) metallic Mo[22] are shown to allow comparison with experimental patterns (λ=1.5432 Å).

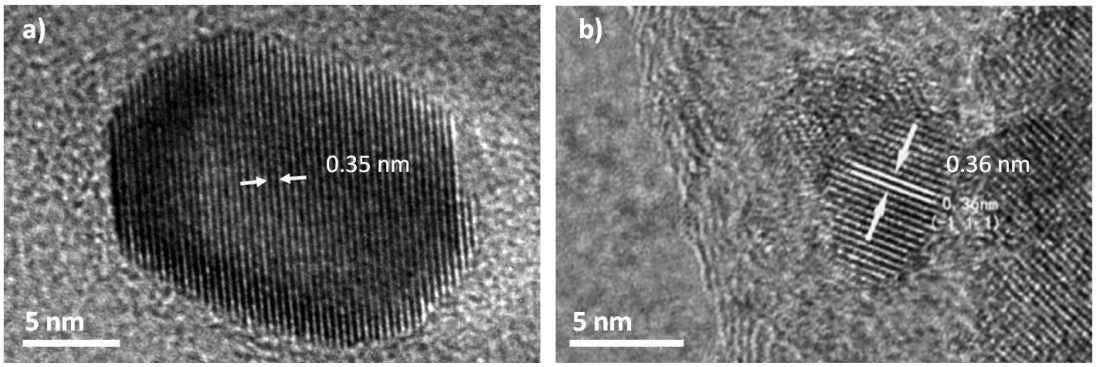


Figure 3-18. TEM images showing the *d* spacing measured between the 011 planes of MoO_2 NPs formed a) in GNFs (0.35 nm) by thermal decomposition of $Mo(CO)_6$@GNF under Ar atmosphere (Experiment 3–5) and b) on graphene oxide (0.36 nm) by the reduction of MoO_3.[23]

In addition, the chemical composition and crystal structure of MoO_2 NPs formed in GNFs and those formed on the surface of graphene oxide *via* the reduction of MoO_3 in an earlier study are found to be consistent.[23] The interlayer *d* spacing measured in TEM

images between the 011 planes of the MoO_2 NPs supported on graphene oxide (0.36 nm) and in GNFs (0.35 nm) are also consistent, see Figure 3-18.[23]

TEM investigation showed that the encapsulation and consecutive decomposition of $Mo(CO)_6$ in GNF under vacuum (Experiment 3–10) led to the formation of irregularly shaped Mo-based NPs (5-15 nm) with a low degree of local crystallinity (Figure 3-19).

EDX spectroscopy confirmed the presence of Mo in the NPs with characteristic peaks observed at 2.3 and 17.5 keV, however only a very weak O signal was detected (Figure 3-20).

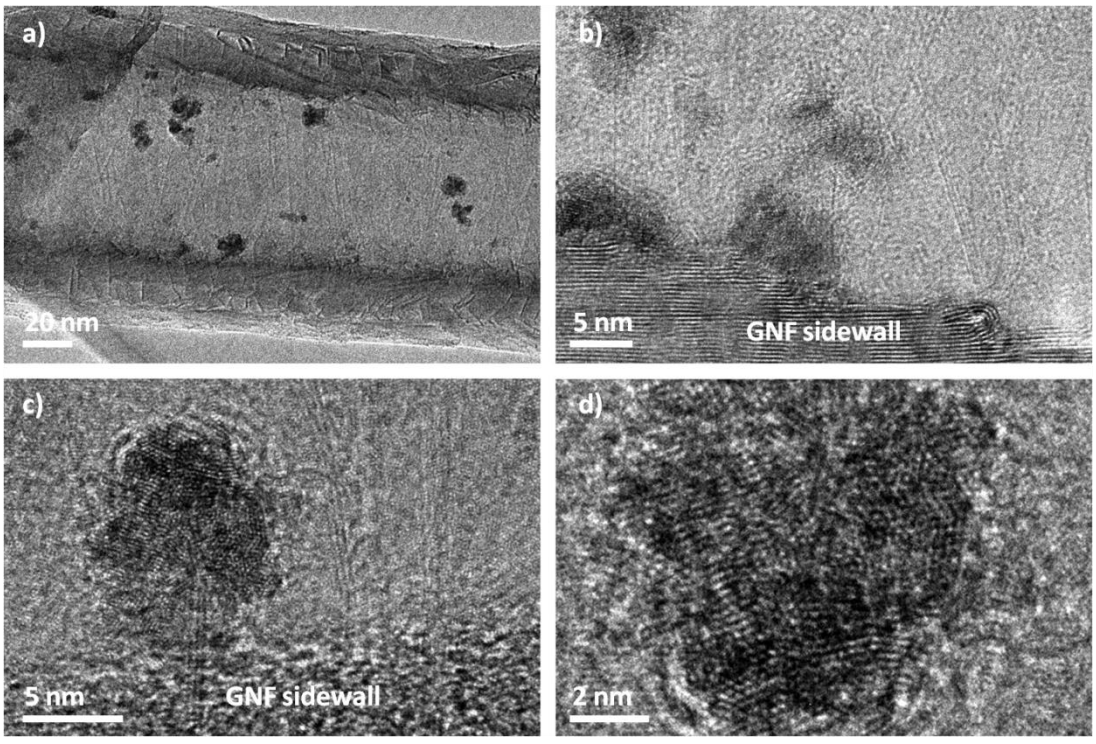


Figure 3-19. TEM images a)—d) show irregularly shaped Mo-based NPs formed by the encapsulation and consecutive thermal decomposition of $Mo(CO)_6$ in GNF under vacuum (Experiment 3–10). b) The step-edges of the GNFs act as templates during NP formation. d) The NPs generally have a low degree of local crystallinity.

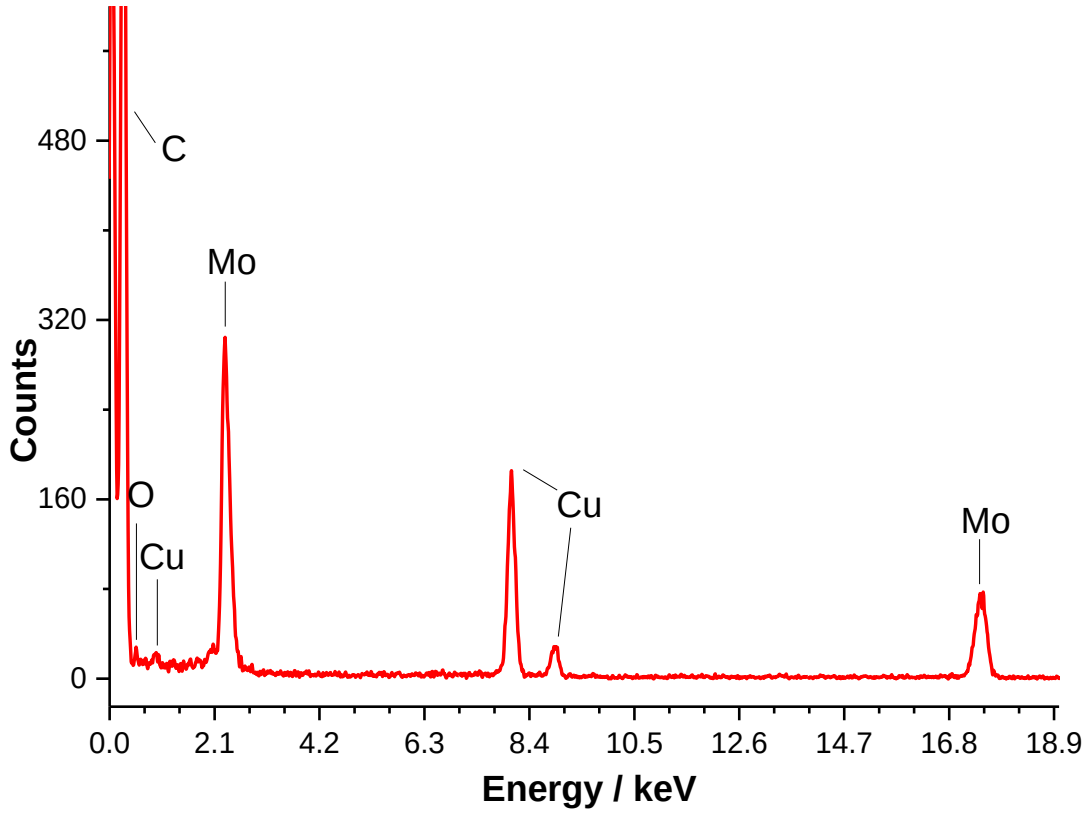


Figure 3-20. EDX spectrum of Mo-based NPs formed by the encapsulation and consecutive thermal decomposition of $Mo(CO)_6$ in GNFs under vacuum (Experiment 3–10). Characteristic peaks of Mo were identified at 2.3 and 17.5 keV. Cu peaks are due to the specimen holder.

The composite material was further analysed by PXRD. In the diffraction pattern only one broad peak with very low intensity was observed in the 2θ=36.7-37.4° region apart from the peaks corresponding to the GNFs (Figure 3-21 a). The new peak might correspond to the 20-2,11-2, 020 002, 200, 111 crystallographic planes of MoO_2 which implies that NPs formed in the GNFs may have MoO_2 stoichiometry. In addition, the width of the peak at 2θ=36.7-37.4° indicates that only small crystalline volumes can be found in the material *i.e.* the NPs are semi-crystalline in agreement with TEM.

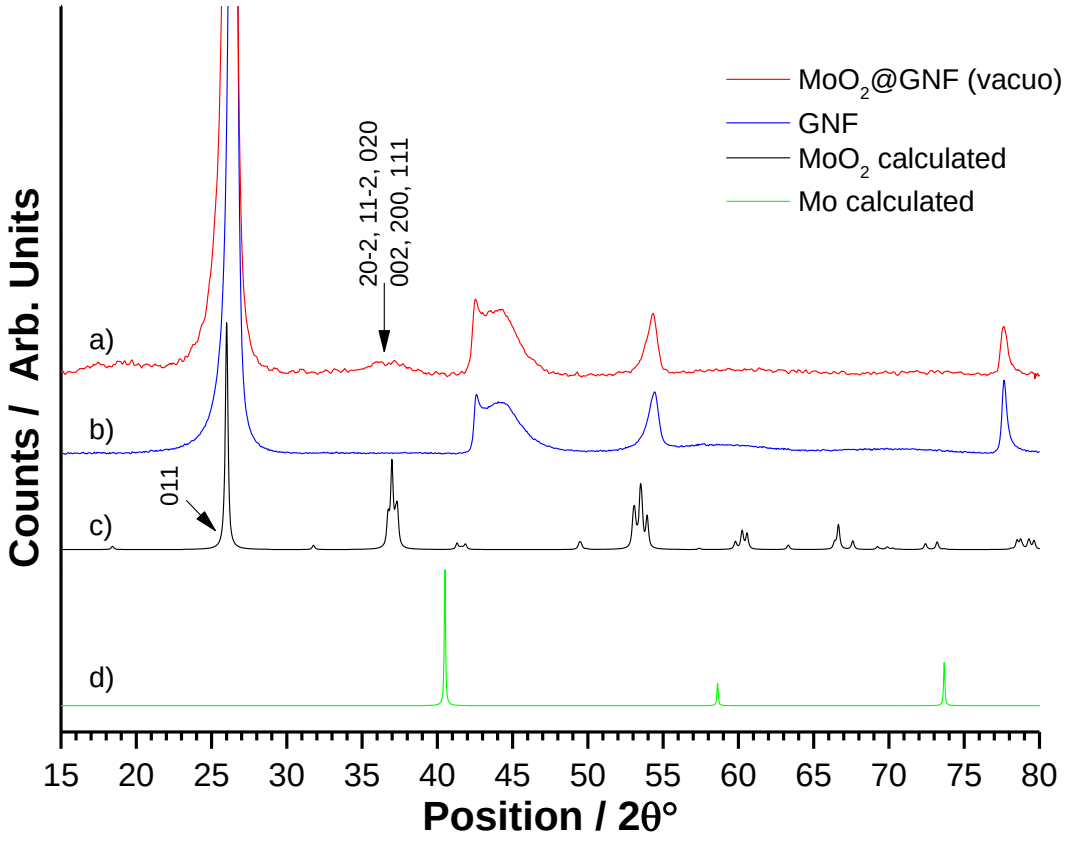


Figure 3-21. PXRD patterns of a) Mo-based NPs formed by the encapsulation and consecutive thermal decomposition of $Mo(CO)_6$ in GNF under vacuum (Experiment 3–10) and b) GNF. Calculated PXRD patterns of c) MoO_2[21] and d) metallic Mo[22] are shown to allow comparison with experimental patterns (λ=1.5432 Å).

TEM investigation of the material formed by the thermal decomposition of $Mo(CO)_6$@GNF under H_2(10%)/Ar flow (Experiment 3–13) showed the formation of relatively small NPs, which have faceted crystalline structure (Figure 3-22). The distance between the observed lattice planes was measured to be 0.35 nm which suggests that the NPs are likely to be MoO_2.

The NPs are favourably formed at the step-edges of the GNFs and examples were found where they connected to each other along the step-edges to form a ring like structure perpendicular to the principal axis of the GNFs (Figure 3-22 c).

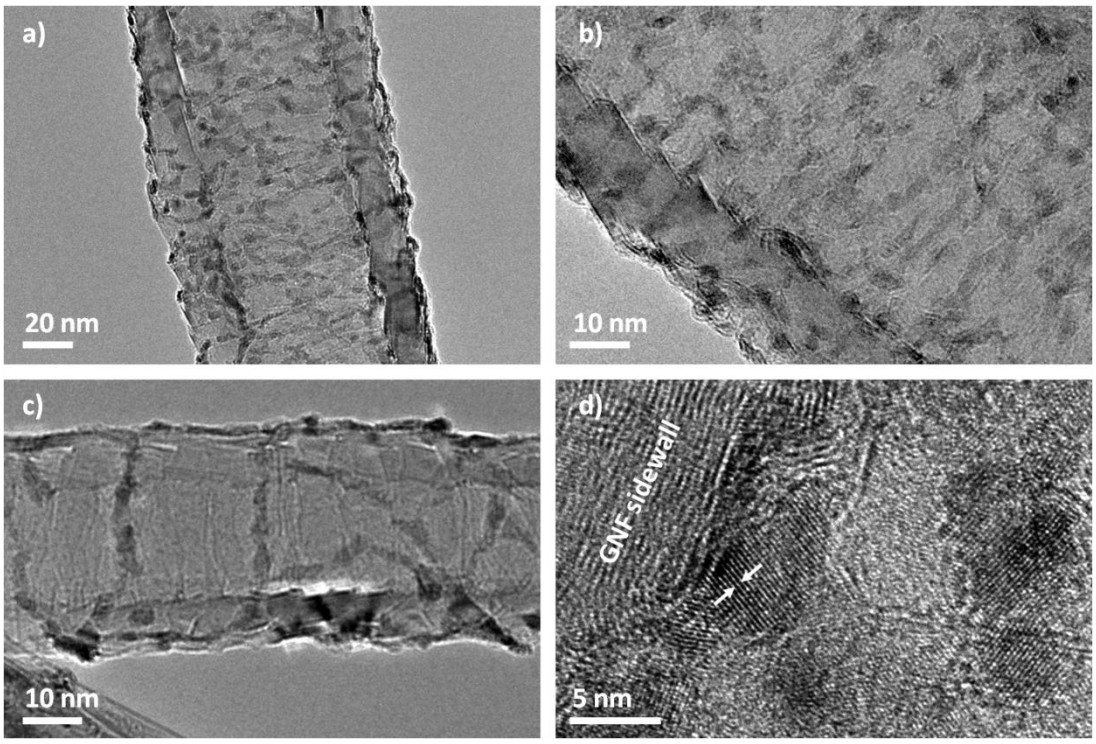


Figure 3-22. TEM images showing Mo-based NPs formed by the thermal decomposition of $Mo(CO)_6$@GNFs under H_2(10%)/Ar flow (Experiment 3–13). d) The arrows indicate the distance (0.35 nm) between the crystallographic lattice planes of the formed NPs.

3.5.2.3 Chemical and structural properties of the materials formed *via* the thermal decomposition of $W(CO)_6$@GNFs

TEM investigation revealed that thermal decomposition of $W(CO)_6$@GNFs under Ar atmosphere (Experiment 3–6, 200 °C) resulted in the formation of spherical NPs (10-30 nm) (Figure 3-23). However, the NPs are amorphous *i.e.* they do not have a crystalline structure.

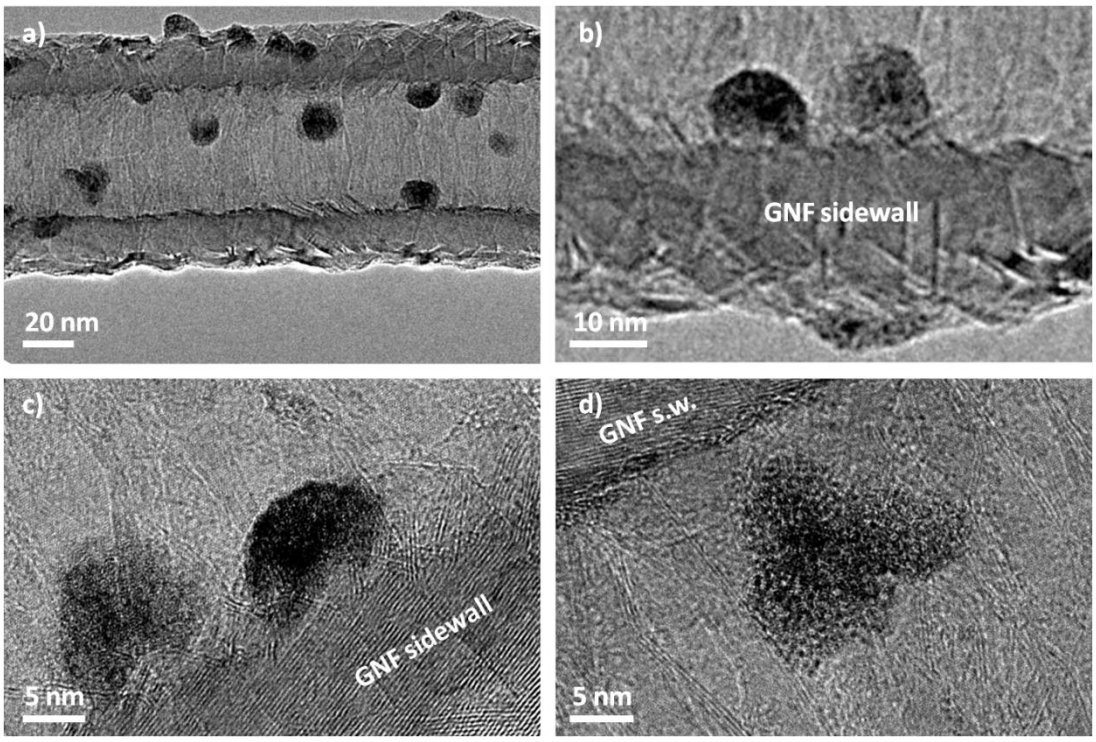


Figure 3-23. TEM images showing W-based NPs (10-30 nm) formed in GNF by the thermal decomposition of $W(CO)_6$@GNFs under Ar ((Experiment 3–6, 200 °C). The NPs are amorphous and most of them have a spherical shape.

During TEM investigation of the material formed by the thermal decomposition of $W(CO)_6$@GNFs under Ar atmosphere (Experiment 3–7, 500 °C) the formation of spherical NPs (10-30 nm) with crystalline structure was observed (Figure 3-24). As demonstrated in Figure 3-24 c the step-edges of the GNFs act as templates for the NP formation and in this particular case the atomic layers of the NP are parallel with the graphitic layers of the GNF. The distance between the crystallographic lattice planes of the NPs was found to be 0.39 nm which suggests that the thermal decomposition of $W(CO)_6$@GNFs lead to the formation of WO_3 NPs (Figure 3-24 c, d).[24]

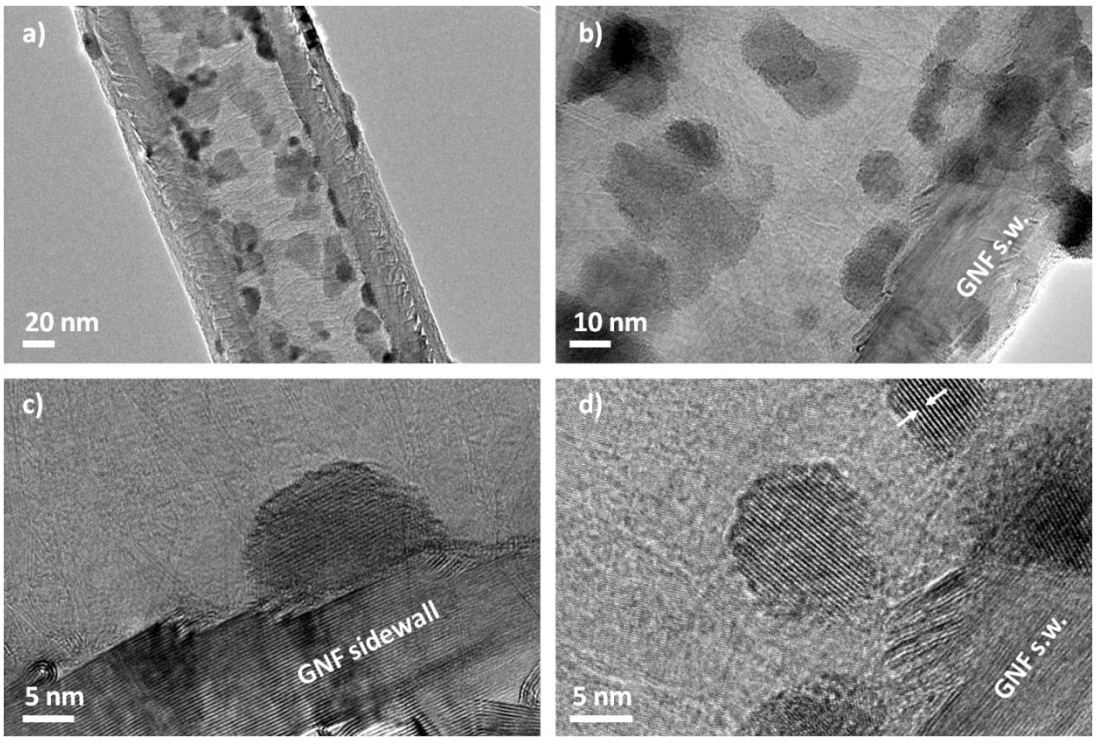


Figure 3-24. TEM images showing W-based NPs formed in GNF by the thermal decomposition of $W(CO)_6$ under Ar (Experiment 3–7, 500 °C). a-b) 10-30 nm NPs were present in GNFs, with NPs located on the step-edge of the GNF. c)-d) High resolution images showing the crystallographic layers of the NPs in which the crystallographic planes of the NP are parallel with the graphitic layers of the GNF. d) The arrows show the distance (0.39 nm) between the crystallographic lattice planes.

To investigate the chemical composition of the NPs the composite material was studied by PXRD (Figure 3-25 a). In the diffraction pattern four new peaks were observed at 2θ=23.1°, 23.8°, 28.6-29.0° and 32.5-34.7°. Comparison of the recorded powder diffraction pattern to the calculated powder diffraction patterns of metallic W,[25] tungsten carbide (WC),[26] tungsten dioxide (WO_2)[27] and tungsten trioxide (WO_3)[24] showed that the decomposition of $W(CO)_6$ in GNFs under Ar led to the formation of ε-WO_3 NPs in GNF. Therefore, the peaks of the NPs at 2θ=23.1°; 23.9°; 28.6-29.0° and 32.5-34.7° correspond to 002, 020; 200; 11-2, 12-1 and 022, 20-2, 220 crystallographic planes of ε-WO_3,

respectively, see Figure 3-25. The *d* spacing corresponding to the peak at 23.1° (0.39 nm) is consistent with the lattice spacing of 0.39 nm measured on the TEM micrographs.

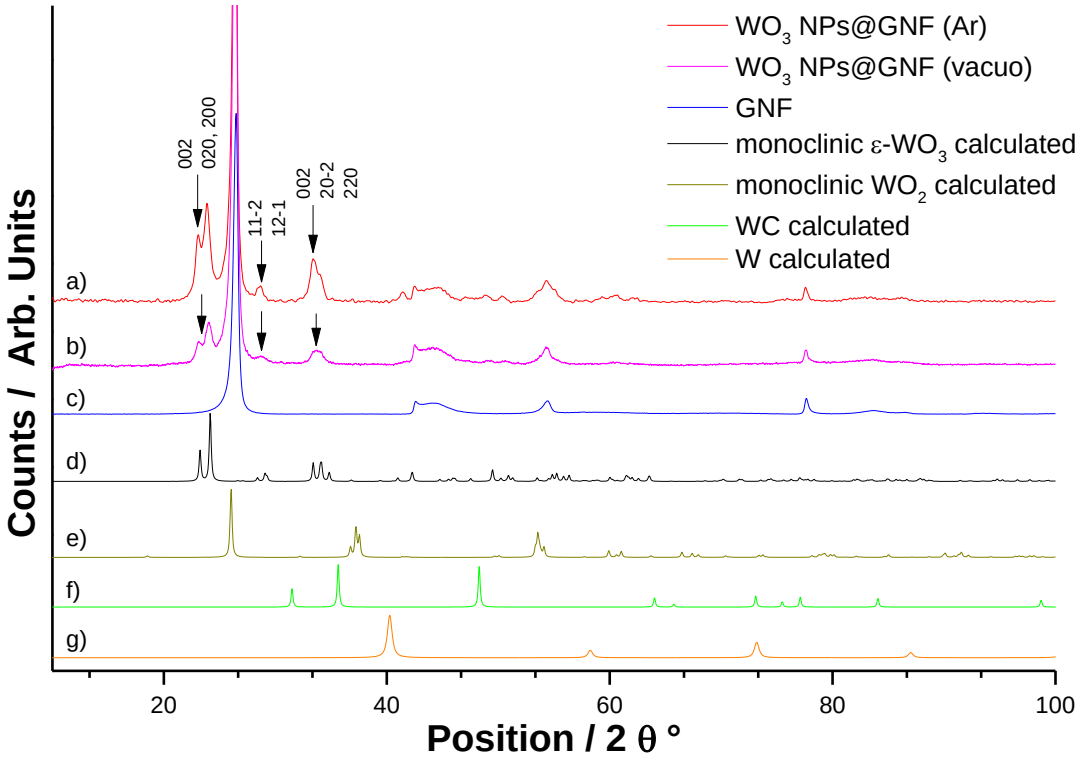


Figure 3-25. PXRD patterns of WO_3 NPs formed in GNF by the thermal decomposition of $W(CO)_6$, a) under Ar (Experiment 3–7, 500 °C) and b) under vacuum (Experiment 3–8), and c) GNF. Calculated PXRD patterns of d) ε-WO_3,[24] e) WO_2,[27] f) WC[26] and g) metallic W[25] are shown to allow comparison with experimental patterns (λ=1.5432 Å).

TEM investigation of the material formed by the thermal decomposition of $W(CO)_6$@GNFs sealed under vacuum (Experiment 3–8) showed the formation of spherical nanoparticles (10-30 nm) with crystalline structure (Figure 3-26). The distance between the crystallographic lattice planes was measured to be 0.39 nm *via* TEM. PXRD analysis of the material revealed new peaks at 2θ=23.2°, 24.0°, 28.6° and 32.5-34.7° indicated by arrows in Figure 3-25 b. Comparison of the recorded PXRD pattern to various calculated diffraction patterns including ε-WO_3[24] showed

that the decomposition of $W(CO)_6$@GNFs under vacuum led to the formation of WO_3 NPs in GNF.

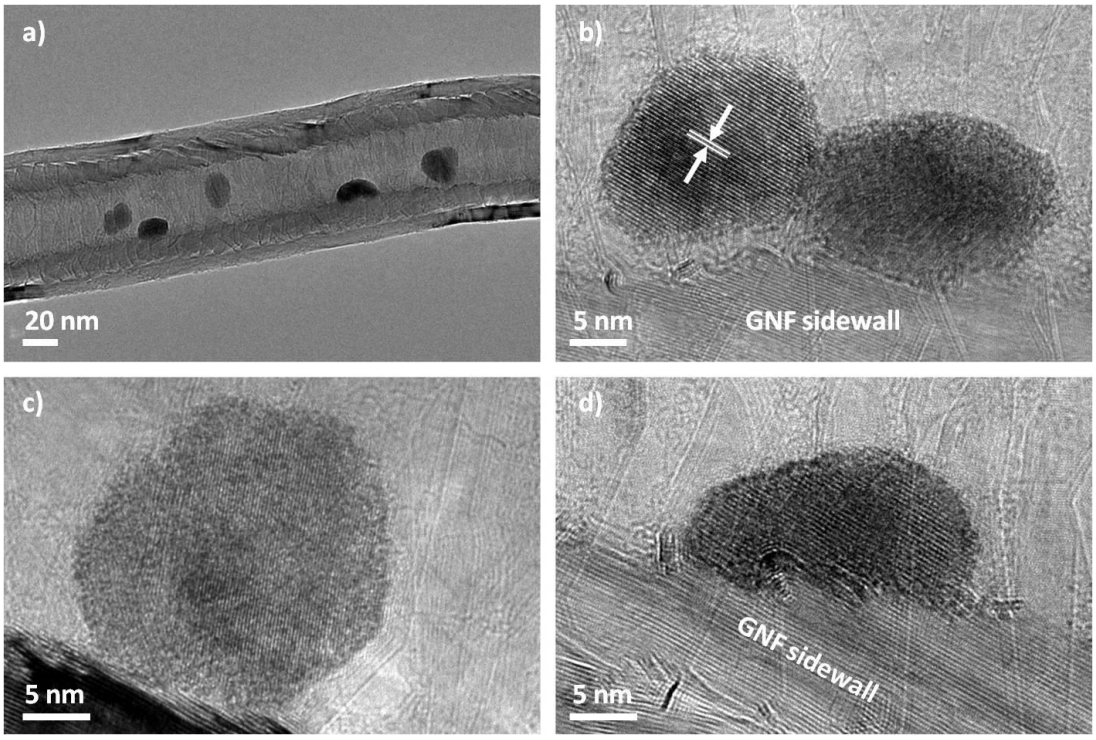


Figure 3-26. TEM images of W-based NPs formed by the thermal decomposition of $W(CO)_6$@GNF under vacuum (Experiment 3–8). Spherical nanoparticles were observed with crystalline structure. The measured *d* spacing (white arrows) was 0.39 nm.

TEM investigation of the material formed by the encapsulation and consecutive decomposition of $W(CO)_6$ in GNFs under vacuum (Experiment 3–11) showed the formation of W-based NPs (2-10 nm) at the step-edges of the GNFs (Figure 3-27). No crystallographic planes of the NPs can be identified on the TEM images suggesting that the NPs are amorphous.

EDX spectroscopy showed the characteristic peaks of W at 1.4, 1.8, 8.4 and 9.6 keV indicating that the NPs formed in GNFs contain W (Figure 3-28).

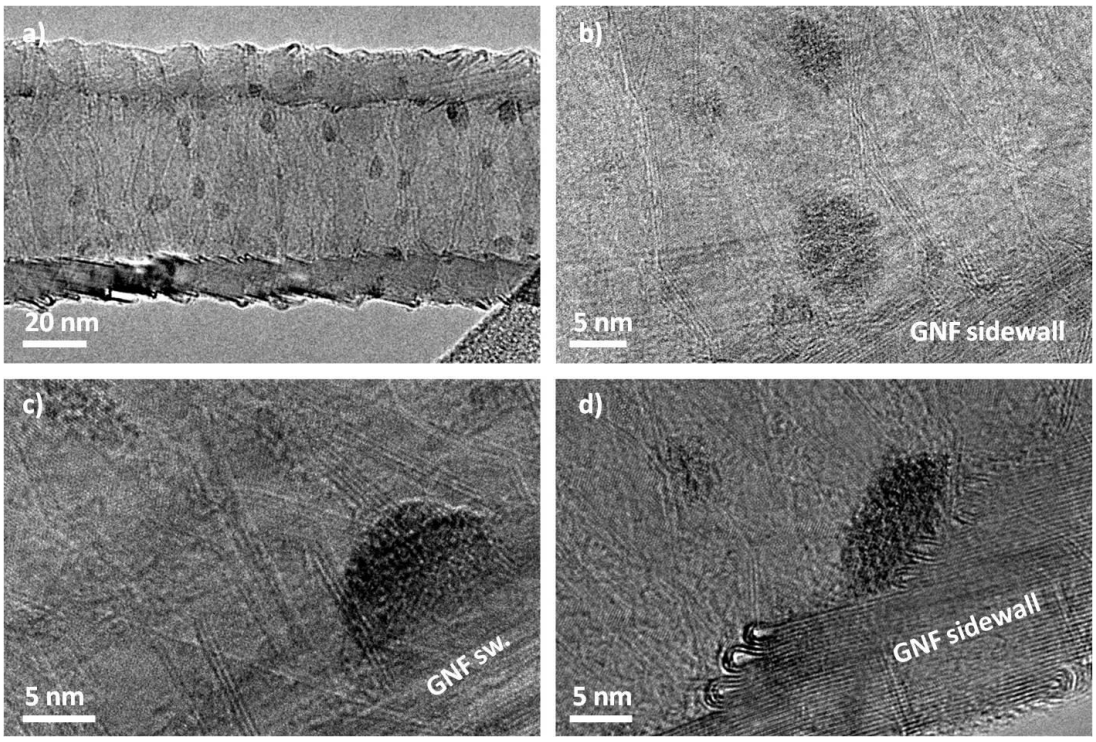


Figure 3-27. TEM images showing amorphous W-based NPs formed by the encapsulation and consecutive thermal decomposition of $W(CO)_6$ in GNFs under vacuum ((Experiment 3–11).

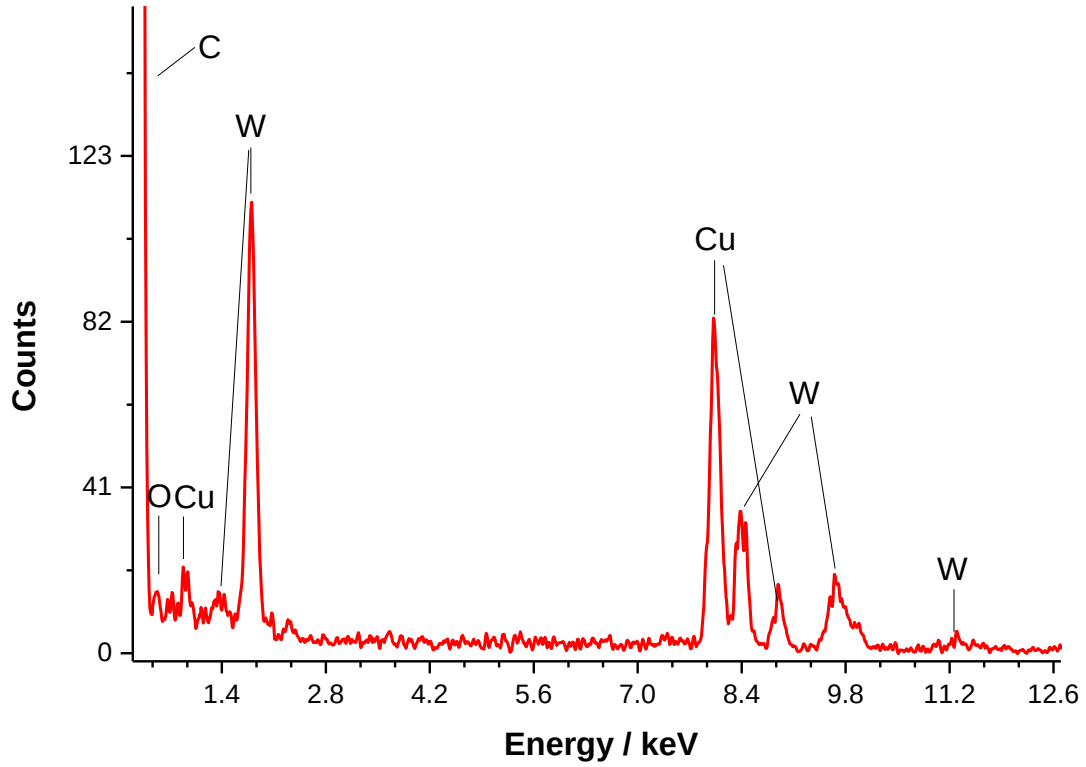


Figure 3-28. EDX spectrum of the W-based NPs formed by the encapsulation and consecutive thermal decomposition of $W(CO)_6$ in GNFs under vacuum (Experiment 3–11). Characteristic peaks of W were identified at 1.4, 1.8, 8.4 and 9.6 keV. Cu peaks are due to the specimen holder.

PXRD analysis of the material formed by the encapsulation and consecutive decomposition of $W(CO)_6$ in GNFs under vacuum (Experiment 3–11) revealed a broad peak at 2θ=33-42° (Figure 3-29 a). Comparison of the recorded PXRD pattern with calculated patterns of various W compounds suggests that the W NPs@GNFs may have small crystalline domains based on the crystal structure of WO_2 *i.e.* they are semi-crystalline, moreover their chemical composition appears to be close to WO_2.

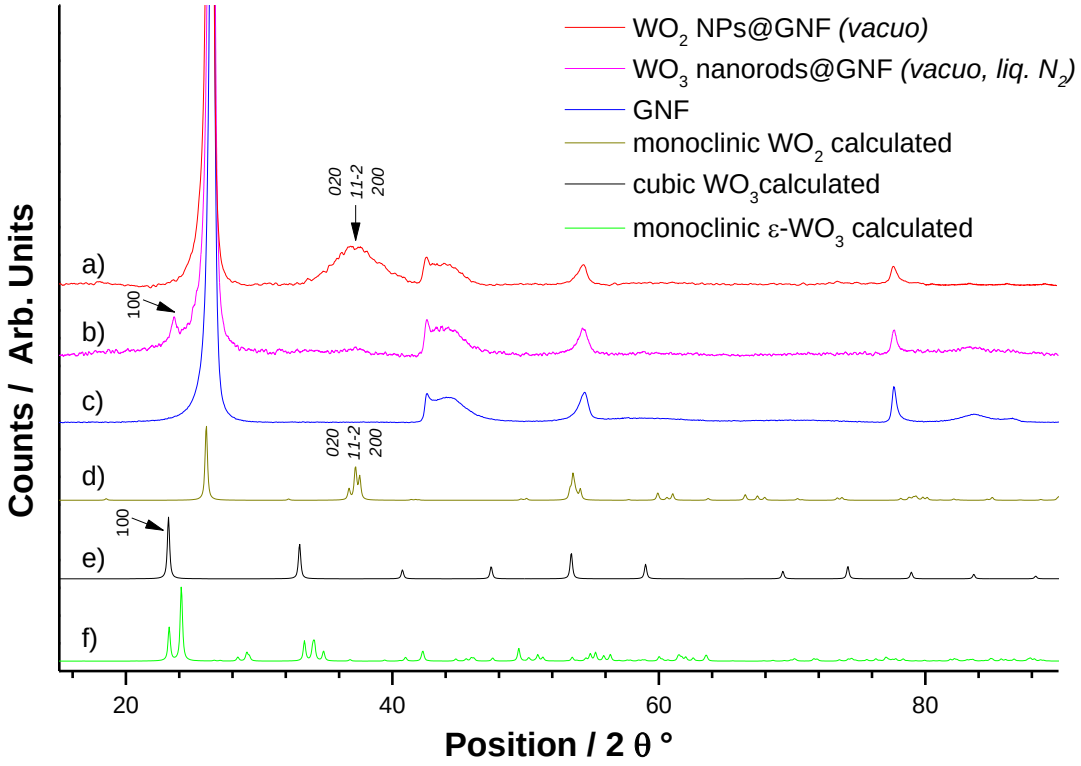


Figure 3-29. PXRD patterns of the materials formed by the encapsulation and consecutive thermal decomposition of $W(CO)_6$ in GNF; a) sealed under vacuum (Experiment 3–11, WO_2 NPs), b) sealed under vacuum using liquid N_2 cooling (Experiment 3–12, WO_3 nanorods), and c) GNF. Calculated PXRD patterns of d) WO_2,[27] e) cubic WO_3[28] and f) ε-WO_3[24] are shown to allow comparison with experimental patterns (λ=1.5432 Å).

TEM investigation of the material formed by the encapsulation

and consecutive thermal decomposition of $W(CO)_6$ in GNFs sealed under vacuum using liquid N_2 cooling (Experiment 3–12) showed the formation of crystalline nanorods (Figure 3-30). Examples of long nanorods bridging the internal channels of GNFs from one step-edge to another were found as shown in Figure 3-30 c. The repeating distance of the crystallographic lattice planes in the nanorods was found to be 0.39 nm both parallel and perpendicular to their principal axis (Figure 3-30 d). EDX spectroscopy detected the characteristic peaks of W which were identified at 1.4, 1.8, 8.4 and 9.6 keV indicating that the nanorods contain W (Figure 3-31).

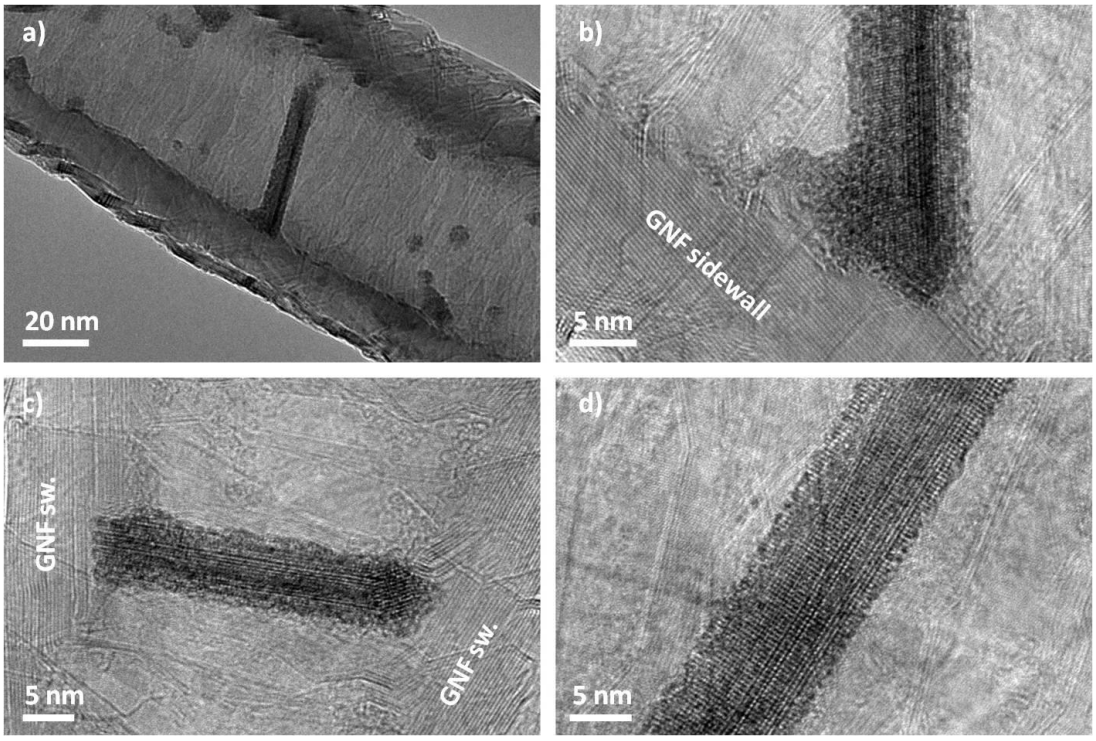


Figure 3-30. TEM images a)-b) showing WO_3 nanorods formed by the encapsulation and consecutive thermal decomposition of $W(CO)_6$ in GNFs under vacuum (Experiment 3–12, liq. N_2 cooling) on the step-edges of the GNF while c) shows another nanorod bridging the step-edges (*l*=10 nm). Image d) shows the crystallographic planes of a WO_3 nanorods separated by a *d* spacing of 0.39 nm.

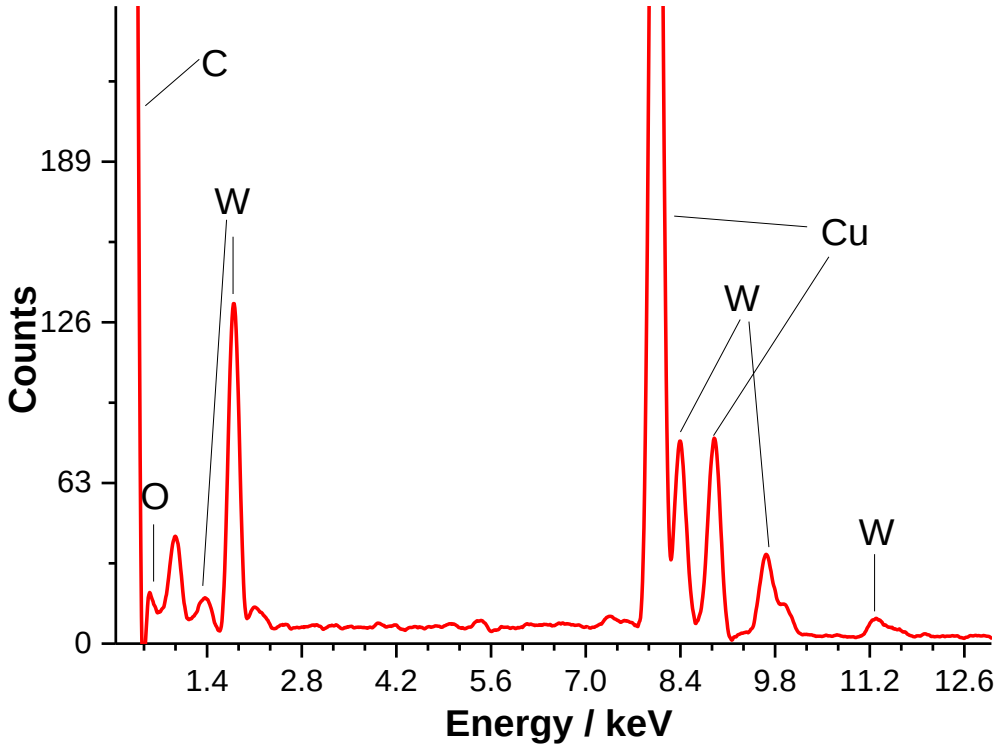


Figure 3-31. EDX spectrum of W-based nanorods formed in GNF by the encapsulation and consecutive thermal decomposition of $W(CO)_6$ in GNFs under vacuum (Experiment 3–12, liq. N_2 cooling). The characteristic peaks of W were identified at 1.4, 1.8, 8.4 and 9.6 keV indicating that the nanorods contain W. Cu peaks are due to the specimen holder.

To gain more information about the structural and chemical composition of the formed nanorods the material was investigated by PXRD. In the recorded diffraction pattern one new peak was observed at $2\theta=23.6°$ (Figure 3-29 b). The *d* spacing (0.38 nm) corresponding to this peak is slightly different than the *d* spacing (0.39 nm) observed by TEM. Comparison of the diffraction patterns of the recorded and various calculated tungsten based crystals suggested that the nanorods consist of cubic WO_3[28] or a related WO_{3-x} species. It has to be noted that an unambiguous assignment of PXRD peaks in the case of tungsten oxides is rather difficult since WO_3 alone exists in at least seven polymorphic forms which can undergo numerous facile crystallographic transitions near room

temperature and its decomposition *in vacuo* can produce various nonstoichiometric (WO_{3-x}) and stoichiometric (W_5O_{14}, $W_{18}O_{49}$, $W_{20}O_{58}$ *etc.*) tungsten oxides.[24] Previously tungsten oxide nanorods with different stoichiometries were synthesised *via* plasma arc gas condensation technique during studying the effect of O_2 partial pressure on the formation of nanocrystalline tungsten oxides (W_5O_{14}),[29] physical vapour deposition (monoclinic WO_3),[30] hot-wire chemical vapour deposition (CVD) either using a W filament and Ar or H_2 gas passed through a water bubbler ($W_{18}O_{49}$)[31], or by controlling the partial pressure of water.[32] However, in the case of W_5O_{14} and monoclinic WO_3 nanorods two different *d* spacings (0.38, 0.28 nm and 0.38, 0.37 nm, respectively) were observed by TEM (Figure 3-32) in contrast to the nanorods formed in GNFs possessing uniform *d* spacing verifying the cubic-like structure of the latter.

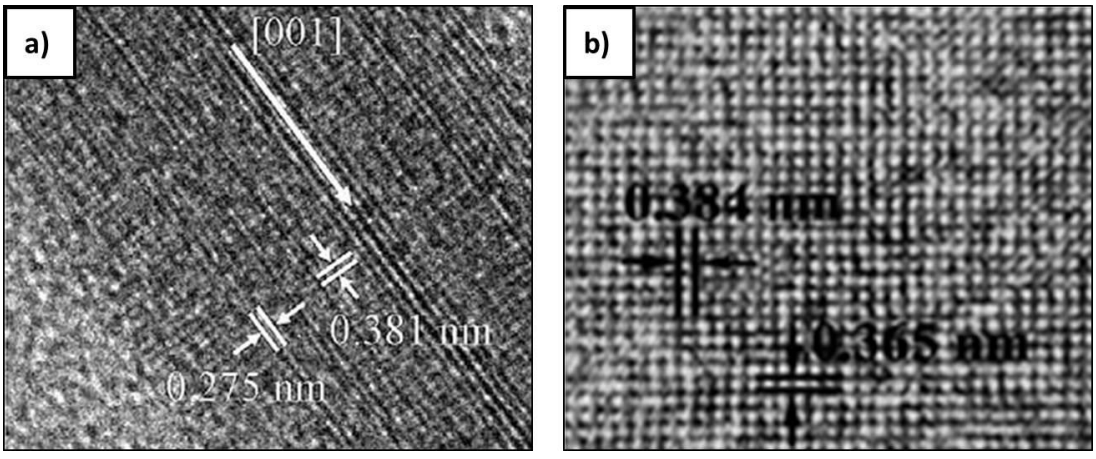


Figure 3-32. TEM images showing the *d* spacings of a) W_5O_{14} nanorod (0.38 and 0.28 nm) formed by plasma arc gas condensation,[29] b) a monoclinic WO_3 nanorod (0.38 and 0.37 nm) formed by physical vapour deposition.[30]

TEM analyses of the material formed by the decomposition of $W(CO)_6$ in GNFs in a stream of H_2(10%)/Ar gas (Experiment 3–14) revealed irregularly shaped crystalline NPs (10-30 nm) with a faceted structure (Figure 3-33).

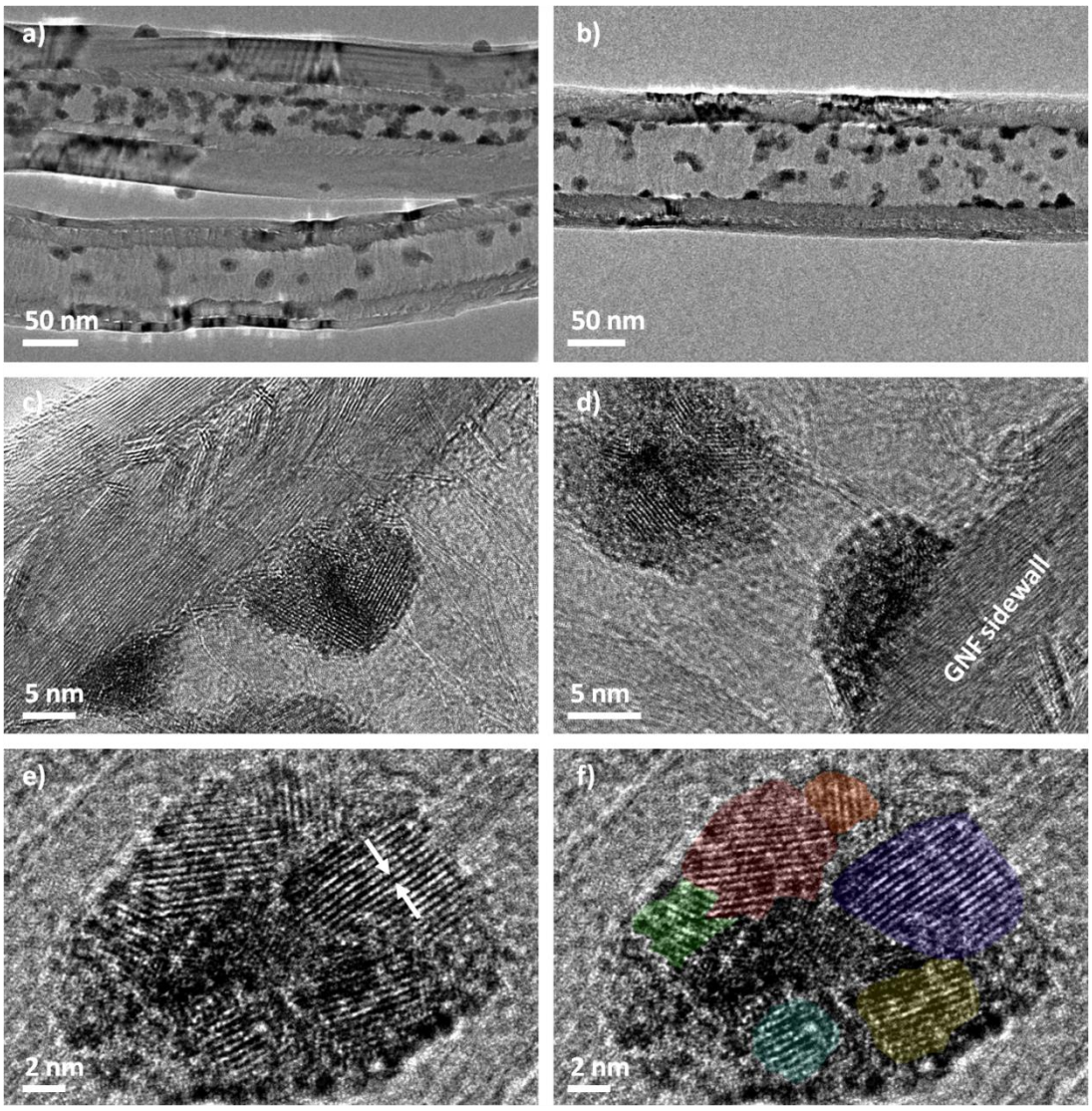


Figure 3-33. TEM images showing the NPs formed by the thermal decomposition of $W(CO)_6$@GNF under H_2(10%)/Ar gas flow (Experiment 3–14). c)-d) The NPs have irregular shape and faceted crystalline structure with a 0.39 nm distance between their crystallographic layers indicted with arrows in e). The coloured areas in image f) show different crystal domains within the individual NP.

The grain boundaries of the facets are highlighted with different colours in image Figure 3-33 f. The distance between the crystallographic lattice planes were measured for various facets of

the different NPs and was found to be 0.39 nm in all cases (Figure 3-33 e).

The material was investigated using PXRD and in the diffraction pattern three new peaks were observed at 2θ=23.5°, 33.5° and 37.4° in addition to the peaks corresponding to the GNFs (Figure 3-34 a). These peaks most likely consist of overlapping peaks from which the peaks at 23.5° and 33.5° correspond to the 002, 020, 200 and 002,20-2, 220 crystallographic planes of a ε-WO_3 phase and the peak at 37.4° corresponds to the 020, 11-2, 200 crystallographic planes of WO_2. The overlapping of the peaks especially the one observed at 23.5° might be caused by factors such as small-sized NPs and/or a low amount of material.

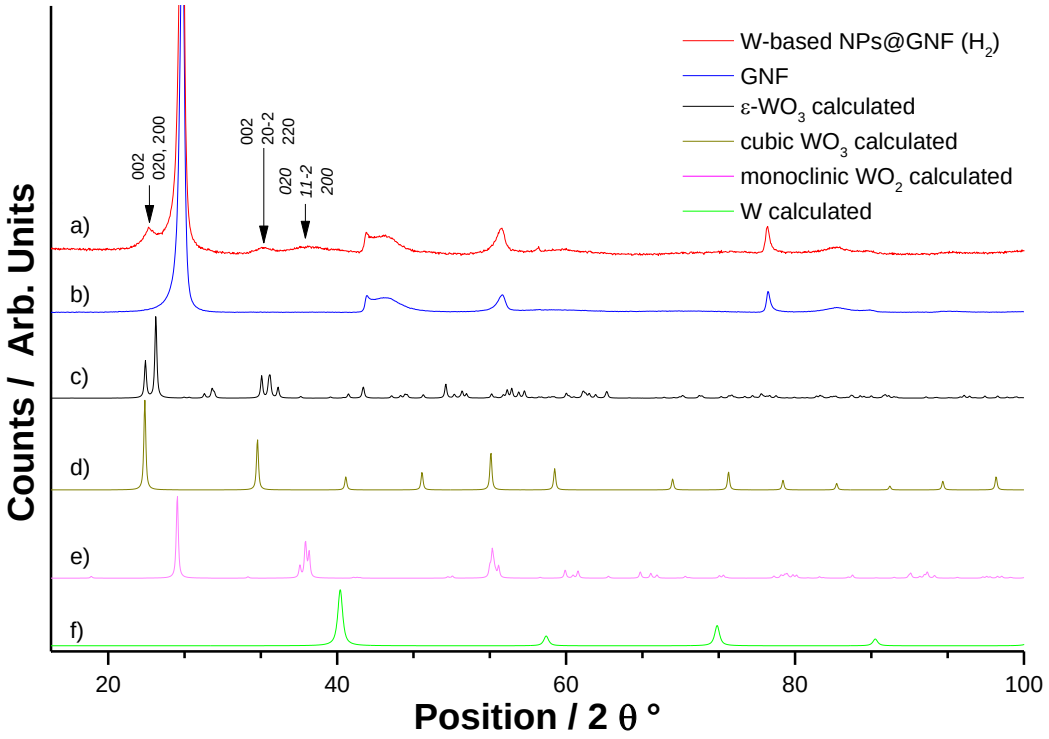


Figure 3-34. a) PXRD patterns of the a) W-based NPs formed by the thermal decomposition of $W(CO)_6$@GNF under H_2(10%)/Ar gas flow (Experiment 3–14), and b) GNFs. Calculated PXRD patterns of c) monoclinic ε-WO_3,[24] d) cubic WO_3,[28] e) monoclinic WO_2[27] and f) metallic W[25] are shown to allow comparison with experimental patterns (*λ*=1.5432 Å).

3.6 Discussion

In this section the results of the different NP formation methods are discussed and compared to each other in order to understand how the interior of GNFs and reaction conditions influence the chemical transformation of $M(CO)_6$.

3.6.1 Behaviour of $M(CO)_6$ in GNFs under the e-beam of TEM

As shown in Section 3.5.1 the encapsulation of $M(CO)_6$ into GNFs from the gas phase was successful using the method described in Section 3.8.2 so they can be used as starting materials towards the formation of NPs in GNFs by thermal decomposition.

Moreover, TEM analysis of $M(CO)_6$@GNF showed that the e-beam induced decomposition of the $M(CO)_6$ molecules led to the formation of NPs in GNFs with no defined crystal structure in all cases (*i.e.* M=Cr, Mo and W). However, the size, shape and structure of the formed materials varied for the different $M(CO)_6$. In the case of Mo and W TEM revealed that the *in situ* formed NPs are built up *via* the aggregation of smaller NPs (~0.5 nm) (Figure 3-6 b and Figure 3-8 d). In contrast, in the case of the NPs formed in $Cr(CO)_6$@GNF no subunits could be identified (Figure 3-4), however this may be due to the lower contrast of Cr in TEM making it difficult to observe the smaller NP subunits.

It is also interesting to note that the NPs preferred to form at the step-edges of GNFs. The reason for this is most likely that the

dangling carbon bonds present at the step-edges provide an anchor point for the reaction intermediates such as $M(CO)_3$ and larger clusters *i.e.* $M_x(CO)_y$ which may be generated during the initial stages of e-beam induced decomposition of $M(CO)_6$ in TEM.[13] This theory is supported by a study on the electron stimulated (500 eV) reactions of $W(CO)_6$ molecules adsorbed on amorphous carbon or Au substrate in which it was shown that the reaction consisted of two separate steps.[33] The first step, CO ligand desorption, leading to the formation of $W_x(CO)_y$ clusters followed by the decomposition of CO in the second step which resulted in the formation of tungsten oxides. The degree of oxidation also depends on the presence of co-adsorbed water which might also be a factor within the $M(CO)_6$@GNF systems.

3.6.2 Comparing the structure and shape of products of the different thermal decomposition processes

As it was demonstrated in Section 3.5.2 using TEM and PXRD the thermal decomposition of $M(CO)_6$ in GNFs resulted in the formation of different nanostructures *i.e.* NPs and nanorods depending on the experimental conditions which were applied during their formation (Table 3-5). Therefore, in this section the structural properties of the nanostructures resulting from the various different thermal decomposition of $M(CO)_6$@GNF are compared to each other.

It was shown that in an Ar atmosphere at 200 °C amorphous

spherical W-based NPs while at the higher temperature of 500 °C crystalline spherical Cr_2O_3 (Figure 3-11), MoO_2, (Figure 3-17) and WO_3 NPs (Figure 3-24) were formed.

Table 3-5. Summary of the materials formed from $M(CO)_6$ encapsulated in GNFs by the various thermal decomposition procedures shown in Figure 3-3. (The text in first column points to the corresponding part of Section 3.8.3.)

Decomposition method	Materials formed in GNFs by the thermal decomposition of		
	$Cr(CO)_6$@GNF	$Mo(CO)_6$@GNF	$W(CO)_6$@GNF
Ar	crystalline Cr_2O_3 NPs	crystalline MoO_2 NPs	crystalline WO_3 NPs (500 °C), amorphous W-based NPs (200 °C)
Vacuum I. (Decomposition)	N/A	N/A	WO_3 NPs
Vacuum II. (Encapsulation+ Decomposition)	amorphous Cr-based NPs	semi-crystalline Mo-based NPs	semi-crystalline W-based NPs, crystalline WO_3 nanorods (liq. N_2 cooling)
H_2/Ar flow	N/A	faceted crystalline MoO_2 NPs@GNFs	faceted crystalline WO_3 NPs@GNFs

The properties such as shape, size, chemical composition and crystal structure (ε-WO_3) including the *d* spacing (0.39 nm) of WO_3 NPs formed by the thermal decomposition of $W(CO)_6$@GNFs under vacuum (Experiment 3–8) and in an Ar atmosphere (Experiment 3–7) were found to be identical.

The encapsulation and consecutive decomposition of $M(CO)_6$ in GNFs (M=Cr, Mo, W) under vacuum led to the formation of spherical amorphous Cr-based and semi-crystalline monoclinic MoO_2 and WO_2 NPs. EDX confirmed only a relatively small amount of O associated with the M-based NPs in all three materials (Figure 3-13, Figure 3-20, Figure 3-28).

In contrast, the encapsulation and consecutive decomposition of $W(CO)_6$ under vacuum, when liquid N_2 cooling was applied during the sealing of the glass ampoule resulting in the entrapment of moisture within the glass ampoule together with $W(CO)_6$ and GNFs, produced crystalline cubic WO_3 nanorods. As it was mention above water has a powerful influence on the metal oxide formation. It was demonstrated in earlier studies that the presence of H_2O promotes the formation of WO_3 nanorods by a so-called evaporation-condensation process over spherical WO_3 NPs.[34,35,36] The role of H_2O in this process is twofold on one hand it acts as a source of O during the formation of spherical WO_3 NPs whilst on the other hand the H_2 present simultaneously reduces the metal resulting in asymmetric growth and the formation of WO_{3-x} nanorods, see Equation 3-1. Although, water clearly promotes nanorod formation it is not clear whether the oxidation of W happens directly (Equation 3-1 a) or by first splitting the H_2O molecules to H_2 and O (Equation 3-1 b).[35]

Equation 3-1[35] *Oxidation*

a) $W + 3H_2O \longrightarrow WO_3 + 3H_2$

b) $H_2O \longrightarrow 1/2O_2 + H_2$

$W + 3/2O_2 \longrightarrow WO_3$

Reduction

$WO_3 + H_2 \longrightarrow WO_{3-x} + xH_2O + (1-x)H_2$

The decomposition of $M(CO)_6$@GNF (M=Mo, W) under a H_2(10%)/Ar flow (Section 3.8.3.4, Table 3-10) led to the formation of faceted crystalline M-based NPs in GNFs. The interlayer *d* spacing of these M-based NPs (Figure 3-22, Figure 3-33) and those MO_x NPs (MoO_2, Figure 3-15 and WO_3, Figure 3-24) formed under Ar are identical suggesting that they have a similar crystal structure and stoichiometry. The formation of faceted MO_x NPs@GNFs during the thermal decomposition of $M(CO)_6$@GNFs under H_2(10%)/Ar flow is likely to be the result of a two-step process which firstly involves the formation of MO_x NPs followed by their subsequent reduction by H_2. This is supported by earlier studies where the reduction of WO_3 NPs was extensively investigated and it was found that at approximately 500 °C the NPs are scarcely reduced in H_2(5%)/N_2 flow during 1.5-2 hour reaction time.[37] In addition, it was also reported that the reduction of WO_3 NPs in H_2 containing gas flow can result in the formation of faceted NPs.[32]

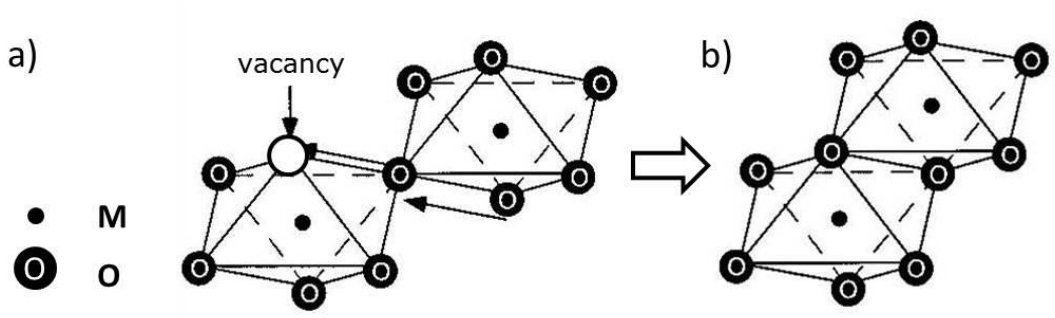


Figure 3-35. a) Illustration of two MO_6 octahedra consisting of a central M atom coordinated by six O atoms sharing a single O at an apex with a single O vacancy. The arrows parallel with the edges of the octahedra indicate the shear movement of the right octahedron which results in the structure shown in diagram b) depicting two MO_6 octahedra sharing two O atoms and along a common edge.[37]

The mechanism which may cause such a faceted structure is the so-called shear process that generates crystallographic shear planes. During the process an O atom hops into a neighbouring vacancy of the WO_3 crystallographic lattice. However, according to the literature it is assumed that instead of a single atom a whole octahedron consisting of a central M atom coordinated by six O atoms hops, and as a result of this two MO_6 octahedra which are used to share a single O at an apex will now share two O atoms along their common edge (Figure 3-35).[37]

3.6.3 Investigation of the metal oxide formation in GNFs

As shown above the thermal decomposition of $M(CO)_6$ encapsulated in GNFs using different conditions led to the formation of various MO_x nanostructures rather than metallic nanoparticles as one might expect (Table 3-5).

The formation of MO_x nanostructures in GNF under vacuum or Ar is unforeseen as in an inert environment above 400 °C the

thermal decomposition of $M(CO)_6$ is expected to lead to formation of the pure metal and CO gas (see Equation 3-2).[38,39]

Equation 3-2[39] $W(CO)_6 \longrightarrow W + 6CO \quad \Delta G^0_{500°C}$=-402 kJ/mol

In addition, the formation of crystalline MO_x nanostructures in GNF under Ar atmosphere is in contrast with earlier observed formation of metal NPs during the thermal decomposition of $M(CO)_6$ molecules situated inside carbon nanotubes.[12,17] As carbon nanotubes and GNFs are built up from the same type of graphitic layer(s) consisting of sp^2-C atoms, making them chemically and structurally similar to each other, it is unexpected that different products are formed in the two nanocontainers. The conditions (500 °C, Ar, 1h) and the procedure used during the formation of M NPs@CNTs are identical to that which resulted in the formation of crystalline Cr_2O_3, MoO_2 and WO_3 NPs in GNFs and is described in Section 3.8.3.1.

As Cr_2O_3, MoO_3 and WO_3 are the most stable oxides of the respective metals and they are the final products of their combustion in air, moreover, MO_3 can be transformed into MO_2 by heating *in vacuo*; the formation of Cr_2O_3, MoO_2 and WO_3 within GNFs is reasonable.[40] However, the presence of MO_x indicates that some kind of O source is present during the NP formation. In addition, the formation of MoO_2 instead of MoO_3 also implies that the amount of O present may be limited.

Furthermore the presence of a limited amount of O is supported by the fact that the encapsulation and consecutive decomposition of $M(CO)_6$ in GNFs (M=Cr, Mo, W) under vacuum led to the formation of semi-crystalline MoO_2 and WO_2 NPs.

Surprisingly the decomposition of $M(CO)_6$@GNFs (M=Mo, W) under H_2/Ar flow led to the formation of faceted crystalline MO_x NPs@GNFs (MoO_2, WO_3), which is unexpected, as under H_2 atmosphere MO_3 can be reduced to MO_{3-x}, then MO_2 and finally to M according to Equation 3-3.[41,42,40] Therefore, the presence of H_2 during the decomposition of $M(CO)_6$ was expected to prevent the formation of MO_x NPs@GNFs.

Equation 3-3[41]

$$4WO_3 + H_2 \longrightarrow W_4O_{11} + H_2O$$

$$W_4O_{11} + 3H_2 \longrightarrow 4WO_2 + 3H_2O$$

$$WO_2 + 2H_2 \longrightarrow W + 2H_2O$$

These observations and considerations lead to the following questions: Why does the thermal decomposition of $M(CO)_6$ encapsulated in GNFs lead to the formation of metal oxides rather than pure metal species, and where has the O in the MO_x nanomaterials come from?

The potential sources of O causing the formation of MO_x nanostructures in GNFs could be; 1) the CO ligands of the $M(CO)_6$ molecules, 2) moisture *i.e.* H_2O present in the reaction environment, or 3) the functional groups *e.g.* carboxylic groups

and impurities associated with the GNFs.

As stated above the decomposition of $M(CO)_6$ at 500°C is expected to produce pure M and CO gas which vents from the GNF as CO is a very stable ($\Delta G^0_{500°C}$=-796 kJmol^{-1}) and volatile molecule and which can be used for the reduction of metal oxides.[38,39,43] Moreover, it was demonstrated previously that even if the liberated CO molecule is split into C and O atoms this is likely to cause a relatively low level of C and O contamination in the formed M layer instead of the formation of MO_x.[38,44,45] It was also shown earlier in the literature that either below 400 °C in inert atmosphere or at higher temperatures (500-1000 °C) in the presence of additional CO gas, metal carbides and oxycarbides can be formed as a result of the decomposition of $M(CO)_6$ but no MO_x was observed.[38,46] In summary, the CO ligands of the $M(CO)_6$ molecules may be excluded as an O source under the conditions applied during the formation of MO_x NPs@GNFs.

The presence of water was demonstrated to be an important factor during the synthesis of Mo and W oxide nanostructures.[31,32] $W_{18}O_{49}$ nanorods were synthesised *via* hot-wire CVD using a W filament and Ar or H_2 gas which was passed through a water bubbler.[31] In another study water vapour was used to synthesise various WO_x nanostructures *via* hot-wire CVD by varying the partial pressure of water.[32] In agreement with these observations the entrapment of moisture during the encapsulation and consecutive

decomposition of $W(CO)_6$ in GNFs resulted in the formation of WO_3 nanorods@GNFs. In contrast, when the chance of any environmental effect was meticulously minimised the encapsulation and consecutive decomposition of $M(CO)_6$ in GNFs led to the formation of semi-crystalline MO_2 NPs@GNFs (M=Mo, W). These observations suggest that if moisture is present during the thermal decomposition of $M(CO)_6$@GNFs it can act as source of O during the thermal decomposition of $M(CO)_6$@GNFs and that GNFs might participate as a source of O during the formation of MO_x nanostructures.

Therefore, it was examined whether GNFs could act as an active reagent *i.e.* a source of O under the conditions used during the thermal decomposition of $M(CO)_6$ in GNFs. GNFs were analysed by TEM and EDX as described in Section 3.8.4 in two different states: 1) as-received GNFs and 2) GNFs which were heated in air at 500 °C identically to a typical filling experiment according to Section 3.8.2.1.

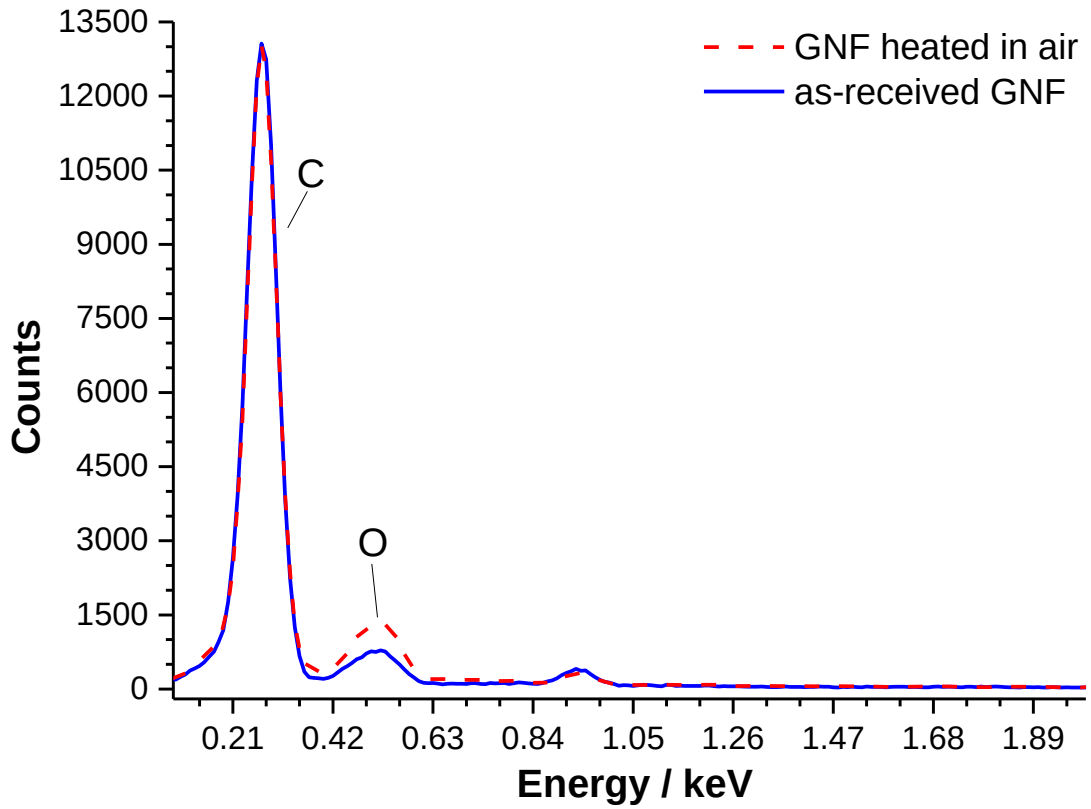


Figure 3-36. EDX spectra of a) GNFs heated in air (500 °C, 30 min) according to Section 3.8.2.1 (red dashed line), b) as-received GNFs (blue line).

It was found that as-received GNFs contain 0.6% O on average (Table 3-6, Figure 3-36). On the other hand EDX measurements showed that the heat treatment of GNFs in air (500 °C, 30 min) prior to encapsulation introduces an extra 1% of O content in addition to those inherently present resulting in a total of 1.6% O on average (Table 3-6, Figure 3-36). Consequently, GNFs have to be considered as a source of O during the formation of MO_x NPs@GNFs by the thermal decomposition of $M(CO)_6$ in GNFs.

Most likely the O content of GNFs may be attributed to O containing groups such as -COOH, =O, -OH *etc*. bonded to the defects of the sp^2 C network in addition to the termini of GNFs.[47] These groups are present most frequently at the step-edges of the

GNFs where the graphene sheets are extremely curved and the resulting strain makes the C atoms at the step-edge more reactive.

Table 3-6. Oxygen content (atomic %) of as-received GNFs and GNFs heated in air according to Section 3.8.2.1 measured by EDX in TEM at different individual GNFs supported by lacey carbon film over vacuum.

	O content of GNF / atomic %			
	Spot 1.	Spot 2.	Spot 3.	Average
GNF heated in air	1.80	1.38	1.65	1.61
as-received GNF	0.61	0.60	0.68	0.63

In conclusion, it can be said that GNFs contain O therefore they can act as a reactant during the thermal decomposition of $M(CO)_6$ providing O atoms for the formation of MO_x NPs. Moreover, the CO group of $M(CO)_6$ can be excluded as the source of O in the MO_x NPs. The presence of H_2O is not necessary to form (semi)crystalline MO_x NPs@GNFs based on our experimental observations.

3.7 Concluding remarks

The main goal of this study was the formation of M-based NPs within GNFs. It was demonstrated using TEM, EDX and PXRD that $M(CO)_6$ precursor molecules can be encapsulated into GNFs using gas phase filling and subsequently transformed into M-based NPs. Depending on the decomposition method *i.e.* e-beam in TEM or heating and the experimental conditions the formation of amorphous M-based NPs, MO_x NPs and nanorods were observed by TEM and PXRD.

The formation of MO_x NPs in GNFs was investigated because the thermal decomposition of $M(CO)_6$ was expected to provide metal NPs. The participation of CO ligands as O source in the MO_x NP formation can be excluded, however, it was revealed that GNFs contain O therefore they can act as a reactant during the thermal decomposition of $M(CO)_6$ providing O atoms for the formation of MO_x NPs. Moreover, it was demonstrated that the presence of H_2O can dramatically alter the morphology of the nanostructure by aiding the formation of nanorods instead of spherical nanoparticles, which is in agreement with previous publications.[32,34,35,36]

In summary, the synthesis of metal based nanoparticles inside GNFs by the encapsulation and *in situ* transformation of metal containing precursor molecules was demonstrated *via* the formation of M-based NPs in GNFs from $M(CO)_6$ molecules.

3.8 Experimental section

3.8.1 Materials

Graphitised carbon nanofibers (PR-24 XT-HHT, *d*=30-40 nm, *l*=1-100 μm, Fe content<100 ppm) were purchased from Pyrograf Products and used without further purification.

$Cr(CO)_6$ (purity≥98%) was obtained from Sigma-Aldrich, Mo and W hexacarbonyls (purity≥98 and 99%, respectively) were purchased from Acros Organics and all hexacarbonyls were used without further purification.

3.8.2 Gas phase filling of GNFs with $M(CO)_6$

3.8.2.1 Heat treatment of GNFs in air prior to encapsulation

To remove moisture and provide access to their interior for the guest species graphitised carbon nanofibers were pre-treated by heating in air for 30 minutes below their oxidation temperature (500 °C) in a crucible.

3.8.2.2 Encapsulation of $M(CO)_6$ into GNFs

Pre-treated graphitised carbon nanofibers were mixed with $M(CO)_6$ and the resultant mixture was sealed in a Pyrex glass vessel (*d*=10 mm, *l*=10 cm) under high vacuum (10^{-6} mbar). The sealed vessel was placed in a preheated box furnace (T=120-150 °C) for several days depending on the experiment, see Table 3-7. Prior to opening, the Pyrex glass vessel was taken out from the furnace and cooled down by immersing it into an ice-water bath for 5 minutes. After opening the Pyrex glass vessel the

samples were transferred into a glass vial and stored in the freezer at **-**15 °C until required.

Table 3-7. Parameters of the gas phase encapsulation of $M(CO)_6$ into GNFs.

Experiment	Precursor molecule	Atmosphere, pressure / bar	Reaction temp. / °C	Reaction time / days
3–1	$Cr(CO)_6$	Vacuum, 10^{-9}	120	5
3–2	$Mo(CO)_6$	Vacuum, 10^{-9}	120	3
3–3	$W(CO)_6$	Vacuum, 10^{-9}	150	3

3.8.3 Chemical transformation of $M(CO)_6$ encapsulated in GNFs into nanoparticles *via* thermal decomposition

3.8.3.1 Thermal decomposition of $M(CO)_6$@GNF under Ar atmosphere

$M(CO)_6$@GNF was placed into a Pyrex glass vessel, which was then evacuated (10^{-6} mbar) and consecutively filled with Ar (repeated 3 times) to remove any reactive compound such as O_2 and moisture that may be present. Prior to sealing, the ampoule was filled with Ar gas (0.7 bar). Taking into account the heat expansion of argon gas the final pressure in the Pyrex tube will be approximately 1.8 bar. The sealed Pyrex glass tube was transferred into a preheated furnace and kept there for the time specified in Table 3-8, then the glass ampoule was transferred onto an asbestos tile to cool down to room temperature.

3.8.3.2 Thermal decomposition of $M(CO)_6$@GNF under vacuum

$M(CO)_6$@GNF was sealed in a Pyrex glass vessel which was evacuated (10^{-6} mbar) and consecutively filled with Ar repeatedly (3 times) and finally the ampoule was evacuated (10^{-6} mbar) prior

to sealing. The sealed glass ampoule was transferred into a preheated furnace and kept there for the time specified in Table 3-8, then the glass ampoule was transferred onto an asbestos tile to cool down to room temperature.

Table 3-8. Parameters of the thermal decomposition of $M(CO)_6$@GNFs under Ar and vacuum.

Experiment	Starting material	Atmosphere, pressure / bar	Reaction temp. / °C	Reaction time / h
3–4	$Cr(CO)_6$@GNF	Argon, 0.7	500	1
3–5	$Mo(CO)_6$@GNF	Argon, 0.7	500	1
3–6	$W(CO)_6$@GNF	Argon, 0.7	200	72
3–7	$W(CO)_6$@GNF	Argon, 0.7	500	1
3–8	$W(CO)_6$@GNF	Vacuum, 10^{-9}	500	1

3.8.3.3 Encapsulation and consecutive thermal decomposition of $M(CO)_6$ in GNFs under vacuum

Pre-treated graphitised carbon nanofibers were mixed with $M(CO)_6$ and the resultant mixture was sealed in a Pyrex glass vessel under high vacuum (10^{-6} mbar). N.B. In Experiment 3–12 the glass ampoule was cooled with liquid N_2 during evacuation. The sealed vessel was placed in a preheated box furnace (120-150 °C) for 3 days. After immersing it into ice-water bath for 5 minutes (0 °C) the glass ampoule was transferred into a preheated furnace (500 °C). After an hour the sample was taken out from the furnace and left on an asbestos tile too cool down to room temperature (Table 3-9).

Table 3-9. Parameters of the encapsulation and consecutive thermal decomposition of $M(CO)_6$ in GNFs under vacuum.

Experiment	Starting materials	Atmosphere, pressure / bar	Reaction temp. / °C		Reaction time	
			Encap.	Decomp.	Encap. / day	Decomp. / h
3–9	$Cr(CO)_6$+ GNF	Vacuum, 10^{-9}	120	500	3	1
3–10	$Mo(CO)_6$+ GNF	Vacuum, 10^{-9}	120	500	3	1
3–11	$W(CO)_6$+ GNF	Vacuum, 10^{-9}	150	500	3	1
3–12	$W(CO)_6$+ GNF	Vacuum, 10^{-9} (liq. N_2 cooling)	150	500	3	1

3.8.3.4 Thermal decomposition of $M(CO)_6$@GNF in H_2/Ar flow

$M(CO)_6$@GNF was transferred into a quartz boat and placed into a closed ceramic working tube (*d*=25 mm, *l*=60 cm) which was provided with the tube furnace (Figure 3-37). The system was purged with H_2(10%)/Ar at room temperature for 1 hour. Then the furnace was heated up to 500 °C (50 °C/min) and kept at this temperature for 1 hour. The system was gradually cooled down to room temperature (10 °C/min) while maintaining the gas flow (Table 3-10).

Table 3-10. Parameters of the thermal decomposition of $M(CO)_6$@GNFs under H_2(10%)/Ar gas flow.

Experiment	Starting material	Atmosphere	Reaction temp. / °C	Temp. ramp / °C min^{-1}		Dwell time / h
				Up	Down	
3–13	$Mo(CO)_6$@GNF	H_2(10%)/Ar	500	50	10	1
3–14	$W(CO)_6$@GNF	H_2(10%)/Ar	500	50	10	1

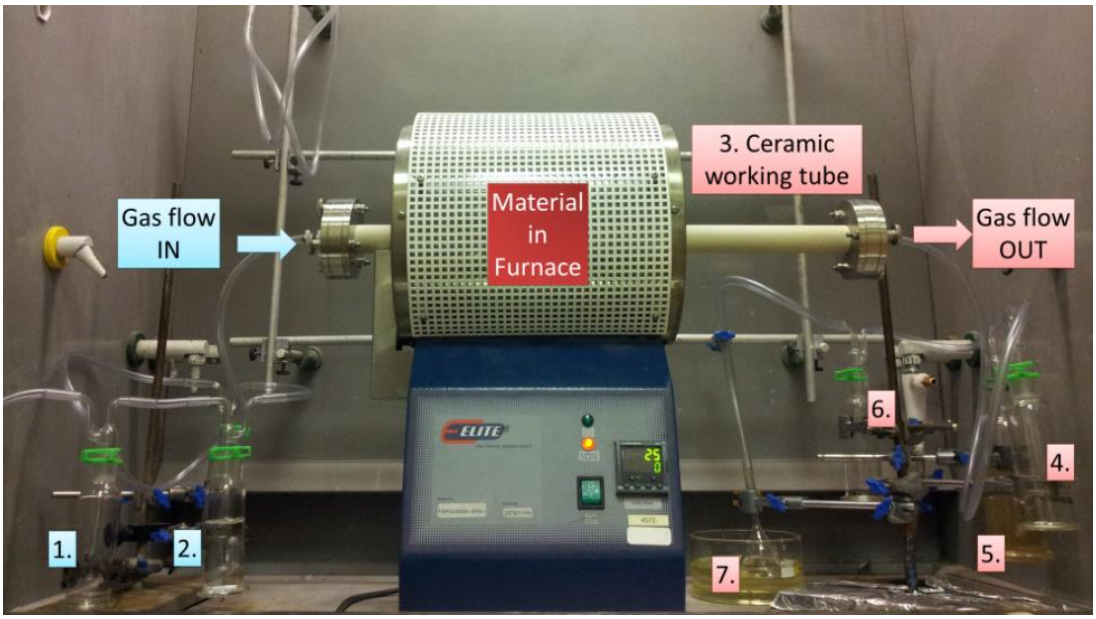


Figure 3-37. Experimental setup used for the thermal decomposition of $M(CO)_6$@GNFs under H_2(10%)/Ar gas flow. The cold gas flow goes through an empty reversed gas bubbler (1.) and another one filled with paraffin oil (2.) before entering the ceramic working tube containing the sample (3.). The hot gas then flows through an empty reversed gas bubbler (4.), one filled with paraffin oil (5.) and another empty reversed gas bubbler (6.) and then through a water bath (7.).

3.8.4 Transmission Electron Microscopy and Energy-dispersive X-ray spectroscopy

TEM images and EDX spectra were acquired with an emission gun JEOL 2100F microscope at 200 kV acceleration voltage. Prior to the investigation, the graphitised carbon nanofibers were dispersed in isopropyl alcohol using an ultrasonic bath (~15 min). Subsequently, a few drops of the suspension were dropped onto a copper TEM grid coated with lacey carbon film (Agar Scientific) to support the graphitised carbon nanofibers. The characteristic Cu peaks in the EDX spectra of the analysed materials are due to the copper grid of the TEM specimen holder.

The relative oxygen content of as-received GNFs and those which were heated in air according to Section 3.8.2.1 were

measured *via* EDX spectroscopy by selecting individual GNFs which were situated over holes of the lacey carbon film to eliminate any contribution from the film.

3.8.5 Powder X-ray diffraction measurements and calculations

The powder X-ray measurements were performed using a PANalytical X'Pert PRO diffractometer equipped with a Cu K_α radiation source (λ=1.5432 Å, 40 kV, 40 mA) in Bragg-Brentano geometry using a Si zero-background holder. The powder sample was poured on the Si surface, which had been wetted with acetone to aid GNF adhesion. As the materials of interest are small nanoparticles inside another structure long acquisition times were required for the powder X-ray diffraction measurements. The parameters of a typical experiment are: start angle: 5°, stop angle: 120°, step size: 0.05°, time/step: 6080 seconds, scan speed: 0.0022°/sec.

The reference powder diffraction patterns were calculated from crystallographic information files acquired from the Royal Chemical Society`s Chemical Database Service with Mercury CSD 3.0 program using the following parameters: λ=1.5432 Å, step size: 0.05°.

The distance of crystallographic lattices (*d*) *i.e.* the *d* spacing which results in the appearance of a certain peak in the diffraction pattern can be calculated using Bragg`s Law (Equation 3-4) where θ is the scattering angle, λ is the wavelength of the X-ray in this

case the Cu K_α radiation (λ=1.5432 Å) and n>0 is an integer.

Equation 3-4 $$2d\sin\theta = n\lambda$$

3.9 References

1. Y. Sun, X. Hu, W. Luo, and Y. Huang, *J. Mater. Chem.*, 2012, **22**, 425–431.
2. S. Hu, W. Chen, J. Zhou, F. Yin, E. Uchaker, Q. Zhang, and G. Cao, *J. Mater. Chem. A*, 2014, **2**, 7862–7872.
3. X. Rui, H. Tan, and Q. Yan, *Nanoscale*, 2014, **6**, 9889–9924.
4. G. Zheng, Y. Yang, J. J. Cha, S. S. Hong, and Y. Cui, *Nano Lett.*, 2011, **11**, 4462–4467.
5. X. Pan and X. Bao, *Acc. Chem. Res.*, 2011, **44**, 553–562.
6. X. Pan, Z. Fan, W. Chen, Y. Ding, H. Luo, and X. Bao, *Nat. Mater.*, 2007, **6**, 507–511.
7. W. A. Solomonsz, G. A. Rance, M. Suyetin, A. La Torre, E. Bichoutskaia, and A. N. Khlobystov, *Chemistry*, 2012, **18**, 13180–13187.
8. W. A. Solomonsz, G. A. Rance, B. J. Harris, and A. N. Khlobystov, *Nanoscale*, 2013, **5**, 12200–12205.
9. G. A. Rance, W. A. Solomonsz, and A. N. Khlobystov, *Chem. Commun. (Camb).*, 2013, **49**, 1067–1069.
10. A. La Torre, M. D. C. Gimenez-Lopez, M. W. Fay, G. A. Rance, W. A. Solomonsz, T. W. Chamberlain, P. D. Brown, and A. N. Khlobystov, *ACS Nano*, 2012, **6**, 2000–2007.

11. A. N. Khlobystov, in *Chemistry of Carbon Nanotubes*, eds. V. A. Basiuk and E. V. Basiuk, 1st edn., 2008, pp. 87–109.

12. T. W. Chamberlain, T. Zoberbier, J. Biskupek, A. Botos, U. Kaiser, and A. N. Khlobystov, *Chem. Sci.*, 2012, **3**, 1919–1924.

13. T. W. Chamberlain, M. del C. Gimenez-Lopez, and A. N. Khlobystov, *Carbon Nanotub.*, 2010, 349–384.

14. P. M. Ajayan, O. Stephan, P. Redlich, and C. Colliex, *Nature*, 1995, **375**, 564–567.

15. X. Sun, X. Jiang, S. Dong, and E. Wang, *Macromol. Rapid Commun.*, 2003, **24**, 1024–1028.

16. M. A. Uppal, A. Kafizas, M. B. Ewing, and I. P. Parkin, *New J. Chem.*, 2010, 34, 2906–2914.

17. T. Zoberbier, T. W. Chamberlain, J. Biskupek, N. Kuganathan, S. Eyhusen, E. Bichoutskaia, U. Kaiser, and A. N. Khlobystov, *J. Am. Chem. Soc.*, 2012, **134**, 3073–3079.

18. B. W. Smith, M. Monthioux, and D. E. Luzzi, *Chem. Phys. Lett.*, 1999, **315**, 31–36.

19. A. W. Hull and W. P. Davey, *Phys. Rev.*, 1919, **14**, 540–540.

20. L. W. Finger and R. M. Hazen, *J. Appl. Phys.*, 1980, **51**, 5362–5367.

21. B. G. Brandt, A. C. Skapski, E. Thom, E. Stoll, G. Eriksson, R. Blinc, S. Paušak, L. Ehrenberg, and J. Dumanović, *Acta Chem. Scand.*, 1967, 21, 661–672.

22. H. E. Swanson and E. Tatge, *Standard X-ray diffraction powder patterns*, National Bureau of Standards (U.S.), Washington, D.C., 1953.

23. Q. Yang, Q. Liang, J. Liu, S. Liang, S. Tang, P. Lu, and Y. Lu, *Mater. Lett.*, 2014, **127**, 32–35.

24. E. K. H. Salje, S. Rehmann, F. Pobell, D. Morris, K. S. Knight, T. Herrmannsdörfer, and M. T. Dove, *J. Phys. Condens. Matter*, 1999, **9**, 6563–6577.

25. V. T. Deshpande and R. Pawar, *Curr. Sci.*, 1962, **31**, 497.

26. W. Pitschke, H. Hermann, and N. Mattern, *Powder Diffr.*, 2013, **8**, 74–83.

27. D. J. Palmer and P. G. Dickens, *Acta Crystallogr. Sect. B Struct. Crystallogr. Cryst. Chem.*, 1979, **35**, 2199–2201.

28. L. S. Palatnik, O. A. Obol'Yaninova, M. N. Naboka, and N. T. Gladkikh, *Inorg. Mater.*, 1973, **9**, 718–720.

29. C.-Y. Su, C.-K. Lin, T.-K. Yang, H.-C. Lin, and C.-T. Pan, *Int. J. Refract. Met. Hard Mater.*, 2008, **26**, 423–428.

30. Y. B. Li, Y. Bando, D. Golberg, and K. Kurashima, *Chem. Phys. Lett.*, 2003, **367**, 214–218.

31. S. Mitra, K. Sridharan, J. Unnam, and K. Ghosh, *Thin Solid Films*, 2008, **516**, 798–802.

32. G. L. Frey, A. Rothschild, J. Sloan, R. Rosentsveig, R. Popovitz-Biro, and R. Tenne, *J. Solid State Chem.*, 2001, **162**, 300–314.

33. S. G. Rosenberg, M. Barclay, and D. H. Fairbrother, *Phys. Chem. Chem. Phys.*, 2013, **15**, 4002–4015.

34. V. K. Sarin, *J. Mater. Sci.*, 1975, **10**, 593–598.

35. A. Rothschild, J. Sloan, and R. Tenne, *J. Am. Chem. Soc.*, 2000, **122**, 5169–5179.

36. M. Homyonfer, B. Alperson, Y. Rosenberg, L. Sapir, S. R. Cohen, G. Hodes, and R. Tenne, *J. Am. Chem. Soc.*, 1997, **119**, 2693–2698.

37. Y. Feldman, V. Lyakhovitskaya, and R. Tenne, *J. Am. Chem. Soc.*, 1998, **120**, 4176–4183.

38. K. A. Gesheva, V. Abrosimova, and G. D. Beshkov, *Le J. Phys. IV*, 1991, **02**, C2–865–C2–871.

39. X. Zhang, W. Liu, L. Yu, Y. Li, and S. Guo, *Plasma Sci. Technol.*, 2013, **15**, 955–960.

40. A. Earnshaw and N. Greenwood, *Chemistry of the Elements*, Elsevier, 1997.

41. J. O. Hougen, R. R. Reeves, and G. G. Mannella, *Ind. Eng. Chem.*, 1956, **48**, 318–320.

42. T. R. Wilken, W. R. Morcom, C. A. Wert, and J. B. Woodhouse, *Metall. Trans. B*, 1976, **7**, 589–597.

43. K. Mondal, H. Lorethova, E. Hippo, T. Wiltowski, and S. B. Lalvani, *Fuel Process. Technol.*, 2004, **86**, 33–47.

44. R. U. Kirss and L. Meda, *Appl. Organomet. Chem.*, 1998, **12**, 155–160.

45. B. Yous, S. Robin, A. Donnadieu, G. Dufour, C. Maillot, H. Roulet, and C. Senemaud, *Mater. Res. Bull.*, 1984, **19**, 1349–1354.

46. J. C. Kim and B. K. Kim, *Scr. Mater.*, 2004, **50**, 969–972.

47. M. J. J. Bleda-Martínez, D. Lozano-Castelló, E. Morallón, D. Cazorla-Amorós, and A. Linares-Solano, *Carbon N. Y.*, 2006, **44**, 2642–2651.

4 Synthesis of metal disulphide-graphitised carbon nanofiber hybrid nanomaterials

4.1 Introduction

As discussed in Chapter I the discovery of carbon based fullerenes and nanotubes has inspired the exploration of several other materials including boron nitride, metal dichalcogenides MQ_2 (M=Mo, W, Re, Nb, Hf; Q=S, Se, Te) and metal oxides. All of which in the bulk phase possess a weakly bonded layered structure comparable to the structure of graphite.[1–7] There are also examples where these different layered materials are combined to form hybrid nanomaterials also known as van der Waals heterostructures.[8] The combination of these layered materials is attracting more and more attention as these heterostructures are predicted to provide unique and tuneable physicochemical properties.[9] For example, a memory device was recently fabricated by combining single layers of MoS_2 and graphene on a SiO_2/Si substrate (Figure 4-1).[10]

Consequently, this study will focus on the exploration of synthetic methods which can be used to fabricate the analogous cylindrical hybrid nanomaterials consisting of metal dichalcogenides and graphitised carbon nanofibers (GNF) with the principle goal of forming MQ_2 nanotubes within GNFs (MQ_2@GNFs). Therefore, a variety of methods and molecules were tested as precursors for the

formation of MQ_2@GNFs as described in the following section.

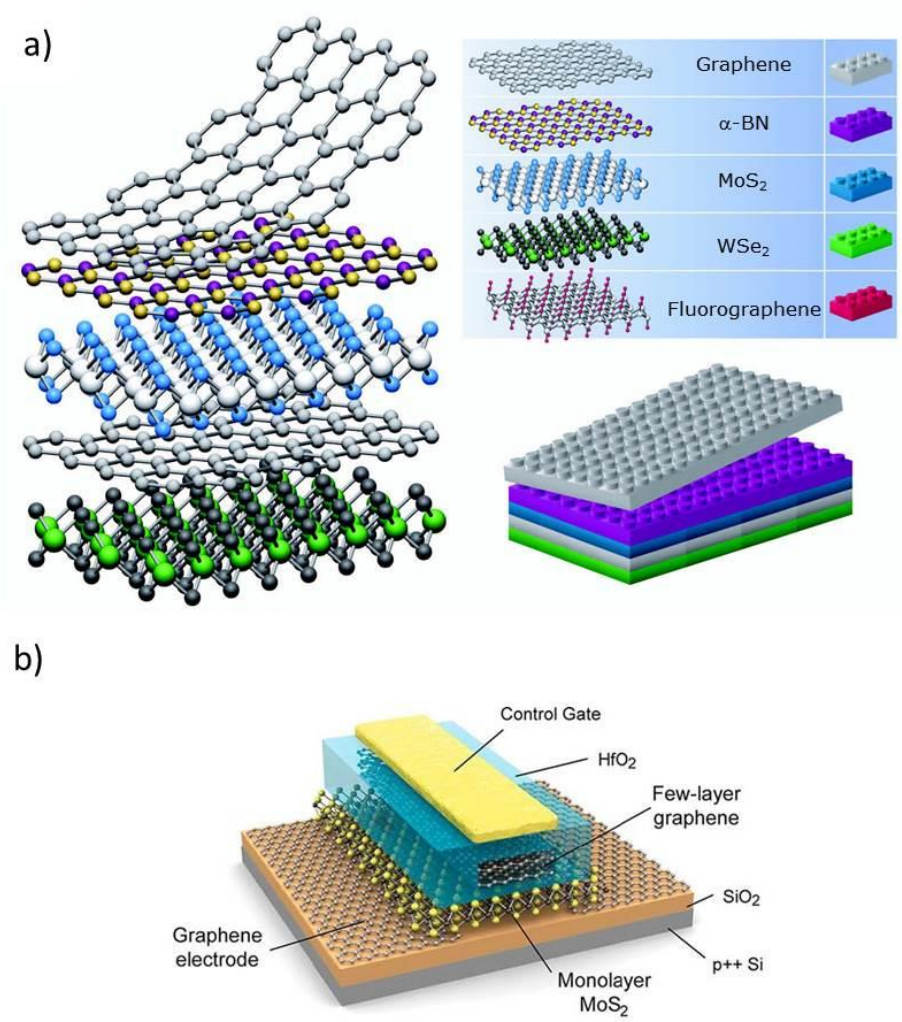


Figure 4-1. a) Illustration of the concept of combining 2D materials as if they were LEGO blocks to build van der Waals heterostructures.[9] b) 3D schematic diagram of a MoS_2/graphene heterostructure based memory device.[10]

4.2 Methods for the synthesis of MoS_2 in GNFs

The synthesis of MS_2 in GNFs (MS_2@GNFs) is a multistep process and was performed in a number of different ways to determine the most successful approach, see Figure 4-2. All methods followed the general route where first, a Mo containing precursor (typically a molecule) was encapsulated into the GNFs from the gas phase (as described in Section 4.6.2) then the resultant material (GNFs containing the Mo precursor) was heated

in a H_2S stream according to Section 4.6.4. H_2S was chosen as the source of sulphur instead of elemental S as the transport of gaseous H_2S through the GNF structures was thought to be much more facile than solid or molten sulphur. In some cases the resultant MoS_2@GNFs was calcined under an Ar atmosphere according to Section 4.6.5 in an effort to improve the crystallinity of the final material.

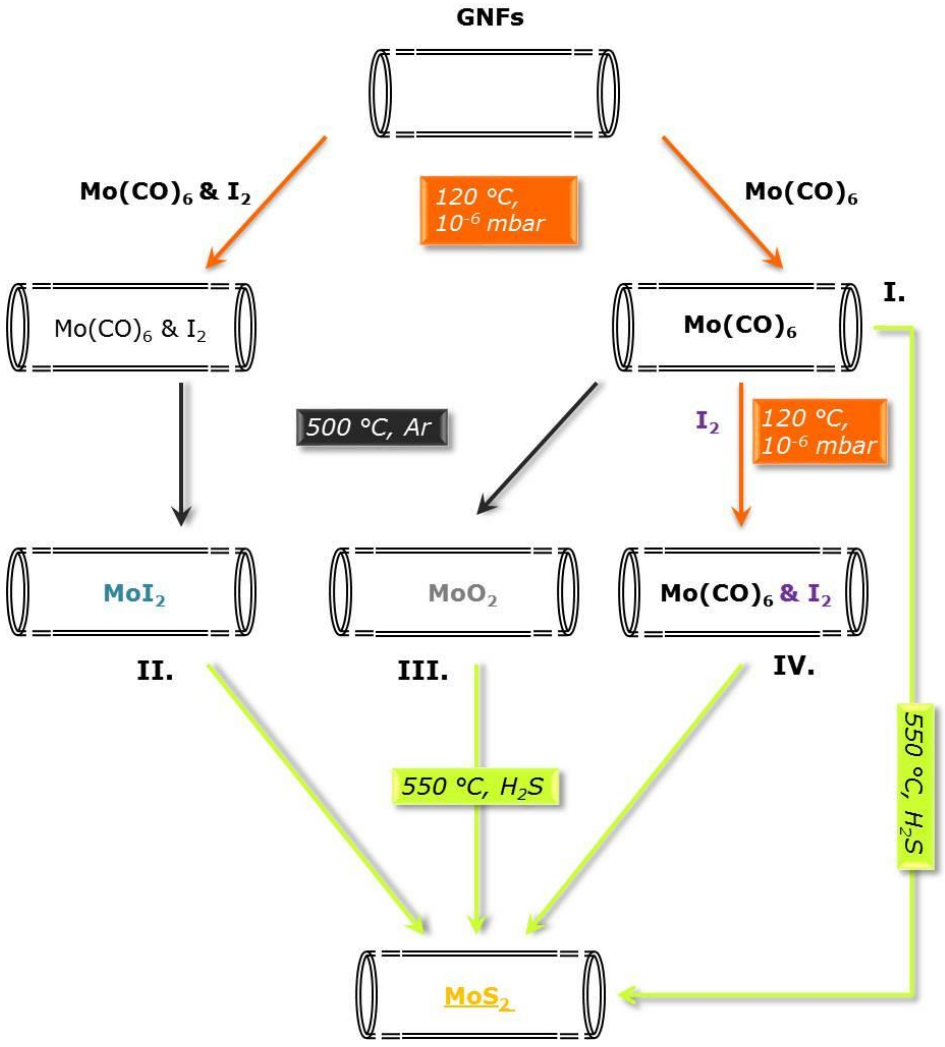


Figure 4-2. Diagram summarising the various synthetic methods utilised to form MoS_2@GNFs. The orange boxes and arrows represent the encapsulation conditions used to insert precursor molecules into GNFs, while the black boxes and arrows correspond to the conversion of given precursor/s inside GNFs. The green boxes and arrows represent the reactions of precursor/s@GNFs (I.-IV.) with H_2S.

4.2.1 Formation of MoS_2@GNFs from $Mo(CO)_6$@GNFs

In the first type of experiment $Mo(CO)_6$ was chosen as a precursor molecule as $M(CO)_6$ (M=Mo, W) and S, Se were utilised successfully by Tremel *et al.* in the preparation of spherical inorganic fullerene (IF) type MoS_2, $MoSe_2$ (5-20 nm) and WS_2 (20-200 nm) nanoparticles by metal-organic chemical vapour deposition (MOCVD) (Figure 25, page 60, Chapter I).[11,12] In our experiment $Mo(CO)_6$@GNF was initially prepared according to Section 4.6.2.2 and was subsequently heated in a H_2S flow to form MoS_2@GNFs as described in Section 4.6.4.

4.2.2 Formation of MoS_2@GNFs from MoO_2@GNFs

In the second type of experiment MoO_2 was chosen as precursor as the transformation of MO_x of Group VI into metal dichalcogenide nanostructures using hydrogen chalcogenides *i.e.* H_2S and H_2Se, has been reported previously.[13,4,14,15] First $Mo(CO)_6$@GNF was prepared and transformed into MoO_2@GNFs under Ar as described in Section 4.6.2.2 and 4.6.3. To produce MoS_2@GNFs the MoO_2@GNFs precursor was heated in a H_2S gas flow as described in Section 4.6.4. The reaction time was increased in comparison to the first type of experiment (Section 4.2.1) as it was shown earlier that the transformation of MoO_x into MoS_2 either requires a high reaction temperature (~800 °C) or a relatively long reaction time.[13,4,15,16]

4.2.3 Formation of MoS_2@GNFs from ($Mo(CO)_6$ and I_2)@GNFs and MoI_2@GNFs

Iodine has been used previously in conjunction with metal containing precursors to aid the formation of MoS_2 nanostructures. Therefore the effect of the presence of I on the synthesis of MoS_2@GNFs was studied in the third and fourth types of experiments.[17,18]

4.2.3.1 Formation of MoS_2@GNFs from MoI_2@GNFs

In the third type of experiment $Mo(CO)_6$ and I_2 were encapsulated into GNFs as described in Section 4.6.2.2 to form ($Mo(CO)_6$ and I_2)@GNFs. The two precursors, *i.e.* $Mo(CO)_6$ and I_2 inside GNFs, were then reacted with each other to form MoI_2@GNFs by heating the material under Ar atmosphere as described in Section 4.6.3. Finally, MoI_2@GNFs was then heated in a H_2S flow as described in Section 4.6.4 to form MoS_2@GNFs.

4.2.3.2 Formation of MoS_2@GNFs from ($Mo(CO)_6$ and I_2)@GNFs

In the fourth type of experiment I_2 was encapsulated into preformed $Mo(CO)_6$@GNFs as described in Section 4.6.2.3 to form ($Mo(CO)_6$ and I_2)@GNFs. The material was then heated directly in a H_2S flow as described in Section 4.6.4 to form MoS_2@GNFs.

4.3 Characterisation of the materials formed by reacting metal precursors encapsulated in GNFs with H_2S

The materials formed in GNFs by reacting the different metal precursors with H_2S were analysed by transmission electron microscopy (TEM), energy dispersive X-ray spectroscopy (EDX) and powder X-ray diffraction (PXRD) as described in Section 4.6.6 and 4.6.7, respectively.

4.3.1 Characterisation of the material formed by reacting $Mo(CO)_6$@GNFs with H_2S

During TEM investigation of the material formed by reacting $Mo(CO)_6$@GNFs with H_2S (Experiment 4-7) multi-layered islands with high TEM contrast were observed on the surface of the GNFs (Figure 4-3). Although, the majority of these layers were located on the outer surface of the GNFs (Figure 4-3 a, b) some of them can be found on the inner surface of the GNFs as well (Figure 4-3 c, d). The layers formed on the inner surface of the GNFs follow the structure of its step-edges as demonstrated in Figure 4-3 c, d. The *d* spacing of the layers observed on or in the GNFs were measured on the TEM micrographs and found to be 0.62 nm suggesting that they consist of MoS_2.[19] In addition, the EDX spectrum of these layers shows characteristic peaks of Mo at 2.3, 17.5 keV and S at 2.3 keV (Figure 4-4) confirming that the layers are MoS_2.

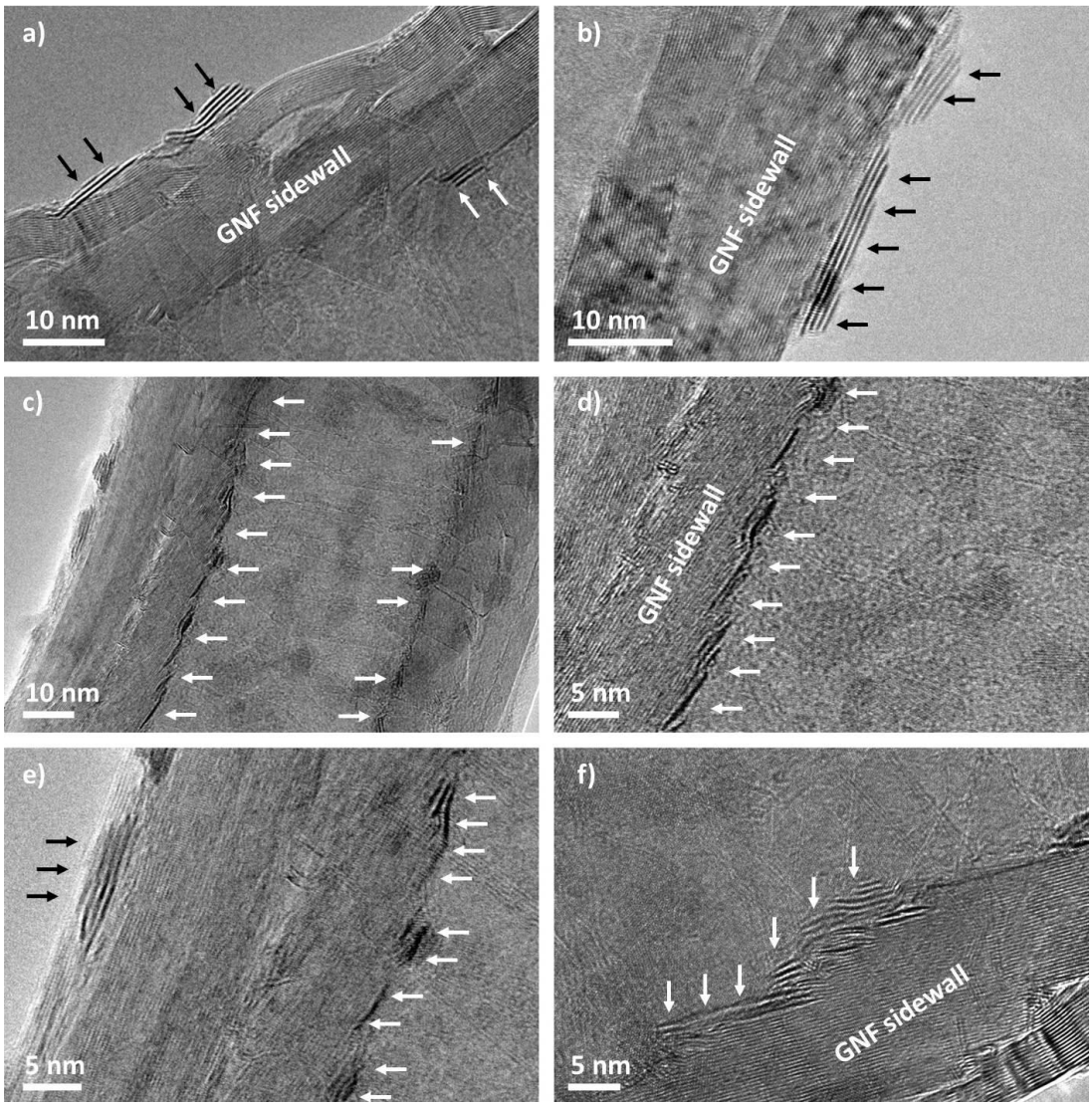


Figure 4-3. TEM images of the material formed by reacting $Mo(CO)_6$@GNFs with H_2S (Experiment 4-7) showing: a)-b) islands of MoS_2 layers on the outer surface of GNFs (black arrows) and c)-d) MoS_2 layers formed in GNFs on their step-edges (white arrows). The interlayer *d* spacing of the MoS_2 formed on GNFs was found to be 0.62 nm.

The chemical composition and crystal structure of the layers formed on the outer surface and inside the GNFs the material was investigated by PXRD. In the recorded diffraction pattern new peaks were observed at 2θ=13.9°; 33.5° and 59.3° (Figure 4-5 b) in addition to the peaks of the GNFs (Figure 4-5 c). Comparison of this diffraction pattern with the calculated PXRD patterns of MoS_2 (Figure 4-5 d) and MoO_2 (Figure 4-5 e) imply that the new peaks

correspond to the 002; 100, 101 and 2-10, 2-12 crystallographic planes of MoS_2. The *d* spacing belonging to the PXRD peak at 14.1° of 0.63 nm and the value of 0.62 nm measured by TEM is within experimental error.

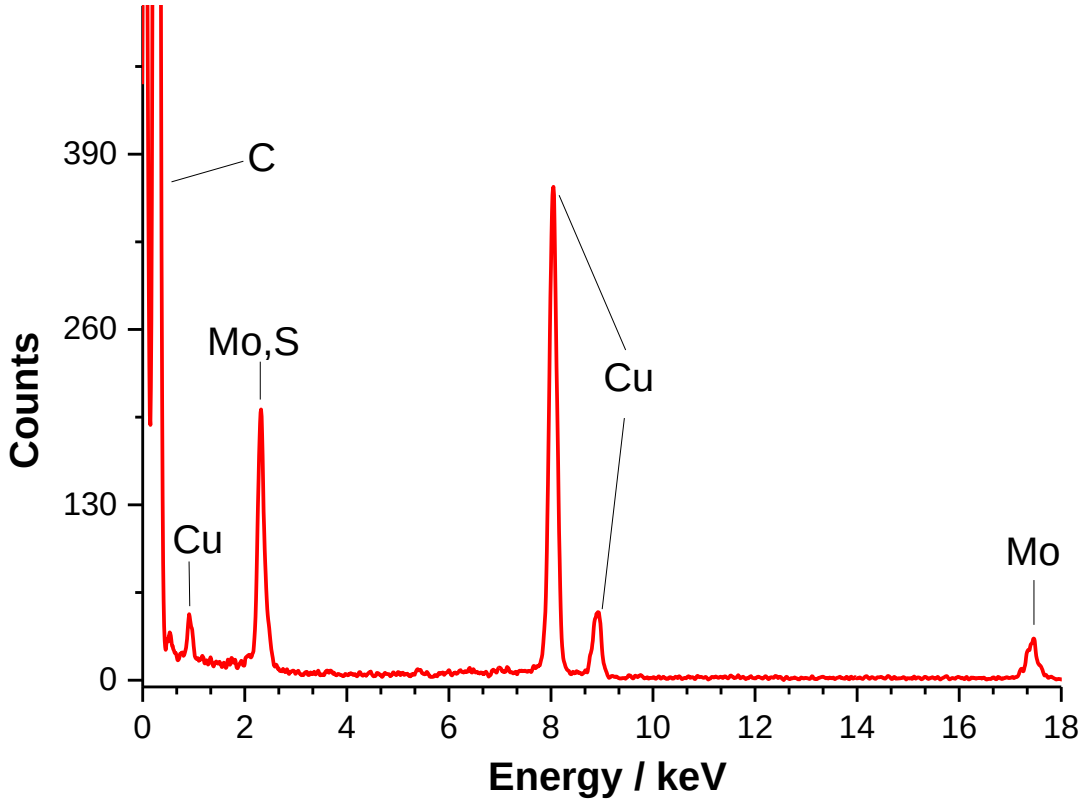


Figure 4-4. EDX spectrum of the material formed by reacting $Mo(CO)_6$@GNFs with H_2S (Experiment 4-7). Characteristic X-ray peaks of Mo and S were identified at 2.3 and 17.5 keV and 2.3 keV, respectively. Cu peaks are due to the specimen holder.

All together these observations confirm that the reaction of $Mo(CO)_6$@GNFs with H_2S (Experiment 4-7) led to the formation of MoS_2@GNFs. The effect of the calcination on MoS_2@GNFs (Experiment 4-11) formed by reacting $Mo(CO)_6$@GNFs with H_2S (Experiment 4-7) was also investigated. TEM analysis of the calcined material showed curved hollow IF-like as well as rectangular solid nanoparticles consisting of several layers of crystalline MoS_2 (Figure 4-6).

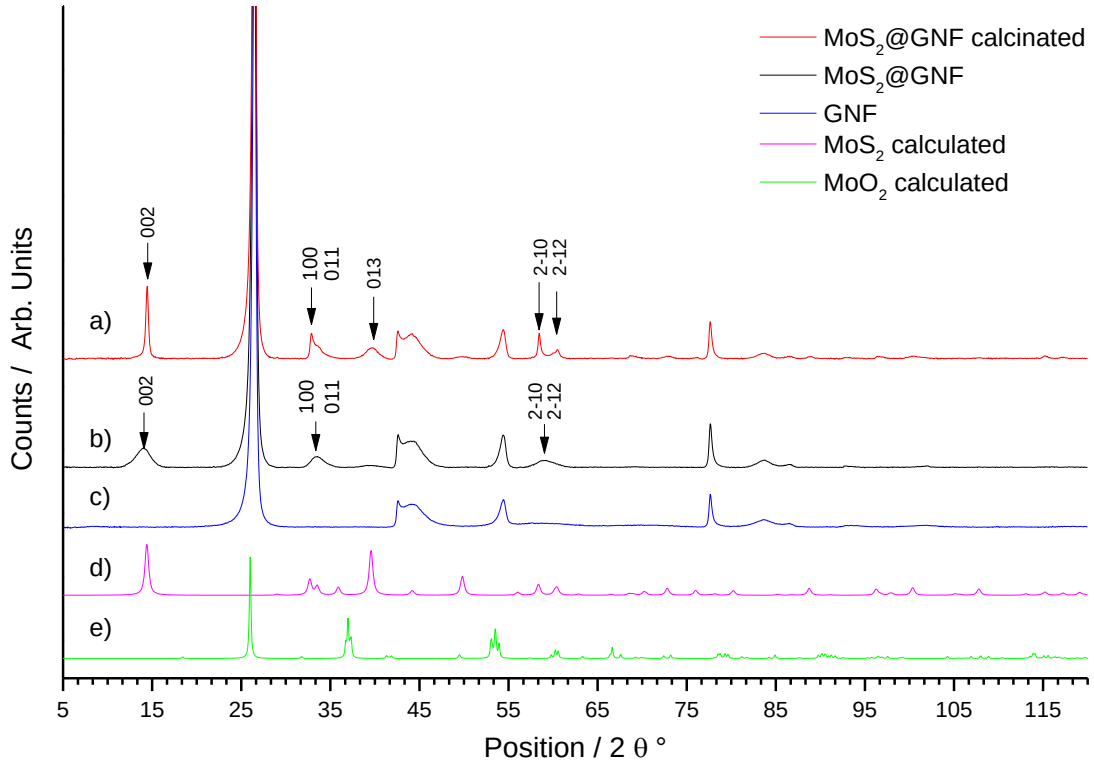


Figure 4-5. PXRD patterns of a) MoS_2@GNF calcined under Ar (Experiment 4-11), b) MoS_2@GNF formed by reacting $Mo(CO)_6$@GNFs with H_2S (Experiment 4-7) and c) pristine GNF. Calculated PXRD patterns of d) MoS_2 and e) MoO_2 are shown for comparison (λ=1.5432 Å).

Some of the IF-like NPs (~30 nm) (Figure 4-6 b) have a structure reminiscent to the previously reported spiral "nano-seashell" of MoS_2 (~4 nm) although their size is quite different.[20,21] Spherical and elongated IF-like structures were also observed in GNFs (Figure 4-6 c). The core of the MoS_2 NPs might be filled with MoO_2 or they might be empty, which cannot be easily distinguished based on the TEM images. However, even if MoS_2 NPs contain MoO_2 it is amorphous as no interlayer *d* spacing can be identified. The interlayer *d* spacing of MoS_2 in the IF-like structures varies from 0.65 nm in flat facets to as high as 0.74 nm at the vertices.

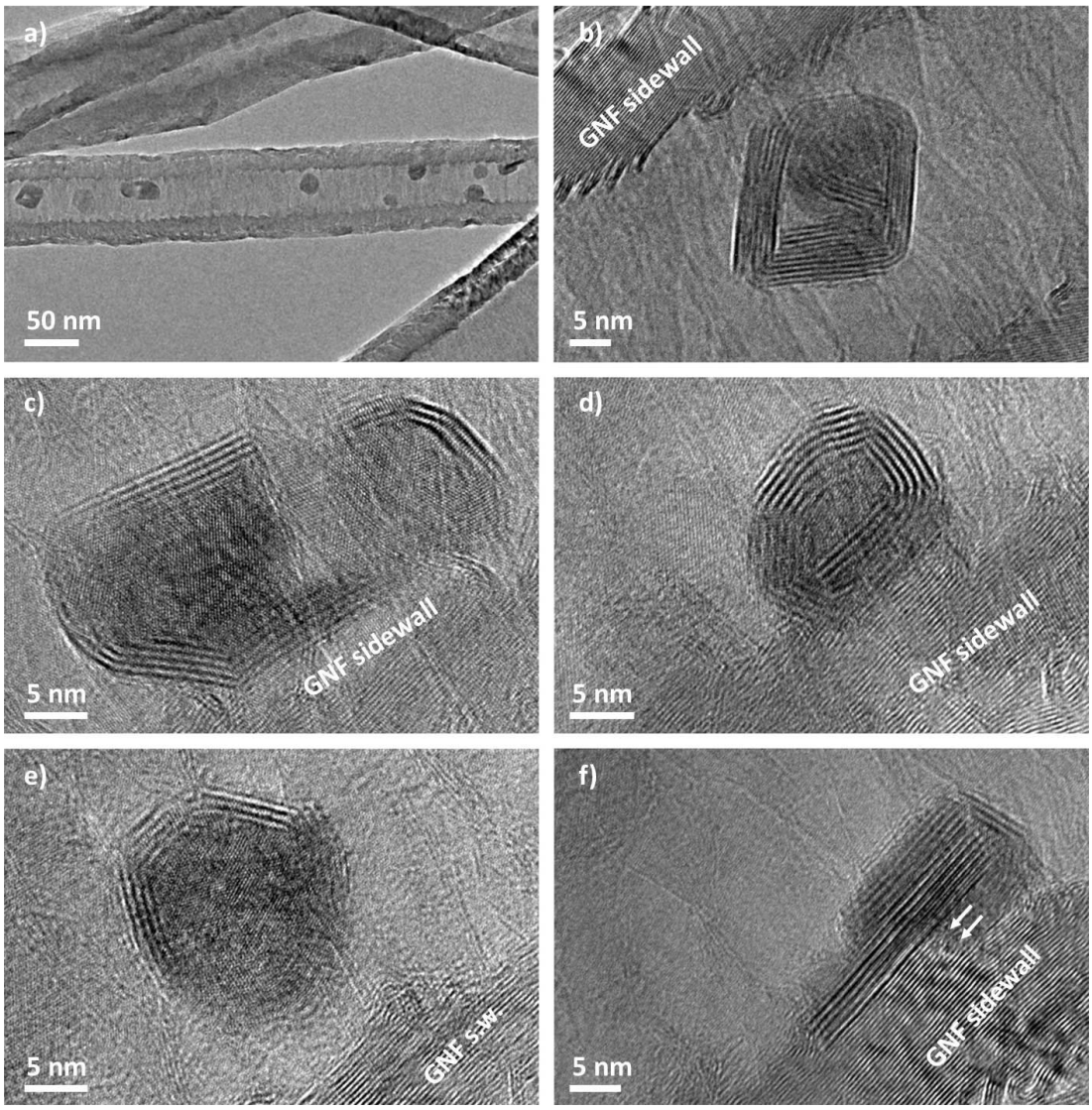


Figure 4-6. TEM images of MoS_2@GNF formed by reacting $Mo(CO)_6$@GNFs with H_2S in Experiment 4-7 then calcined under Ar (Experiment 4-11) showing; a) a GNF containing several MoS_2 NPs, b) a MoS_2 NP (22 nm) that has a structure similar to the previously reported spiral "nano-seashells",[20,21] c) an elongated MoS_2 NP (36 nm) similar to the smaller more spherical particles (~18 nm) shown on image d) and e) (the core of these NPs might be empty or filled with MoO_2), and f) MoS_2 grown on the step-edges of the GNFs, arrows show where the graphitic layers terminate and the MoS_2 layers start. The interlayer *d* spacing of the curved MoS_2 layers shown in images b)-e) was found to be between 0.65-0.74 nm while the flat layers shown in image f) are separated by 0.64 nm.

In addition, a rod like MoS_2 nanostructures are observed to have grown parallel to the graphitic layers of the step-edges of the GNF (Figure 4-6 d). The resultant MoS_2 step-edge is four times higher (~12 nm) than the original graphitic step-edge (~3 nm). The layers of MoS_2 and graphitic layers have complementary

dimensions as the interlayer *d* spacing of MoS_2 layers (0.62 nm) is approximately twice that of the interlayer *d* spacing of the graphitic C layers (0.33 nm).

PXRD investigation of the calcined MoS_2@GNFs showed that the peaks belonging to MoS_2 became sharper and more intense. In addition, the peak corresponding to the 002 plane of MoS_2 shifted from 14.1° (Figure 4-5 b) to 14.5° (Figure 4-5 a) indicating that the average *d* spacing of MoS_2 layers decreased to 0.61 nm. Moreover, after calcination the broad peak at 59.3° (Figure 4-5 b) was replaced by two sharp peaks, 58.5° and 60.5° (Figure 4-5 a) corresponding to 2-10 and 2-12 planes of MoS_2. These observations are consistent with the literature and indicate that the crystallinity of MoS_2@GNFs was improved by calcination.[12]

4.3.2 Characterisation of the material formed by reacting MoO_2@GNFs with H_2S

4.3.2.1 Characterisation of MoO_2@GNFs

PXRD was used to analyse the MoO_2@GNFs precursor formed by the thermal decomposition of $Mo(CO)_6$@GNF under Ar (Experiment 4-5). In the diffraction pattern of MoO_2@GNFs (Figure 4-7 c) new peaks were identified at 2θ=37.1°, 53.0°, 60.4° and 66.8°. Comparison of this diffraction pattern with the calculated PXRD pattern of MoO_2 (Figure 4-7 d) confirmed that the overlapping peaks centred at ~37° and ~54° correspond to the 20-2, 11-2, 020, 002, 200, 111 and to the 21-3, 22-2, 022, 220,

112, 211, crystallographic planes of MoO_2 respectively, indicating that the formation of MoO_2@GNFs was successful.

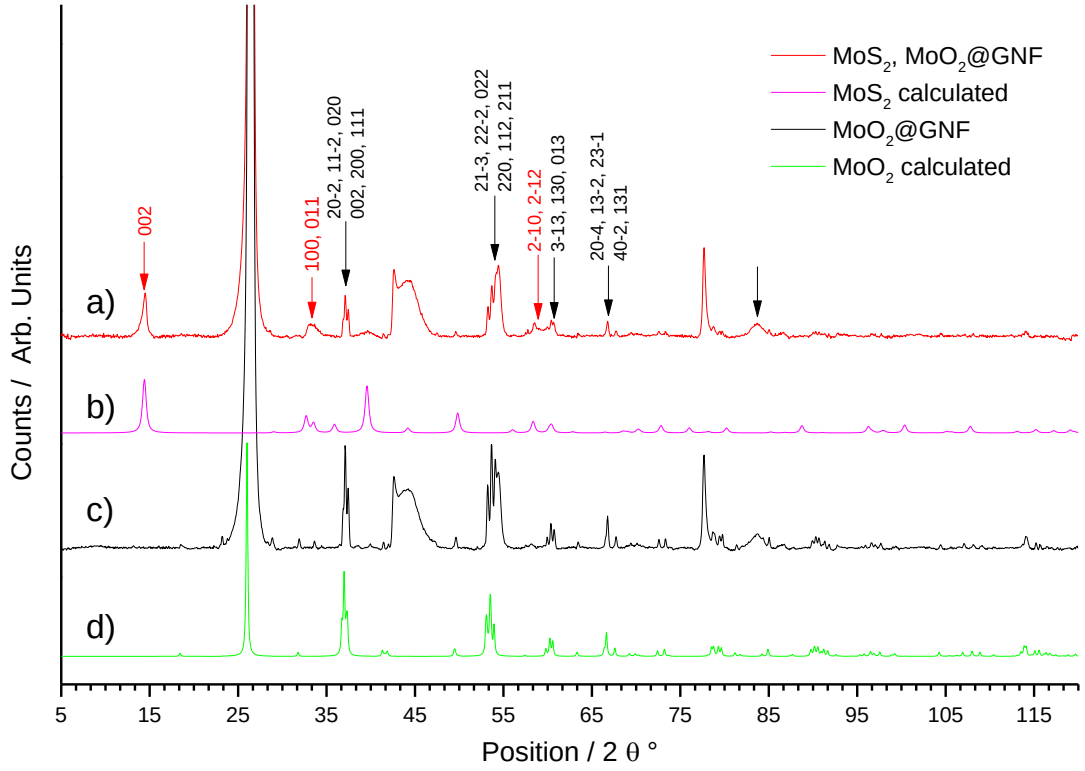


Figure 4-7. PXRD patterns of a) (MoS_2 and MoO_2)@GNF formed by reacting MoO_2@GNF with H_2S (Experiment 4-8), and c) MoO_2@GNF formed by the thermal decomposition of $Mo(CO)_6$@GNF under Ar (Experiment 4-5). The red and black arrows and indices indicate peaks corresponding to MoS_2 and MoO_2, respectively. Calculated PXRD patterns of b) MoS_2 and d) MoO_2 are shown for comparison (λ=1.5432 Å).

4.3.2.2 Characterisation of the material formed by reacting MoO_2@GNFs with H_2S

TEM investigation of MoS_2@GNF made by reacting MoO_2@GNF with H_2S (Experiment 4-8) showed large MoS_2 nanostructures which completely fill the internal channel of the GNFs (internal diameter 44 nm) over the length of 534 nm. Higher magnification TEM images revealed that the MoS_2 nanostructure consists of a network of curved MoS_2 (~10 layers thick) bundles in which the MoS_2 layers are separated by ~0.70 nm on average (Figure

4-8 b, c), but in areas curved at almost 90° the MoS_2 layers reach interlayer *d* spacing up to 0.8 nm. In addition, unreacted MoO_2 crystals were also observed in the channels of the GNFs. The large MoO_2 crystals (*d*=~60 nm, *l*=~100 nm) fill the entire channel of GNFs as shown in Figure 4-8. The *d* spacing of these crystals was found to be 0.35 nm which is consistent with the value (0.35 nm) observed in the case of MoO_2 NPs formed in GNFs (Chapter III) or on graphene oxide.[22]

The GNFs containing the different crystalline materials were analysed by EDX spectroscopy. The spectra of MoS_2@GNFs (Figure 4-9 a) and MoO_2@GNFs (Figure 4-9 b) look very similar to each other as they contain the same signals at 0.5, 2.3 and 17.5 keV of which the 0.5 and 17.5 keV signals confirm the presence of O and Mo in both materials. However, the interpretation of the peak at 2.3 kV is not straight forward as it could also belong to Mo as well as S. To determine whether S has a contribution to the peak at 2.3 kV the ratio of the peaks at 2.3 and 17.5 keV has to be calculated and compared to the ratio calculated from an EDX spectrum in which exclusively Mo contributes to the peak at 2.3 keV. In the case of the GNF, which based on TEM contains only MoO_2, this ratio is ~4 while in the case of GNF that contains MoS_2 (Figure 4-9 a) it is ~10 which confirms the presence of S in the latter material. Moreover, after unifying the intensity of the EDX spectra of MoS_2@GNFs and MoO_2@GNFs using the Mo

peak at 17.5 keV as a reference there is a clear difference in intensity of the peaks at 2.3 and 0.5 kV indicating the higher O content in MoO_2@GNFs (Figure 4-9).

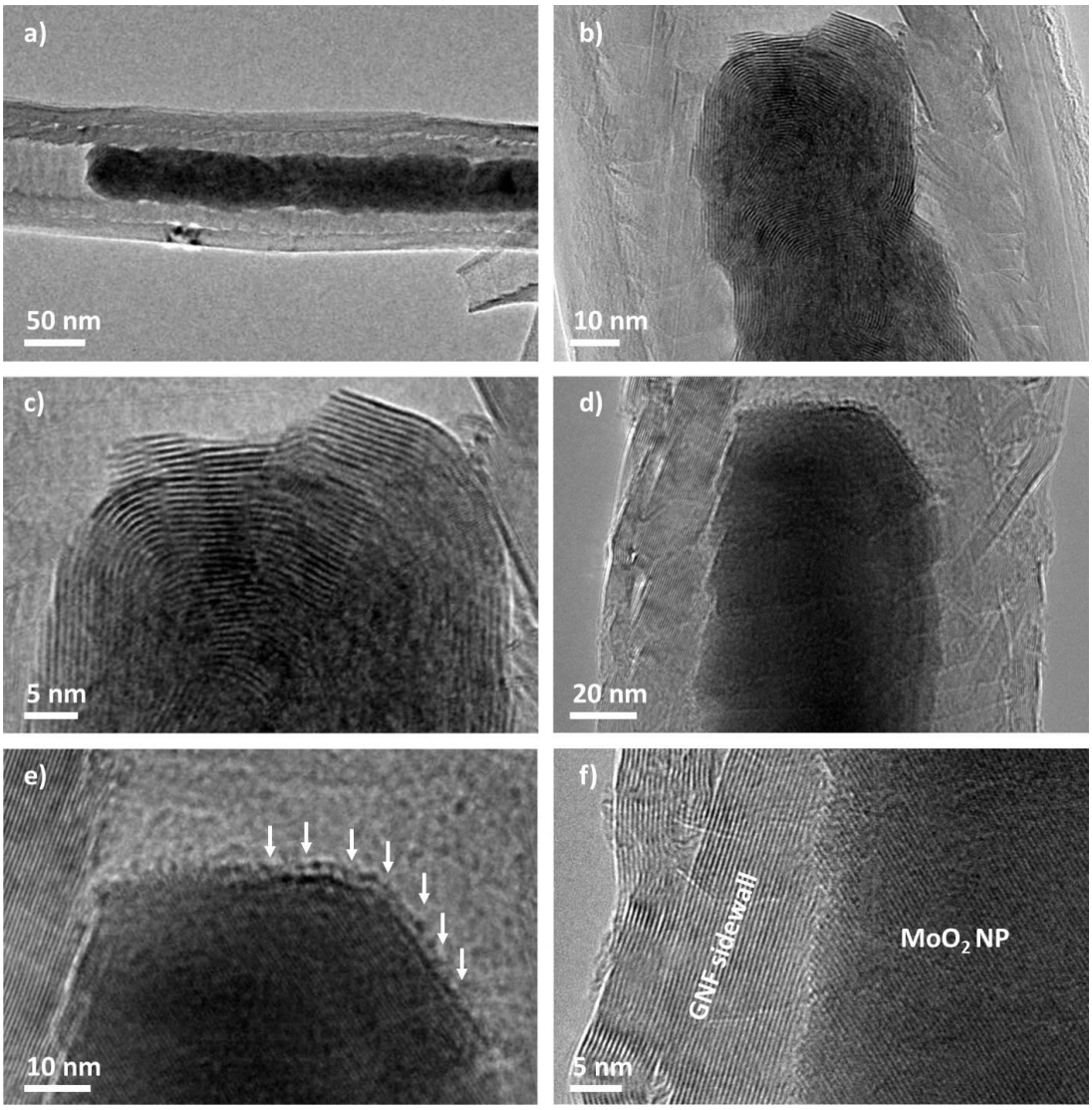


Figure 4-8. TEM images of the material formed by reacting MoO_2@GNFs with H_2S (Experiment 4-8) showing: a) a large, approximately 500 nm long and 44 nm wide MoS_2 nanostructure in a GNF that has b) concentric interpenetrating MoS_2 fringes in which c) the interlayer distances reach 0.7 nm. TEM images show d) a large MoO_2 particle in GNF which seems to have S layers on its tip marked by arrows in image e) and f) its crystallographic planes are separated by 0.35 nm which is consistent with MoO_2.

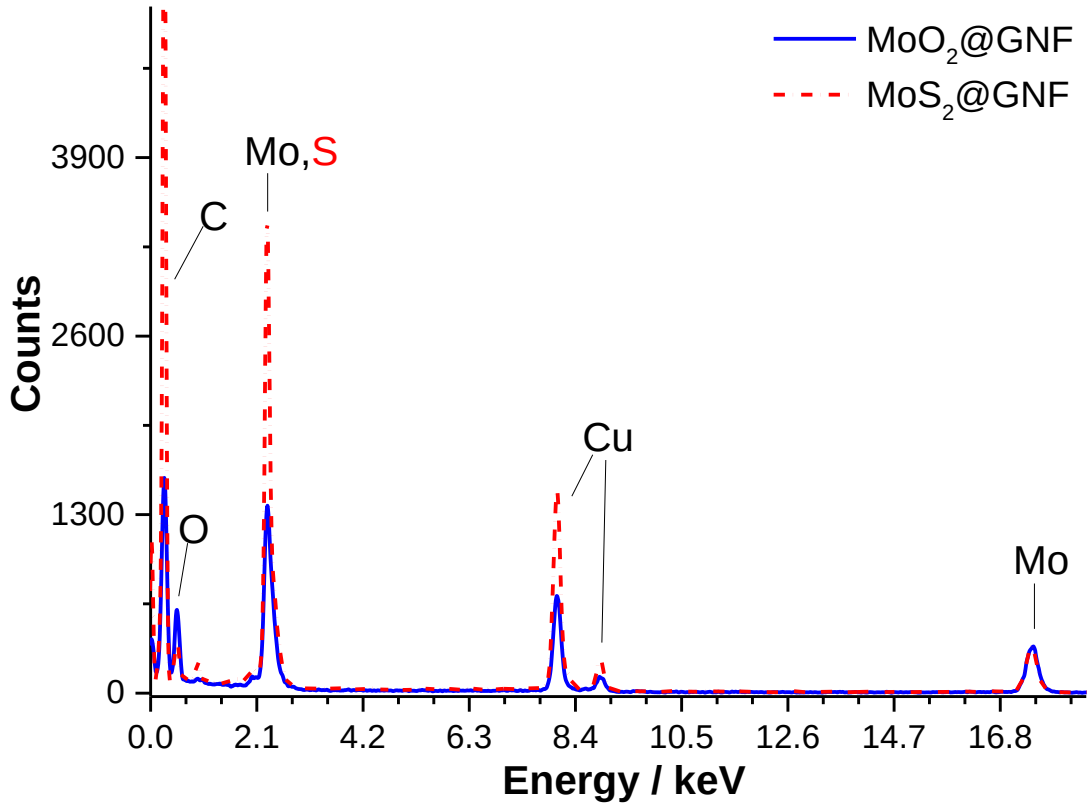


Figure 4-9. EDX spectra of (red, dash dot) the MoS_2 nanostructure formed in Experiment 4-8 and (blue, solid) the unreacted MoO_2 nanoparticle which can be seen in Figure 4-8, images a)-c) and d)-f), respectively. The low ratio of the peaks at 2.3 and 17.5 kV in spectra b) (blue, solid) clearly indicates that only an infinitesimally small amount of S might be present in or on the surface of the unreacted MoO_2 particles. Cu peaks are due to the specimen holder.

The diffraction pattern of the material formed in the reaction of MoO_2@GNFs with H_2S (Experiment 4-8) contains new peaks at 2θ=14.6°, 33.3° and 58.6° (marked with red arrows) which belong to the 002; 100, 101 and 2-10, 2-12 crystallographic planes of MoS_2 in addition to the peaks belonging to MoO_2 (marked with black arrows). This suggests that the transformation of MoO_2@GNFs into MoS_2@GNFs was only partially successful. In summary, PXRD confirmed the formation of MoO_2@GNFs precursors and suggests that the conversion of MoO_2@GNFs into MoS_2@GNFs was only partial. The presence of residual MoO_2 in

GNFs was verified by the TEM and EDX analysis of the material which indicated that the conversion of MoO_2@GNFs into MoS_2@GNFs was not complete.

4.3.3 Characterisation of MoI_2@GNFs and the MoS_2@GNFs formed by the reaction of MoI_2@GNFs with H_2S

4.3.3.1 Characterisation of MoI_2@GNFs

TEM investigation of MoI_2@GNFs (prepared in Experiment 4-6) showed large crystals in the GNFs filling the entire cross section of the channels (Figure 4-10 a, c).

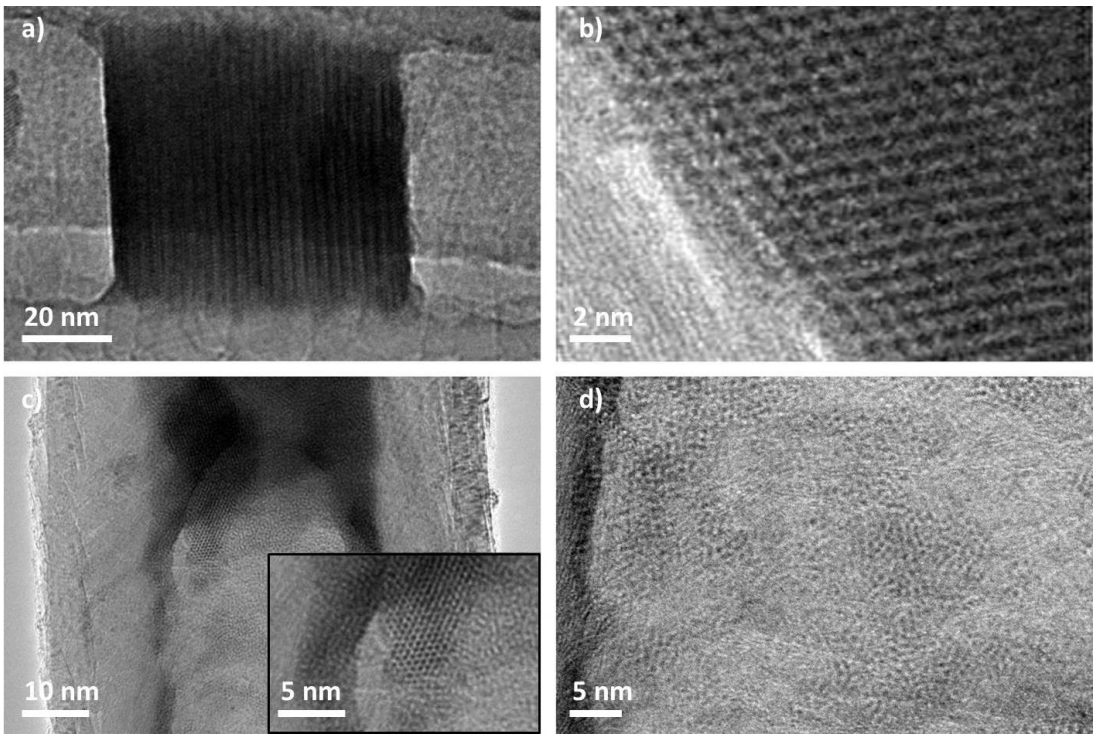


Figure 4-10. TEM images of MoI_2@GNFs formed in Experiment 4-6 showing dark spots which correspond to $[Mo_6I^i_8]I^a_2I^{a\text{-}a}_{4/2}$ clusters which build up MoI_2 crystals. The diameter of the spots is approximately 0.7 nm which can be assigned to the $Mo_6I^i_8$ core of the clusters.

High magnification images revealed that the crystals consist of spherical units (Figure 4-10 c, d), which have a diameter of 0.7 nm, and their centres were found to be 0.8-0.9 nm apart. EDX

spectroscopy showed characteristic peaks of Mo and I at 2.3, 17.5 and 3.9 keV confirming their presence within the crystals observed in GNFs (Figure 4-11).

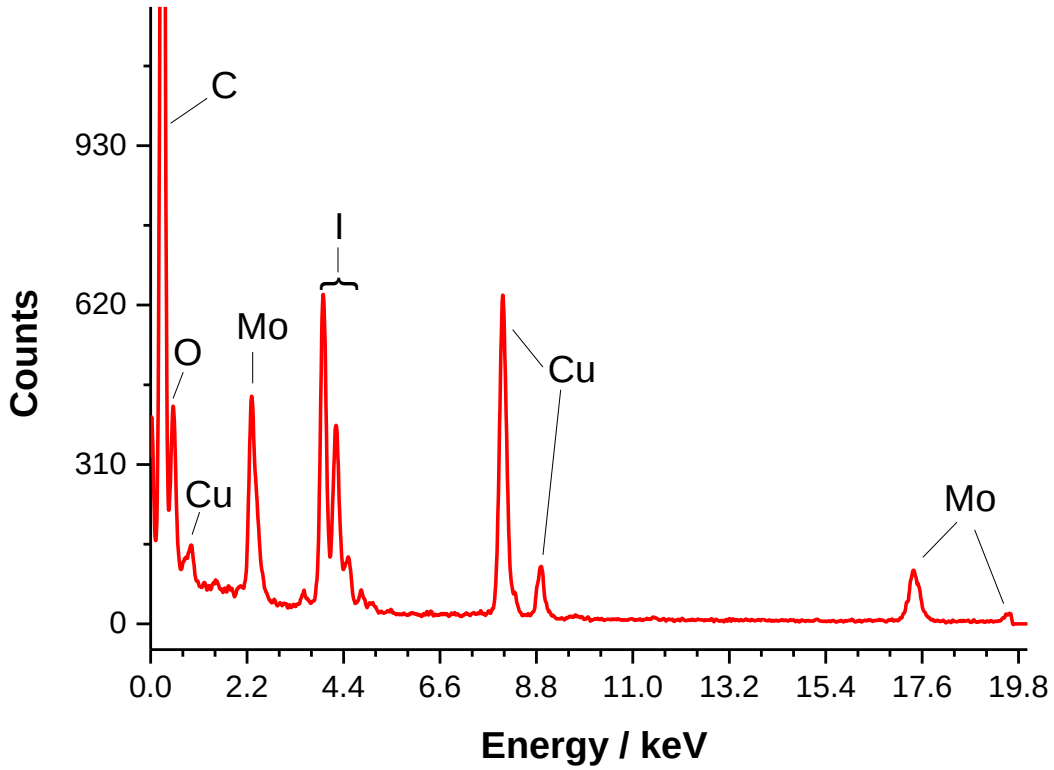


Figure 4-11. EDX spectrum of MoI_2 crystal observed in MoI_2@GNF formed in Experiment 4-6. Characteristic X-ray peaks of Mo at 2.3, 17.5 keV and I 3.9 keV were identified. Cu peaks are due to the specimen holder.

It is known that bulk MoI_2 possesses a layered structure in which each layer is built from interconnected clusters consisting of octahedral Mo cores surrounded by two type of I atoms.[23] Every face of an Mo_6 octahedron is capped with so-called internal μ^3 I^i atom and each Mo atom is bonded to an axial I^a atom resulting in a $[Mo_6I^i_8I^a_6]$ cluster. In the MoI_2 crystal each $[Mo_6I^i_8I^a_6]$ unit is interconnected with four other units by shared I^a atoms (I^{a-a}) resulting in layers of $[Mo_6I^i_8I^a_2I^{a-a}{}_{4/2}]$ (Figure 4-12) with an overall Mo:I ratio of 1:2.[23]

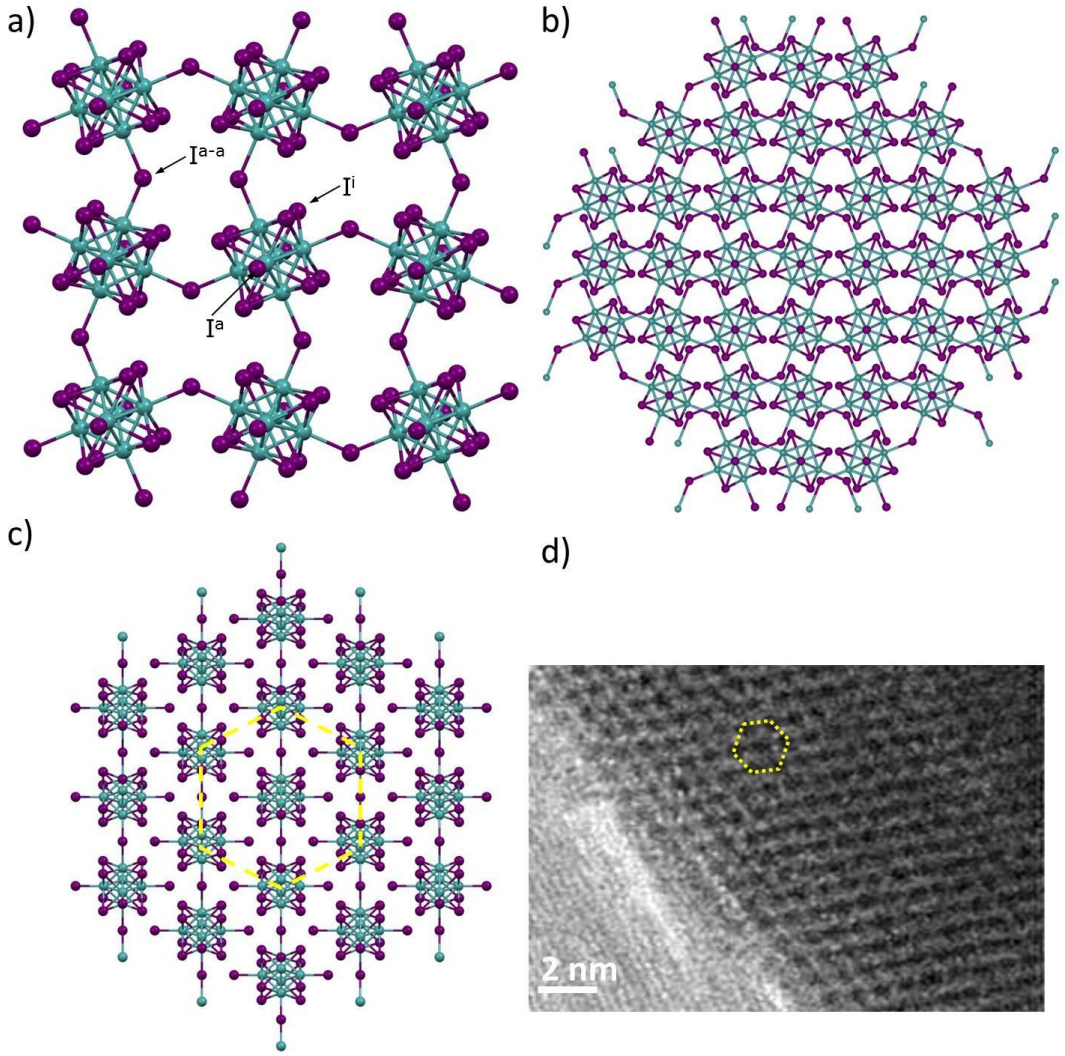


Figure 4-12. Images show: a) $[Mo_6I^i_8]I^a_2I^{a-a}_{4/2}$ octahedral hexanuclear Mo clusters which have 8 μ^3 face capping I^i atoms and 6 terminal I^a atoms from which 4 I^{a-a} atoms are shared with the neighbouring clusters resulting in layers with a global Mo:I ratio of 1:2; MoI_2 layers on top of each other looked b) from the direction of I^a atoms. Image c) and d) show the structural model and TEM image of MoI_2 layers looked parallel with the layers and perpendicular to the direction of I^a atoms with yellow hexagons highlighting a typical structural motif. The green and magenta colours represent Mo and I atoms, respectively.[23]

The comparison of the diameter (0.7 nm) and distance (0.8-0.9) nm of the dark spots (Figure 4-12 f) to the diameter (0.7 nm) of the clusters and to their distance (0.9 nm) in the MoI_2 crystal (Figure 4-12 a-d) suggests that the spots represent the $[Mo_6I^i_8I^a_6]$ units of MoI_2.[23]

The formation of MoI_2@GNF from ($Mo(CO)_6$ and I_2)@GNFs

(Experiment 4-6) was also investigated by PXRD. Comparison of the recorded pattern (Figure 4-13 a) and the calculated XRD pattern of MoI_2 (Figure 4-13 b) confirmed the successful formation of MoI_2@GNF, moreover, indicated that no MoO_2 contamination is present in GNFs.

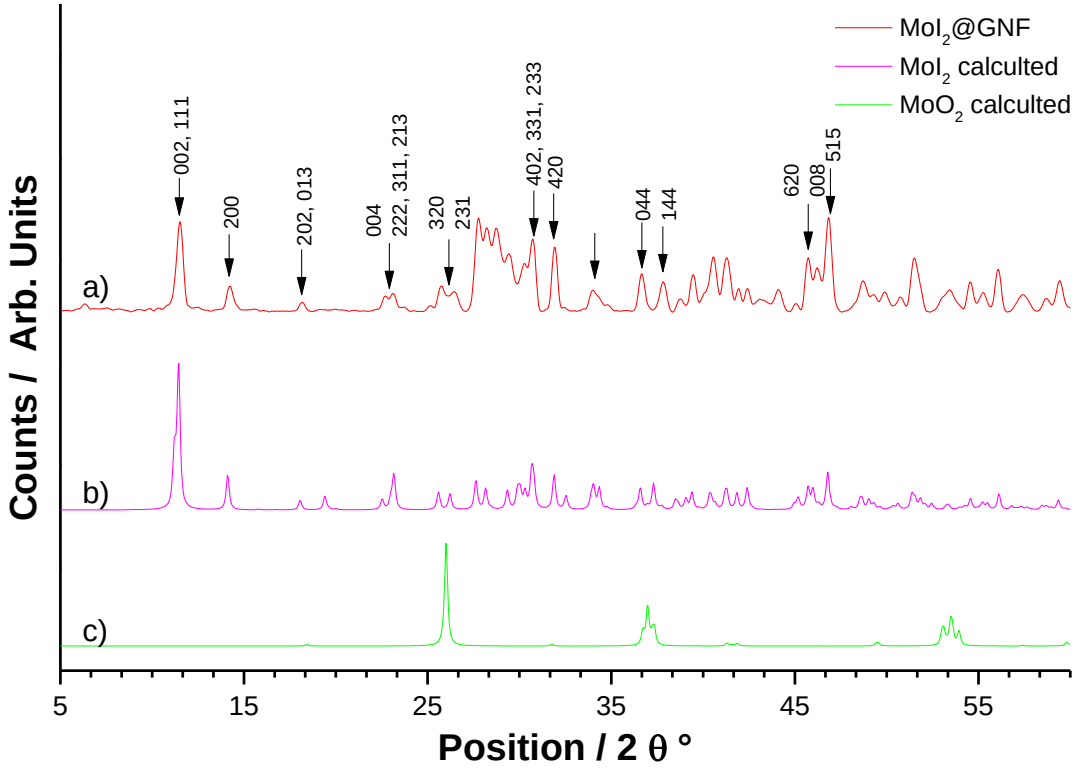


Figure 4-13. PXRD pattern of a) MoI_2@GNF formed by heating ($Mo(CO)_6$ and I_2)@GNFs under Ar (Experiment 4-8). Calculated PXRD patterns of b) MoI_2 are c) MoO_2 are shown for comparison (λ=1.5432 Å). The arrows indicate those peaks which can be unambiguously assigned to MoI_2.

4.3.3.2 Characterisation of the material formed by reacting MoI_2@GNFs with H_2S

TEM investigation of the material formed in the reaction of MoI_2@GNF and H_2S (Experiment 4-9) revealed layered MoS_2 structures inside GNFs (Figure 4-14). Some of the MoS_2 filaments appear to grow perpendicular to the sidewalls of the GNFs creating barriers in the internal channel of GNFs in a similar fashion to what

was observed in the case of the so-called bamboo structured multi-walled carbon nanotubes.[24]

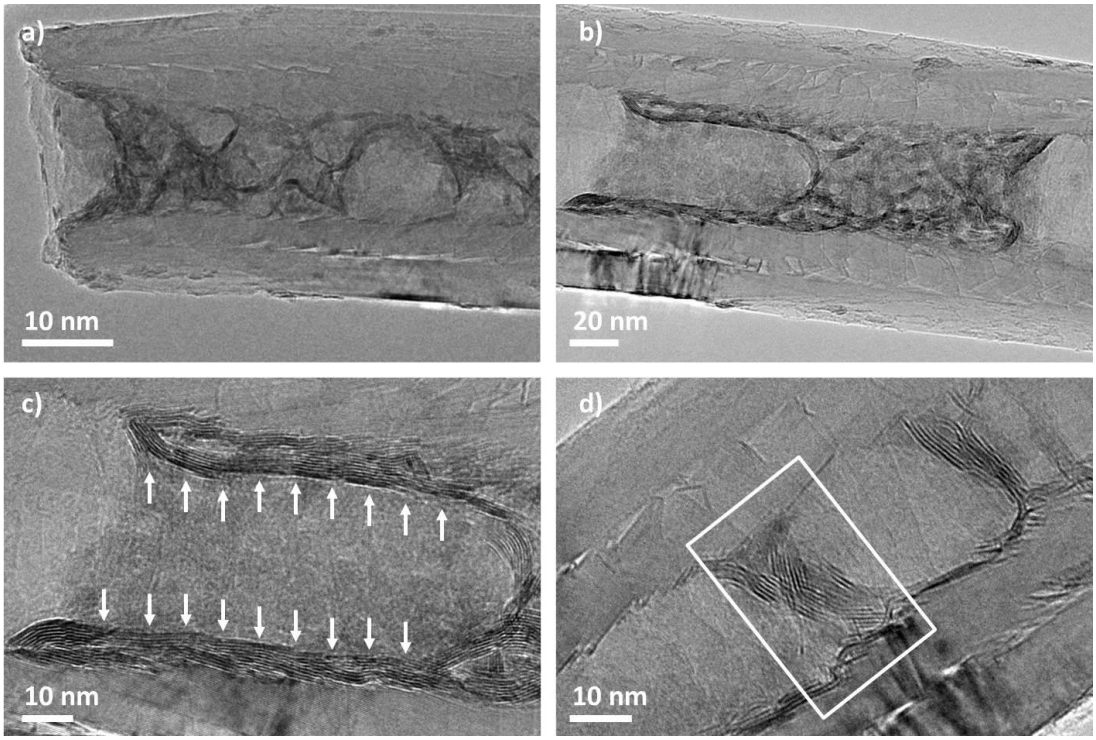


Figure 4-14. TEM images of the material formed by reacting MoI_2@GNFs with H_2S in Experiment 4-9 showing: a) curved interpenetrating layers of MoS_2 in GNF, b)-c) relatively short tubular MoS_2 structure which follows the wall of the GNF highlighted with arrows on image c), d) MoS_2 pillars or presumably membranes grown from one side of the GNF (highlighted with a box) to the other possibly converting it into a bamboo type of structure.

Also an example of a MoS_2 nano test tube (d=33 nm, l=80 nm) was observed in GNF, see Figure 4-14 c. The d spacing of the MoS_2 layers observed in GNFs was found to be between 0.65-0.71 nm. EDX analysis of the material showed characteristic peaks of Mo at 2.3, 17.5 keV, S at 2.3 keV and I at 3.9 keV indicating their presence in the material (Figure 4-15). This means that although the conversion of MoI_2@GNFs to MoS_2@GNFs was successful a small amount of I is still present in the material.

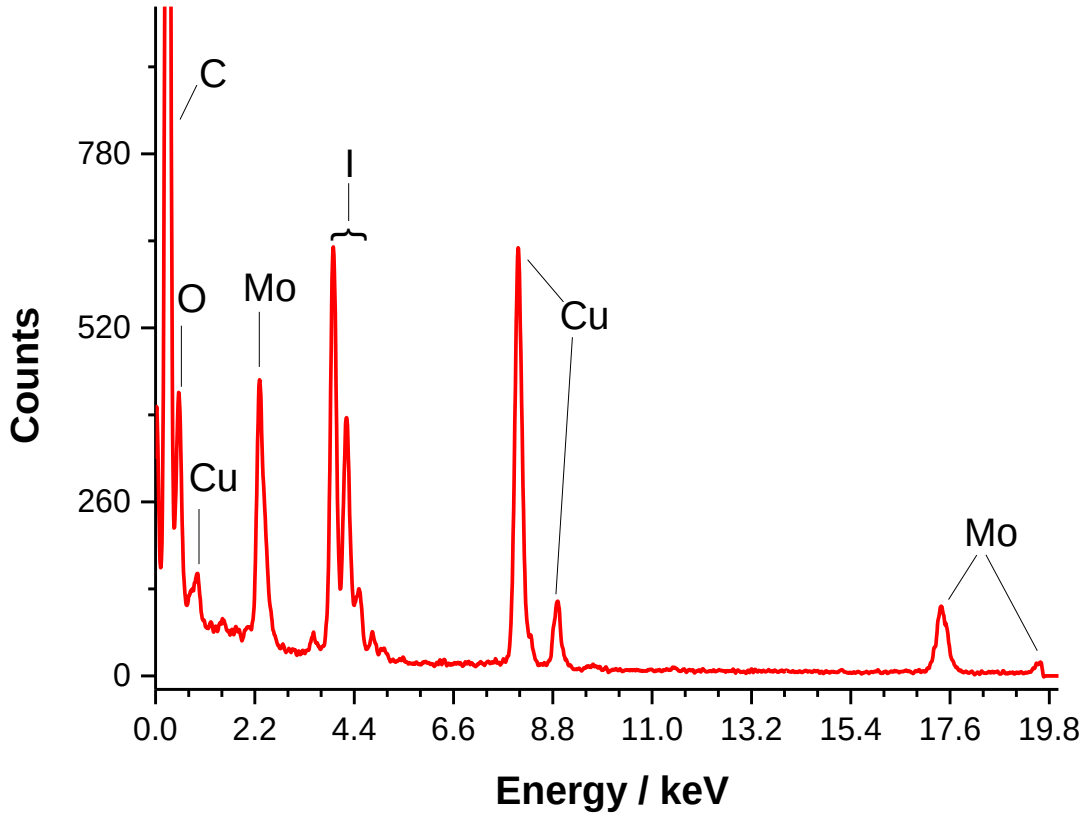


Figure 4-15. EDX spectrum of MoS_2@GNF formed in Experiment 4-9. Characteristic X-ray peaks of Mo at 2.3, 17.5 keV, S 2.3 keV and I 3.9 keV were identified. The copper peaks are due to the specimen holder.

4.3.4 Characterisation of ($Mo(CO)_6$ and I_2)@GNFs and the MoS_2@GNFs formed by reacting it with H_2S

4.3.4.1 Characterisation of ($Mo(CO)_6$ and I_2)@GNFs

TEM investigation of the material formed by the sequential encapsulation of $Mo(CO)_6$ and I_2 in GNFs (prepared in Experiment 4-2) showed that the inner and outer surface of GNFs is covered with amorphous material (Figure 4-16). This material consists of aggregated small NPs (~1 nm) which have presumably formed from $Mo(CO)_6$ molecules by decomposition due to the knock on damage of the e-beam as discussed in Chapters II and III. In addition to Mo the amorphous material possibly contains I as well. EDX spectroscopy showed characteristic

peaks of Mo and I at 2.3, 17.5 and 3.9 keV, respectively confirming their presence in the material (Figure 4-17). These observations confirm that $Mo(CO)_6$ and I_2 are both present in GNFs and form an intimate mixture *i.e.* the formation of MoI_2 was avoided during the preparation of the precursor.

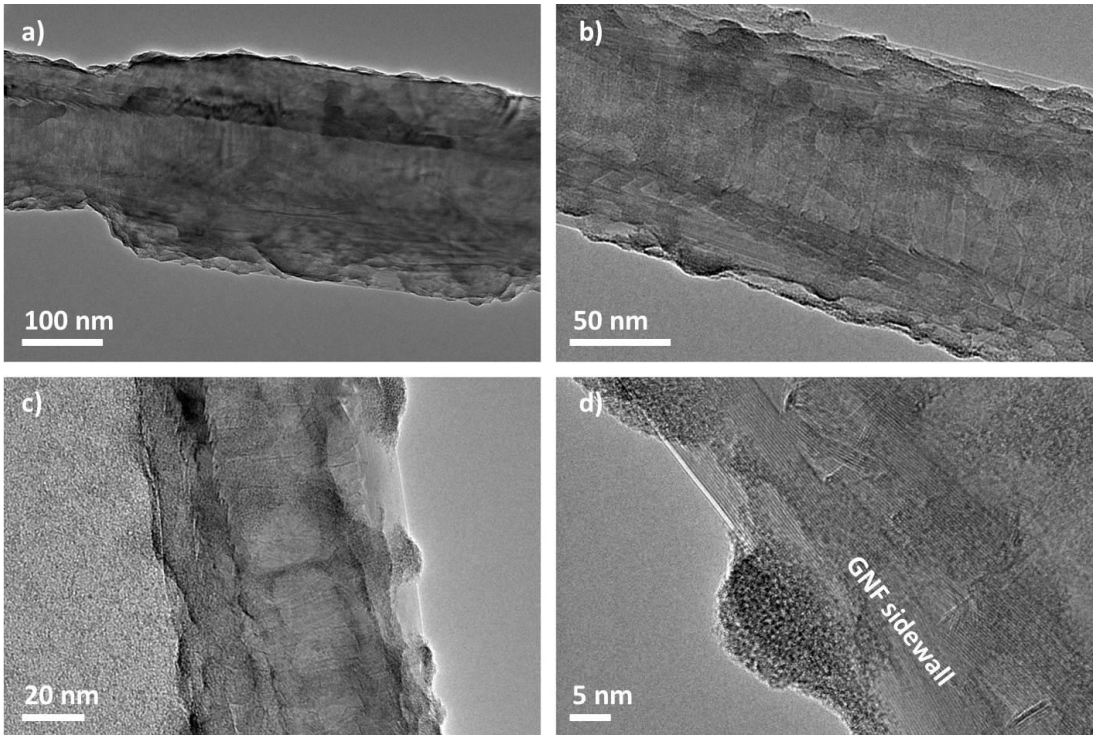


Figure 4-16. TEM images show ($Mo(CO)_6$ and I_2)@GNFs prepared in Experiment 4-2. Image a) and b) show that both the inner and outer surface of GNFs are covered with an amorphous material. Image c) and d) show that the material consists of aggregates of Mo NPs (~1 nm) presumably mixed with residual I.

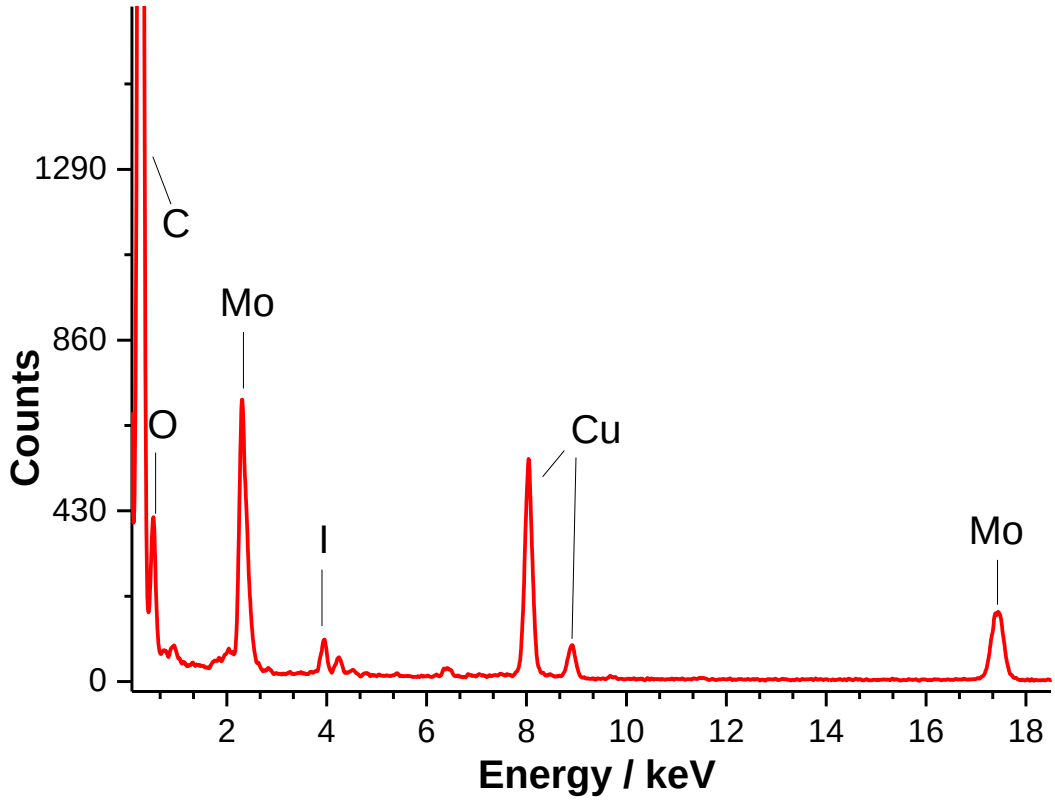


Figure 4-17. EDX spectrum of ($Mo(CO)_6$ and I_2)@GNFs prepared in Experiment 4-2. Characteristic X-ray peaks of Mo at 2.3, 17.5 keV and I 3.9 keV were identified. Cu peaks are due to the specimen holder.

4.3.4.2 Characterisation of the material formed by reacting ($Mo(CO)_6$ and I_2)@GNFs with H_2S

TEM analysis of the material formed by the reaction of ($Mo(CO)_6$ and I_2)@GNFs (prepared in Experiment 4-2) and H_2S (according to Experiment 4-10) showed multiple layers (~4-8) of MoS_2 located on the inner wall of the GNFs (Figure 4-18). The layers of MoS_2 cover the step-edges of the GNFs and create a smoother internal surface. A few examples of MoS_2 layers diverging from the sidewalls of the GNFs and creating IF-like structures fused into each other were also observed. The *d* spacing of the MoS_2 layers was ~0.7 nm and the separation from the graphitic carbon layer ~0.5 nm.

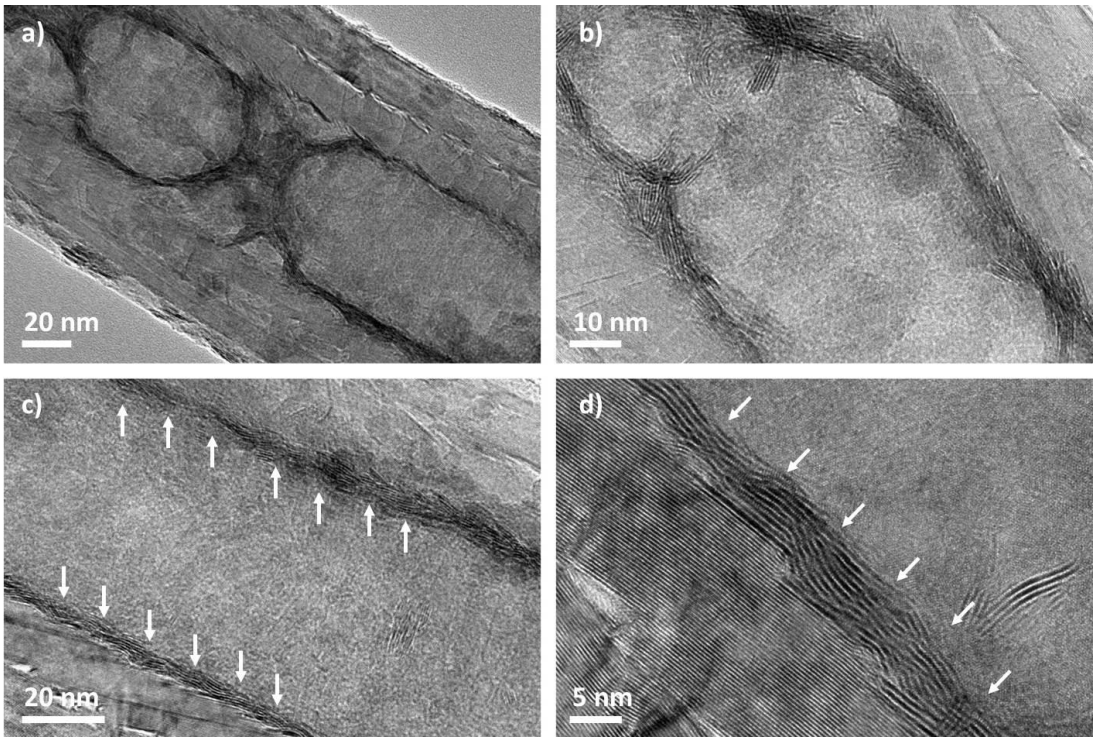


Figure 4-18. TEM images of the material formed by reacting ($Mo(CO)_6$ and I_2) with H_2S in Experiment 4-10 showing: a) tubular MoS_2 structure lining the internal channel of GNF, b) fringes curving away from the surface of GNFs, c)-d) parallel dark contrast in the GNF highlighted with arrows corresponding to MoS_2 layers attached to the inner wall of GNFs.

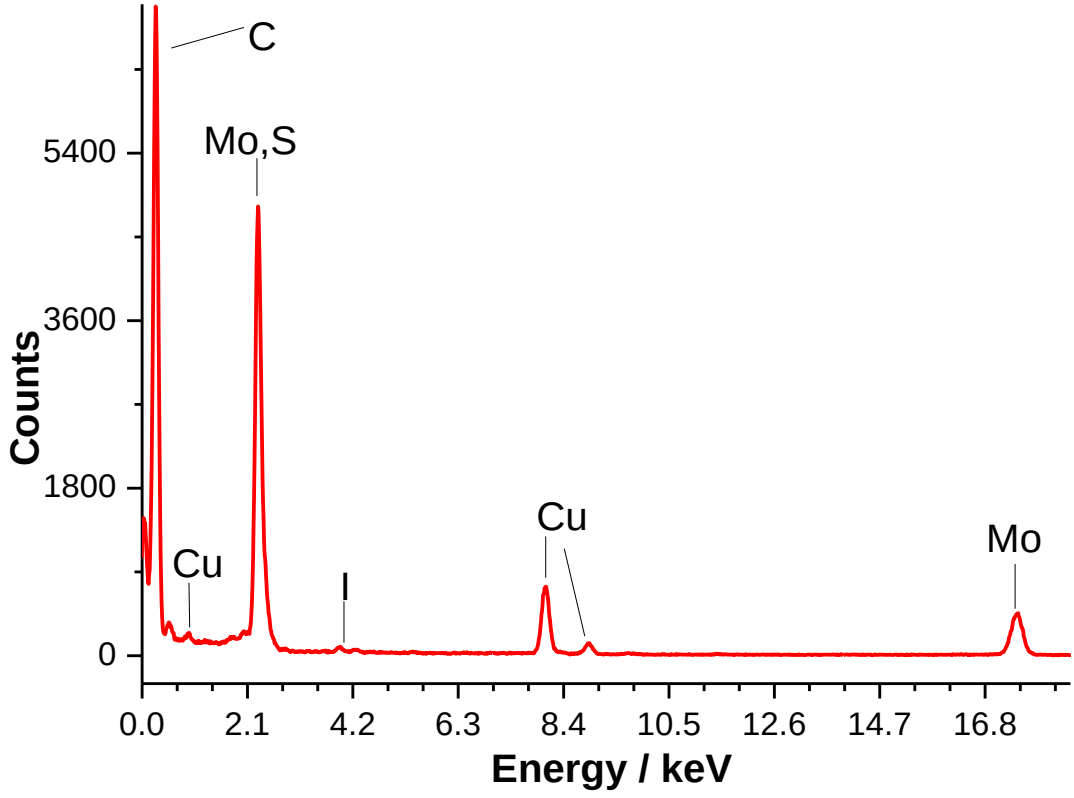


Figure 4-19. EDX spectrum of MoS_2@GNF formed in Experiment 4-10. Characteristic X-ray peaks of Mo at 2.3, 17.5 keV, S 2.3 keV and I 3.9 keV were identified. Cu peaks are due to the specimen holder.

In the EDX spectrum of the material the characteristic peaks of Mo at 2.3, 17.5 keV, S 2.3 keV and I 3.9 keV were identified suggesting that the conversion of ($Mo(CO)_6$ and I_2)@GNFs to MoS_2@GNFs was successful, however traces of I are present (Figure 4-19).

PXRD investigation of the material showed new peaks at 2θ=14.2°, 33.3°, 39.6°, 58.8° in addition to the GNF peaks (Figure 4-20 b). Although these peaks are relatively broad they can be assigned to the 002; 100, 101; 103 and 2-10, 2-12 crystallographic planes of MoS_2, based on earlier studies where I was used as a transport agent (as described in Section 4.4.4) and the calculated PXRD pattern of MoS_2 (Figure 4-20 c).[25]

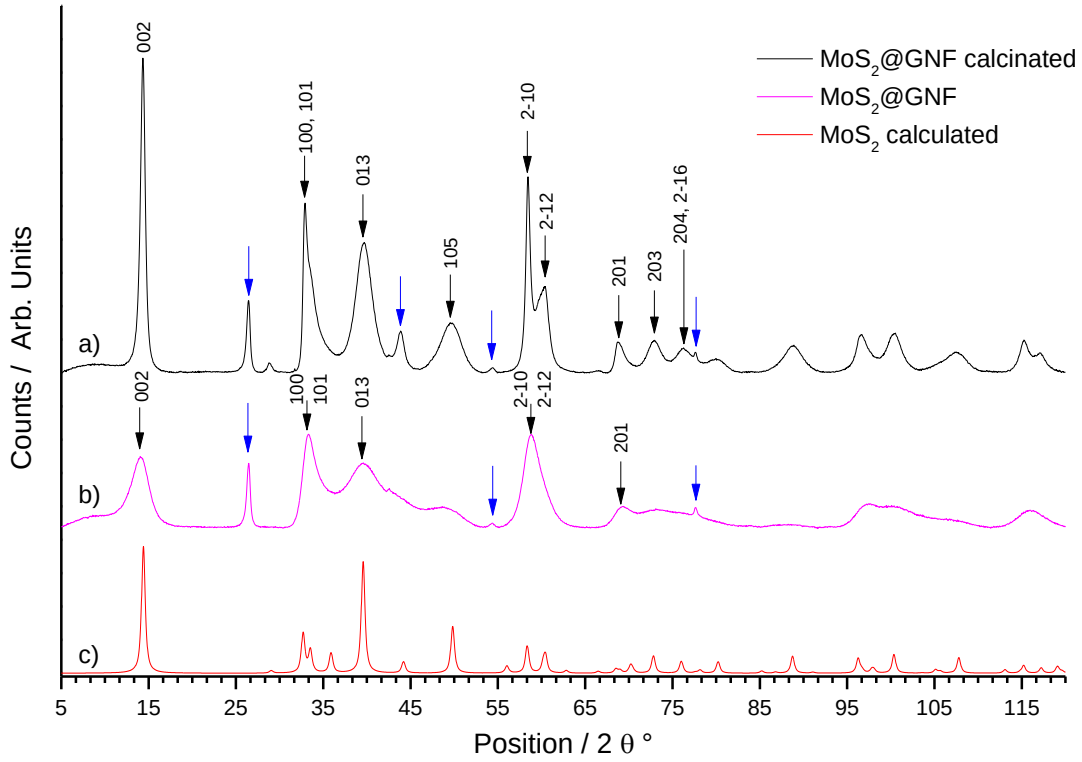


Figure 4-20. The PXRD patterns of the MoS_2@GNF composite a) after and b) prior to calcination. The calculated pattern of c) MoS_2 is shown for comparison (λ=1.5432 Å). The peaks related to pristine GNF are marked with blue arrows.

The interlayer *d* spacing which corresponds to the 14.2° peak *i.e.* the 002 planes of MoS_2 was calculated to be 0.62 nm. Due to the calcination (Experiment 4-12) of MoS_2@GNF the peaks corresponding to the 002; 100, 101 and 103 crystallographic planes of MoS_2 became sharper and shifted to 2θ=14.3°, 33.0°, 39.7°, moreover additional peaks corresponding to MoS_2 appeared at 2θ=49.6°, 58.4°, 60.3°, 68.8°, 73.0° and 76.2° (Figure 4-20 a). After calcination the interlayer *d* spacing belonging to the 14.3° peak equates to a separation of 0.62 nm.

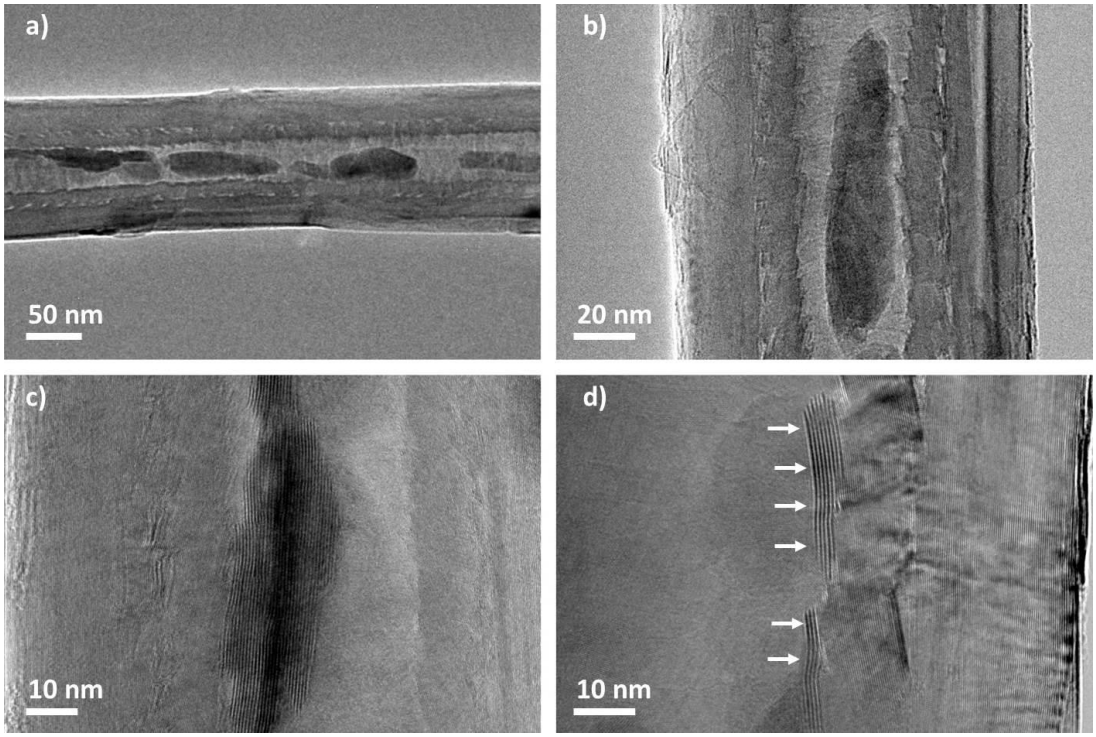


Figure 4-21. TEM micrographs of the material formed by the reaction of ($Mo(CO)_6$ and I_2)@GNFs (prepared in Experiment 4-2) and H_2S (according to Experiment 4-10) then calcined under Ar (Experiment 4-12). TEM images show: a) a large MoS_2 particle length: 100 nm, width: 20 nm, b) a crystalline MoS_2 particle, c) layers of MoS_2 following the curvature on the inner surface of the GNF and d) MoS_2 layers on the step-edges of the GNF parallel to the graphitic layers highlighted with arrows.

TEM investigation of the material showed that most of the MoS_2 layers which were situated on the sidewalls of the GNFs have been

transformed into large elongated MoS_2 particles (length: 100 nm, width: 20 nm) during calcination (Figure 4-21 a and b). However, examples of MoS_2 layers attached to the inner surface of the GNFs were observed as well (Figure 4-21 c and d). The *d* spacing of the layers in the particles is 0.62 nm, while in the layers attached to the sidewalls of the GNF is between 0.60-0.64 nm.

4.4 Analysis of the mechanism of MoS_2 formation in GNFs

4.4.1 Formation of MoS_2@GNFs from $Mo(CO)_6$@GNFs

As shown above the reaction of $Mo(CO)_6$@GNFs and H_2S successfully produced multi-layered MoS_2 islands on the step-edges of GNFs (Figure 4-3). The isolated nature and relatively small lateral size of the layers (4-10 nm, equivalent to 1-2 step-edges) and the appearance of MoS_2 on the outer surface of GNFs suggest that during the initial phase of the procedure $Mo(CO)_6$ molecules may have been vaporised and left the GNFs before they could react with the H_2S. This was most likely due to the temperature of the reaction environment not being high enough to promote the decomposition of the $Mo(CO)_6$ molecules fully which was shown to be a key element during the formation of MQ_2 from $M(CO)_6$.[11,12] Those $Mo(CO)_6$ molecules which remained encapsulated in GNFs may have decomposed in the gas phase and turned into small MoS_2 nuclei by reacting with H_2S. These MoS_2 nuclei then adsorbed at the step-edges of the GNFs and promoted

the growth of MoS_2 layers until the Mo source was depleted.

The absence of IFs and other curved MoS_2 structures and the measured interlayer d spacing (0.62 nm) identical to bulk MoS_2 suggest that the conditions of the chemical reaction in GNFs were close to the thermodynamic equilibrium which resulted in the formation of short flat MoS_2 layers similar to bulk MoS_2.[12,19] Such short 2D MoS_2 flakes considered to be metastable due to the large number of dangling bonds present at the termini of the layers.[19] Indeed, high temperature calcination of the material resulted in IF-like MoS_2 structures which probably formed from the flat MoS_2 layers by folding over. This is in agreement with previous observations which conclude that high temperature can promote the formation of curved structures from 2D layered materials including metal dichalcogenides by providing the activation energy of the process.[8,12,19] The *d* spacing of the MoS_2 layers in the case of curved structures is increased due to lattice expansion caused by the curvature of the MoS_2 sheets as shown previously.[8,11,12]

4.4.2 Formation of MoS_2@GNFs from MoO_2@GNFs

The transformation of MoO_2@GNFs into MoS_2@GNFs was demonstrated to be possible as it was shown above (Figure 4-8 a-c). The mechanism of the chemical transformation may be similar to the thoroughly studied mechanism of MO_3 (M=Mo, W) sulphidisation.[16] This assumption is based on the fact that during the aforementioned sulphidisation H_2 was added to the gas mixture

leading to the reduction of the MO_3 to MO_{3-x} and MO_2. Based on this mechanism the conversion of MoO_2 particles located in GNFs starts with the formation of a few layer thick MoS_2 coat initiated by the replacement of O atoms with S. The conversion of the remaining metal oxide part may happen by a growth mechanism propagating from the surface of the particle towards the core of it resulting in incomplete MoS_2 spheres (Figure 4-22 a).[26] In the case of the large MoO_2 particles observed in GNFs there might be multi grains of layered material which could explain the formation of the interpenetrating network of ~10 layer thick MoS_2 fringes observed in GNFs by TEM (Figure 4-8 b, c).

As shown above the conversion of MoO_2 into MoS_2 was not 100 % efficient meaning that only some of the MoO_2 NPs were completely transformed into MoS_2 NPs while others stayed intact (Figure 4-22 b). The most likely reason for this is that some sections of the internal channel of the GNFs were blocked by the large MoO_2 NPs which act as plugs preventing H_2S molecules from reaching the rest of the encapsulated MoO_2 NPs and reacting with them. The use of extended reaction times still resulted in incomplete conversion which supports this hypothesis.

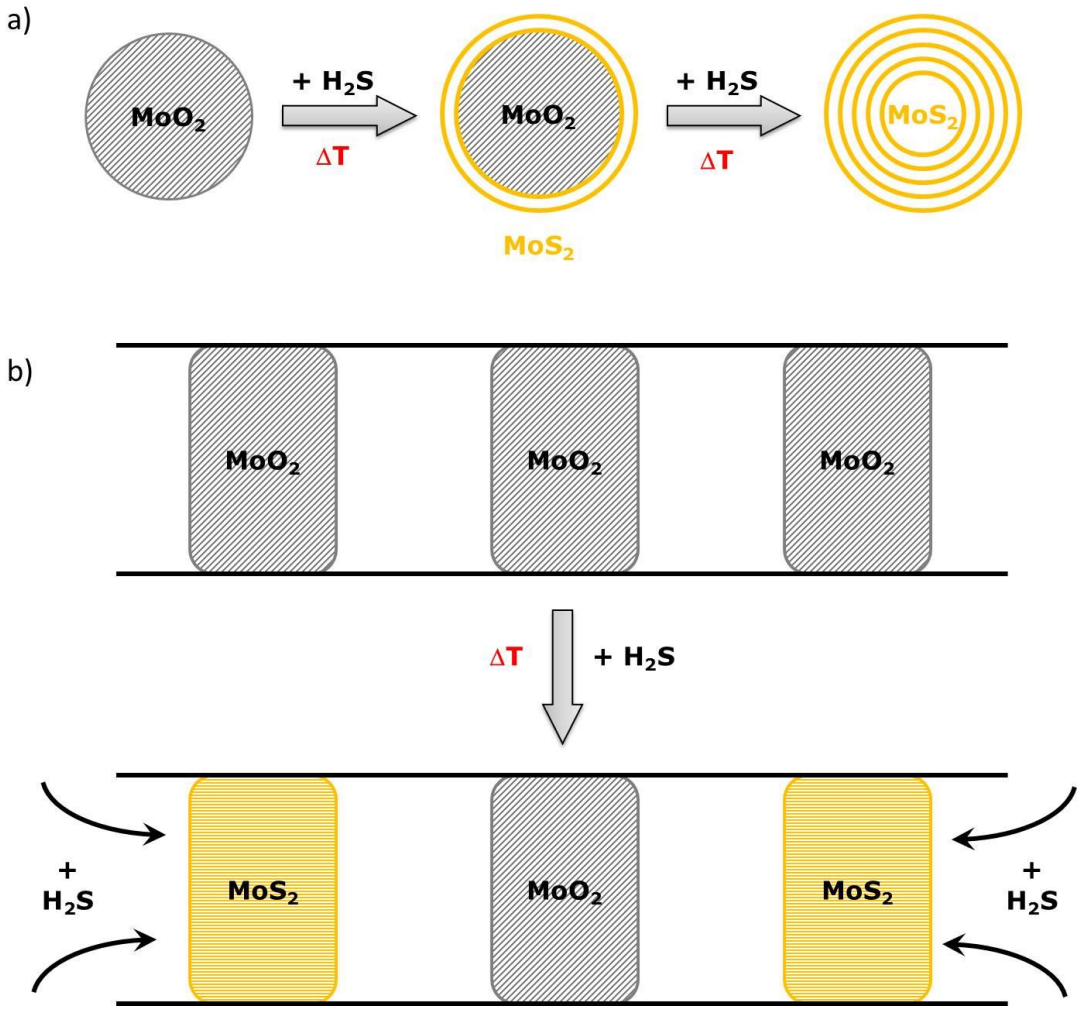


Figure 4-22. a) Schematic representation of the proposed mechanism by which MoO_2 particles transform into IF-like MoS_2 particles. First, initiated by the replacement of O atoms with S, a few layer thick MoS_2 coat grows on the surface of the MoO_2 particle, then the remaining metal oxide core is converted into MoS_2. b) Schematic representation of how MoO_2 plugs the GNF *i.e.* the large MoO_2 particles can block the transport of H_2S in the internal channel of the GNFs thus preventing the complete transformation of inner MoO_2 particles.

4.4.3 Formation of MoS_2@GNFs from MoI_2@GNFs

It was shown above that MoI_2 forms large crystals in GNFs which consist of spherical subunits and span across the whole internal channel of the GNFs (Figure 4-10). The spherical objects were identified as the $[Mo_6I^i_8]I^a_2I^{a\text{-}a}_{4/2}$ building units of bulk MoI_2. This structural motif is considered to play a key role in the

mechanism of the conversion of MoI_2@GNFs into MoS_2@GNFs as several hexanuclear Mo compounds are known such as $[M_6X^i_{8-n}Q^i_n]$ (Q=Se, Te; X=Br, I), $Mo_6S_6X_2$, $Mo_6S_3Br_6$ in which the halogen and chalcogen ligands coexist. The unusual stoichiometry and number of ligands (less than 14) in mixed chalcogenide halides (chalcohalides) is a result of the axial as well as internal ligands (defined in Figure 4-12) shared between two Mo_6 octahedral units *i.e.* they become μ_2 bridging ligands. Metal chalcohaildes with two *i.e.* $[M_6X^i_8]L^a_2L^{a\text{-}a}_{2/2}$, four *i.e.* $[M_6X_8]L^a_2L^{a\text{-}a}_{4/2}$ such as MoI_2 and even six bridging ligands *i.e.* $[M_6X_8]L^a_2L^{a\text{-}a}_{6/2}$ (L=X and/or Q) have been synthesised by various methods.[23,27] Some of these methods involve the substitution of the different kind of anions *i.e.* halogenide or chalcogenide to achieve metal chalcohalides using high temperature solid state reactions.[23,27] It was found that preferential replacement of either internal or the axial ligands is possible; although axial ligands are more labile, therefore they can be replaced easier than the internal ones.[23,27] It was also demonstrated that the thermal decomposition of trinuclear Mo chalcohalides such as $Mo_3Q_7X_4$ terminates at the binary chalcogenide of the metal *i.e.* MoS_2 *etc*. *in vacuo* or inert atmosphere and it has a stepwise nature in hydrogen atmosphere.[27] Consequently, during the synthesis of MoS_2 from MoI_2 the chalcohalides of Mo may be formed as intermediate compounds.[27,28]

Based on the above described information the formation of the MoS_2 nanostructures shown above (Figure 4-14) is very likely to be based on the stepwise substitution of the halogen atoms of MoI_2 *i.e.* $[Mo_6I^i_8]I^a_{2+4/2}$ with S resulting in $[Mo_6I^i_{8-n}S^i_n]I^a_{2+4/2-m}S^a_m$ (n=0-8, m=0-6) intermediates and finally MoS_2. The overall process may be described by Equation 4-1.

Equation 4-1 $$Mo_6I_{12} + 12H_2S \longrightarrow 6MoS_2 + 12HI + 6H_2$$

During the substitution process some of the intermediates $[Mo_6I^i_{8-n}S^i_n]X^a_{6-m}S^a_m$ might leave the crystal, then, potentially in an even further substituted form enter into the gas phase to become condensed at a different location. The presence of the intermediates in the gas phase may aid the distribution of Mo in the GNFs which may be the reason why the curved and tubular MoS_2 nanostructures (Figure 4-8) formed from MoI_2 are less compact than those grown from MoO_2 (Figure 4-14).

4.4.4 Formation of MoS_2@GNFs from ($Mo(CO)_6$ and I_2)@GNFs

As shown above the conversion of ($Mo(CO)_6$ and I_2)@GNFs resulted in the coating of the inner surface of GNFs with a uniform deposit of few layer thick MoS_2, although the formation of sparsely distributed curved MoS_2 nanostructures was also observed (Figure 4-18). It can be clearly seen that I_2 has a positive effect on the formation of MoS_2 in GNFs in comparison to using purely $Mo(CO)_6$, presumably by retaining the Mo source inside the GNFs

during the transformation. As the conversion of encapsulated MoI_2 (Section 4.2.3.1) and $Mo(CO)_6$ and I_2 (Section 4.2.3.2) provided morphologically different products inside GNFs presumably the two reactions follow different mechanisms and proceed *via* different intermediates. This strongly suggests that $Mo(CO)_6$ and I_2 do not form $Mo_6I_8I_2I_{4/2}$ *i.e.* MoI_2 or other hexanuclear Mo chalcohalide upon heating ($Mo(CO)_6$ and I_2)@GNFs, although the temporary presence of smaller Mo_xI_y clusters cannot be excluded.[29] However, it is more likely that in GNFs $Mo(CO)_6$ and I_2 molecules form intermediates, which then converted into some yet unidentified ternary Mo-S-I phase.[18]

It is reported in the literature that I_2 is capable of forming a solid mixture with $Mo(CO)_6$ and also enhances surface diffusion of Mo and S during the formation of MoS_2 nanostructures *i.e.* inorganic fullerenes and nanotubes by catalytic chemical transport reaction.[17,18] This means that at high temperatures on the inner surface of hollow amorphous inorganic nanostructures, iodine forms a film which makes Mo and S atoms more mobile in comparison to solid state diffusion by lowering the activation energy.[18] In the case of the synthesis of freestanding IF particles the evaporation of I from the surface film increases the pressure inside the IF until the bursting threshold is reached and the shell of the particle opens to release the pressure.[18] The bursting threshold depends not only on the inside pressure but also on the surface

tension and elastic properties of the MoS_2 structure. After a series of repeated bursting smaller IFs and IFs encapsulated in tubular MoS_2 structures form.[18]

The formation of MoS_2@GNFs from ($Mo(CO)_6$ and I_2)@GNFs is likely to follow the key motifs of the above described growth mechanism of freestanding MoS_2 IF from $Mo(CO)_6$ and I_2 mixtures although slight deviations might be possible. First of all, presumably a MoS_2 nanostructure can withstand significantly higher pressure without bursting than a freestanding MoS_2 IF as the walls of GNFs will provide additional support (Figure 4-23 a). Moreover, the size or diameter of a MoS_2 structure will be retained since they are attached to the inner surface of the GNFs by van der Waals interactions. When the front of a growing MoS_2 structure cannot withstand the pressure caused by the evaporated species, predominantly iodine, it bursts (Figure 4-23 b), however, the growth of the MoS_2 is not necessarily terminated if a supply of Mo and S is maintained. This would result in perturbation in the sidewall structure of the MoS_2 tubes manifesting in fringes which curve away from the surface of GNFs as shown above (Figure 4-18) and illustrated in (Figure 4-23 c).

As I_2 is used as a transport agent ideally it should not be incorporated into the final MoS_2 nanostructures. Indeed, the level of trace I is found to be significantly lower in MoS_2@GNFs formed using $Mo(CO)_6$ and I_2 precursors than in the case of MoS_2@GNFs

which was prepared using the MoI_2 precursor. The reason for this may be that in the case of the $Mo(CO)_6$ and I_2 precursors I_2 forms an intimate mixture with $Mo(CO)_6$ instead of being chemically bonded to Mo as it is in MoI_2.

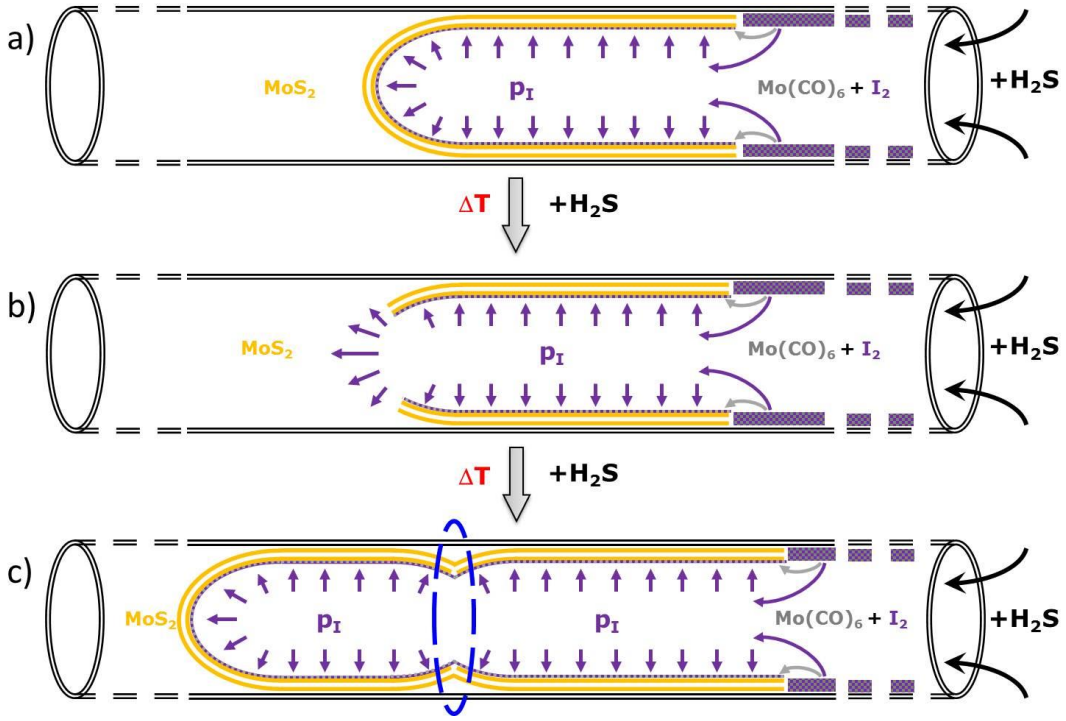


Figure 4-23. Schematic representation of the growth mechanism of tubular MoS_2 structures templated by the inner surface of GNFs. The initial state of the system, a), before the bursting threshold is reached, b) bursting of the front of a growing MoS_2 structure results in the final structure c) which has some imperfections in its sidewall due to the mismatch between fringes created by continued growth after a bursting event (highlighted by the dashed blue oval). The chess

As shown above the calcination of inorganic MoS_2 nanotubes embedded in GNFs resulted in the collapse of the hollow structure (Figure 4-21). This is in agreement with the observations of Tremel and co-workers who reported that the threshold of collapse for freestanding MoS_2 nanostructures is in the 800-900 °C region and is rationalised by considering that these hollow inorganic nanostructures are only thermodynamically stable if they do not

exceed a critical crystallite size.[17,12,19]

4.5 Concluding remarks

The main goal of this study was to develop a methodology with which MoS_2 nanostructures especially inorganic nanotubes can be fabricated within GNFs. It was demonstrated using TEM, EDX and PXRD that $Mo(CO)_6$ and other molecules, such as I_2, can be encapsulated into GNFs *via* gas phase filling to serve as precursors for the subsequent formation of MoS_2 nanostructures using H_2S. It was shown that the chemical nature and structure of encapsulated precursor/s *i.e.* $Mo(CO)_6$, $Mo(CO)_6$ and I_2, MoO_2, MoI_2 dramatically alters the morphologically of the formed MoS_2 nanostructures with a wide variety of structures observed. These included flat layers of MoS_2 on the GNF step-edges, small and large IF-like NPs, large tightly packed particles built from 10 layer thick fringes and tubular structures. From all the tested precursors the mixture of $Mo(CO)_6$ and I_2 was found to be the most efficient at forming MoS_2 layers on the inner surface of GNFs resulting in uniform (MoS_2 nanotube)@GNF structures. It was shown that calcination of (MoS_2 nanotube)@GNF hetero-structures resulted in the collapse of the inner MoS_2 nanotube due to its larger than critical crystallite size.[17,12,19]

In summary, the formation of a hetero van der Waals layered materials with a "tube inside a tube" structure was achieved *via* the encapsulation and *in situ* transformation of the appropriate

precursor molecules into an inner tube using the shape of the existing graphitic tube as a template.

4.6 Experimental section

4.6.1 Materials

Graphitised carbon nanofibers (PR-24 XT-HHT, *d*=30-40 nm, *l*=1-100 μm, Fe content<100 ppm) were purchased from Pyrograf Products and used without further purification.

Mo and W hexacarbonyls (purity≥98 and 99%, respectively) were purchased from Acros Organics and all hexacarbonyls were used without further purification.

I_2 (purity ≥99.8%) and H_2S gas (purity≥99.5%) were purchased from Fischer Scientific and Sigma-Aldrich, respectively and used without further purification.

4.6.2 Gas phase filling of GNFs

It is important to note that the amount of $Mo(CO)_6$ and I_2 reported in Table 4-1 are the initial masses of reagents used for all filling experiments, however due to the application of high vacuum during the sealing procedure some of the molecular precursors are anticipated to be lost due to unwanted sublimation prior to sealing. Obviously this is non-ideal and a number of steps were taken to limit this and an excess of precursor materials were used in each case to ensure effective GNF filling.

4.6.2.1 Heat treatment of GNFs in air prior to encapsulation

To remove moisture and provide access to their interior for the guest species GNFs were pre-treated by heating in air for 30 minutes below their oxidation temperature (500 °C) in a crucible.

4.6.2.2 Encapsulation of $Mo(CO)_6$ or $Mo(CO)_6$ and I_2 together into GNFs

Pre-treated GNFs were combined with the precursor molecule(s) *i.e.* $Mo(CO)_6$ or $Mo(CO)_6$ and I_2 and the resultant mixture was sealed in a Pyrex glass vessel (*d*=10 mm, *l*=10 cm) under high vacuum (10^{-6} mbar). The sealed vessel was placed into a preheated box furnace (T=120-150 °C) for several days depending on the experiment, see Table 4-1. Prior to opening the Pyrex glass vessel was taken out from the furnace and cooled down by immersing it into an ice-water bath for 5 minutes. After opening the Pyrex glass vessel the samples were transferred into a glass vial and stored in the freezer (**-**15 °C) until required.

4.6.2.3 Encapsulation of I_2 into $Mo(CO)_6$@GNFs

$Mo(CO)_6$@GNFs (prepared as described in Section 4.6.2.2) and I_2 were sealed in a Pyrex glass vessel, which was first evacuated (10^{-6} mbar) then filled with argon gas (0.7 bar). The sealed vessel was placed in a preheated box furnace (T=120 °C) for 12 hours, see Table 4-1.

4.6.3 Chemical transformation of $Mo(CO)_6$ or $Mo(CO)_6$ and I_2 precursor molecules into MoO_2 or MoI_2 in GNFs

The GNFs containing the precursor molecules ($Mo(CO)_6$ or $Mo(CO)_6$ and I_2) were sealed in a Pyrex glass vessel which was first evacuated (10^{-6} mbar) then filled with Ar gas (0.7 bar). The sealed Pyrex glass tube was then transferred into a preheated furnace (500 °C). After an hour the sample was taken out from the furnace and left on an asbestos tile to cool down to room temperature. After opening the glass ampoule the sample was transferred into a glass vial and stored in the freezer (-15 °C) until further treatment. The parameters of the experiments can be found in Table 4-2.

Table 4-1. Parameters of the gas phase encapsulation of $Mo(CO)_6$ or $Mo(CO)_6$ and I_2 into GNFs.

Experiment	Starting materials			Product	Atmosphere, pressure / bar	Reaction	
	Guest-molecule(s) / mg	Precursor / mg	Formed in Experiment	Molecule(s) in GNF		temp. / °C	time / h
4-1	$Mo(CO)_6$, 20 mg	GNF, 5 mg	N/A	$Mo(CO)_6$	Vacuum, 10^{-9}	120	72
4-2	I_2, 400 mg	$Mo(CO)_6$@GNF, 10 mg	**4-1**	$Mo(CO)_6$, I_2	Argon, 0.7	120	12
4-3	$Mo(CO)_6$, 200 mg	GNF, 5 mg	N/A	$Mo(CO)_6$	Vacuum, 10^{-9}	120	72
4-4	$Mo(CO)_6$, 50 mg; I_2, 100 mg	GNF, 5 mg	N/A	$Mo(CO)_6$, I_2	Vacuum, 10^{-9}	120	96

Table 4-2. Parameters of the chemical transformation of $Mo(CO)_6$ or $Mo(CO)_6$ and I_2 precursor molecules into MoO_2 or MoI_2 in GNFs.

Experiment	Starting material		Product	Atmosphere, pressure / bar	Reaction	
	Precursor	Formed in Experiment	Molecules in GNF		temp. / °C	time / h
4-5	$Mo(CO)_6$	**4-3**	MoO_2	Argon, 0.7	500	1
4-6	($Mo(CO)_6$, I_2)	**4-4**	MoI_2	Argon, 0.7	500	1

4.6.4 Reaction of the different precursors situated in GNFs with H_2S gas

The GNFs containing the precursor molecules were transferred into a quartz boat and placed into a closed ceramic working tube (*d*=25 mm, *l*=60 cm) located within a tube furnace (Figure 4-24).

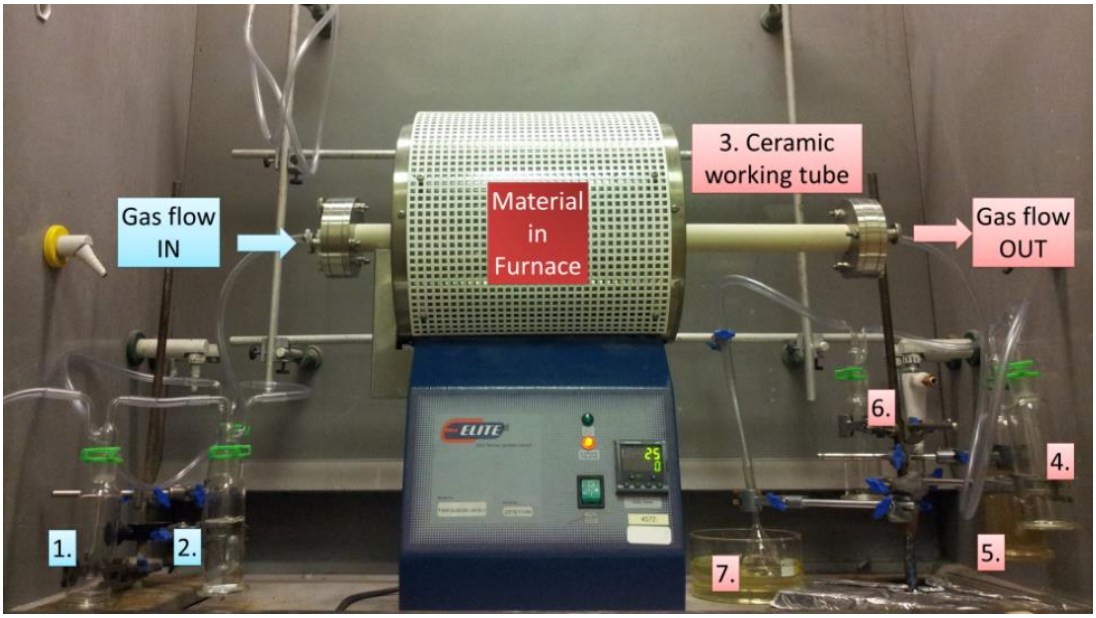


Figure 4-24. Experimental setup used for the reaction of H_2S gas with the different precursors situated in GNFs. The cold gas flow (Ar or H_2S) goes through an empty reversed gas bubbler (1.) and another one filled with paraffin oil (2.) before entering the ceramic working tube containing the sample (3.). The hot gas then flows through an empty reversed gas bubbler (4.), one filled with paraffin oil (5.) and another empty reversed gas bubbler (6.) and through a bleach bath (7.) before reaching the environment.

The system was purged at room temperature with Ar then H_2S for 1 hour each at ~15 mL/min. The furnace was heated up to 550 °C (50 °C/min) and kept at this temperature for 2 hours while maintaining a moderate (~15 mL/min) H_2S gas flow. Then the system was cooled down (10 °C/min) to room temperature under Ar gas flow, see Table 4-3. The exhaust of the system was released into the fume hood through a bleach bath in order to

neutralise any excess H_2S.

4.6.5 Calcination of MoS_2@GNFs under an Ar atmosphere

MoS_2@GNF was sealed in a Pyrex glass vessel, which was first evacuated (10^{-6} mbar) then filled with Ar gas (0.7 bar). The sealed ampoule was placed into a box furnace and heated at 850 °C for an hour using a 5 °C/min heating and cooling rate, see Table 4-4.

4.6.6 Transmission Electron Microscopy and Energy-dispersive X-ray spectroscopy

TEM micrographs and EDX spectra were acquired with an emission gun JEOL 2100F microscope operated at 200 kV acceleration voltage at the Nottingham Nanotechnology and Nanoscience Centre, University of Nottingham.

Prior to the investigation, the graphitised carbon nanofibers were dispersed in isopropyl alcohol using an ultrasonic bath (~15 min). Subsequently, a few drops were dropped onto a copper TEM grid coated with lacey carbon film (Agar Scientific) to support the graphitised carbon nanofibers. The characteristic Cu peaks in the EDX spectra of the analysed materials are due to the copper grid of the TEM specimen holder.

Table 4-3. Parameters of the reaction of H_2S gas with the different precursors situated in GNFs.

Experiment	Starting material		Product	Atmosphere, pressure / bar	Reaction temp. / °C	Dwell time / h	Heating	Cooling
	Precursor	Formed in Experiment	Molecules in GNF				rate / °C min^{-1}	
4-7	$Mo(CO)_6$@GNF	**4-1**	MoS_2	H_2S, 1	550	2	50	10
4-8	MoO_2@GNF	**4-5**	MoS_2	H_2S, 1	550	4	50	10
4-9	MoI_2@GNF	**4-6**	MoS_2	H_2S, 1	550	4	50	10
4-10	($Mo(CO)_6$, I_2)@GNF	**4-2**	MoS_2	H_2S, 1	550	2	50	10

Table 4-4. Parameters of the calcination of MS_2@GNFs.

Experiment	Starting material		Atmosphere, pressure / bar	Reaction temp. / °C	Dwell time / h	Heating	Cooling
	Precursor	Formed in Experiment				rate / °C min^{-1}	
4-11	MoS_2@GNF	**4-7**	Argon, 0.7	850	1	5	5
4-12	MoS_2@GNF	**4-10**	Argon, 0.7	850	1	5	5

4.6.7 Powder X-ray diffraction measurements and calculations

The powder X-ray measurements were performed using a PANalytical X'Pert PRO diffractometer equipped with a Cu K_α radiation source (λ=1.5432 Å, 40 kV, 40 mA) in Bragg-Brentano geometry using a Si zero-background holder. The powder sample was poured on the Si surface, which had been wetted with acetone to aid GNF adhesion. Since the materials of interest are small nanoparticles inside another structure long acquisition times were required for the powder X-ray diffraction measurements. The parameters of a typical experiment are: start angle: 5°, stop angle: 120°, step size: 0.05°, time/step: 6080 seconds, scan speed: 0.0022°/sec.

The reference powder diffraction patterns were calculated from crystallographic information files acquired from the Royal Chemical Society`s Chemical Database Service with Mercury CSD 3.0 program using the following parameters: λ=1.5432 Å, step size: 0.05°.

The distance of crystallographic lattices (d) *i.e.* the d spacing which results in the appearance of a certain peak in the diffraction pattern can be calculated using Bragg`s Law (Equation 4-2) where θ is the scattering angle, λ is the wavelength of the X-ray in this case the Cu K_α radiation (λ=1.5432 Å) and n>0 is an integer.

Equation 4-2 $$2d\sin\theta = n\lambda$$

4.7 References

1. N. G. Chopra, R. J. Luyken, K. Cherrey, V. H. Crespi, M. L. Cohen, S. G. Louie, and A. Zettl, *Science*, 1995, **269**, 966–967.
2. A. L. Tiano, C. Park, J. W. Lee, H. H. Luong, L. J. Gibbons, S.-H. Chu, S. Applin, P. Gnoffo, S. Lowther, H. J. Kim, P. M. Danehy, J. a. Inman, S. B. Jones, J. H. Kang, G. Sauti, S. a. Thibeault, V. Yamakov, K. E. Wise, J. Su, and C. C. Fay, *Proc. SPIE*, 2014, **9060**, 906006–906019.
3. R. Tenne, L. Margulis, M. Genut, and G. Hodes, *Nature*, 1992, **360**, 444–446.
4. L. Margulis, G. Salitra, R. Tenne, and M. Talianker, *Nature*, 1993, **365**, 113–114.
5. Y. Feldman, E. Wasserman, D. J. Srolovitz, and R. Tenne, *Science*, 1995, **267**, 222–225.
6. Y. Wang, K. Takahashi, H. Shang, and G. Cao, *J. Phys. Chem. B*, 2005, **109**, 3085–3088.
7. P. Roy, S. Berger, and P. Schmuki, *Angew. Chemie - Int. Ed.*, 2011, 50, 2904–2939.
8. C. N. R. Rao and M. Nath, *Dalt. Trans.*, 2003, 1–24.
9. A. K. Geim and I. V. Grigorieva, *Nature*, 2013, **499**, 419–25.
10. S. Bertolazzi, D. Krasnozhon, and A. Kis, *ACS Nano*, 2013, **7**, 3246–3252.

11. J. Etzkorn, H. a. Therese, F. Rocker, N. Zink, U. Kolb, and W. Tremel, *Adv. Mater.*, 2005, **17**, 2372–2375.
12. N. Zink, J. Pansiot, J. Kieffe, H. A. Therse, M. Panthöfer, F. Rocker, U. Kolb, and W. Tremel, *Chem. Mater.*, 2007, **19**, 6391–6400.
13. M. Hershfinkel, L. A. Gheber, V. Volterra, J. L. Hutchison, L. Margulis, and R. Tenne, *J. Am. Chem. Soc.*, 1994, **116**, 1914–1917.
14. A. Rothschild, J. Sloan, and R. Tenne, *J. Am. Chem. Soc.*, 2000, **122**, 5169–5179.
15. I. Wiesel, H. Arbel, A. Albu-Yaron, R. Popovitz-Biro, J. M. Gordon, D. Feuermann, and R. Tenne, *Nano Res.*, 2010, **2**, 416–424.
16. Y. Feldman, V. Lyakhovitskaya, and R. Tenne, *J. Am. Chem. Soc.*, 1998, **120**, 4176–4183.
17. F. Hoshyargar, A. Yella, M. Panthöfer, and W. Tremel, *Chem. Mater.*, 2011, **23**, 4716–4720.
18. A. Yella, M. Panthöfer, M. Kappl, and W. Tremel, *Angew. Chem. Int. Ed. Engl.*, 2010, **49**, 2575–80.
19. R. Tenne, *Adv. Mater.*, 1995, **7**, 965–995.
20. A. N. Enyashin, M. Bar-Sadan, J. Sloan, L. Houben, and G. Seifert, *Chem. Mater.*, 2009, **21**, 5627–5636.

21. A. Albu-Yaron, M. Levy, R. Tenne, R. Popovitz-Biro, M. Weidenbach, M. Bar-Sadan, L. Houben, A. N. Enyashin, G. Seifert, D. Feuermann, E. a. Katz, and J. M. Gordon, *Angew. Chemie - Int. Ed.*, 2011, **50**, 1810–1814.
22. Q. Yang, Q. Liang, J. Liu, S. Liang, S. Tang, P. Lu, and Y. Lu, *Mater. Lett.*, 2014, **127**, 32–35.
23. E. J. Welch and J. R. Long, in *Progress in Inorganic Chemistry*, ed. K. D. Karlin, John Wiley & Sons, Inc., Hoboken, NJ, USA., 2005, vol. 54, pp. 1–46.
24. Y. Lu, Z. Zhu, D. Su, D. Wang, Z. Liu, and R. Schlögl, *Carbon N. Y.*, 2004, **42**, 3199–3207.
25. M. Remskar, A. Mrzel, M. Virsek, M. Godec, M. Krause, A. Kolitsch, A. Singh, and A. Seabaugh, *Nanoscale Res. Lett.*, 2010, **6**, 26–1–26–6.
26. Y. Feldman, G. L. Frey, M. Homyonfer, V. Lyakhovitskaya, L. Margulis, H. Cohen, G. Hodes, J. L. Hutchison, and R. Tenne, *J. Am. Chem. Soc.*, 1996, **118**, 5362–5367.
27. V. Fedorov, A. Mishchenko, and V. Fedin, *Russ. Chem. Rev.*, 1985, **54**, 408–423.
28. K. Kirakci, S. Cordier, A. Shames, B. Fontaine, O. Hernandez, E. Furet, J.-F. Halet, R. Gautier, and C. Perrin, *Chemistry*, 2007, **13**, 9608–9616.
29. J. D. Franolic, J. R. Long, and R. H. Holm, *J. Am. Chem. Soc.*, 1995, **117**, 8139–8153.

5 Synthesis of inorganic nanomaterials inside carbon nanotubes

5.1 Introduction

It has been shown in previous chapters that the hollow channel of carbon nanotubes can be filled with different materials using a variety of encapsulation techniques, see Chapter I. As carbon nanotubes (CNT) are chemically highly stable nanoscale vessels they provide a template to form quasi 1D structures and allow studying fundamental physicochemical properties of low-dimensional inorganic materials. Moreover, as single-walled carbon nanotubes (SWNTs) are atomically thin *i.e.* transparent to the beam of accelerated electrons used in transmission electron microscopy (TEM), the structural properties of the encapsulated materials can be studied directly at the atomic level, in real space by high-resolution TEM (HRTEM).

It was demonstrated using the encapsulation in nanotubes that C_{60} molecules, which crystallise in a face-centered cubic structure in the bulk crystal, arrange in various types of molecular arrays inside nanotubes, determined by the nanotube internal diameter (Figure 9, Chapter I.).[1] Similarly TEM revealed that I atoms form chains in CNTs, and these chains arranged into different 1D phases *i.e.* single chains, or double and triple helices, depending on the nanotube diameter.[2,3] It is interesting that not only CNTs are

capable of influencing the packing of encapsulated material, the confined material can affect the structure of the host nanotubes. It was shown that encapsulated materials such as helical chains of $La@C_{82}$ molecules (Figure 5-1 a)[4] or I atoms (Figure 11, in Chapter I.),[2] nanoribbons (NR) of sulphur-terminated graphene (Figure 5-2 c)[5] and Group VI metal disulphides[6] (Figure 5-1 b and c) *etc.* can distort the normally cylindrical shape of CNTs.

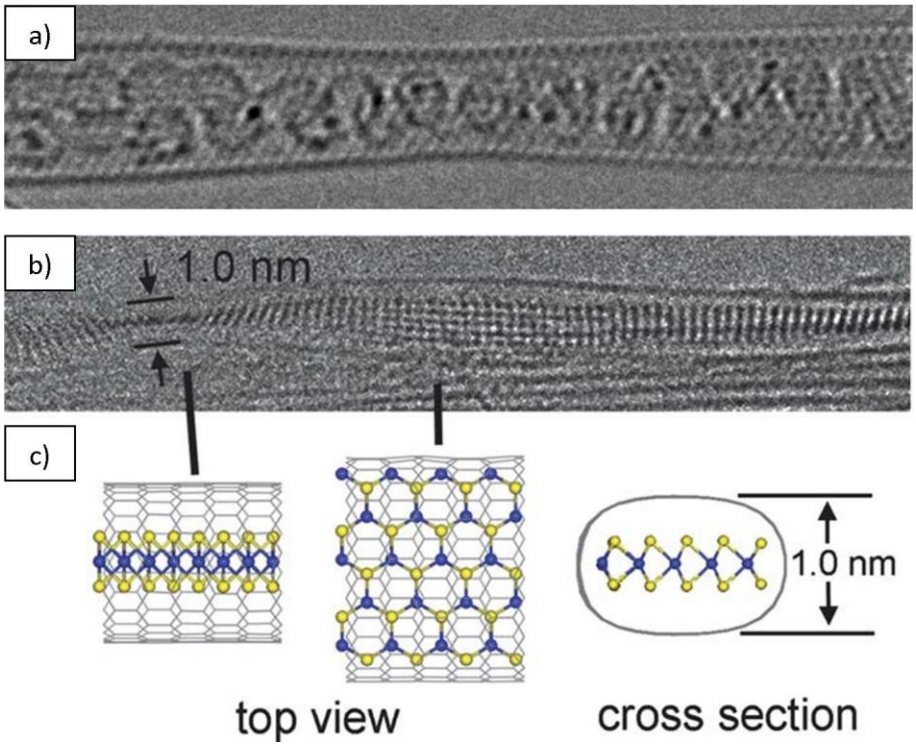


Figure 5-1. HRTEM image showing the distortion of the SWNTs in a) $La@C_{82}$@SWNT and b) twisted single-layer WS_2 nanoribbon@SWNT. c) Structural model showing top and cross section view of single-layer WS_2 nanoribbon in SWNT and the distortion caused by the ribbon, blue: W, yellow: S, grey: C.[4,5]

In addition to altering their structures, the physicochemical properties of both the encapsulated material and the nanotubes may be mutually modified by the composite formation.

For example, in case of I chains encapsulated in CNTs the

electronic properties of both the guest iodine species and the host CNTs were altered as a result of electron transfer from the CNTs to the I atoms.[2,7] Similarly, the encapsulation of elemental sulphur in CNTs led to the formation of previously unknown 1D sulphur chains which in contrast to bulk sulphur (a known insulator), were found to be conductive.[8] The encapsulation of SnTe in CNTs lead to 1D SnTe crystals and a hybrid material with new optical properties which are attributed to the hybridisation of SnTe and CNT electronic bands rather than to charge transfer.[9]

As the inner surface of nanotubes is relatively inert, CNTs may be used as nanosized reaction vessels for known and new chemical reactions,[10,11] where, in contrast to regular reaction environments, CNTs may influence the outcome of the reactions through confinement effects imparted by the size and shape of the nanosized tubular channel. The narrow channels of CNTs especially of SWNTs may be able to promote the formation of a desired product, at the expense of another product energetically favoured under traditional reaction conditions (*i.e.* without confinement), by sterically prohibiting otherwise accessible geometrical conformations as a consequence of the limited space available around the reacting molecules.[12] For example it was demonstrated that the polymerisation and decomposition of C_{60} in SWNTs result in the formation of double-walled carbon nanotubes (DWNT), while the polymerisation of $C_{60}O$ molecules inside SWNTs leads

exclusively to linear rather than branched polymers.[1,13] (Figure 5-2) Moreover, it was demonstrated that otherwise inaccessible materials, such as sulphur-terminated graphene (Figure 5-2 c) or metal dichalcogenide (MQ_2, M=Mo, W, Q=S, Se) nanoribbons, can be synthesised in CNTs.[5,14,6,15]

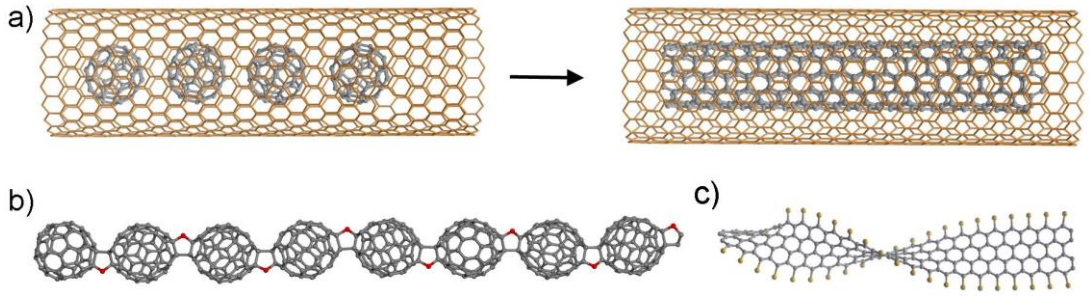


Figure 5-2. A selection of unusual molecular nanostructures which can be synthesised inside single-walled carbon nanotubes: a) C_{60} transform into an internal nanotube, b) polymers $(C_{60}O)_n$, c) sulphur-terminated graphene nanoribbon.[1,13,14,5]

These distinctive properties make CNTs indispensable in the preparation of unique novel (hybrid) nanomaterials which could not be prepared by any other method. This study will focus on the expansion of this methodology, exploiting the possibilities provided by the quasi 1D internal channel of CNTs and exploring the processes of the inorganic chemical transformations in the CNTs.

5.2 Methods of inorganic nanomaterials synthesis inside carbon nanotubes

The methodology to synthesise inorganic nanomaterials in CNTs combines the steps which were established for the encapsulation of $M(CO)_6$ into SWNTs (Chapter II) and those were used to prepare MoS_2 nanostructures in GNFs (Chapter IV).

In order to explore how different starting materials and

experimental conditions affect the formation of binary inorganic compounds (metal iodides and sulphides) in nanotubes, precursors such as $M(CO)_6$ or the mixture of $M(CO)_6$ and I_2 were encapsulated into CNTs from the gas phase (as described in Section 5.6.2), and transformed into M_6I_{14}@CNTs *via* thermal treatment inside the nanotube channel of CNTs according to Section 5.6.3 (Figure 5-3).

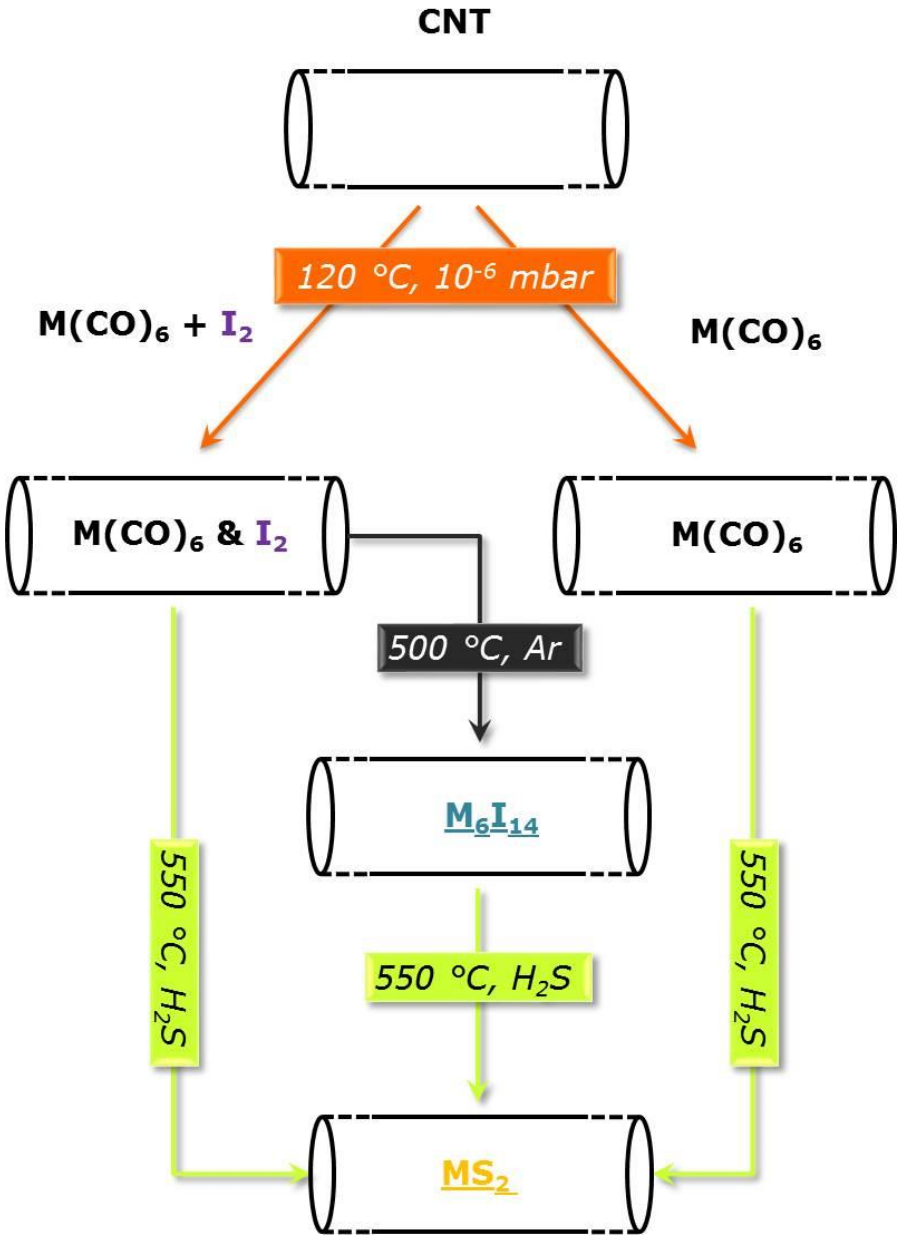


Figure 5-3. Schematic diagram summarising the different synthetic strategies utilised to form M_6I_{14}@CNTs and MS_2@CNTs. The orange boxes and arrows represent the encapsulation conditions used to insert precursor molecules into CNTs, while the black box

and arrow corresponds to the conversion of $M(CO)_6$ and I_2 precursors inside CNTs and the green boxes and arrows represent the reactions of precursor(s)@CNTs with H_2S.

Furthermore, the formation of metal sulphides in nanotubes was explored by reacting $M(CO)_6$, $M(CO)_6$ and I_2 or M_6I_{14} encapsulated in CNTs with H_2S gas, according to Section 5.6.4.

In some cases the resultant materials were calcined under an Ar atmosphere, as described in Section 5.6.5, in an effort to improve the packing or crystallinity of the inorganic material in CNTs.

5.3 Characterisation of the encapsulated molecules and products of chemical reactions performed inside CNTs

The materials formed *via* the gas phase encapsulation of $M(CO)_6$ or the mixture of $M(CO)_6$ and I_2 in CNTs were analysed by transmission electron microscopy (TEM), energy dispersive X-ray spectroscopy (EDX) to ensure the presence of the precursor molecules in the CNTs.

Inorganic nanomaterials formed by chemical reactions performed in CNTs were analysed by TEM, EDX, Matrix-assisted laser desorption/ionisation time of flight mass spectrometry (MADLI-ToF MS) and Raman spectroscopy, as described in Section 5.6, in order to determine their structure, chemical composition, physicochemical properties and to investigate their dynamic behaviour under electron beam (e-beam) irradiation.

5.3.1 Characterisation of the materials formed by the encapsulation and subsequent reaction of $M(CO)_6$ and I_2 in CNTs

5.3.1.1 Characterisation of the materials formed by reacting $W(CO)_6$ and I_2 precursors in SWNTs

TEM analysis of the material formed by the thermal treatment of $(WCO)_6$, I_2)@SWNT (Experiment 5-7) showed single-chain arrays of high-contrast circular features with a diameter of 0.7 nm filling the narrow channels of SWNTs (d_{NT}=1.4 nm) (Figure 5-4 a, b). EDX spectroscopy showed characteristic peaks of W and I at 1.4, 1.8, 8.4, 9.6 keV and 3.9 keV respectively indicating their presence within SWNTs (Figure 5-5).

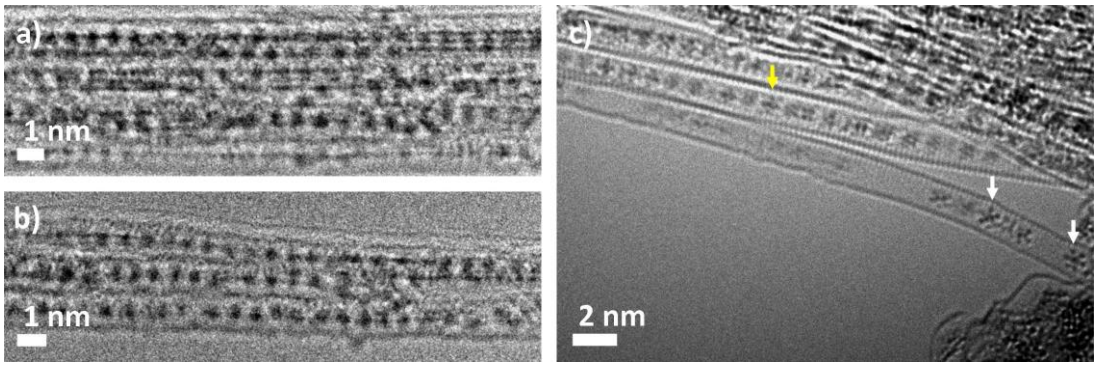


Figure 5-4. TEM images of W_6I_{14}@SWNTs formed in Experiment 5-7 show a)-b) dark circular features (*d*=0.7 nm), while c) shows AC-TEM micrographs revealing well-defined geometric shapes, such as star and rhombus, marked with white and yellow arrows.

Aberration corrected TEM (AC-TEM) investigation was able to resolve atomic structures of the features inside SWNT, which have appeared to be circular in conventional TEM (without aberration correction), showing that they have a well-defined geometric shapes which can be labelled as a star-, H-, rhombus- and θ-shape (Figure 5-4 c and Figure 5-6).

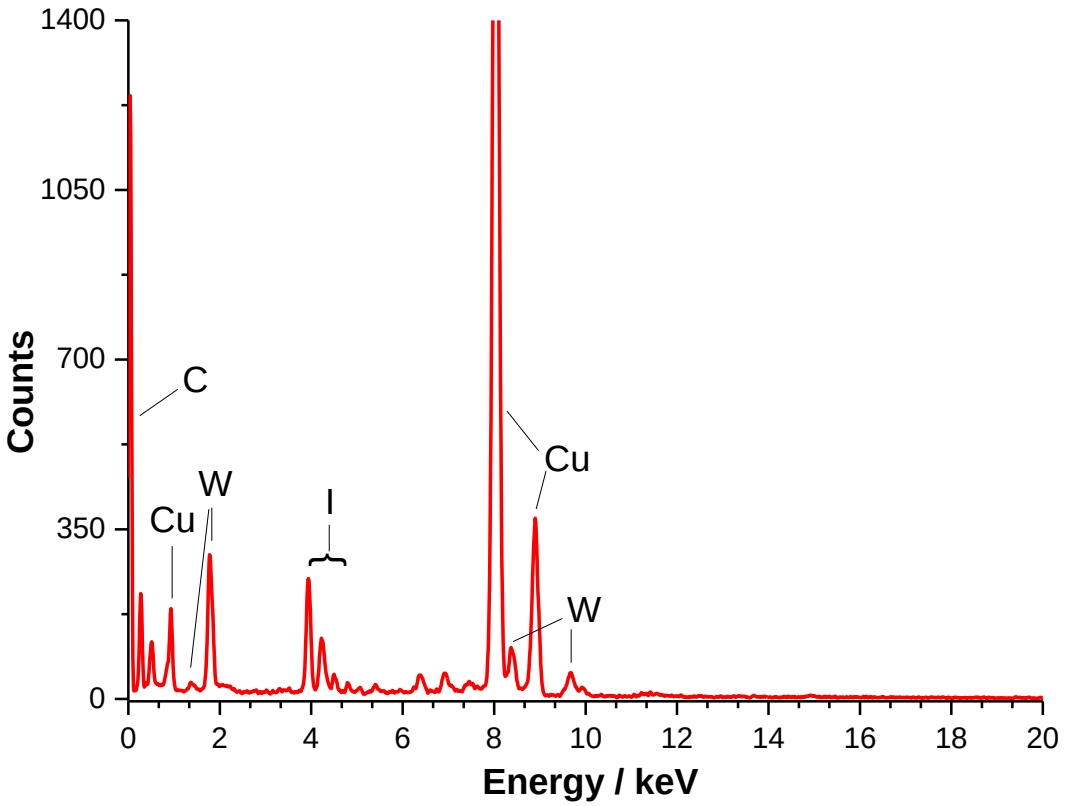


Figure 5-5. EDX spectrum of W_6I_{14}@SWNTs formed in Experiment 5-7. Characteristic X-ray peaks of W at 1.4, 1.8, 8.4 and 9.6 keV and I 3.9 keV were identified. Cu peaks are due to the specimen holder.

TEM image simulation (preformed as described in Section 5.6.7) demonstrated that these high-contrast geometric shapes correspond to the different projections of octahedral $W_6I^i_8I^a_6$ clusters (W_6I_{14}) (Figure 5-7) and that the observed star-, H-, rhombus- and θ-shapes emerge when the incident e-beam is parallel to C_3, tilted C_3, C_4 or tilted C_4 W_6I_{14} clusters, respectively as shown in Figure 5-7 d-g. In addition, time series AC-TEM imaging demonstrated that W_6I_{14} clusters rotate fast in nanotubes thus producing different projections over time (Figure 5-6, Video 1, Video 2). Overall observations of W_6I_{14} dynamics in nanotubes under the e-beam in AC-TEM indicate that the clusters are extremely stable, retaining their structure even after 8 minute

irradiation (e-beam energy 80 keV and dose rate on specimen ~10^6 e^-/nm·s), and translate freely along the SWNTs channel.

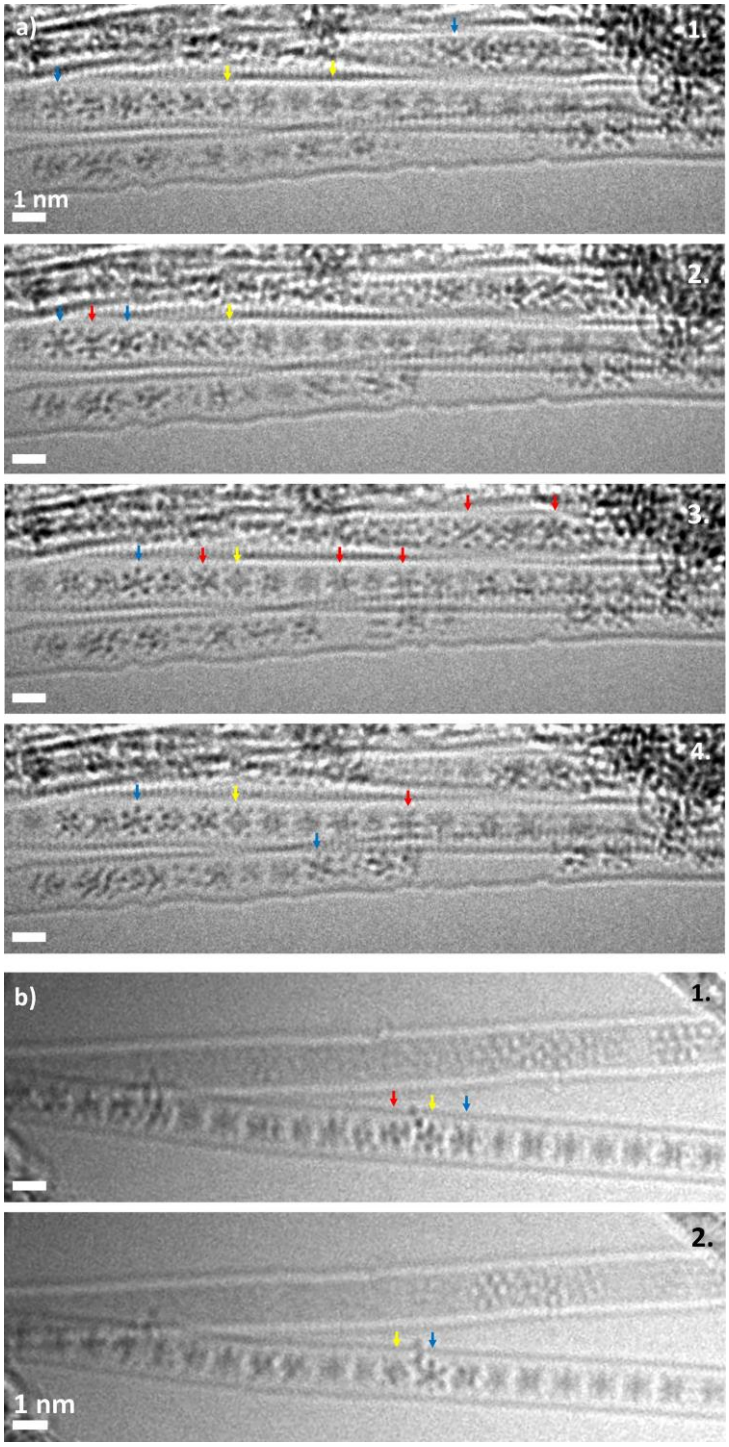


Figure 5-6. Time series AC-TEM images a) 1-4 and b) 1-2 demonstrate the star-, H-, rhombus- and θ-shaped features, which correspond to the projections of the encapsulated W_6I_{14} clusters in C_3, tilted C_3, C_4 orientation (marked with blue, red, yellow arrows, respectively), and their rotation in SWNTs (see Figure 5-7 d-g) (Video 1, Video 2).

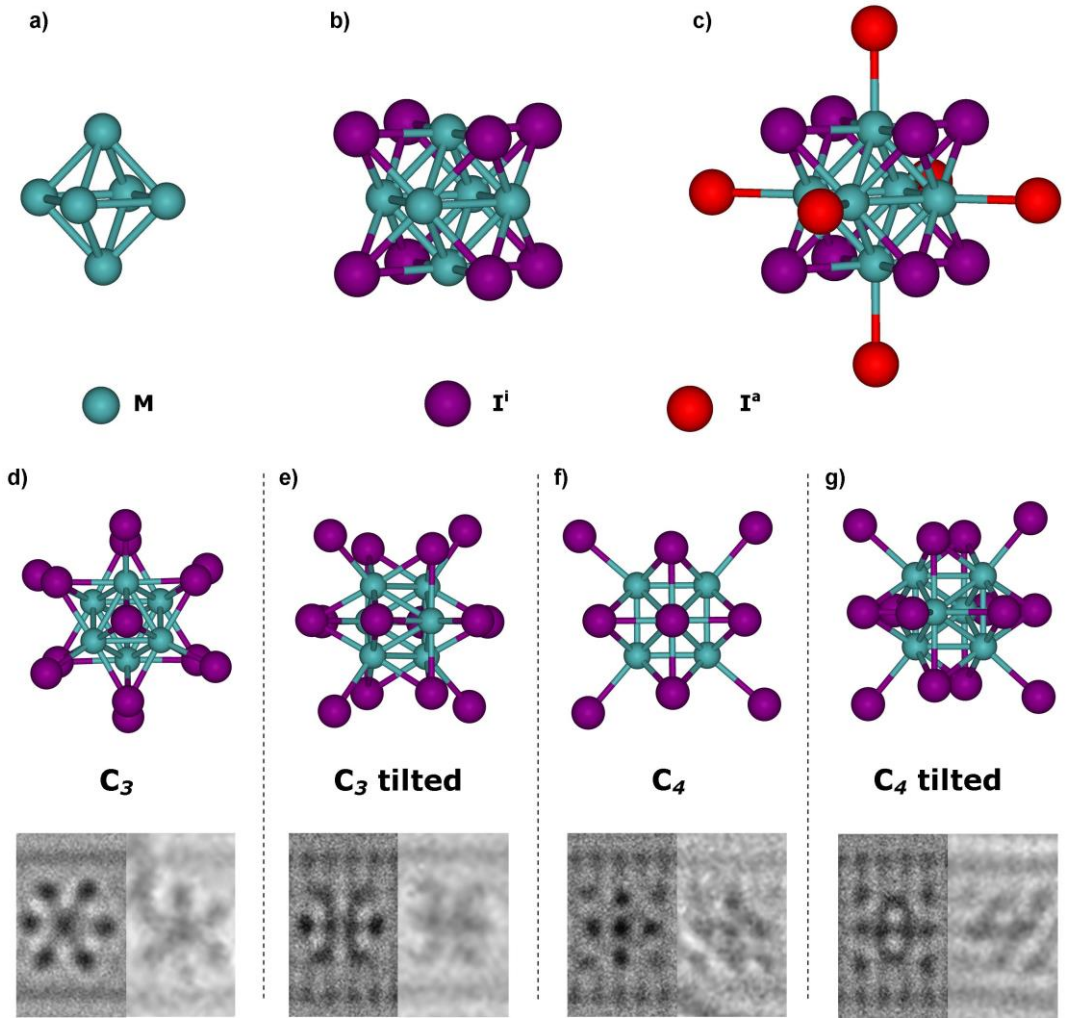


Figure 5-7. Panel a)-c) show the structure of a $M_6I^i_8I^a_6$ clusters (M=Mo, W) which have O_h symmetry and consist of a) an octahedral hexanuclear M clusters which have b) 8 μ^3 face capping internal I^i atoms and c) 6 terminal *i.e.* axial I^a atoms. Opposite pairs of I^a and diagonally opposite pairs of I^i atoms are located on the C_4 and C_3 rotation axis of $M_6I^i_8I^a_6$ clusters and their distances are 0.9 and 0.7 nm, respectively. Panel d)-g) show structural models, simulated and experimentally obtained AC-TEM micrographs of $M_6I^i_8I^a_6$ clusters which emerge when the incident e-beam is parallel to clusters in C_3, tilted C_3, C_4 or tilted C_4 orientation. The green and purple/red spheres correspond to M and I atoms, respectively.

The host-guest interaction between the SWNTs and the guest-molecules was investigated with Raman spectroscopy (as described in Section 5.6.8) after the encapsulation of ($W(CO)_6$, I_2) (Experiment 5-4) then the formation of W_6I_{14} clusters (Experiment 5-7) in SWNTs.

In ($W(CO)_6$, I_2)@SWNTs (Experiment 5-4) the G band of the

nanotube is blueshifted to 1602 cm^{-1} by 21 cm^{-1} in comparison to the empty SWNTs (Figure 5-8, Table 5-1). Similar blueshifts were observed for the D (Figure 5-9) and G* bands (Figure 5-10) to an extent of 8 and 12 cm^{-1} respectively (Table 5-1). No peak corresponding to I_2 was observed in the low frequency region of the spectrum (~210 cm^{-1}), however a new band appeared at ~100 cm^{-1} (Figure 5-11, Table 5-1). Moreover, the RBM of SWNTs was blueshifted by 6 cm^{-1} to (163 cm^{-1}) and its shape has been altered. These observations suggest the transfer of electrons from the SWNTs to I_2 which transforms to polyiodide ions in SWNTs, such as I_3^- and I_5^- as the emergence of the new band at ~100 cm^{-1} may be the result of the presence of I_3^-, while I_5^- may contribute to the RBM of the SWNTs at ~170 cm^{-1}.[16,7] Once $W(CO)_6$ and I_2 are transformed in nanotube to W_6I_{14}@SWNT by heating at 500 ^oC under Ar, (W_6I_{14}@SWNTs, Experiment 5-7) the G band of the SWNTs is blueshifted by 15 cm^{-1} (1596 cm^{-1}) in comparison to the empty SWNTs (1581 cm^{-1}), which is a slightly smaller shift in comparison to ($W(CO)_6$, I_2)@SWNTs (21 cm^{-1}) (Figure 5-8, Table 5-1). In contrast, D (Figure 5-9) and G* bands (Figure 5-10) in W_6I_{14}@SWNT are blueshifted by 12 and 17 cm^{-1} respectively which is larger than the corresponding shifts in case of ($W(CO)_6$, I_2)@SWNTs (8 and 12 cm^{-1}) (Table 5-1). Interestingly, Raman spectroscopy of W_6I_{14}@SWNT shows a set of new bands (76, 88, 94 117 cm^{-1}), not observed in ($W(CO)_6$, I_2)@SWNTs or

empty nanotubes, which can be attributed to $[W_6I_8I_6]^{2-}$ clusters, and a peak at 210 cm^{-1} corresponding to residual I_2 molecules (Figure 5-11, Table 5-1).[17] Moreover, the shape of the RBM changed *i.e.* a shoulder appeared at 148 cm^{-1} while the position of the main RBM peak (158 cm^{-1}) became almost identical to empty SWNTs (157 cm^{-1}) suggesting that polyiodide is no longer present in the material (Figure 5-11, Table 5-1).

Table 5-1. Raman spectroscopy data of empty SWNTs, $(W(CO)_6, I_2)$@SWNTs and W_6I_{14}@SWNTs.

	Vibrational mode / cm^{-1}						Shift vs SWNT / cm^{-1}				
	RBM		D	G	G*	$[W_6I_{14}]^{2-}$	RBM		D	G	G*
SWNT	157	-	1330	1581	2660	-	-	-	-	-	-
$(W(CO)_6, I_2)$@SWNT	163	-	1338	1602	2672	-	6	-	8	21	12
W_6I_{14}@SWNT	148	158	1342	1596	2677	76, 88, 94 117	-9	1	12	15	17

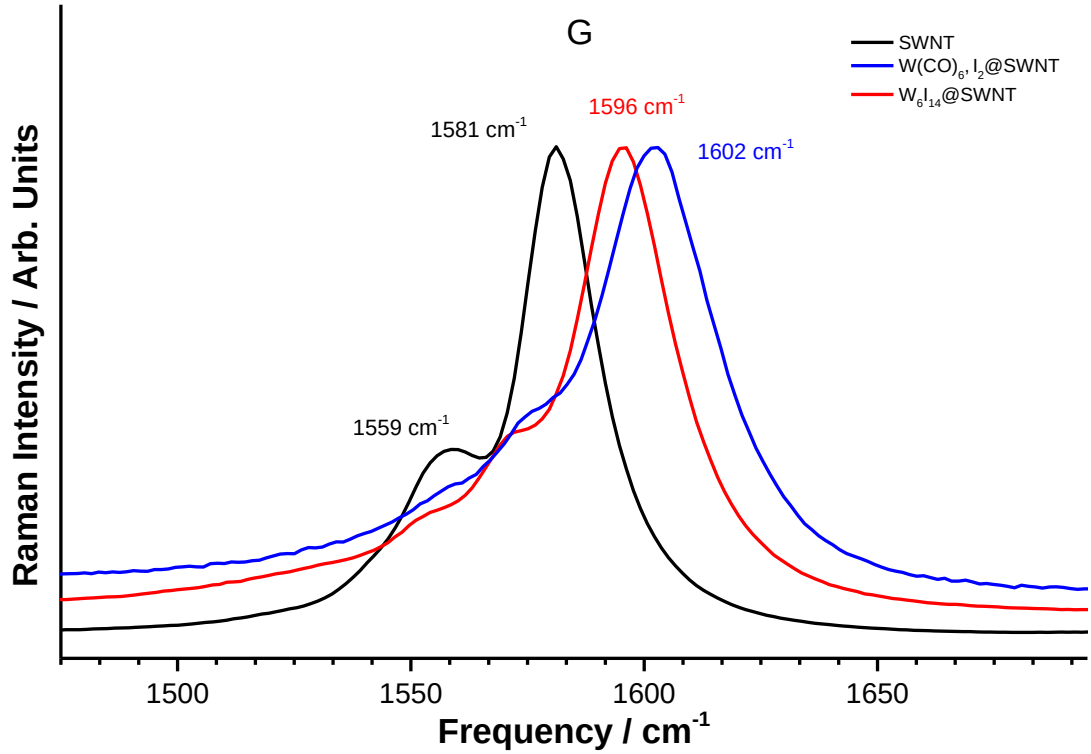


Figure 5-8. Raman spectra show the G band of empty SWNTs (1581 cm^{-1}, black), $(W(CO)_6, I_2)$@SWNTs (1602 cm^{-1}, blue) and W_6I_{14}@SWNT (1596 cm^{-1}, red).

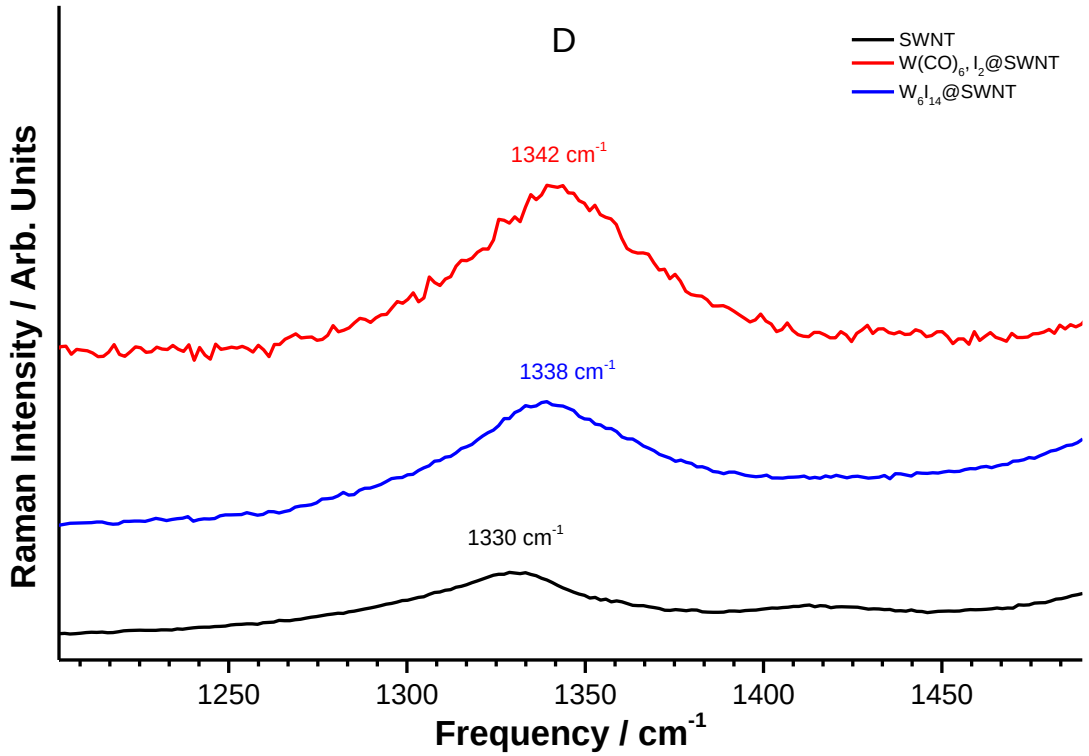


Figure 5-9. Raman spectra show the D band of empty SWNTs (1330 cm^{-1}, black), ($W(CO)_6$, I_2)@SWNTs (1338 cm^{-1}, blue) and W_6I_{14}@SWNT (1342 cm^{-1}, red).

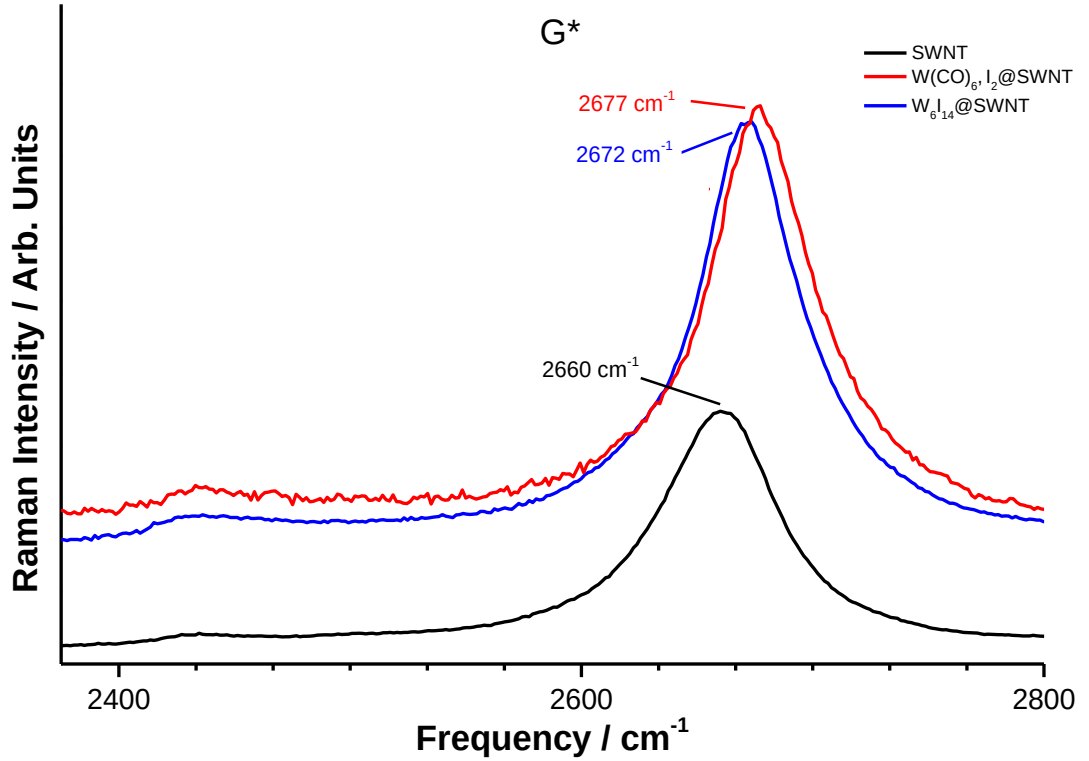


Figure 5-10. Raman spectra show the G* band of empty SWNTs (2660 cm^{-1}, black), ($W(CO)_6$, I_2)@SWNTs (2672 cm^{-1}, blue) and W_6I_{14}@SWNT (2677 cm^{-1}, red).

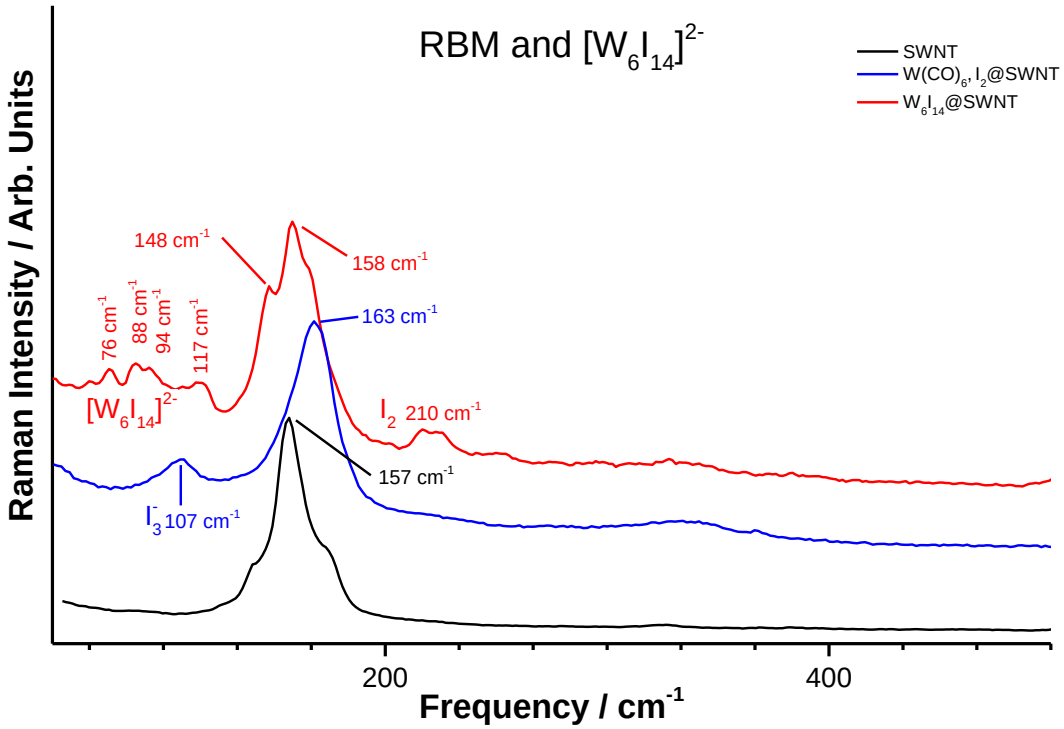


Figure 5-11. Raman spectra show the low frequency region containing RBM of empty SWNTs (157 cm^{-1}, black), ($W(CO)_6$, I_2)@SWNTs (163 cm^{-1}, blue) with a peak of polyiodide I_3^- ions (107 cm^{-1}) and W_6I_{14}@SWNT (148, 158 cm^{-1}, red) in addition to peaks corresponding to W_6I_{14} clusters (76, 88, 94 117 cm^{-1}) and I_2 molecules (210 cm^{-1}).

5.3.1.2 Characterisation of the materials formed by reacting $Mo(CO)_6$ and I_2 in SWNTs

TEM analysis of the material formed by the thermal treatment of ($Mo(CO)_6$, I_2)@SWNT (Experiment 5-6) showed single-chain arrays of high-contrast circular features (d=0.7 nm) inside SWNTs (Figure 5-12). The size and the shape of these features were found to be very similar to those which have been observed and assigned to W_6I_{14} clusters in the case of W_6I_{14}@SWNTs, therefore suggesting the formation of Mo_6I_{14} clusters in SWNTs. As the separation of the circular features in Mo_6I_{14}@SWNTs were found to be irregular (0.7-1 nm) in TEM images and changing over time, Mo_6I_{14} clusters are likely to have no bonding to each other, *i.e.* isostructurally to the tungsten complex they correspond to individual $Mo_6I^i_8I^a_6$ units.

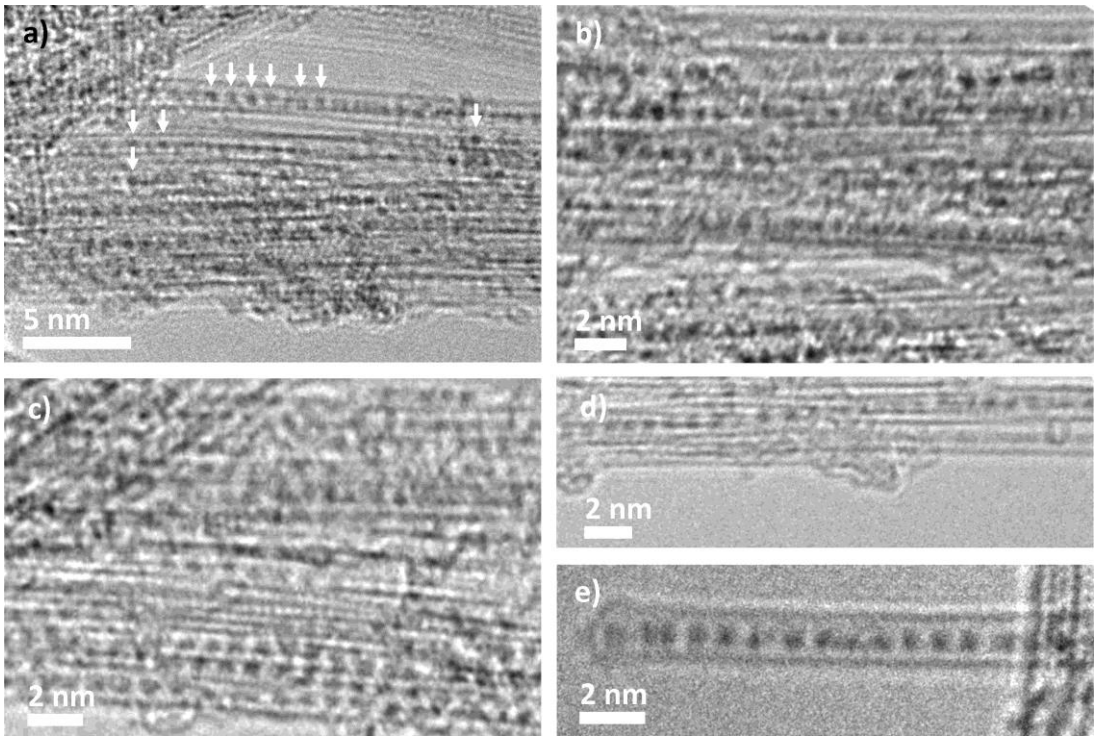


Figure 5-12. TEM images of Mo_6I_{14}@SWNTs (Experiment 5-6) show high-contrast circular features (*d*=0.7 nm) which can be assigned to the $Mo_6I^i_8I^a_6$ clusters. The irregular separation (0.7-1 nm) of the clusters, such as in e), suggests that the circular features correspond to individual $Mo_6I^i_8I^a_6$ units.

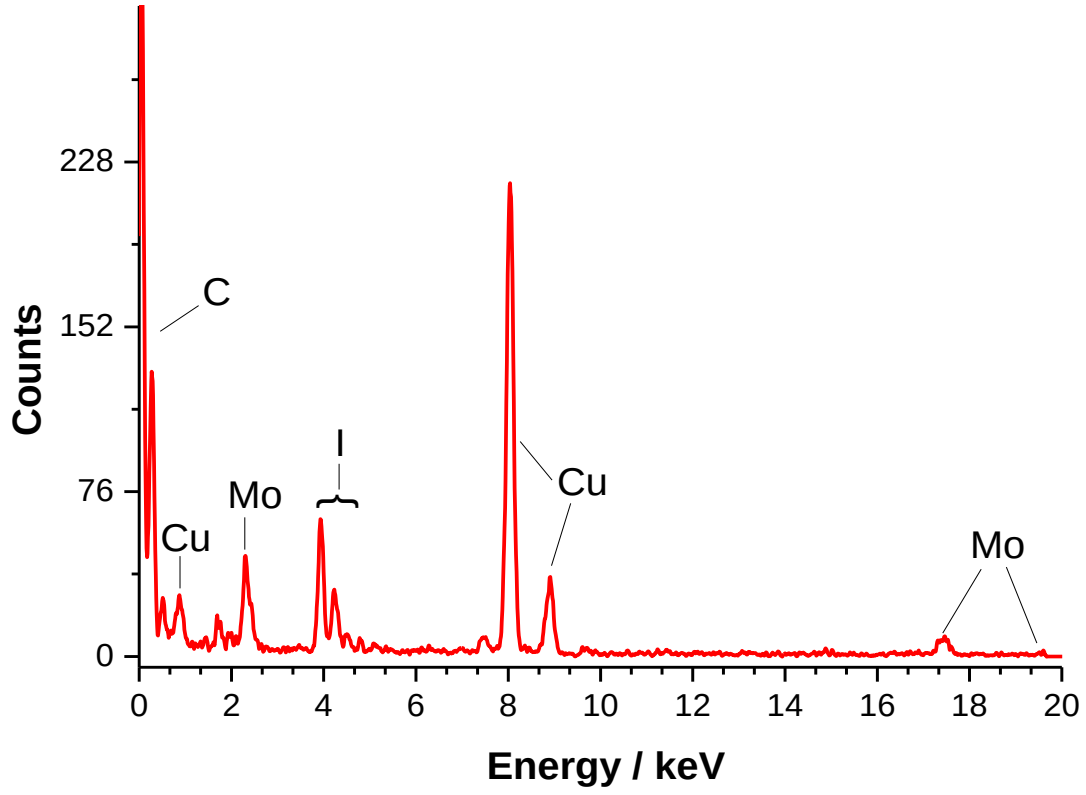


Figure 5-13. EDX spectrum of Mo_6I_{14}@SWNTs formed in Experiment 5-6. Characteristic X-ray peaks of Mo at 2.3, 17.5 keV and I 3.9 keV were identified. Cu peaks are due to the specimen holder.

EDX spectroscopy showed characteristic peaks of Mo and I at 2.3, 17.5 and 3.9 keV respectively confirming the presence of these elements within the material observed in SWNTs (Figure 5-13).

Time-series TEM imaging of Mo_6I_{14}@SWNTs showed that the arrays of high-contrast circular features translate along the nanotube channel with a fast rate (Figure 5-14, Video 3) supporting the presumption that they correspond to individual unconnected Mo_6I_{14} clusters.

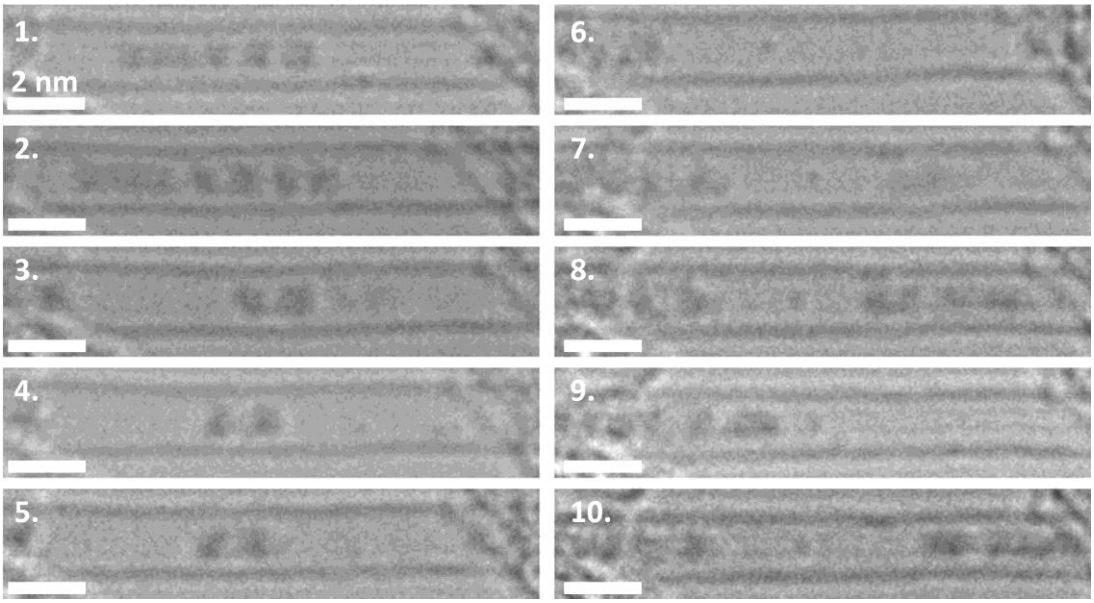


Figure 5-14. Time series TEM images of Mo_6I_{14}@SWNTs shows the movement of high-contrast circular features, corresponding to Mo_6I_{14} clusters, (d=0.7 nm) in SWNTs in MoI_2@SWNTs (Experiment 5-6). The scale bars are 2 nm (Video 3).

AC-TEM investigation of Mo_6I_{14}@SWNTs was able to resolve atomic structures of the clusters, showing star- and H-shaped features (Figure 5-15) identical to those found in W_6I_{14}@SWNTs (Figure 5-7). Based on TEM image simulation these features correspond to the projections of Mo_6I_{14} clusters in C_3 and tilted C_3 orientations (Figure 5-7 d-c).

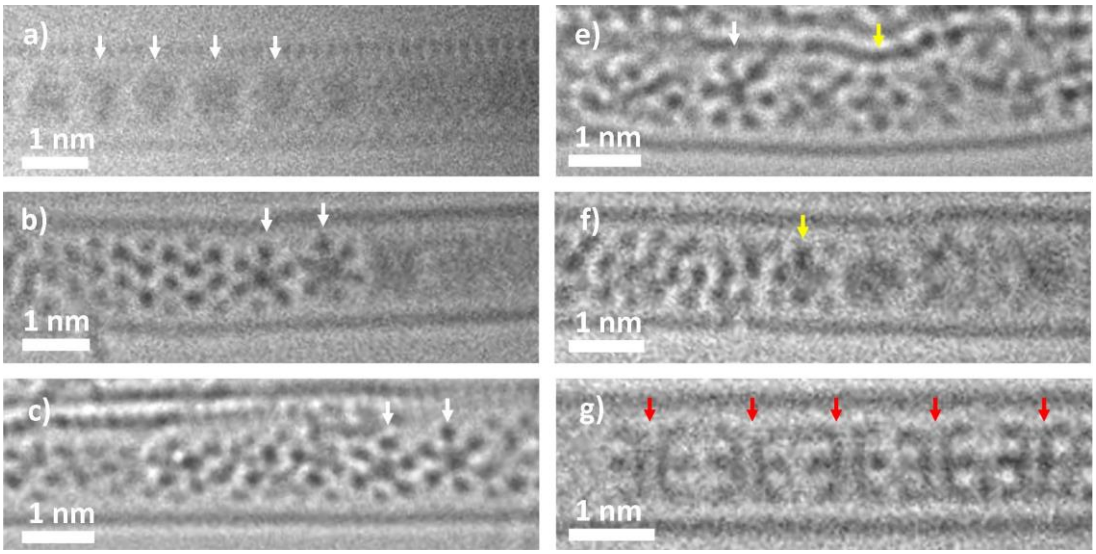


Figure 5-15. AC-TEM images of Mo_6I_{14}@SWNTs (Experiment 5-6) show a) high-contrast circular features. Images b)-e) show star-, ef) rhombus- and g) series of H-shaped features (indicated with white, yellow and red arrows, respectively) which correspond to the projections of C_3, C_4 or tilted C_3 orientations of Mo_6I_{14} clusters, respectively.

Time series imaging by AC-TEM of Mo_6I_{14}@SWNT, similarly to conventional TEM, showed that the Mo_6I_{14} clusters can move inside the SWNTs with a fast rate. More importantly, it was also revealed that prolonged e-beam irradiation of the Mo_6I_{14} clusters inside nanotubes causes a structural transformation of the molecules which appear to be polymerising into a continuous 1D crystal (Figure 5-16, Video 4). TEM image simulation was performed as described in Section 5.6.7 to investigate the structural relationship between Mo_6I_{14} clusters and the 1D crystal formed in SWNT. The comparison of a simulated TEM image for the proposed structure of the 1D crystal $[(Mo_6I^i_8I^{i\text{-}a}{}_2I^a{}_2)_{n+2}I_2]^{2-}$ (Figure 5-17 b) and an experimentally observed image show a good agreement and thus strongly supporting the formation of continuous 1D crystal from discrete Mo_6I_{14} clusters under the 80 kV electron beam (Figure 5-17).

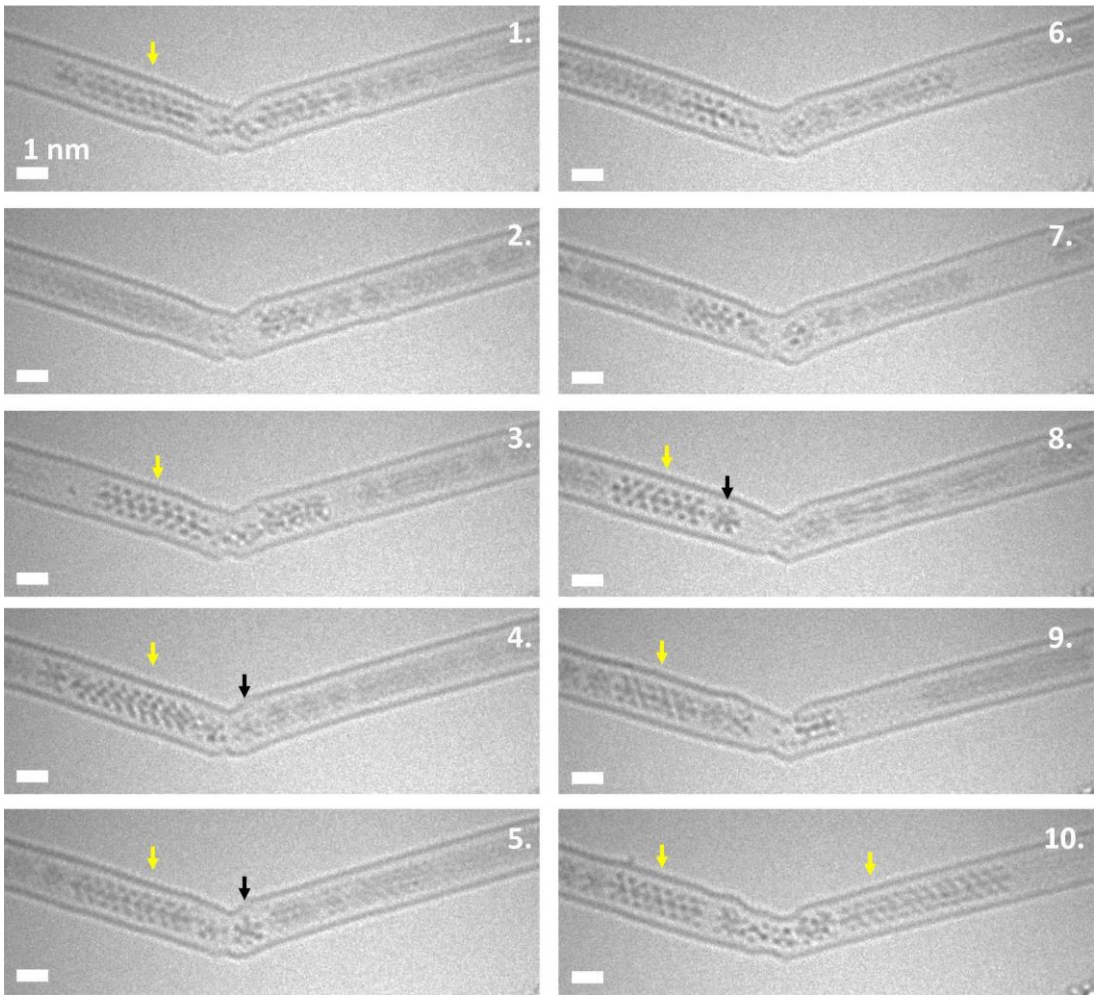


Figure 5-16. Time series imaging by AC-TEM of Mo_6I_{14}@SWNT showed that discrete star-shaped clusters (marked with black arrows) were temporarily merged into extended 1D crystals (marked with yelow arrows) due to the knock-on impact of the e-beam.

Raman spectroscopy showed that after encapsulating $Mo(CO)_6$ and I_2 inside SWNTs, ($Mo(CO)_6$, I_2)@SWNTs (Experiment 5-2), the G band of the nanotube is blueshifted to 1596 cm^{-1} by 15 cm^{-1} in comparison to the empty SWNTs (Figure 5-18, Table 5-2). Similar blueshifts were observed for the D (Figure 5-19) and G* bands (Figure 5-20) to an extent of 9 and 12 cm^{-1} respectively. No I_2 peaks were observed in the low frequency region of the spectrum (~210 cm^{-1}), however a new band was observed at ~100 cm^{-1} and the shape and maximum of the SWNT`s radial breathing mode (RBM) (156 cm^{-1}) was also altered (Figure 5-21) similarly to

$(W(CO)_6, I_2)$@SWNTs. These changes of the spectrum suggest that polyiodide ions such as I_m^- (m=5, 4, 3) were formed upon encapsulation of iodine, as I_3^- and I_5^- may contribute to the Raman spectrum in this frequency region.[16,7]

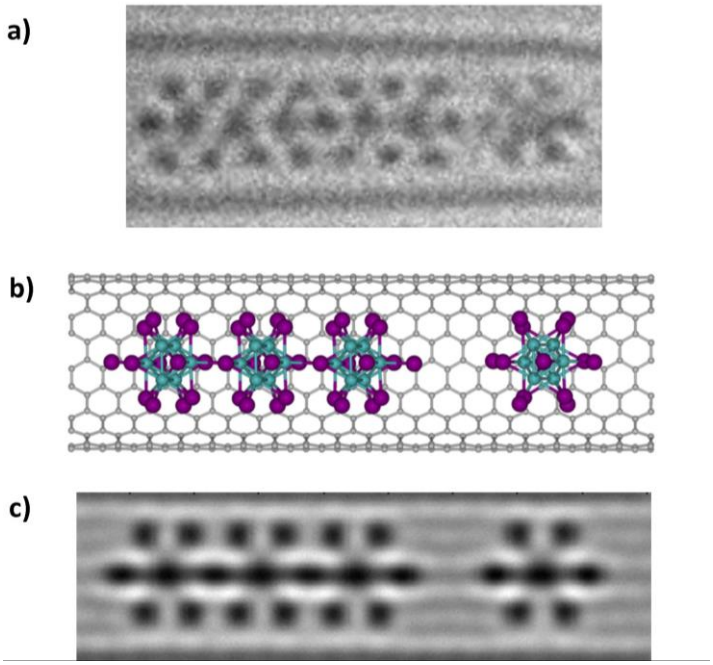


Figure 5-17. a) AC-TEM micrograph, b) structural model and c) simulated TEM micrograph of a section of a 1 D crystal ($Mo_{18}I_{36}$) formed in (10,10)SWNTs (Experiment 5-6) by joining three Mo_6I_{14} clusters after losing one I atom per cluster and forming covalent bonds *via* shared $I^{i\text{-}a}$ ligands. The incident e-beam is perpendicular to the sheet of paper. The green and purple spheres correspond to Mo and I atoms respectively.

Table 5-2. Raman spectroscopy data of empty SWNTs, $(Mo(CO)_6, I_2)$@SWNTs and Mo_6I_{14}@SWNTs.

	Vibrational mode / cm^{-1}						Shift vs SWNT / cm^{-1}				
	RBM		D	G	G*	$[Mo_6I_{14}]^{2-}$	RBM		D	G	G*
SWNTs	157	-	1330	1581	2660	-	-	-	-	-	-
$(Mo(CO)_6, I_2)$ @SWNT	161	-	1339	1596	2672	-	4	-	9	15	12
Mo_6I_{14}@SWNT	151	158	1339	1596	2672	59, 91, 107, 124	-6	1	9	15	12

Raman spectroscopy analysis of Mo_6I_{14}@SWNTs formed by thermal treatment of $(Mo(CO)_6, I_2)$@SWNTs (Experiment 5-6), showed a small change in the overall Raman spectrum. The

frequency of the G (Figure 5-18), D (Figure 5-19) and G* bands (Figure 5-20) were found to be identical to those observed in case of $(Mo(CO)_6, I_2)$@SWNT. In the low frequency region of the spectrum new bands were observed confirming the formation of $Mo_6I_8I_6^{2-}$ clusters (59, 91, 107, 123, 273 cm^{-1}) and I_2 molecules (210 cm^{-1}) (Figure 5-21, Table 5-2),[17] moreover, the shape of the RBM changed and became reminiscent of empty SWNTs. These results suggest that polyiodide molecules are no longer present in the material as iodine atoms have been consumed to form Mo_6I_{14} clusters in nanotubes.

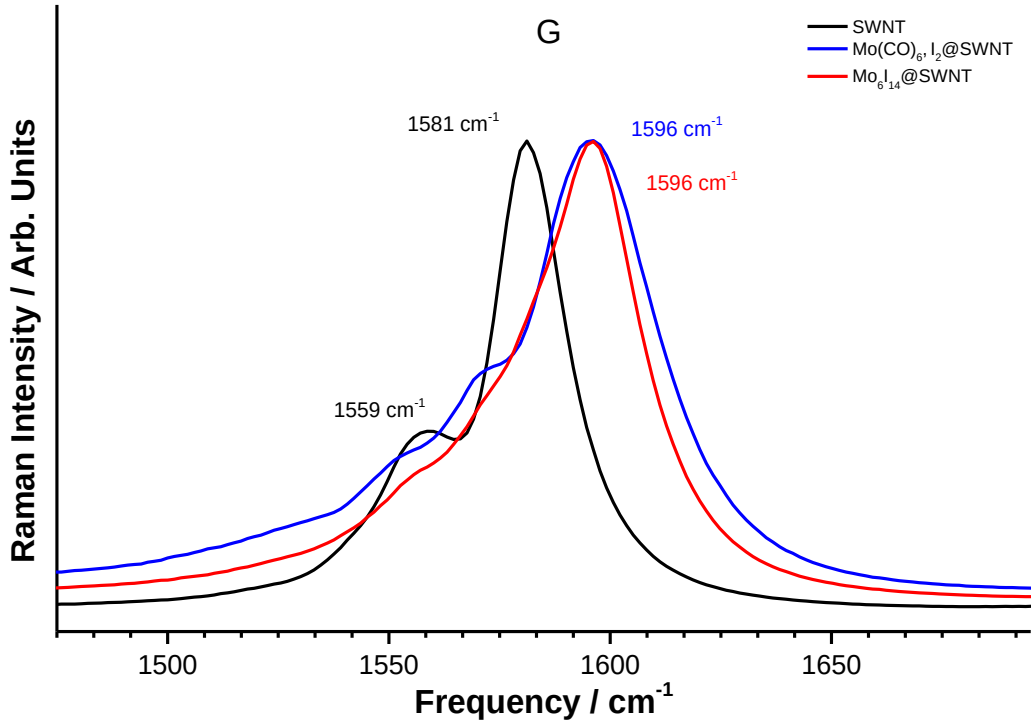


Figure 5-18. Raman spectra show the G band of empty SWNTs (1581 cm^{-1}, black), $(Mo(CO)_6, I_2)$@SWNTs (1596 cm^{-1}, blue) and Mo_6I_{14}@SWNT (1596 cm^{-1}, red) (λ=532 nm).

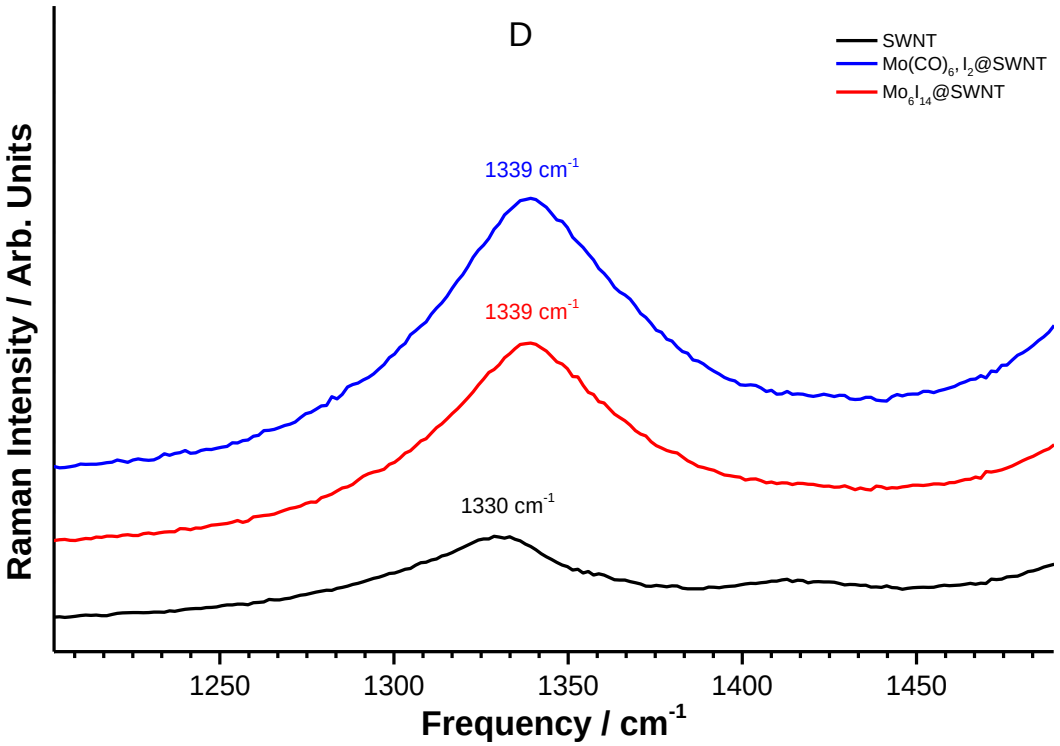


Figure 5-19. Raman spectra show the D band of empty SWNTs (1330 cm^{-1}, black), ($Mo(CO)_6$, I_2)@SWNTs (1339 cm^{-1}, blue) and Mo_6I_{14}@SWNT (1339 cm^{-1}, red) (λ=532 nm).

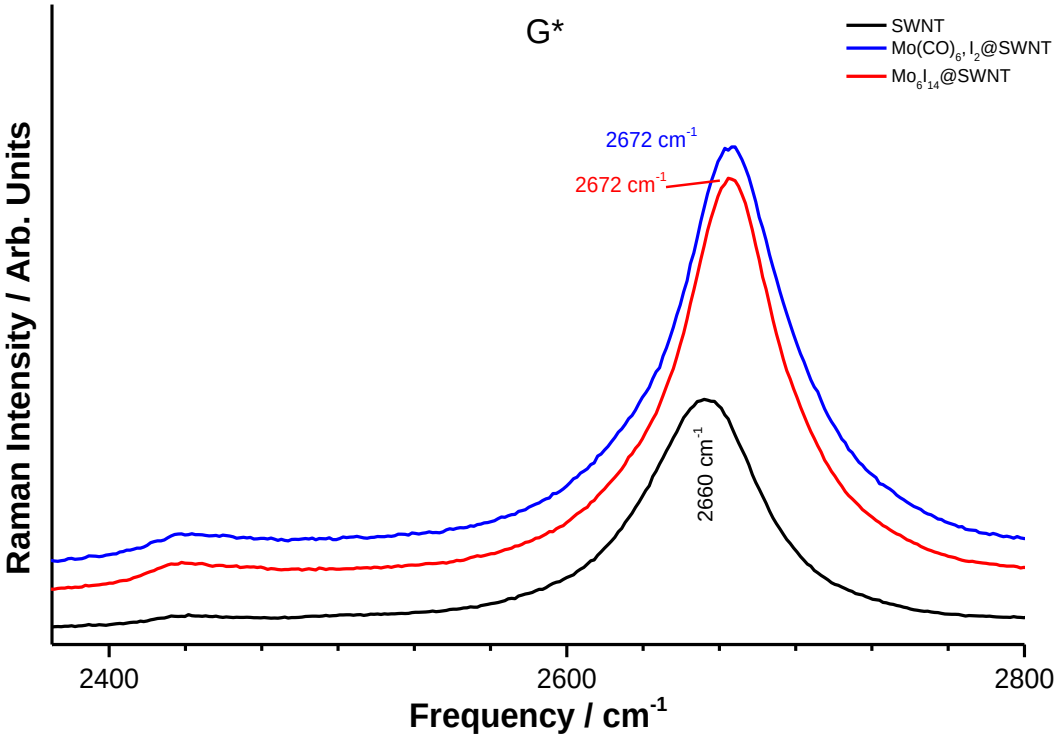


Figure 5-20. Raman spectra show the G* band of empty SWNTs (2660 cm^{-1}, black), ($Mo(CO)_6$, I_2)@SWNTs (2672 cm^{-1}, blue) and Mo_6I_{14}@SWNT (2672 cm^{-1}, red) (λ=532 nm).

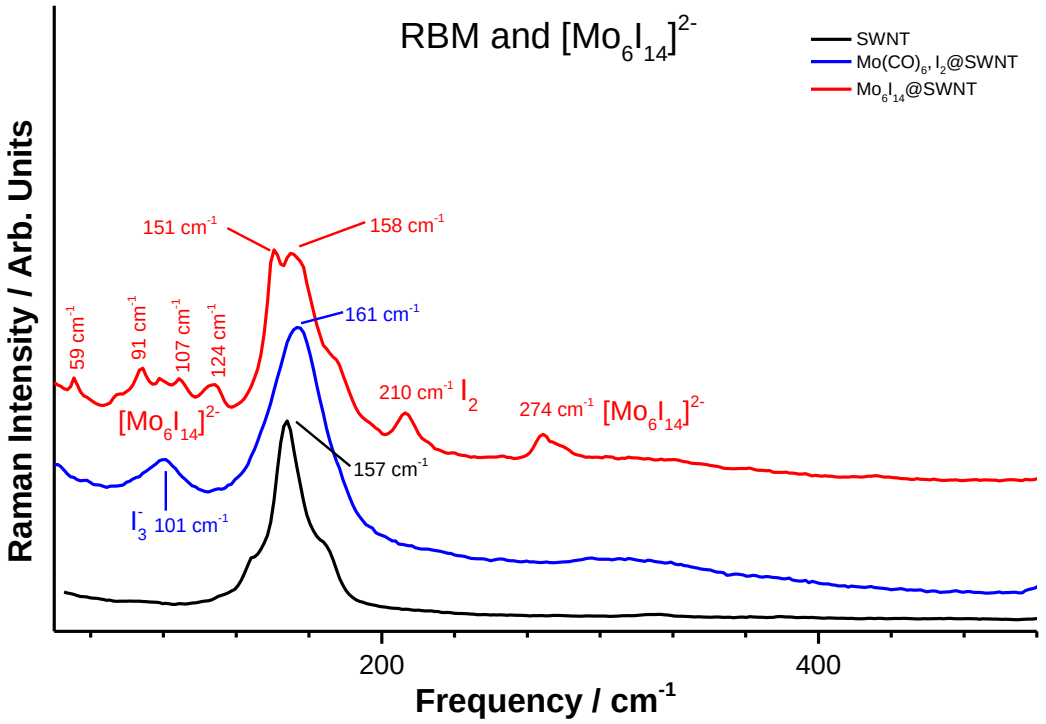


Figure 5-21. Raman spectra show the low frequency region containing RBM of empty SWNTs (157 cm^{-1}, black), ($Mo(CO)_6$, I_2)@SWNTs (161 cm^{-1}, blue) with a peak of I_3^- ions (101 cm^{-1}) and Mo_6I_{14}@SWNT (151, 158 cm^{-1}, red) in addition to peaks corresponding to Mo_6I_{14} clusters (59, 91, 107, 123, 274 cm^{-1}) and I_2 molecules (210 cm^{-1}) (λ=532 nm).

5.3.1.3 Characterisation of the material formed by the encapsulation of $Mo(CO)_6$ and I_2 in MWNTs

TEM analysis of the material, which was prepared by simultaneously encapsulating $Mo(CO)_6$ and I_2 from the gas phase in MWNTs (Experiment 5-1), showed dark contrast with no clearly defined structures inside the MWNTs (Figure 5-22). This material appears to consist of small aggregated nanoparticles (~1 nm) which were formed from I_2 and $Mo(CO)_6$ molecules under the e-beam, as discussed in previous chapters. EDX spectroscopy revealed characteristic peaks of Mo and I at 2.3, 17.5 and 3.9 keV (Figure 5-23) confirming their presence within the material observed in MWNTs as indication of successful encapsulation of $Mo(CO)_6$ and I_2 in MWNTs.

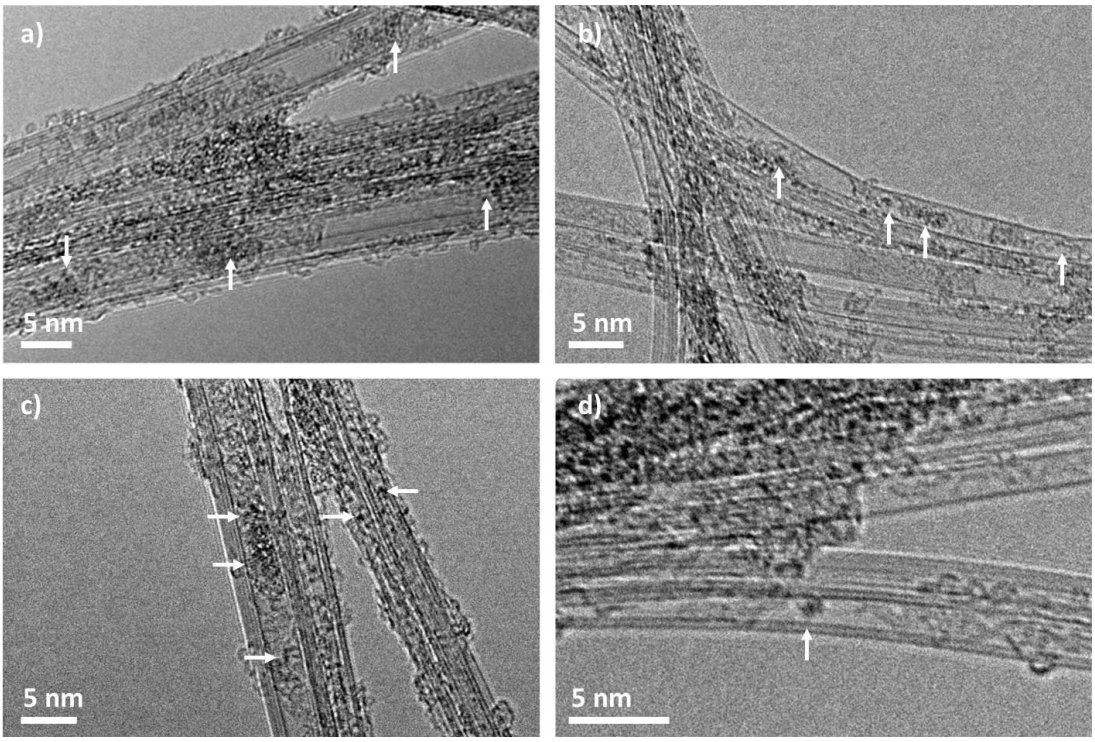


Figure 5-22. TEM images of ($Mo(CO)_6$, I_2)@MWNTs (formed in Experiment 5-1) showing high-contrast material with no particular structure inside the MWNTs.

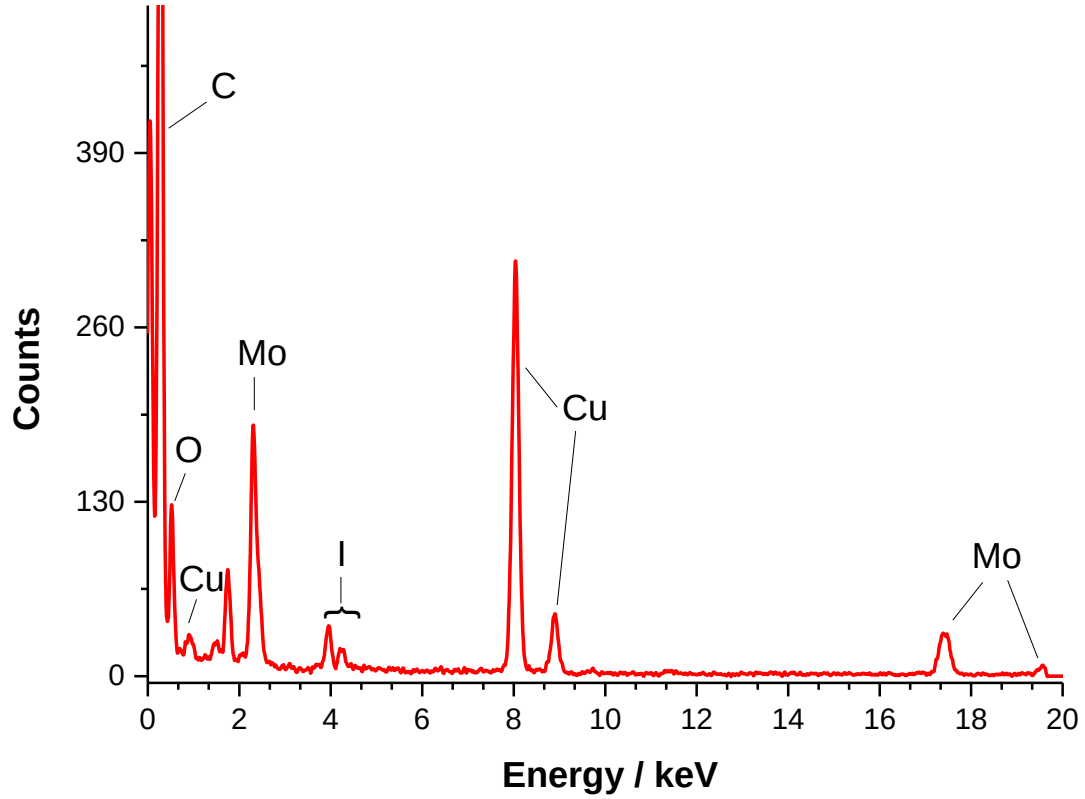


Figure 5-23. In the EDX spectrum of ($Mo(CO)_6$, I_2)@MWNTs (Experiment 5-1) characteristic X-ray peaks of Mo at 2.3, 17.5 keV and I 3.9 keV were identified. Cu peaks are due to the specimen holder.

5.3.1.4 Characterisation of the materials formed by reacting $Mo(CO)_6$ and I_2 in MWNTs and further calcination of the product

TEM investigation of the material which was prepared *via* the thermal treatment of ($Mo(CO)_6$, I_2)@MWNT (Experiment 5-5) showed high-contrast circular features in the channels of MWNTs (d_{NT} internal=2-5 nm) (Figure 5-24). The circular features have a diameter of 0.7 nm and their centres are located 0.8-0.9 nm from each other.

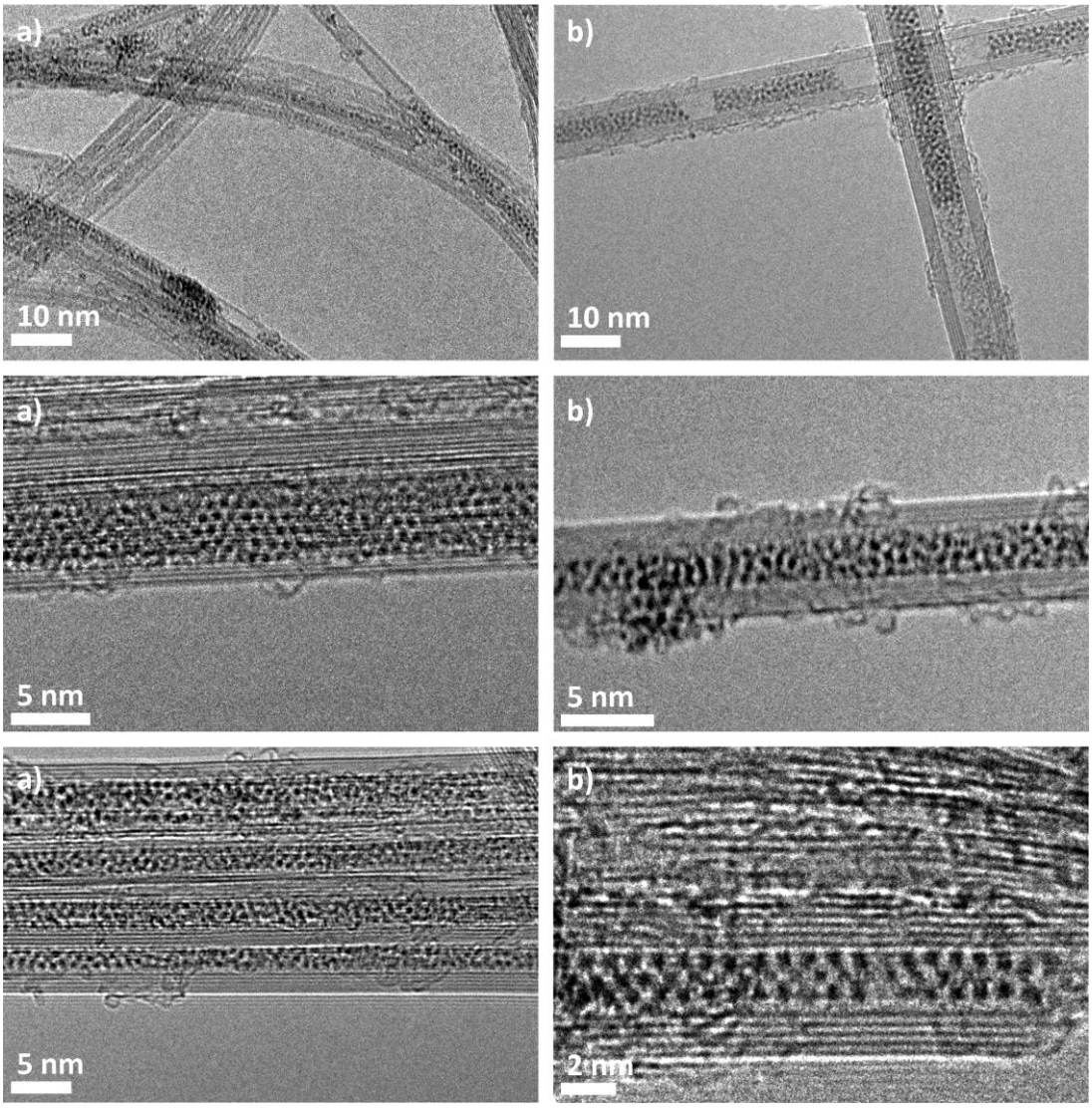


Figure 5-24. TEM images of the material formed *via* the thermal treatment of ($Mo(CO)_6$, I_2)@MWNT in Experiment 5-5 showing high-contrast circular features (d=0.7 nm) in the MWNTs (d_{NT} internal=2-5 nm) which might correspond to $[Mo_6I^i_8I^a_2I^{a\text{-}a}_{4/2}]$ clusters.

EDX spectroscopy showed characteristic peaks of Mo and I at 2.3, 17.5 and 3.9 keV confirming their presence in the encapsulated material (Figure 5-25) and suggesting that the circular features might correspond to $[Mo_6I^i_8]I^a_2I^{a\text{-}a}_{4/2}]$ clusters, the building units of MoI_2.

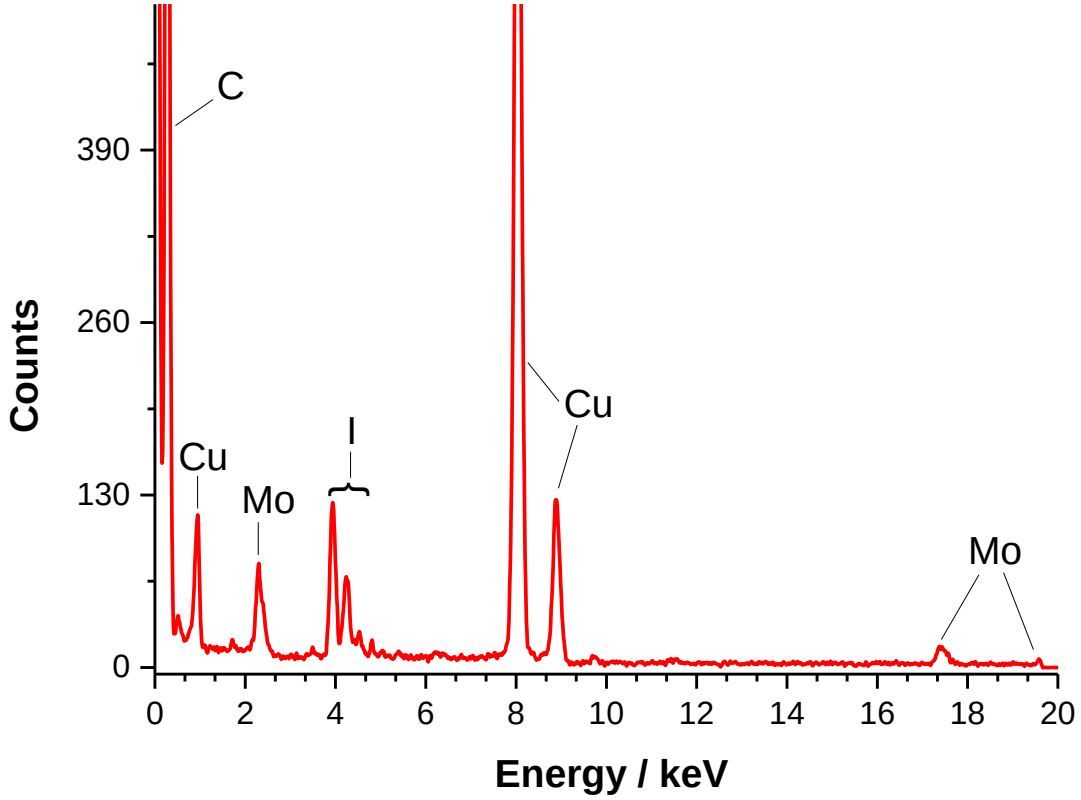


Figure 5-25. EDX spectrum of the martial formed *via* the thermal treatment of $(Mo(CO)_6, I_2)$@MWNT in Experiment 5-5. Characteristic X-ray peaks of Mo at 2.3, 17.5 keV and I 3.9 keV were identified. Cu peaks are due to the specimen holder.

As it was discussed in Chapter IV 4.3.3.1 bulk MoI_2, which belongs to A $2_1/b$ $2/a$ $2/m$ space group, possesses a layered structure (Figure 5-26 a) in which each layer is built from $[Mo_6I^i_8I^a_2I^{a\text{-}a}_{4/2}]$ clusters (Figure 5-26 b) interconnected by four bridging iodides ($I^{a\text{-}a}$ atoms), which are structurally closely related to $[M_6I_{14}]$ observed in SWNTs (Figure 5-12).[18] The comparison of the diameter (0.7 nm) and distance (0.8-0.9) nm of the circular

features observed by TEM in MWNTs (Figure 5-26 d-e) to the diameter (0.7 nm) and distance (0.9 nm) of the octahedral hexanuclear Mo clusters *i.e.* $[Mo_6I^i_8I^a_2I^{a\text{-}a}_{4/2}]$ located in the MoI_2 crystal (Figure 5-26 a-d) suggests that the arrays of high-contrast features in MWNTs correspond to layers of interconnected $[Mo_6I^i_8I^a_2I^{a\text{-}a}_{4/2}]$ clusters, similar to the bulk crystal.[18]

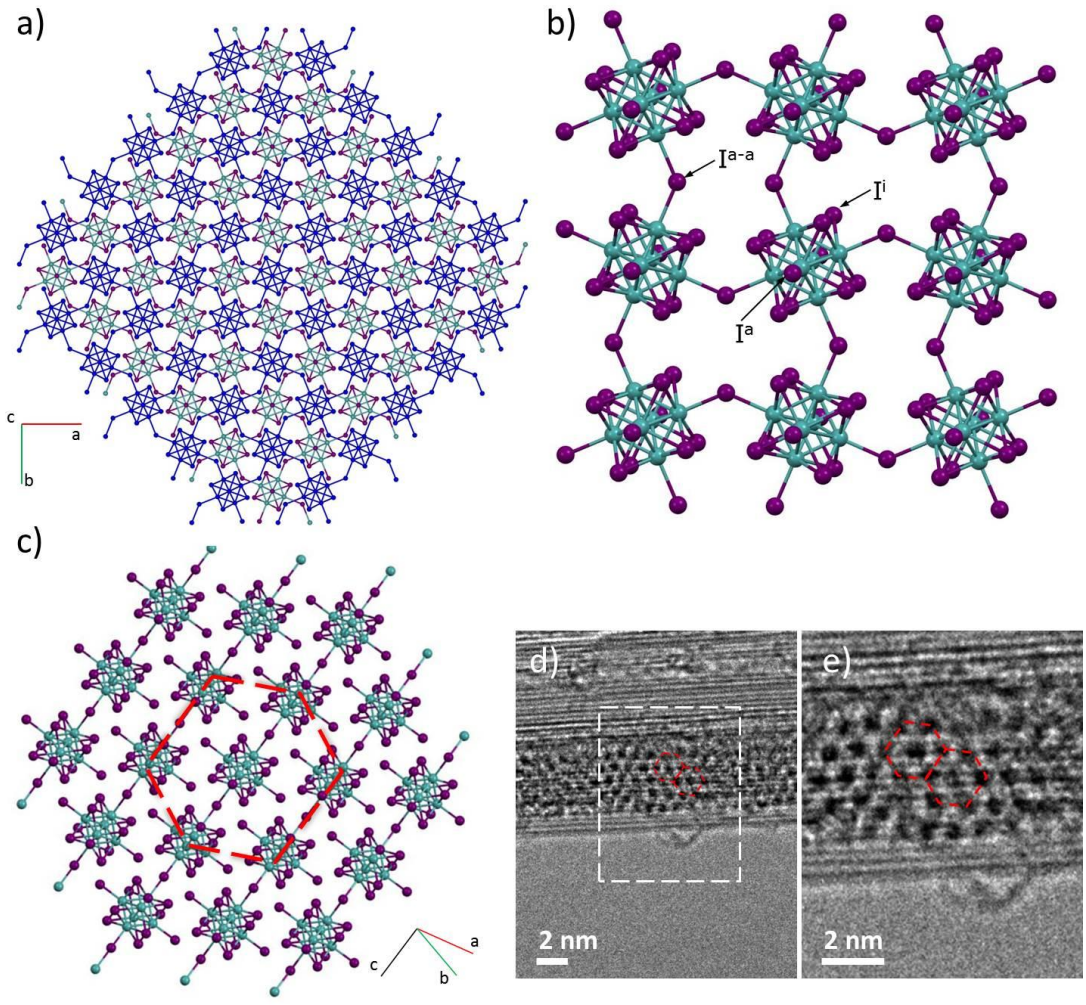


Figure 5-26. Images show: a) MoI_2 layers (ABA, B shown in blue) of bulk MoI_2 in A $2_1/b$ $2/a$ $2/m$ space group of symmetry, b) $[Mo_6I^i_8I^a_2I^{a\text{-}a}_{4/2}]$ octahedral hexanuclear Mo clusters which have 8 μ^3 face capping I^i atoms and 6 terminal I^a atoms from which 4 $I^{a\text{-}a}$ atoms are shared with the neighbouring clusters resulting in layers with an overall Mo:I ratio of 1:2. Both a) and b) show MoI_2 from the direction of *c* crystallographic axis. Structural diagram c) and TEM images d-e) show the structural model and TEM images of MoI_2 layers, respectively with red hexagons highlighting a structural motif observed in TEM images (d, e). The green and magenta colours represent Mo and I atoms, respectively.

The material was investigated with MALDI-ToF MS (as described in Section 5.6.9) and a series of complex peaks were observed with a regular difference of 127 Da suggesting a sequential I loss during the fragmentation process (Figure 5-27). Based on the comparison of the observed peaks and the calculated molecular weight (M) of Mo_xI_y fragments, the peaks may correspond to a series of Mo_xI_y clusters (Table 5-3) formed by the fragmentation of the $[Mo_6I^i_8I^a_2I^{a\text{-}a}_{4/2}]$ unit, which confirms the existence of these clusters in nanotubes and supports the proposed assignment of the TEM images *i.e.* the formation of $[Mo_6I^i_8I^a_2I^{a\text{-}a}_{4/2}]$@MWNTs.

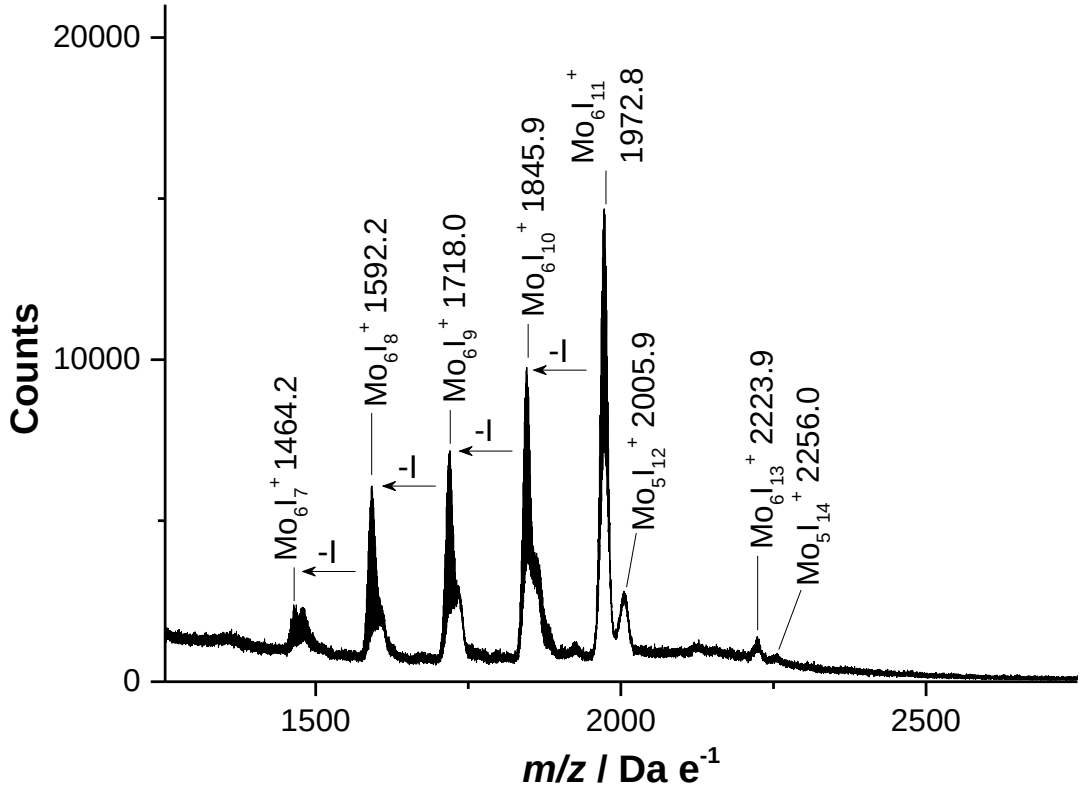


Figure 5-27. MALDI-ToF mass spectrum of $Mo_6I^i_8I^a_2I^{a\text{-}a}_{4/2}$@MWNTs, acquired in positive ionisation mode, showing a series of complex peaks with a periodic distance of 127 Da corresponding to a series of Mo_xI_y clusters formed by the fragmentation of $[Mo_6I^i_8I^a_2I^{a\text{-}a}_{4/2}]$.

Table 5-3. List of the fragments and the corresponding observed *m/z* values (including the observed mass difference $\Delta_{m/z}$) formed from Mo_6I_{14} clusters in MALDI-ToF MS in addition to their calculated molecular weight (M).

n_{Mo}	n_I	M / g mol^{-1}	*m/z* / Da e^{-1}	$\Delta_{m/z}$ / Da e^{-1}
6	14	2352	N/A	N/A
6	13	2225	2224	251
6	12	2099	N/A	
6	11	1972	1973	
6	10	1845	1846	127
6	9	1718	1719	127
6	8	1591	1592	127
6	7	1464	1464	128
5	14	2256	2256	250
5	13	2130	N/A	
5	12	2003	2006	

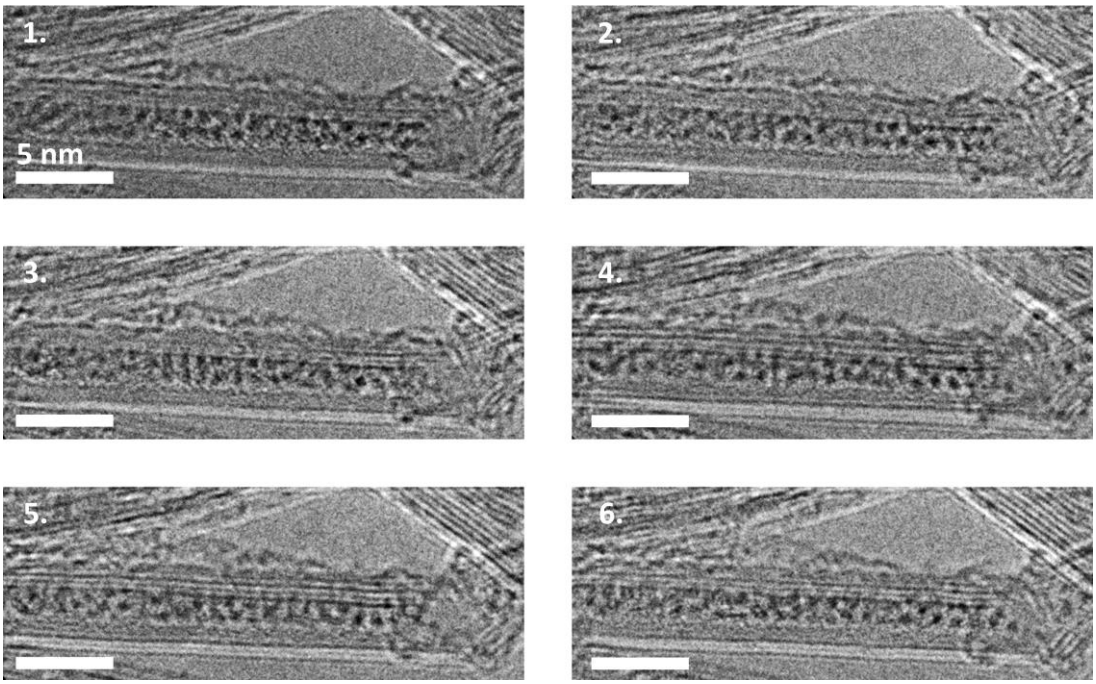


Figure 5-28. TEM image time series shows the structural changes of the high-contrast circular features (*d*=0.7 nm) corresponding to $[Mo_6I^i_8I^a_2I^{a\text{-}a}_{4/2}]$ in MWNT. The scale bars are 5 nm (Video 5).

Time series TEM imaging showed that the packing of the $[Mo_6I^i_8I^a_2I^{a\text{-}a}_{4/2}]$ clusters in MWNT is evolving over time *i.e.* the

clusters rotate and translate in the channels of MWNTs on the timescale of few seconds (ambient temperature, 80 kV) (Figure 5-28, Video 5). However, the motion of the clusters is rather slowly in comparison to Mo_6I_{14}@SWNTs.

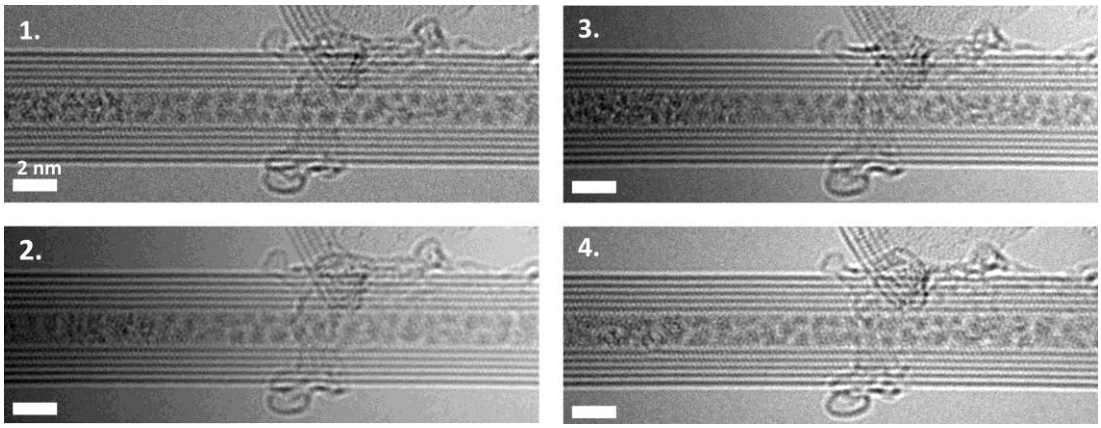


Figure 5-29. AC-TEM image series shows the movement of high-contrast circular features corresponding to Mo_6I_{14} clusters (d=0.7 nm) in calcined $[Mo_6I^i_8I^a_2I^{a\text{-}a}_{4/2}]$@MWNT (Experiment 5-13). The scale bars are 2 nm. (Video 6)

After high temperature calcination (Experiment 5-13) the material was further investigated with AC-TEM and the molybdenum iodide clusters in CNTs were found to be still rotating and translating, thus preventing their structural investigation with the atomic resolution (Figure 5-29, Video 6). Such mobility of the clusters suggests that inter-cluster bonding formed during the calcination procedure is not sufficiently strong to suppress molecular motion in MWNTs during TEM imaging.

5.3.2 Characterisation of the materials formed by reacting metal containing precursors encapsulated in CNTs with H_2S

5.3.2.1 Characterisation of the material formed by reacting $Mo(CO)_6$@SWNT with H_2S

TEM investigation of the material formed by reacting $Mo(CO)_6$@SWNTs with H_2S (Experiment 5-10) revealed high-contrast chains in narrow SWNTs (d_{NT}=0.9 nm) (Figure 5-31). The dynamic behaviour of the chains was investigated by acquiring a time series of TEM images showing that the chains twist and vibrate inside the SWNTs under the conditions of the TEM measurement (room temperature, acceleration voltage 100 kV) (Figure 5-31 a1-3, Video 7).

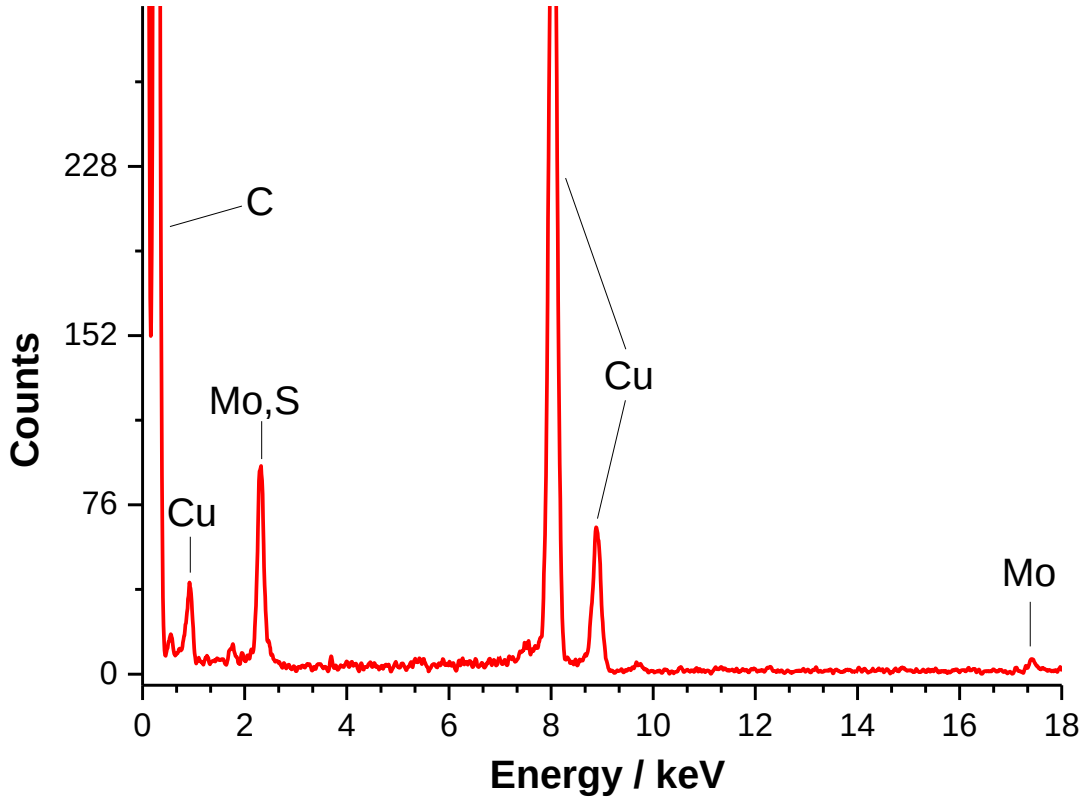


Figure 5-30. EDX spectrum of the material formed by reacting $Mo(CO)_6$@SWNTs with H_2S (Experiment 5-10). Characteristic X-ray peaks of Mo and S were identified at 2.3, 17.5 keV and 2.3 keV, respectively. Cu peaks are due to the specimen holder.

EDX spectroscopy of the material showed characteristic peaks of Mo and S at 2.3, 17.5 keV and 2.3 keV confirming their presence in the sample (Figure 5-30). This suggests that the chains observed in SWNTs consist of a MoS_2.

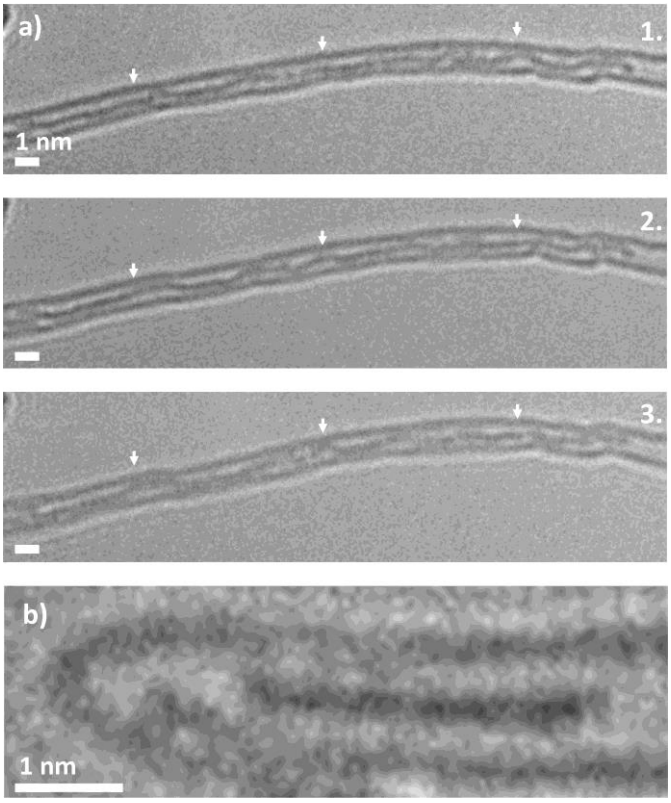


Figure 5-31. TEM images of MoS_2@SWNTs formed by reacting $Mo(CO)_6$@SWNTs with H_2S (Experiment 5-10). Image a)1-3 shows the vibration of a MoS_2 chain in a SWNT (d_{NT}=0.9 nm) (Video 7), while b) shows a MoS_2 chain in a SWNT (d_{NT}=0.9 nm).

5.3.2.2 Characterisation of the material formed by reacting Mo_6I_{14}@SWNT with H_2S

TEM investigation of the material formed by the reaction of H_2S with Mo_6I_{14}@SWNTs (Experiment 5-11) showed high-contrast parallel lines in SWNTs (d_{NT}=1.6 nm) separated by 0.6 nm from each other and ~0.4 nm from the sidewalls of the nanotube (Figure 5-32 a). The distance of the dark lines is in agreement with the interlayer separation of 002 MoS_2 layers (0.62 nm), as

discussed in Chapter I and IV,[19] suggesting that they correspond to the projection of a two-layer thick MoS_2NR which is in edge-on orientation in respect to the incident e-beam as demonstrated in Figure 5-32 b.

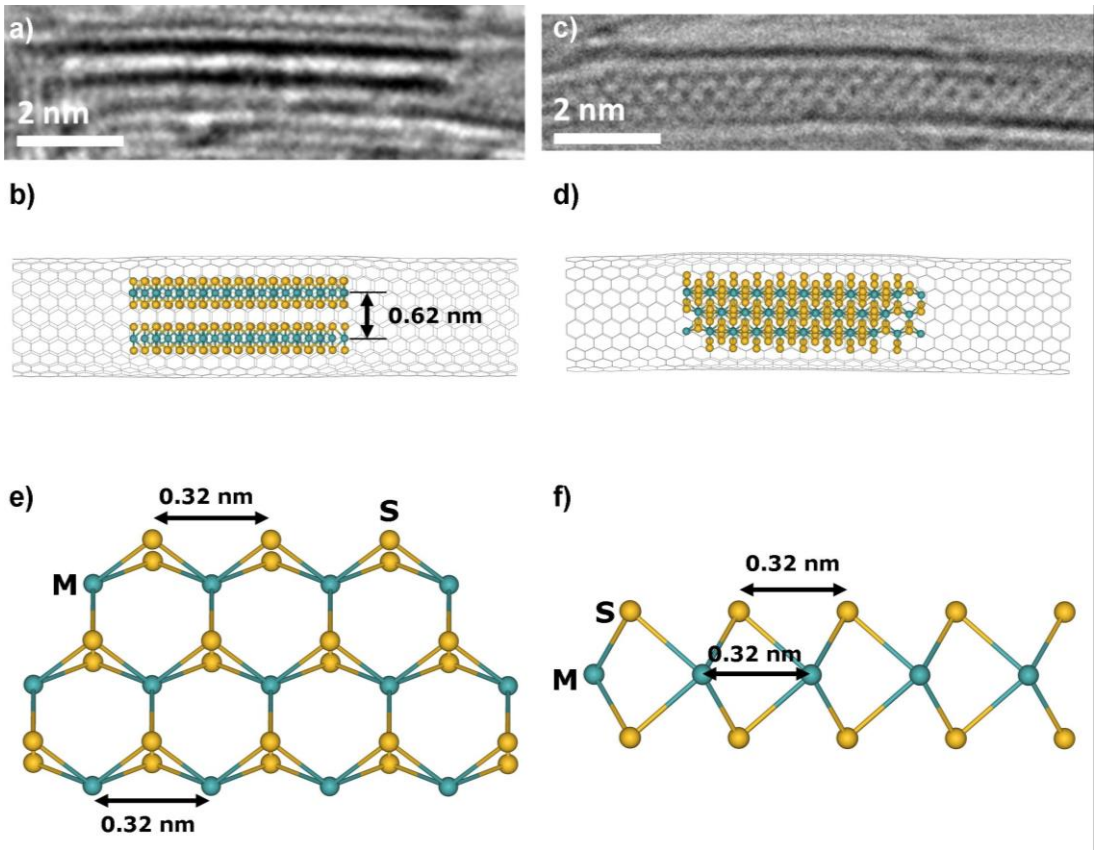


Figure 5-32. Images show a) TEM micrograph of parallel dark lines with a *d* spacing of 0.6 nm corresponding to a two layer thick MoS_2NR in SWNT (d_{NT}=1.6 nm) and b) a model demonstrating the structure. Images show c) a hexagonal atomic lattice corresponding to a two layer thick tilted MoS_2NR, as demonstrated on d) Model the hexagonal MS_2 lattice in face- and edge-on orientation showing the typical distance (0.32 nm) between adjacent M or S atoms. The green and yellow spheres correspond to Mo and S atoms respectively.

If a MoS_2NR were positioned with its 002 lattice plane perpendicular to the e-beam, TEM imaging would show a hexagonal atomic lattice with a period of 0.32 nm (Figure 5-32 e). However, as the observed (~0.4 nm) and typical (0.32 nm) periods do not match the projection observed in TEM (Figure 5-32 c) is most likely corresponding to a two-layer thick MoS_2NR which is not

in a face-on nor edge-on orientation in respect to the incident e-beam (Figure 5-32 d). EDX spectroscopy of the material formed in SWNT showed characteristic peaks of Mo and S at 2.3, 17.5 keV and 2.3 keV confirming their presence in the sample (Figure 5-33) which supports that the NRs in the SWNTs consist of MoS_2.

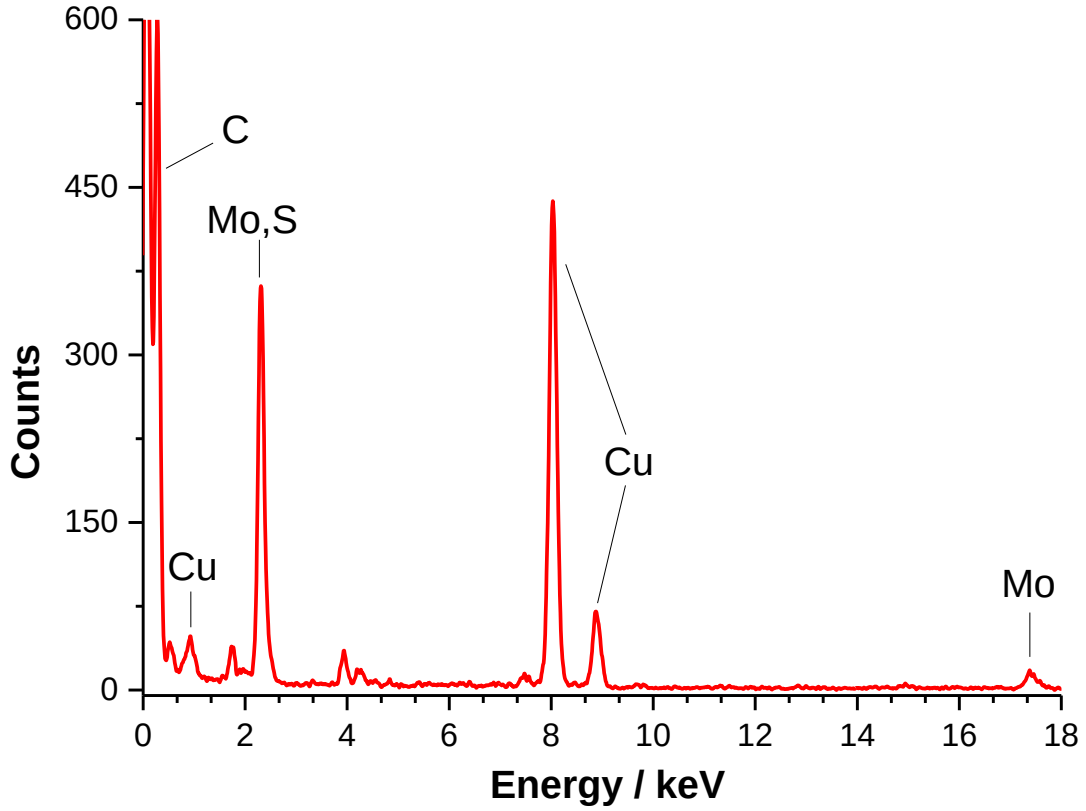


Figure 5-33. EDX spectrum of the material formed by reacting Mo_6I_{14}@SWNTs with H_2S (Experiment 5-11). Characteristic X-ray peaks of Mo and S were identified at 2.3, 17.5 keV and 2.3 keV, respectively. Cu peaks are due to the specimen holder.

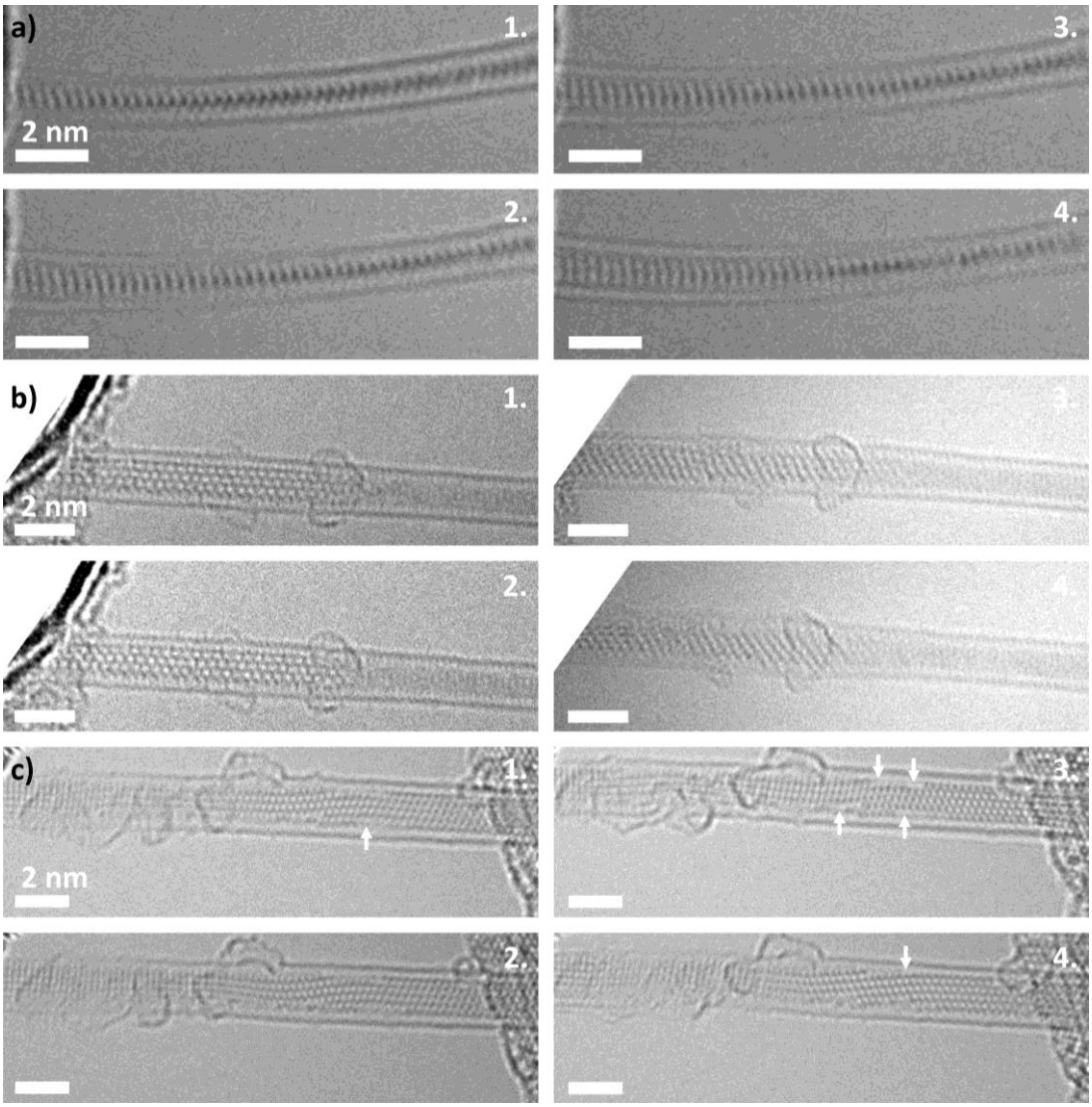


Figure 5-34. AC-TEM images show time series of a)1-4 ~1 nm wide twisted monolayer MoS_2NR (d_{NT}=1.2 nm), b)1-4 0.9 nm wide face-on monolayer MoS_2NR and c)1-4 structural changes of defects (marked with arrows) on the edge of a 1.2 nm wide MoS_2NR.

AC-TEM analysis showed twisted monolayer MoS_2NR with ~1 nm maximum width in a relatively narrow SWNT (d_{NT}=1.2 nm) (Figure 5-34 a1-4). Face-on MoS_2NR (width=0.9 nm) was also observed in SWNT (d_{NT}=1.6 nm) with hexagonal atomic lattice with a typical period of 0.32 nm between adjacent Mo atoms (Figure 5-34 b1-4). In addition, time series AC-TEM imaging showed defects on the edge of a 1.2 nm wide MoS_2NR in a SWNT (d_{NT}=2.0 nm), most likely induced by the knock on damage of the

e-beam, which were structurally changing during imaging (Figure 5-34 c1-4).

The host-guest interaction between the SWNTs and the material formed by reacting Mo_6I_{14}@SWNTs with H_2S (Experiment 5-11) was investigated with Raman spectroscopy. The G band was found to be blueshifted (1589 cm^{-1}) compared to empty SWNTs, but to a significantly smaller extent (8 cm^{-1}) than in the case of iodine containing samples (Figure 5-35, Table 5-4).

Similar blueshifts were observed for the D (Figure 5-36) and G* bands (Figure 5-37) to an extent of 8 and 9 cm^{-1} respectively (Table 5-4). The RBM of the SWNTs was found to be blueshifted by 7 cm^{-1} to (164 cm^{-1}), and two new peaks were observed (373, 400 cm^{-1}) which may be assigned to the in plane E_{2g} and out-of-plane A_{1g} vibrations of the newly formed MoS_2 (Figure 5-38, Table 5-4).[15] Moreover, no bands corresponding to the Mo_6I_{14} clusters was observed in the spectrum of the material indicating the complete transformation of Mo_6I_{14}@SWNTs into MoS_2@SWNTs.

Table 5-4. Raman spectroscopy data of empty SWNTs, $(Mo(CO)_6, I_2)$@SWNTs, Mo_6I_{14}@SWNTs and MoS_2@SWNTs.

	Vibrational mode / cm^{-1}							Shift vs SWNT / cm^{-1}				
	RBM		D	G	G*	$[Mo_6I_{14}]^{2-}$	MoS_2	RBM		D	G	G*
SWNT	157	-	1330	1581	2660	-	-	-	-	-	-	-
$(Mo(CO)_6, I_2)$ @SWNT	161	-	1339	1596	2672	-	-	4	-	9	15	12
Mo_6I_{14}@SWNT	151	158	1339	1596	2672	59, 91, 107, 124	-	-6	1	9	15	12
MoS_2@SWNT	164	-	1338	1589	2669	-	373, 400	7	-	8	8	9

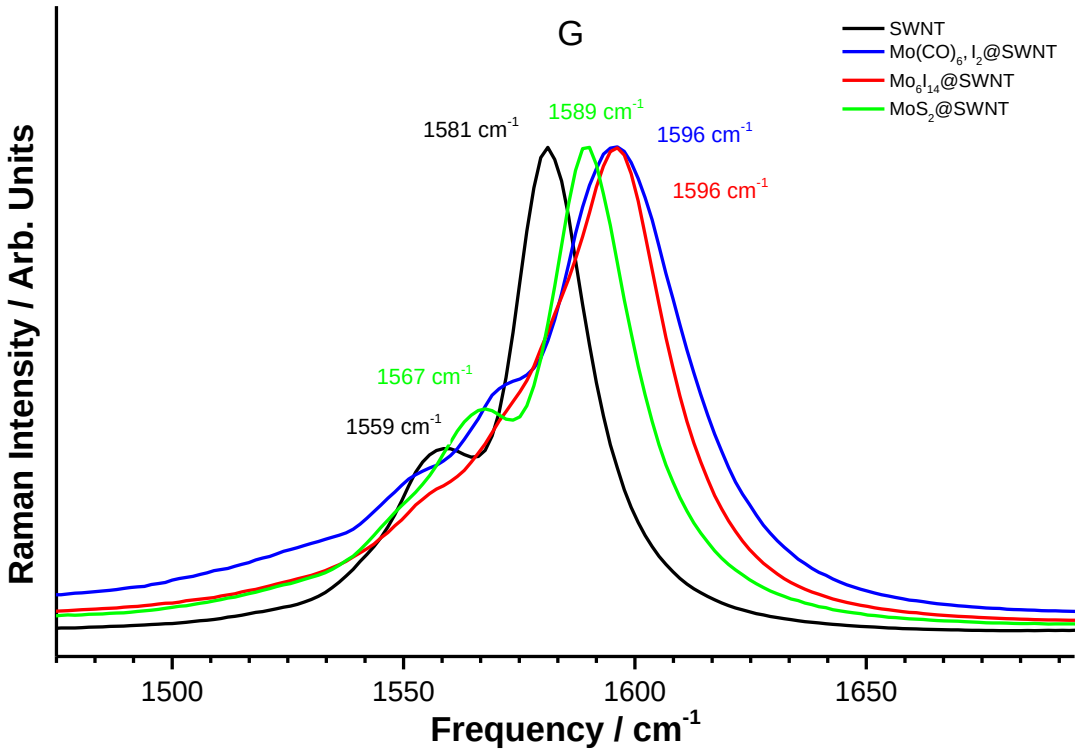


Figure 5-35. Raman spectra show the G band of empty SWNTs (1581 cm^{-1}, black), ($Mo(CO)_6$, I_2)@SWNTs (1596 cm^{-1}, blue), Mo_6I_{14}@SWNT (1596 cm^{-1}, red) and MoS_2@SWNT (1589 cm^{-1}, green) (λ=532 nm).

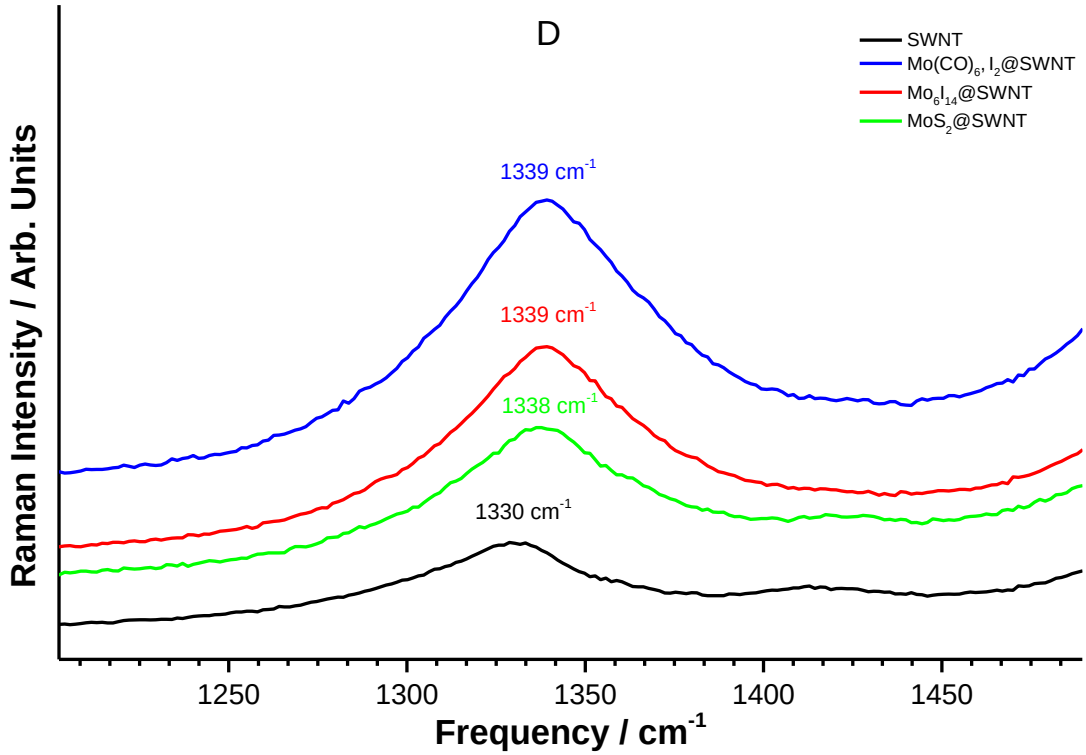


Figure 5-36. Raman spectra show the D band of empty SWNTs (1330 cm^{-1}, black), ($Mo(CO)_6$, I_2)@SWNTs (1339 cm^{-1}, blue) Mo_6I_{14}@SWNT (1339 cm^{-1}, red) and MoS_2@SWNT (1338 cm^{-1}) (λ=532 nm).

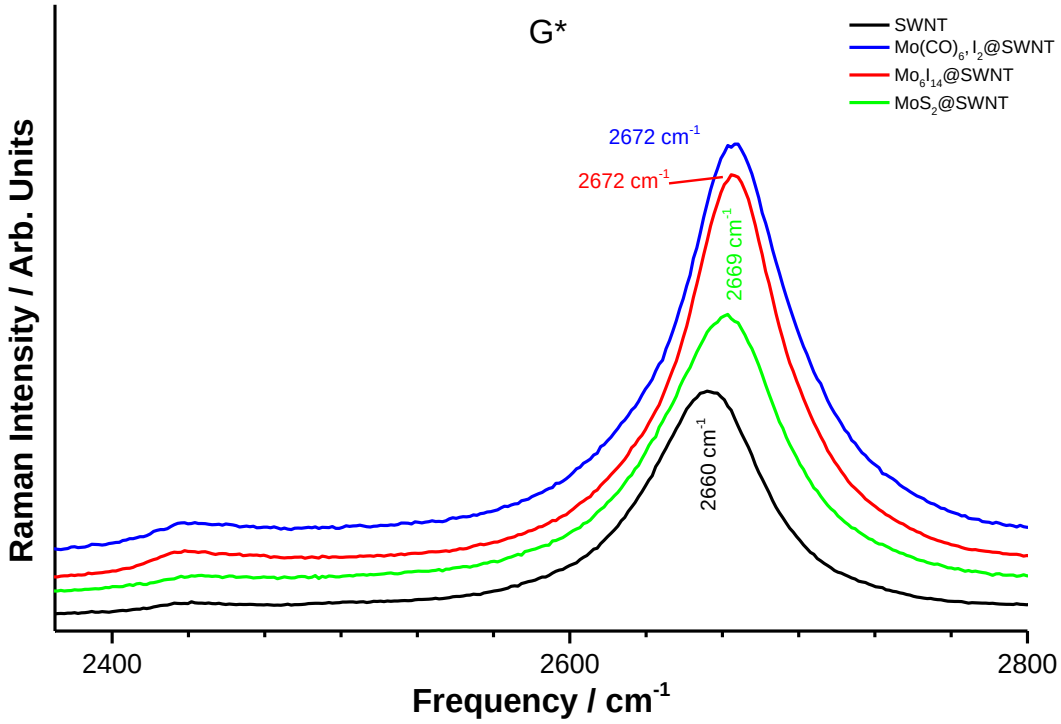


Figure 5-37. Raman spectra show the G* band of empty SWNTs (2660 cm^{-1}, black), ($Mo(CO)_6$, I_2)@SWNTs (2672 cm^{-1}, blue) Mo_6I_{14}@SWNT (2672 cm^{-1}, red) and MoS_2@SWNT (2669 cm^{-1}) (λ=532 nm).

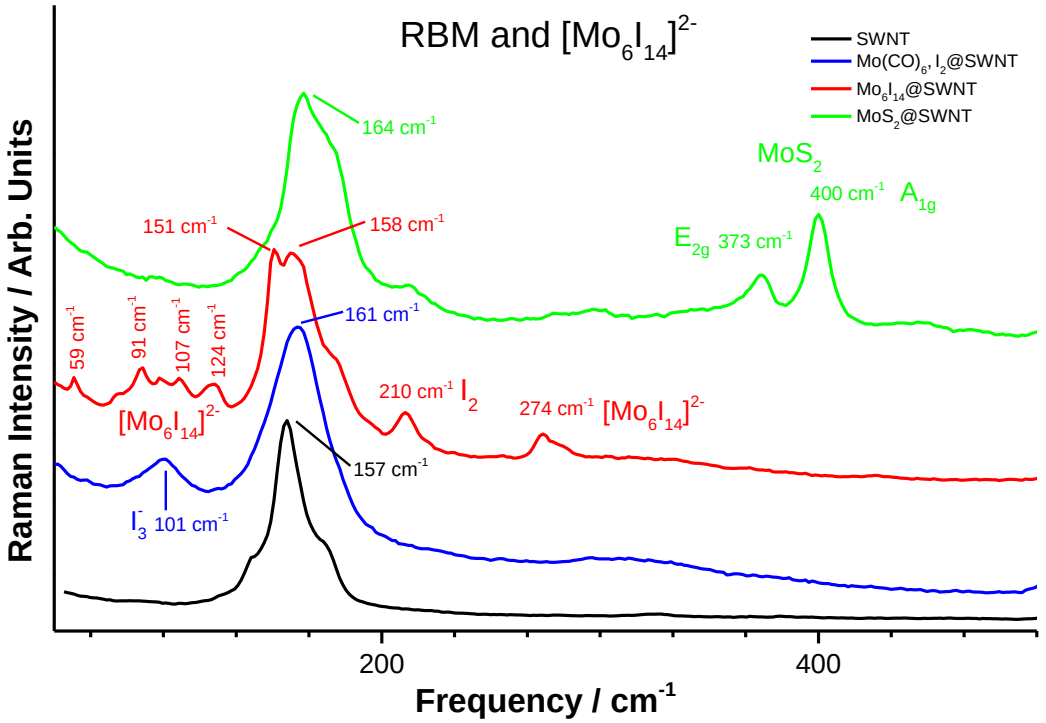


Figure 5-38. Raman spectra show the low frequency region containing RBM of empty SWNTs (157 cm^{-1}, black), ($Mo(CO)_6$, I_2)@SWNTs (161 cm^{-1}, blue) and a peak corresponding to I_3^- ions (101 cm^{-1}), Mo_6I_{14}@SWNT (151, 158 cm^{-1}, red) in addition to peaks corresponding to Mo_6I_{14} clusters (59, 91, 107, 123, 273 cm^{-1}, red) and I_2 molecules (210 cm^{-1}) and MoS_2@SWNT (164 cm^{-1}) in addition to peaks corresponding to the E_{2g} and A_{1g} vibrations of MoS_2 (373, 400 cm^{-1}) (λ=532 nm).

5.3.2.3 Characterisation of the materials formed by reacting W_6I_{14}@SWNT with H_2S

TEM investigation of the material formed by the reaction of H_2S with W_6I_{14}@SWNTs (Experiment 5-12) showed a dark continuous contrast in the SWNTs (d_{NT}=1.5 nm), but no structural information could be extracted from the images (Figure 5-39 a). EDX analysis showed characteristic peaks of W and S at 1.4, 1.8, 8.4, 9.6 keV and 2.3 keV, respectively confirming their presence in the nanotube, while and no peak corresponding to I was observed suggesting the successful transformation of W_6I_{14}@SWNTs into WS_2@SWNTs (Figure 5-40).

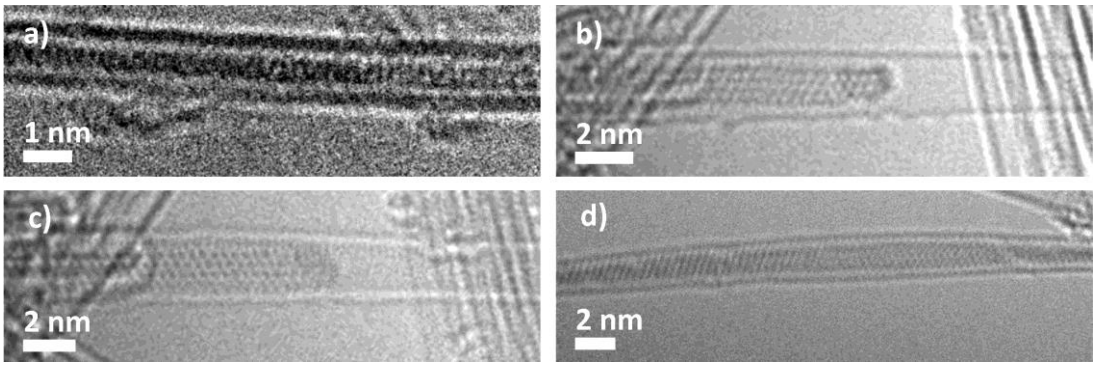


Figure 5-39. TEM images of the material formed by the reaction of H_2S with W_6I_{12}@SWNTs (Experiment 5-12) show a) dark continuous contrast in a SWNT, while AC-TEM images, b)-d) show hexagonal atomic lattice with a typical period of 0.32 nm between adjacent atoms suggesting that the dark spots correspond to W atoms of a WS_2NR.

AC-TEM investigation of the material showed hexagonal atomic lattice in SWNTs (d_{NT}=1.6 nm) which have a typical period of 0.32 nm between adjacent atoms (Figure 5-39 b-d), both being a typical structural property of the WS_2 lattice.[6] It has to be noted that no dark parallel lines were observed in SWNTs which would correspond to multilayers of WS_2 suggesting the exclusive formation of monolayer WS_2NR in SWNTs.

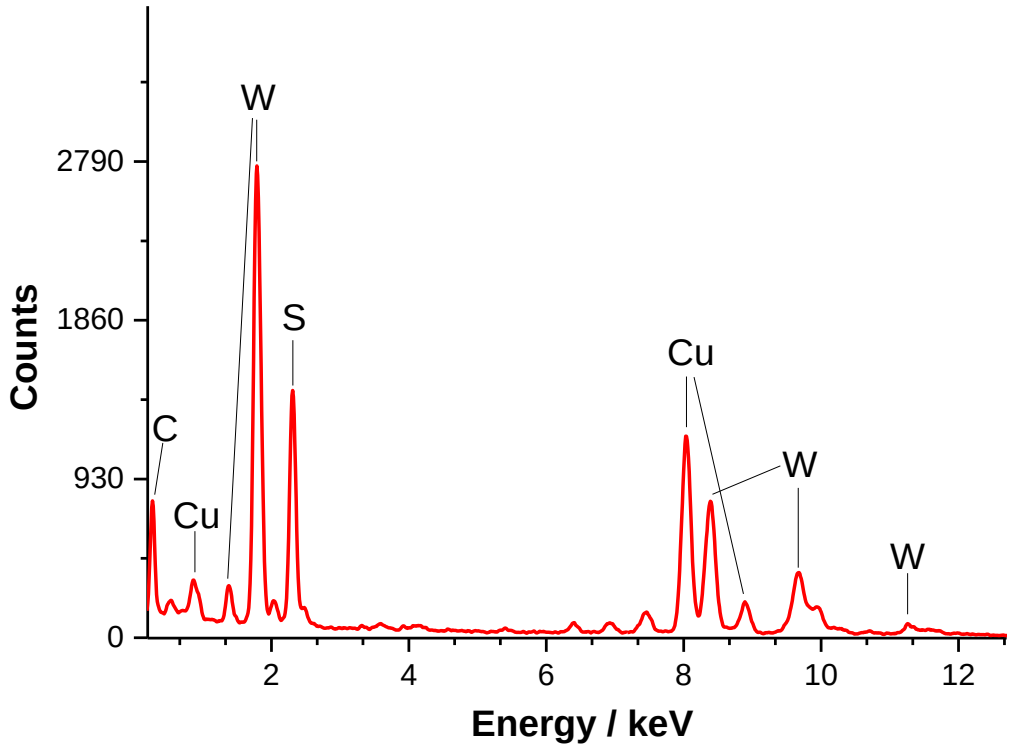


Figure 5-40. EDX spectrum of the material formed by reacting W_6I_{14}@SWNTs with H_2S (Experiment 5-12). Characteristic X-ray peaks of W and S were identified at 1.4, 1.8, 8.4, 9.6 keV and 2.3 keV, respectively. Cu peaks are due to the specimen holder.

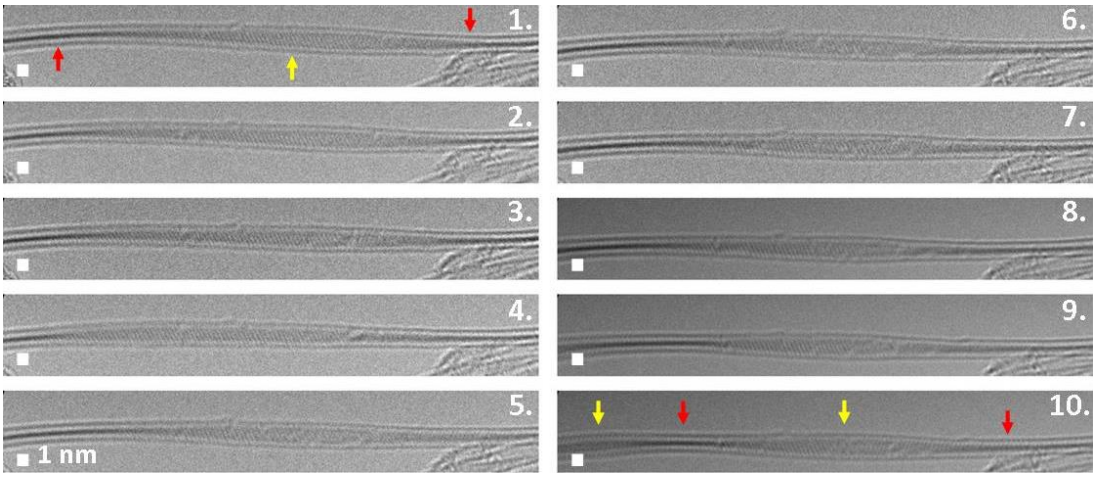


Figure 5-41. Time series AC-TEM images show how the dynamically twisting WS_2NR causes a elliptical distortion of SWNT (projections of nanotube diameters fluctuate between $d_{NT\ max}$=1.7 nm and $d_{NT\ min}$=1.0 nm). Narrow high intensity contrast in SWNTs corresponds to an edge-on orientation of WS_2NR and the wide sections with hexagonal atomic lattice correspond to a face-on orientation of WS_2NR with respect to the viewing plane (marked with yellow and red arrows respectively) (Video 8).

Time series AC-TEM imaging showed that WS_2NRs are dynamically twisting in SWNTs, which distorts the cylindrical SWNT with a nominal diameter of 1.4 nm to an elliptic shape with TEM

projections measured between 1.7 and 1.0 nm (Figure 5-41, Video 8).

The host-guest interaction between the SWNTs and the material formed by reacting W_6I_{14}@SWNTs with H_2S (Experiment 5-12) was investigated with Raman spectroscopy. It was found that the G band remains blueshifted (1583 cm^{-1}) compared to empty SWNTs, but to a significantly smaller extent (2 cm^{-1}) in comparison to the two iodine containing samples (Figure 5-42, Table 5-5). A similar blueshift was observed in case of D (Figure 5-43) band (3 cm^{-1}), while the frequency of the G* band (Figure 5-44) was found to be identical to that of empty SWNTs. In the low frequency region of the Raman spectrum the RBM of the SWNTs was found to be blueshifted by 3 cm^{-1} to (160 cm^{-1}), and two new peaks were observed (344, 410 cm^{-1}) which can be assigned to the E_{2g} and A_{1g} vibrations of the newly formed WS_2 (Figure 5-45, Table 5-5).[6] In addition, all the bands corresponding to the W_6I_{14} clusters became completely absent indicating the complete transformation of W_6I_{14}@SWNTs into WS_2@SWNTs.

Table 5-5. Raman spectroscopy data of empty SWNTs, $(W(CO)_6, I_2)$@SWNTs, W_6I_{14}@SWNTs and WS_2@SWNTs.

	Vibrational mode / cm^{-1}							Shift vs SWNT / cm^{-1}				
	RBM		D	G	G*	$[W_6I_{14}]^{2-}$	WS_2	RBM		D	G	G*
Empty SWNTs	157	-	1330	1581	2660	-	-	-	-	-	-	-
$(W(CO)_6, I_2)$ @SWNTs	163	-	1338	1602	2672	-	-	6	-	8	21	12
W_6I_{14}@SWNTs	148	158	1342	1596	2677	76, 88, 94 117	-	-9	1	12	15	17
WS_2@SWNT	160	-	1333	1583	2660	-	344, 410	3	-	3	2	0

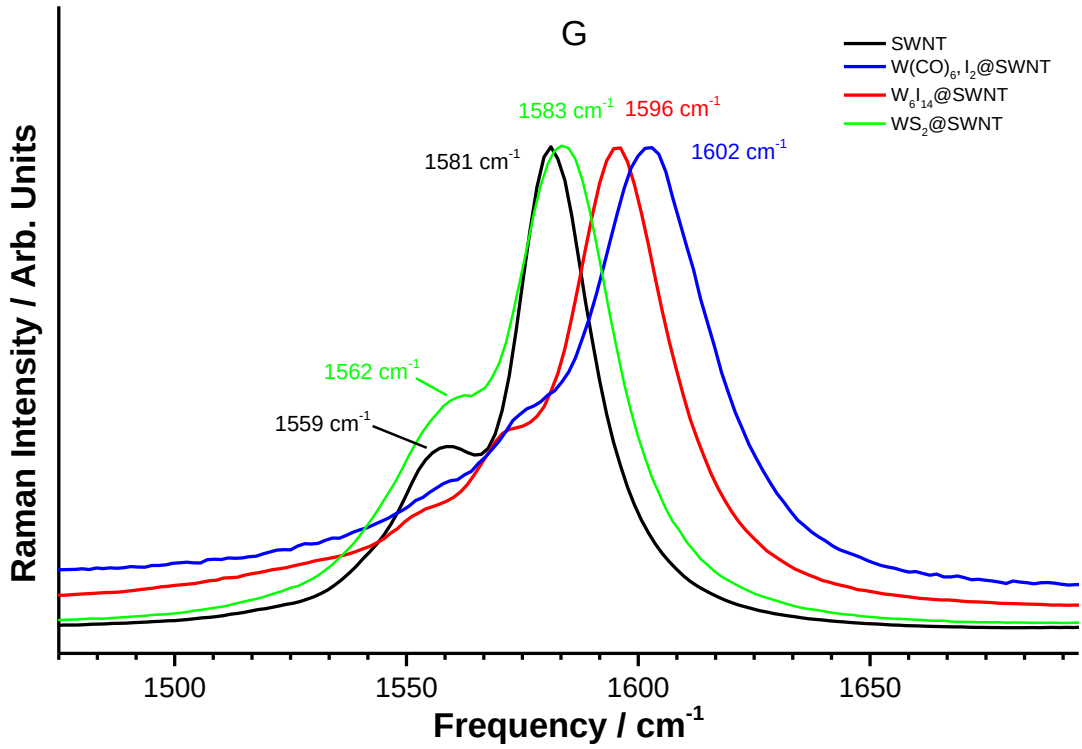


Figure 5-42. Raman spectra show the G band of empty SWNTs (1581 cm^{-1}, black), $(W(CO)_6, I_2)$@SWNTs (1602 cm^{-1}, blue), W_6I_{14}@SWNT (1596 cm^{-1}, red) and WS_2@SWNT (1596 cm^{-1}, green) (λ=532 nm).

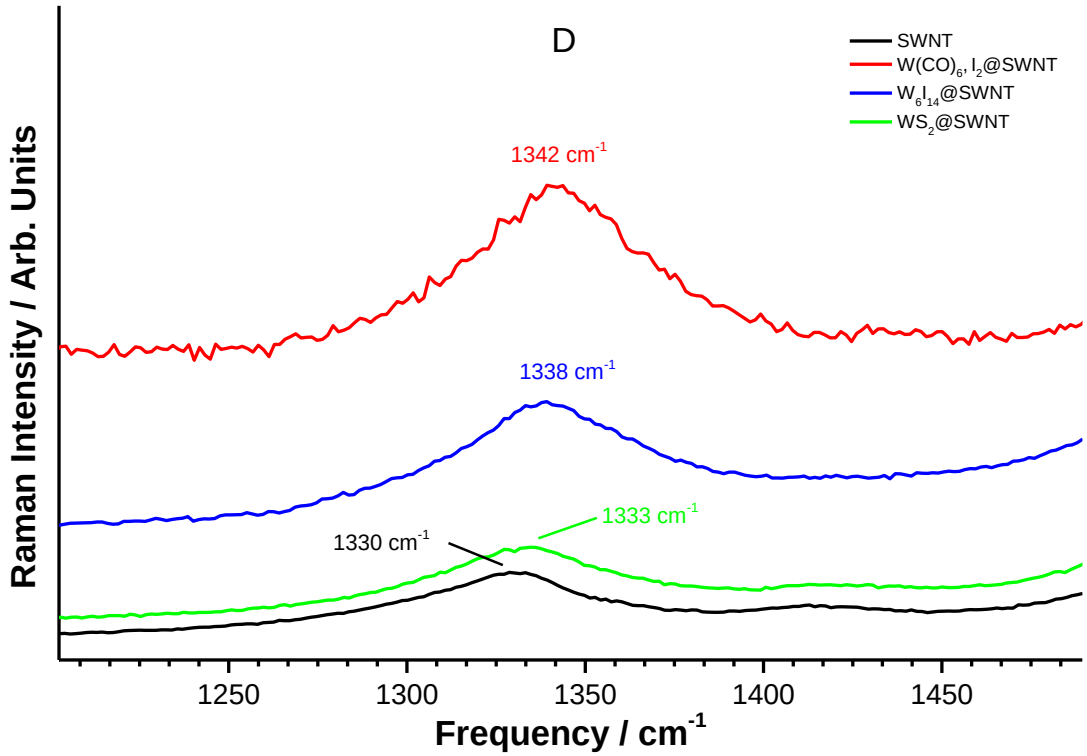


Figure 5-43. Raman spectra show the D band of empty SWNTs (1330 cm^{-1}, black), ($W(CO)_6$, I_2)@SWNTs (1338 cm^{-1}, blue), W_6I_{14}@SWNT (1342 cm^{-1}, red) and WS_2@SWNT (1333 cm^{-1}) (λ=532 nm).

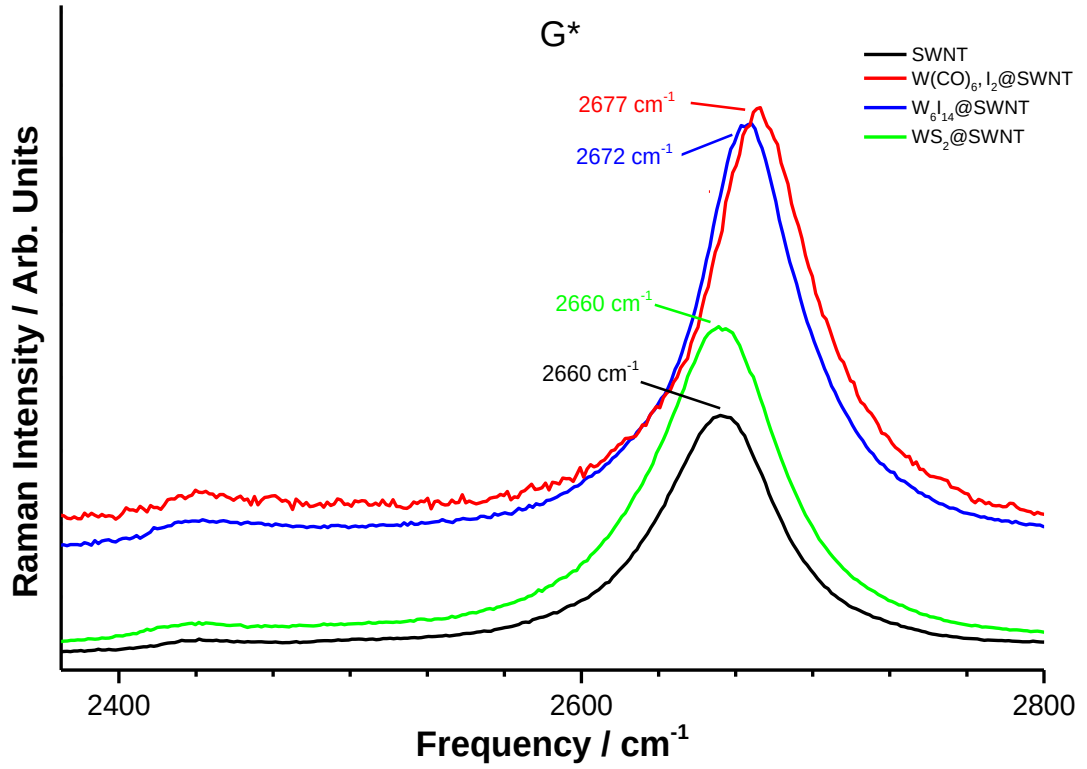


Figure 5-44. Raman spectra show the G* band of empty SWNTs (2660 cm^{-1}, black), ($W(CO)_6$, I_2)@SWNTs (2672 cm^{-1}, blue), W_6I_{14}@SWNT (2677 cm^{-1}, red) and WS_2@SWNT (2660 cm^{-1}) (λ=532 nm).

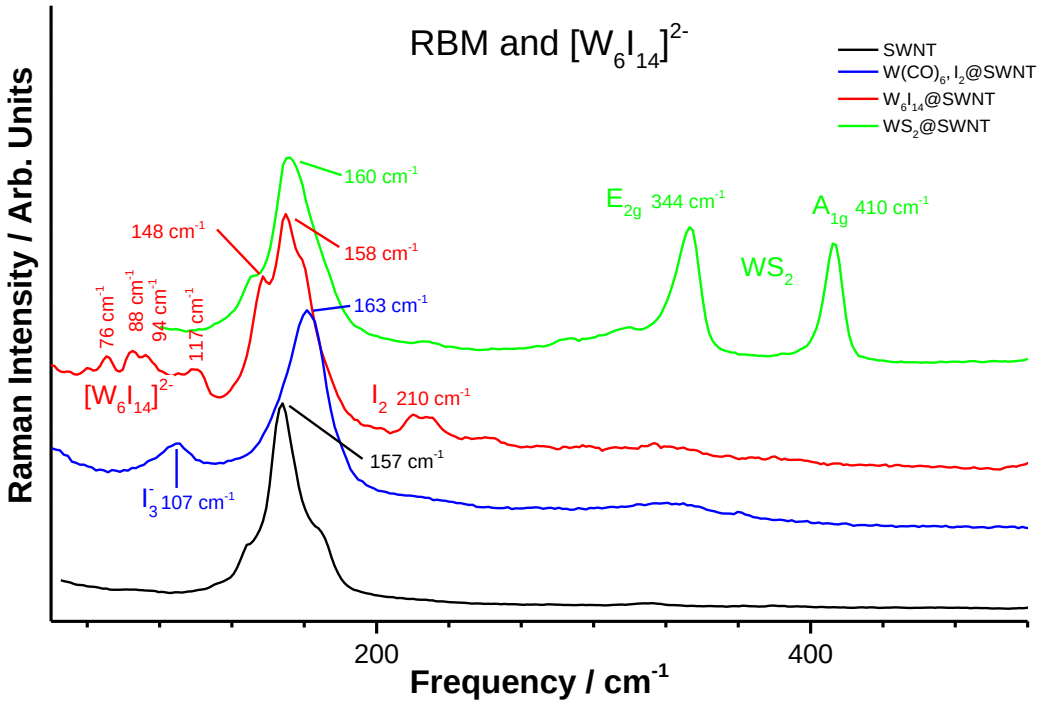


Figure 5-45. Raman spectra show the low frequency region containing RBM of empty SWNTs (157 cm^{-1}, black), ($W(CO)_6$, I_2)@SWNTs (163 cm^{-1}, blue) and a peak corresponding to I_3^- ions (107 cm^{-1}), W_6I_{14}@SWNT (148, 158 cm^{-1}, red) in addition to peaks corresponding to W_6I_{14} clusters (76, 88, 94 117 cm^{-1}) and I_2 molecules (210 cm^{-1}) and WS_2@SWNT (160 cm^{-1}) in addition to peaks corresponding to the E_{2g} and A_{1g} vibrations of WS_2 (344, 410 cm^{-1}) (λ=532 nm).

5.3.2.4 Characterisation of the material formed by reacting ($Mo(CO)_6$, I_2)@MWNT with H_2S

TEM analysis of the material formed by reacting ($Mo(CO)_6$, I_2)@MWNTs with H_2S (Experiment 5-8) showed dark contrast in MWNTs (d_{NT}=3.3 nm) emerging from the formed MoS_2 (Figure 5-46). The Mo atoms shown in Figure 5-46 a correspond to a tilted *i.e.* not face-on nor edge-on MoS_2NR while Figure 5-46 a shows a MoS_2NR in face-on orientation *i.e.* the 002 plane of MoS_2 is perpendicular to the incident e-beam (Figure 5-46 b). EDX spectroscopy of the material in MWNTs showed characteristic peaks of Mo and S at 2.3, 17.5 keV and 2.3 keV and no peak corresponding to I was observed (Figure 5-47). Consequently, both

TEM and EDX indicate that the transformation of ($Mo(CO)_6$, I_2)@MWNTs into MoS_2@MWNTs was successful.

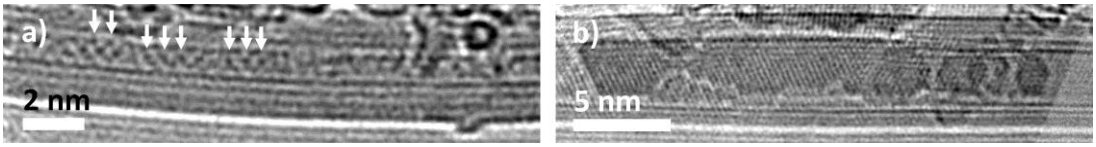


Figure 5-46. TEM images of MoS_2@MWNTs formed by reacting ($Mo(CO)_6$, I_2)@MWNTs with H_2S (Experiment 5-8) show a) high-contrast circular features corresponding to Mo atoms (marked with arrows) and b) large MoS_2 flake.

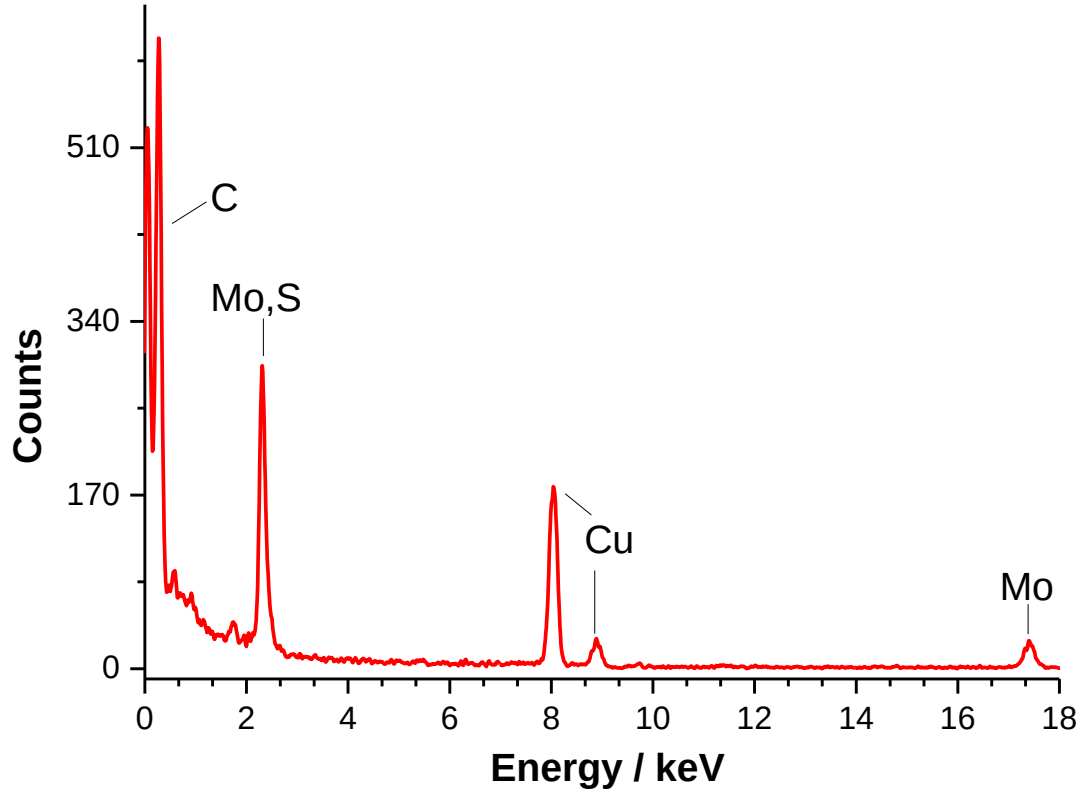


Figure 5-47. EDX spectrum of the material formed by reacting ($Mo(CO)_6$, I_2)@MWNTs with H_2S (Experiment 5-8). Characteristic X-ray peaks of Mo and S were identified at 2.3, 17.5 keV and 2.3 keV, respectively. Cu peaks are due to the specimen holder.

5.3.2.5 Characterisation of the material formed by reacting $Mo_6I^i_8I^a_2I^{a\text{-}a}_{4/2}$@MWNT with H_2S

TEM investigation of the material formed by reacting $Mo_6I^i_8I^a_2I^{a\text{-}a}_{4/2}$@MWNTs with H_2S (Experiment 5-9) revealed a nanoribbon (width=3.3 nm) in a MWNT ($d_{NT\ internal}$=3.5 nm) with a hexagonal atomic lattice and typical period of 0.32 nm (Figure 5-48 a-e).

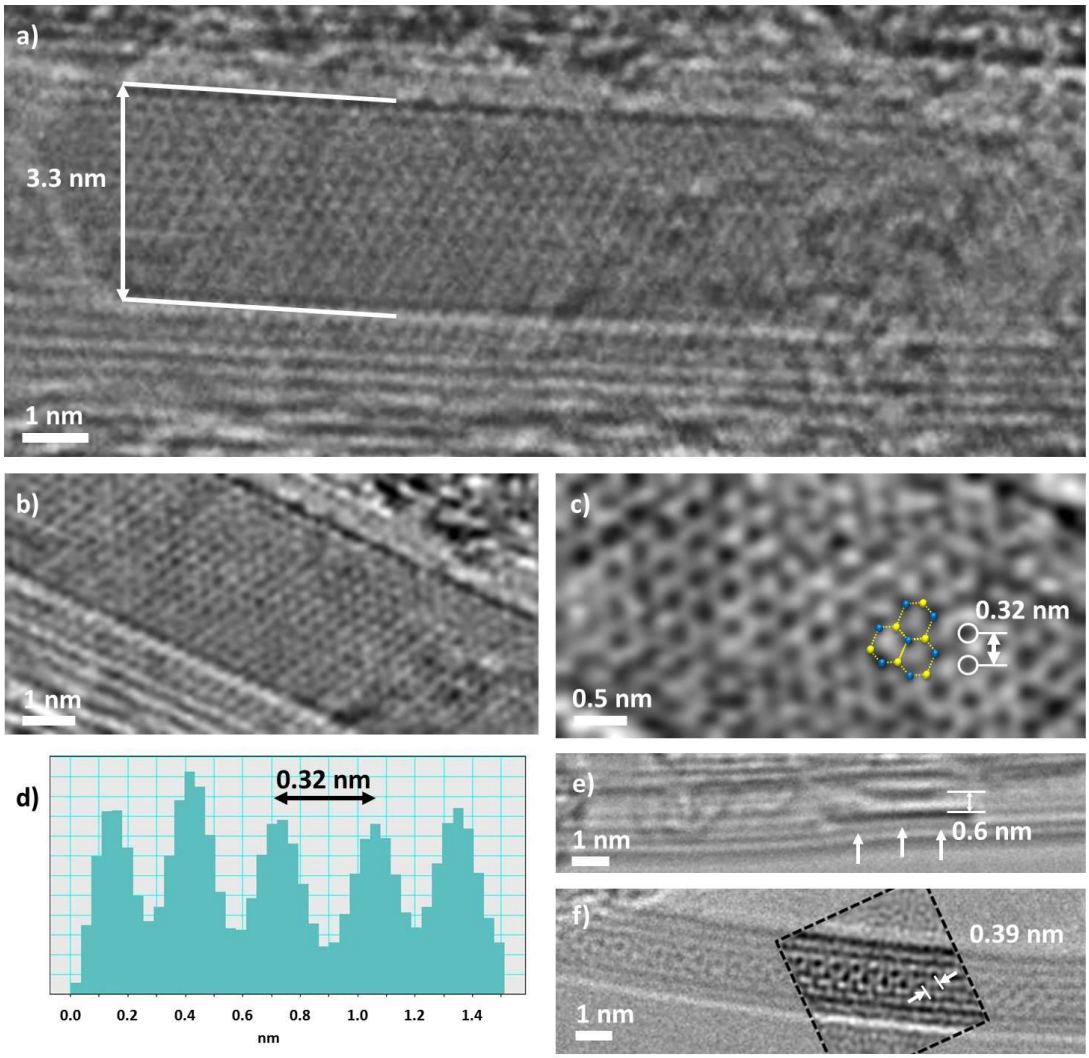


Figure 5-48. TEM images of MoS_2@MWNTs formed by reacting $Mo_6I^i_8I^a_2I^{a\text{-}a}_{4/2}$@MWNTs with H_2S (Experiment 5-9) show a) a face-on MoS_2NR (width=3.3 nm) in a MWNT ($d_{NT\ internal}$=3.5 nm) b) in which the dark spots, c) with a uniform distance (0.32 nm) similar to the theoretical distance (0.316 nm) correspond to adjacent Mo atoms in the 002 plane of MoS_2. Intensity line profile (d) along a row of Mo atoms shows the uniform Mo-Mo separation of 0.32 nm. Image e) shows two dark lines separated by 0.6 nm which correspond to edge-on orientation MoS_2 layers bending the MWNT (marked by arrows) (marked by arrows) due to van der Waals interaction. Image d) shows dark spots corresponding to Mo atoms that appear to be separated by 0.39 nm indicating that the 002 plane of MoS_2NR is tilted in both directions in respect to the incident e-beam.

The symmetry and period of the atomic lattice both match those in layers of MoS_2 in bulk crystal thus strongly suggesting that the dark features correspond to Mo atoms in a face-on MoS_2 layer(s).[19] In addition, high-contrast parallel lines were observed in MWNTs corresponding to the edge-on orientation of MoS_2NRs

(Figure 5-48 e). The nanoribbons are separated by ~0.4 nm from the sidewall of the innermost CNT and 0.6 nm from each other which is identical to the *d* spacing of 002 lattice of MoS_2 layers.[19]

EDX spectroscopy of the material in MWNTs showed characteristic peaks corresponding to Mo and S at 2.3, 17.5 keV and 2.3 keV, moreover no peak of I was observed (Figure 5-49), which suggests that the transformation of $Mo_6I^i_8I^a_2I^{a\text{-}a}_{4/2}$@MWNTs into MoS_2@MWNTs was completed successfully and the above described layered structures in MWNTs are indeed MoS_2 layers.

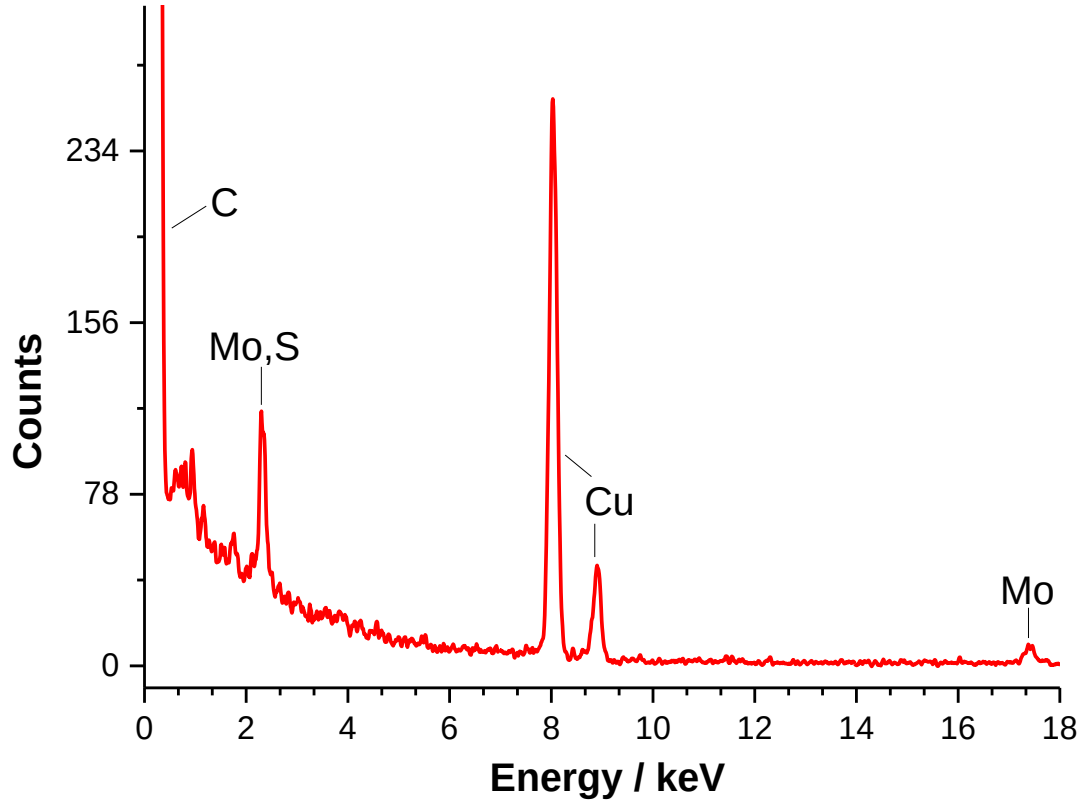


Figure 5-49. EDX spectrum of the material formed by reacting $Mo_6I^i_8I^a_2I^{a\text{-}a}_{4/2}$@MWNTs with H_2S (Experiment 5-9). Characteristic X-ray peaks of Mo and S were identified at 2.3, 17.5 keV and 2.3 keV, respectively. Cu peaks are due to the specimen holder.

5.4 Discussion

5.4.1 Analysis of the mechanism of metal iodide formation in CNTs

As TEM, EDX and Raman investigations showed the reaction of $M(CO)_6$ and I_2 resulted in the formation of M_6I_{14} clusters forming a liner array in SWNTs (M=Mo, Figure 5-12; W, Figure 5-4) or closely packed structures consisting of $Mo_6I^i_8I^a_2I^{a\text{-}a}_{4/2}$ in MWNTs (M=Mo, Figure 5-24).

According to the literature using molecular $M(CO)_6$ precursor is a vital part of the mechanism as its decomposition provides M(0) atoms (Figure 5-50 a) which then readily react with I_2, in contrast to the extremely low yield reaction of bulk metal and iodine.[20] The mechanism of M_6I_{14} clusters formation from $M(CO)_6$ and I_2 in CNTs is most likely related to the mechanism proposed for their formation in the solid state.[20] However, carbon nanotubes may promote the formation of metal iodide clusters *via* charge transfer interactions as it was shown that in CNTs electrons are transferred from the CNTs to I_2 resulting in I_m^- polyiodide anions,[7,16] while from M atoms, encapsulated in CNTs, electrons may be transferred to the CNTs resulting in partially oxidised $M^{\delta+}$cations.[21,22,23] Consequently, the electrostatic attraction between the ionic species may facilitate the formation of metal iodide clusters. Furthermore, in the case of SWNTs the formation of $[M_6I_{14}]^{2-}$ clusters may be templated by the nanotubes (d_{NT}=1.4 nm) as their cavity and the

size of the cluster (~0.7 nm), which is identical to a C_{60} molecule, is close to a perfect match (See Equation 2-1 in Chapter II).

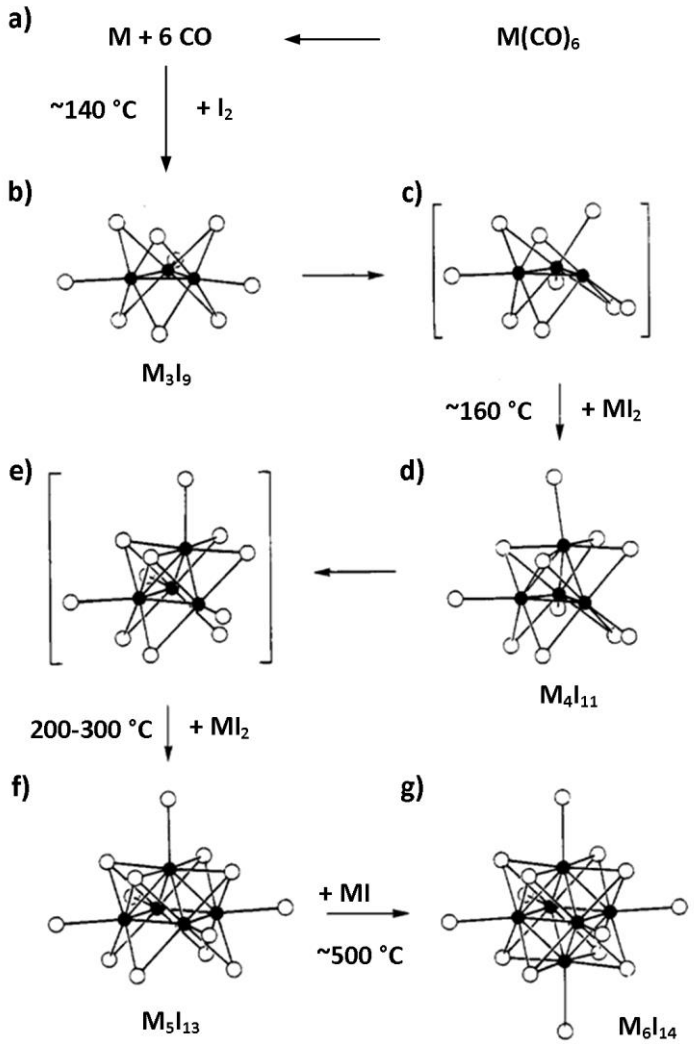


Figure 5-50. Figure shows the proposed mechanism of M_6I_{14} cluster formation in CNTs by the reaction of $M(CO)_6$ and I_2. First a) the decomposition of $M(CO)_6$ precursor provides M(0) atoms which b) then readily react with I_2 to form triangular M_3I_9, in which c) at higher temperature (~160 °C) a M-I bond brakes and d) a MI_2 unit is added to form tetrahedral M_4I_{11}. As shown on e) in the 200-300 °C region M-I and M-M bonds brake up and f) another MI_2 unit is added to form M_5I_{13} then g) finally at ~500 °C the addition of a MI unit provides the final product, the M_6I_{14} cluster.[20]

The formation of $[M_6I_{14}]^{2-}$ clusters from M and I atoms is a sequential process that involves smaller intermediate clusters as discussed below. At lower temperature (~140 °C) the reaction of M and I atoms results in the formation of the first intermediate cluster, the triangular $[M_3I_9]^-$ (Figure 5-50 b), in which at higher

temperature (~160 °C) a M-I bond brakes (Figure 5-50 c) and a MI_2 unit is added to form tetrahedral $[M_4I_{11}]^-$ (Figure 5-50 d). At even higher temperature (200-300 °C) after the breakage of a M-I and a M-M bond (Figure 5-50 e) another MI_2 unit is added to the cluster to form the last intermediate cluster $[M_5I_{13}]^-$ (Figure 5-50 f). Finally, the addition of a MI^- unit at ~500 °C provides the final product, the $[M_6I_{14}]^{2-}$ cluster (Figure 5-50 g).

5.4.2 Analysis of the mechanism of MS_2 formation in CNTs

5.4.2.1 Formation of MoS_2@SWNTs from $Mo(CO)_6$@SWNTs

Although the reaction of $Mo(CO)_6$ resulted in the formation of MoS_2 chains (Figure 5-31) in SWNTs they have only been observed in relatively narrow nanotubes (d_{NT}=0.7 or 0.9 nm) while the wider nanotubes in this sample (average d_{NT}=1.4 nm) remained empty after this experiment. This suggest that during the initial phase of the procedure some of the $Mo(CO)_6$ molecules may have been vaporised and left wider SWNTs before they could react with the H_2S, similarly to what was observed case of wider nanocontainers such as $Mo(CO)_6$@GNFs (see Chapter IV). However, van der Waals interactions between narrower SWNTs and $Mo(CO)_6$ molecules are expected to be stronger so that metal complexes are retained in the nanotubes until the temperature of the reaction environment is high enough to promote their decomposition which was shown to be a key element during the formation of MS_2 from $M(CO)_6$.[24,25]

Equation 5-1 $[Mo(CO)_6]_n@SWNT + 2n\ H_2S \longrightarrow [MoS_2]_n{}^{\delta-}@SWNT^{\delta+} + 6n\ CO + 4n\ H_2$

Those $Mo(CO)_6$ molecules remained encapsulated in narrow SWNTs have been decomposed in the gas phase and turned into small Mo nuclei which then reacted with H_2S to eventually result in the formation of MoS_2 chains (Equation 5-1).

5.4.2.2 Formation of MS_2@CNTs from M_6I_{14}@CNTs and $(M(CO)_6, I_2)$@CNTs

Due to the potential loss of $M(CO)_6$ from the SWNTs during the reaction of $M(CO)_6$@SWNTs with H_2S, it was considered to be not an ideal candidate for the synthesis of MS_2@CNTs. Therefore, as iodine has been used successfully in conjunction with $M(CO)_6$ for the formation of MS_2 nanostructures inside GNFs (see Chapter IV), $(M(CO)_6, I_2)$@CNTs and M_6I_{14}@CNTs were chosen as alternative precursor materials.

5.4.2.2.1 Formation of MS_2@CNTs from M_6I_{14}@CNTs

It was shown above that M_6I_{14}@SWNTs (M=Mo, W) contain high-contrast circular features in a liner arrangement corresponding to discrete M_6I_{14} clusters (Figure 5-12). In $[Mo_6I^i_8I^a_2I^{a\text{-}a}_{4/2}]$@MWNTs similar features were identified although M_6I_{14} clusters are packed into hexagonal arrays similar to bulk MoI_2 which span across the whole internal channel of MWNTs (Figure 5-24). As M_6I_{14} clusters are common in the structures observed in SWNTs and MWNTs they are considered to play a key

role in the mechanism of the conversion of metal iodides into metal sulphides in nanotubes, similarly to the conversion of MoI_2@GNFs into MoS_2@GNFs. Therefore, the formation of the MS_2 nanostructures is very likely based on the stepwise substitution of the halogen atoms of in the metal iodide cluster *i.e.* $M_6I^i_8I^a_6$ units with S resulting in $[Mo_6I^i_{8-n}S^i_n]I^a_{6-m}S^a_m$ (n=0-8, m=0-6) intermediates and finally MoS_2. The overall process may be described by Equation 5-2.

Equation 5-2
$$[M_6I^i_8I^a_6{}^{2-}]_n@SWNT^{2n+} + 12n\ H_2S \longrightarrow [MS_2]_{6n}{}^{\delta-}@SWNT^{\delta+} + 14n\ HI + 5n\ H_2$$

This hypothesis is supported by the fact that the iodide ligands in hexanuclear Mo and W compounds, being either axial or internal, can be replaced to results in the formation of compounds similar to the above described intermediates in which the halogen and chalcogen ligands coexist *i.e.* chalcohalides and may be shared between two M_6 octahedral units *i.e.* they become μ_2 bridging ligands as in $[M_6X^i_{8-n}Q^i_n]$ (Q=Se, Te; X=Br, I), $Mo_6S_6X_2$, $Mo_6S_3Br_6$ (Figure 5-52 b-c).[18,26] This mechanism is also supported by the fact that the thermal decomposition of smaller chalcohalide clusters such as $Mo_3Q_7X_4$ results in the formation binary chalcogenide of the metal such as MoS_2 *in vacuo*, inert atmosphere or hydrogen atmosphere.[26] Consequently, it is very likely that the conversion of the $Mo_6I^i_8I^a_2I^{a\text{-}a}{}_{4/2}$ and $Mo_6I^i_8I^a_6$ clusters into multi-layered MoS_2

ribbons in MWNTs (Figure 5-48) and monolayer MS_2NRs in SWNTs, respectively involves the formation of metal chalcohalides as intermediate compounds.[26,27]

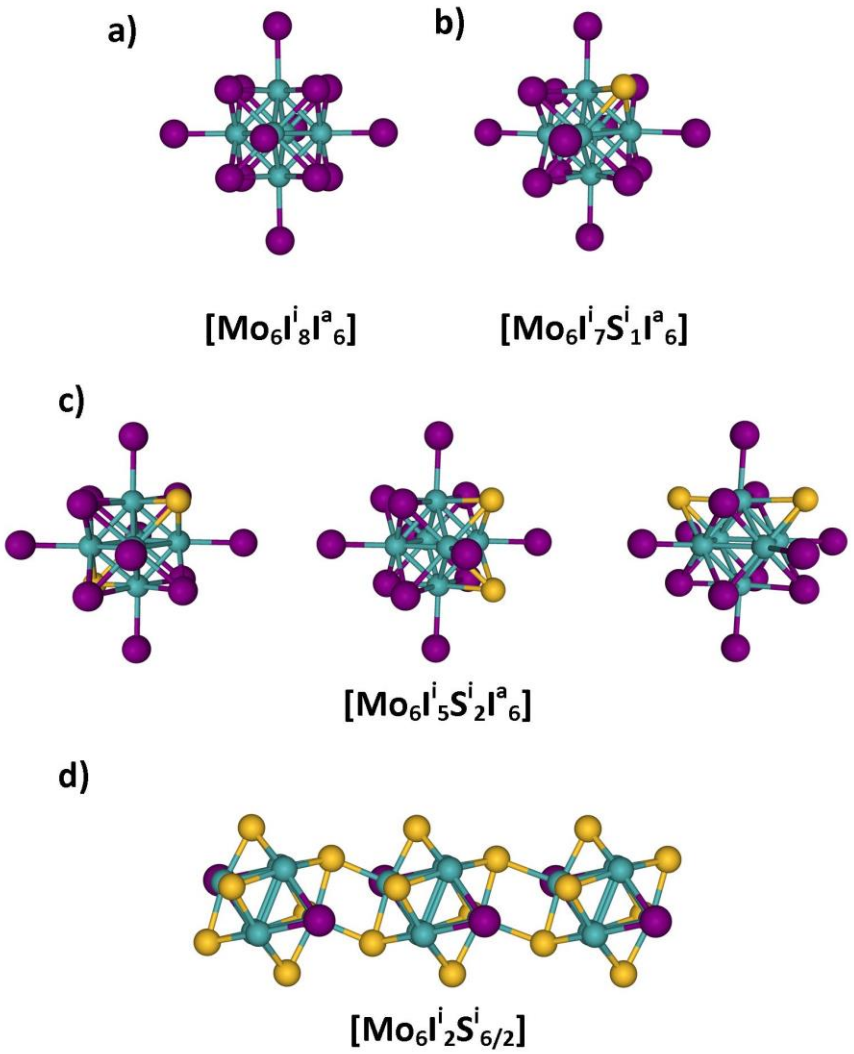


Figure 5-51. Image show the structure of a) $Mo_6I^i_8I^a_6$ metal iodide and mixed chalcohalides such as b) $Mo_6I^i_7S^i_1I^a_6$, c) isomers of $Mo_6I^i_5S^i_2I^a_6$, d) $Mo_6I^i_2S^i_{6/2}$ in which all S atoms are shared by the octahedral M_6 clusters in the 3D network of the bulk crystal.

The effectiveness of using metal iodide precursors enclosed in SWNTs and MWNTs for the formation of MS_2 is superior in comparison to using $M(CO)_6$ as it retains the metal atoms in the CNTs so they can react with H_2S gas. The thickness of MS_2NRs formed in CNTs is determined by the diameter of the host

nanotube, therefore in SWNTs 1-3 layer thick may be synthesised while in MWNTs MS_2NRs always have 2 or more layers.

5.4.2.2.2 Formation of MS_2@MWNTs from ($M(CO)_6$, I_2)@MWNTs

The reaction of $M(CO)_6$ and I_2 precursors with H_2S gas in MWNTs $Mo(CO)_6$ and I_2 molecules most likely form intermediates *i.e.* smaller M_xI_y clusters,[20] which then converted into some yet unidentified ternary Mo-S-I phase by H_2S similarly to ($Mo(CO)_6$, I_2)@GNFs.[28] This means that, in contrast to M_6I_{14}@CNTs, it is not likely that hexanuclear halogenide $M_6I^i_8I^a_6$ or chalcohalide $[M_6X^i_{8-n}Q^i_n]$ clusters are involved in the formation of MS_2 from $M(CO)_6$ and I_2 precursors in MWNTs. Comparing the TEM images of MoS_2@MWNTs formed by using the mixture of $M(CO)_6$ and I_2 or $Mo_6I^i_8I^a_2I^{a\text{-}a}_{4/2}$ precursors showed no significant difference between the two methods.

5.4.3 Analysis of the chemistry behind the formation of MS_2 (M=Mo, W) nanoribbons in SWNTs

The chemistry behind the formation of MS_2 (M=Mo, W) nanoribbons in SWNTs and the host-guest interaction between SWNTs and each intermediate guest-compound *i.e.* ($M(CO)_6$, I_2) M_6I_{14} was investigated by Raman spectroscopy. It was found that ($M(CO)_6$, I_2)@SWNTs (M=Mo, W) the G band of the nanotube is blueshifted, in relation to empty SWNTs, which based on the literature can be attributed to electron transfer from the carbon nanotube`s π–electron system to polyiodine molecules such as

I_m^- (m=5, 4, 3) resulting in the contraction of C-C bonds and partial charge separation.[16,7] This means that based on Raman data $(M(CO)_6, I_2)$@SWNTs may be better described as $n[M(CO)_6 + 2I_2 + 2I_5^-]$@$SWNT^{2n+}$.

The position of the G band remained unchanged (1596 cm^{-1}) in the case of Mo_6I_{14}@SWNTs which indicates that the total amount of electron transfer from the carbon nanotubes to the polyiodide molecules is similar to that for $Mo_6I_8I_6$ clusters. In contrast, the blueshift of G band in $(W(CO)_6, I_2)$@SWNTs is greater than in W_6I_{14}@SWNTs by 6 cm^{-1} due to an excess of iodine relative to the W content i. *i.e.* I:W>6:14 in $(W(CO)_6, I_2)$@SWNTs. The excess of I_2 was released from nanotube upon the formation of W_6I_{14}@SWNTs, and the G band shifted back to 1596 cm^{-1} same as in Mo_6I_{14}@SWNTs.

The G band of the SWNTs were found to be blueshifted, in comparison to empty SWNTs, after the conversion of M_6I_{14}@SWNTs to MS_2@SWNTs by 8 and 3 cm^{-1} in case of MoS_2 and WS_2. This blueshift of the G band in MS_2@SWNT is in good agreement with previous theoretical[29] and experimental[30] results showing that there is a moderate charge transfer from graphitic structures to MS_2 (M=Mo, W) and other metal dichalcogenides such as GaSe.[31]

In summary, based on Raman spectroscopy and HRTEM results the formation of MS_2@SWNTs through the isolated intermediate compounds of $(M(CO)_6, I_2)$@SWNTs and M_6I_{14}@SWNTs can be

described by the process and balanced chemical equations shown in Figure 5-52. First the encapsulation of $M(CO)_6$ and I_2 results in a material in which electrons are transferred from the SWNTs to the iodine atoms, therefore the material is best described as follows: $n[6M(CO)_6+2I_2+2I_5^-]@SWNT^{2n+}$. Second, upon heating at high temperature the encapsulated $M(CO)_6$ and iodine forms discrete M_6I_{14} (M=Mo, W) clusters which, as showed by Raman spectroscopy, retain electrons previously removed from SWNTs by iodine to stabilise their structure by reaching their natural $M_6I_{14}^{2-}$ form. Therefore, this material is best described as $[M_6I_{14}^{2-}]_n@SWNT^{2n+}$.

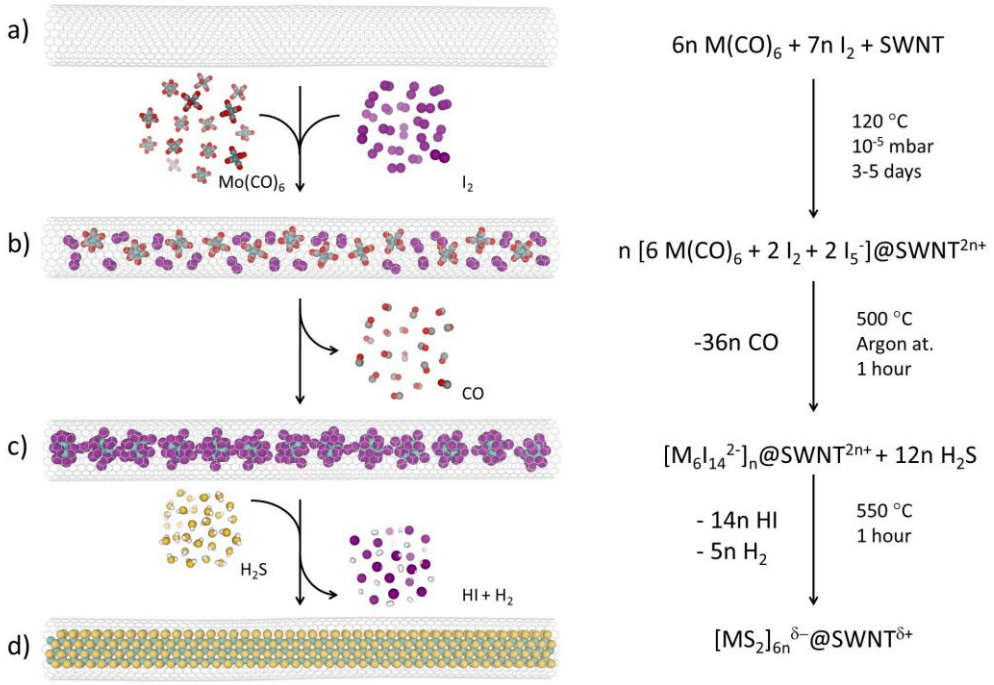


Figure 5-52. Scheme detailing the synthesis of MS_2@SWNTs; a) open, freshly annealed SWNTs are exposed to gaseous $M(CO)_6$ and I_2 at 120 °C, which enter the internal cavity of the nanotube; b) the molecules condense inside the nanotube to form $n[6M(CO)_6+2I_2+2I_5^-]@SWNT^{2n+}$; c) upon thermal treatment at 500 °C in an inert atmosphere the molecules react to form metal iodide, $[M_6I_{14}^{2-}]_n@SWNT^{2n+}$, and gaseous CO which escapes from the nanotube; d) subsequent thermal treatment in a flow of H_2S gas at 550 °C leads to the formation of metal sulphide, $[MS_2]_{6n}^{\delta-}@SWNT^{\delta+}$, and the displaced iodine atoms leave the nanotube as gaseous HI along with H_2 gas.

In the last reaction metal iodide clusters are reacted with H_2S which results in the formation of MS_2NRs in SWNTs, moreover, the liberation of the encapsulated iodine from the SWNTs in the form of HI. Consequently, this means that the charge transfer interaction between SWNTs and iodine atoms is not present anymore. However, as charge transfer from the SWNTs to the MS_2NRs was indicated by Raman spectroscopy, in agreement with the literature, these material are precisely best described as $[MS_2]_n^{\delta-}@SWNT^{\delta+}$.[29–31]

5.4.4 Dynamic behaviour of M_6I_{14} clusters (M=Mo, W) in CNTs

As it was shown above by time-series (AC-)TEM imaging M_6I_{14} clusters encapsulated in CNTs showed various dynamic behaviour in CNTs during TEM analysis.

It was demonstrated that both Mo_6I_{14} and W_6I_{14} clusters translate in the channel of SWNTs. Also the rotation of the octahedral M_6I_{14} clusters were identified in SWNTs by observing the interchange of their different projections in TEM images (C_3, tilted C_3, C_4 or tilted C_4 orientations, Figure 5-6, Figure 5-7). Such movement *i.e.* translation and rotation of the clusters can be attributed to the thermal motion of molecules constrained by the nanotube sidewalls as the TEM imaging was performed at room temperature.

Furthermore, in case of Mo_6I_{14} clusters encapsulated in SWNTs time-series AC-TEM imaging showed that in the TEM under the

e-beam discrete $Mo_6I^i_8I^a_6$ clusters (Figure 5-53 a) temporarily transform into structurally continuous 1D crystal within the carbon nanotubes (Figure 5-53 c). It should be emphasised that while 1D binary molybdenum iodide structures do not exist in bulk, calcohalides such as $Mo_6I^i_2S^i_{6/2}$ (Figure 5-52 c) with similar μ_3-μ_1 bridging of the clusters have been reported.[32,33] The 1D $[(Mo_6I^i_8I^{i\text{-}a}{}_2I^a{}_2)_{n+2}I_2]^{2-}$ crystals observed in our experiments are only possible due the confinement effect of the SWNTs which serve as templates for the crystal growth.

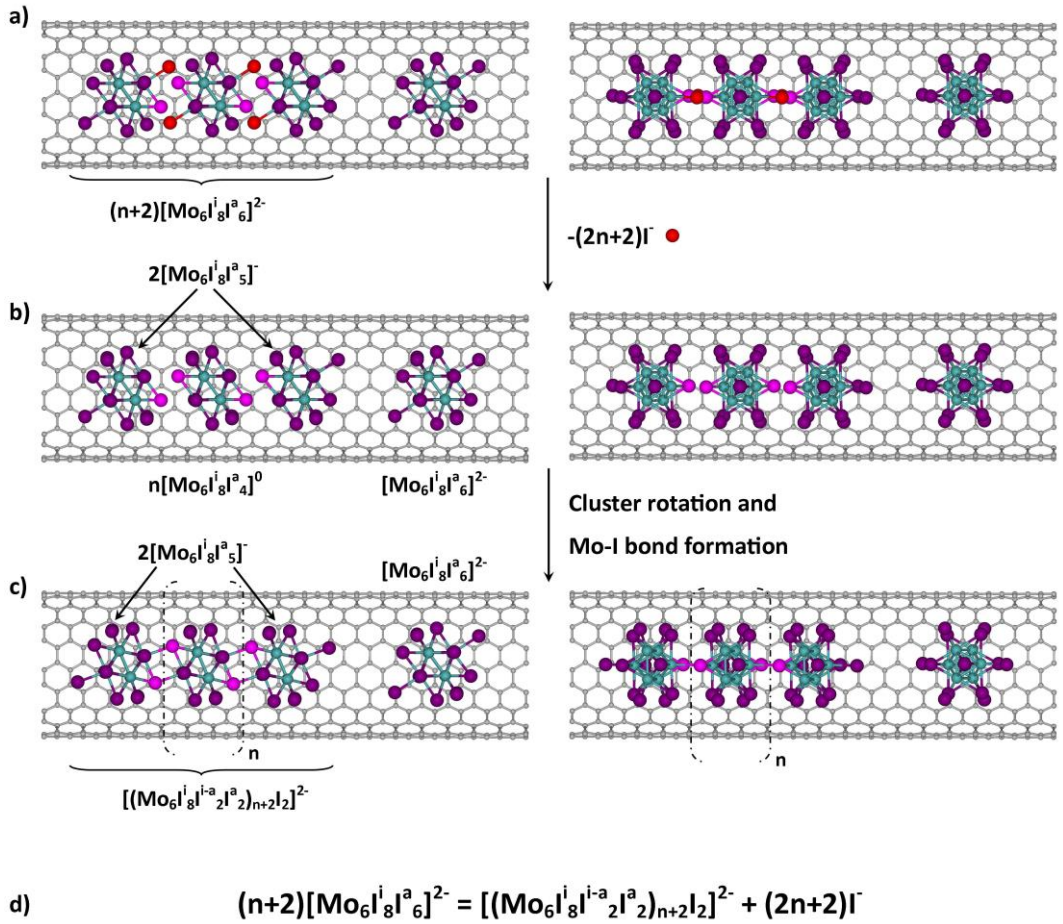


Figure 5-53. Proposed formation mechanism of 1D crystal from a) $[Mo_6I^i_8I^a_6]^{2-}$ clusters by first the elimination of I^{a-} ions (red) and the formation of b) $[Mo_6I^i_8I^a_{6-n}]^{(2-n)-}$ (n=1, 2) species due to the knock-on damage of the e-beam, then bridging every two intermediates *via* two shared μ_4 I^{i-a} atoms (pink) to yield c) a 1D crystal of $[(Mo_6I^i_8I^{i-a}{}_2I^a{}_2)_{n+2}I_2]^{2-}$ by cross-linking n $[Mo_6I^i_8I^a_6]^{2-}$ clusters *e.g.* if n=1 $[Mo_{18}I_{38}]^{2-}$. Left and right columns represent two

orthogonal views of the same structure to aid understanding. d) Balanced equation of the mechanism of 1D crystal formation from (n+2)$[Mo_6I^i_8I^a_6]^{2-}$ clusters.

The process is most likely the consequence of the knock-on damage *i.e.* kinetic energy transfer of the e-beam which results in the dissociation of the Mo-I^a bond and loss of I^{a-} ions and the formation of $[Mo_6I^i_8I^a_{6-n}]^{(2-n)-}$ (n=1, 2) species (Figure 5-53 b). Any two of these intermediates can then join together *via* two shared μ_4 I^{i-a} atoms which eventually leads to the formation of a 1D crystal $[(Mo_6I^i_8I^{i-a}{}_2I^a{}_2)_{n+2}I_2]^{2-}$ (Figure 5-53 c).

Interestingly, in the case of $W_6I^i_8I^a_6$ clusters no 1D crystal formation was observed in SWNTs in contrast to $Mo_6I^i_8I^a_6$. The reason for the increased stability of the W-based cluster over the Mo-based is the higher atomic weight of W (M_W/M_{Mo}=1.9), as the lighter Mo atoms receive significantly more kinetic energy from the collisions with incident electrons of the 80 keV e-beam of TEM. The higher stability of molecules made of heavier atoms under e-beam was demonstrated for isotopically substituted coronene molecules (protium vs. deuterium) which led to the increase in stability by a factor of two as a result of doubling the atomic weight of hydrogen, under TEM imaging conditions identical to those used for the imaging of M_6I_{14} clusters in SWNTs (80 kV, room temperature).[34]

In the case of $[Mo_6I^i_8I^a{}_2I^{a-a}{}_{4/2}]$@MWNTs a moderate mobility (rotation and translation) of molybdenum iodide clusters was observed on the timescale of few seconds (Figure 5-28, Video 5).

This suggests that the knock-on damage of the 80 keV e-beam

is able to disrupt the Mo-$I^{a\text{-}a}$-Mo bridges (Figure 5-26 b) thus enabling the clusters rotation or, if all Mo-$I^{a\text{-}a}$ bonds are broken, translation of the discrete Mo_6I_{14} cluster in the channels of MWNTs. This Mo-I bond dissociation induced by the e-beam is the essential step in the formation of 1D molybdenum iodide crystal observed in SWNT.

5.5 Concluding remarks

In this study a multistep inorganic synthesis has been demonstrated within carbon nanotubes enabling the analysis of the resultant products at each step.

It was demonstrated that M_6I_{14} can be successfully synthesised by reacting previously encapsulated $M(CO)_6$ and I_2 precursors inside CNTs. Even more importantly it was shown that M_6I_{14} clusters, which reside inside SWNTs can be completely converted into MS_2NRs.

Moreover, a mechanism of formation was postulated for the synthesis of M_6I_{14} inside SWNTs based on the sequential formation of binary metal iodide clusters.

In addition, a mechanism for the formation of MS_2NRs was postulated which involves the step-by-step conversion of M_6I_{14} through the formation of mixed metal chalcohalides.

Raman spectroscopy and TEM have been used successfully to unravel the mechanisms of the multistep inorganic chemical synthesis leading to the formation of M_6I_{14}@SWNTs and

MS_2NR@SWNTs.

Moreover, the dynamic behaviour of M_6I_{14} clusters (translation and rotation) and MS_2 nanoribbons (twisting) in SWNTs was demonstrated by time series AC-TEM imaging. The observed twisting of MS_2NRs was found to be good agreement with earlier publications showing the same behaviour in case of sulphur-terminated graphene nanoribbon and WS_2NR.[5,14,6]

5.6 Experimental section

5.6.1 Materials

Arc-discharge SWNTs (HELIX, average d_{NT}=1.4 nm, purity 90%) and CVD MWNTs (Timesnano, d_{NT}=0.7-2.7) were purchased from Helix Material Solutions and Chengdu Organic Chemicals Co. Ltd. and Chinese Academy of Sciences, respectively.

Mo and W hexacarbonyls (purity≥98 and 99%, respectively) were purchased from Acros Organics and all hexacarbonyls were used without further purification.

I_2 (purity ≥99.8%) and H_2S gas (purity≥99.5%) were purchased from Fischer Scientific and Sigma-Aldrich, respectively and used without further purification.

5.6.2 Gas phase filling of CNTs

It is important to note that the amount of $M(CO)_6$ and I_2 reported in Table 5-6 are the initial masses of reagents used for all filling experiments, however due to the application of high vacuum

during the sealing procedure some of the molecular precursors are anticipated to be lost due to unwanted sublimation prior to sealing. Obviously this is non-ideal and a number of steps were taken to limit this, and an excess of precursor materials were used in each case to ensure effective NT filling.

5.6.2.1 Opening CNTs by oxidation in air

To provide access for the guest species to their interior SWNTs and MWNTs were heated in air at 380 °C for 20 minutes or 500 °C for 15 minutes, respectively to open their closed ends and remove any adsorbed water.

5.6.2.2 Encapsulation of $M(CO)_6$ or $M(CO)_6$ and I_2 together into CNTs

Freshly opened CNTs (5 mg) were mixed with a large excess of precursor molecules *i.e.* $M(CO)_6$ or $M(CO)_6$ and I_2 (M=Mo, W) and the resultant mixture was sealed in a Pyrex glass vessel (d=10 mm, l=10 cm) under high vacuum (10^{-6} mbar).

The sealed vessel was placed into a preheated box furnace (T=120 °C) for several days depending on the experiment, see Table 5-6. Prior to opening the Pyrex glass vessel was taken out from the furnace and cooled down by immersing it into an ice-water bath for 5 minutes. After opening the Pyrex glass vessel the samples were transferred into a glass vial and stored in the freezer (-15 °C) until required.

5.6.3 Chemical transformation of $M(CO)_6$ and I_2 precursor molecules into M_6I_{14} in CNTs

The CNTs containing $M(CO)_6$ and I_2 precursor molecules were sealed in a Pyrex glass vessel which was first evacuated (10^{-6} mbar) then filled with Ar gas (0.7 bar). The sealed Pyrex glass tube was then transferred into a preheated furnace (500 °C). After an hour the sample was taken out from the furnace and left on an asbestos tile to cool down to room temperature. After opening the glass ampoule the sample was transferred into a glass vial and stored in the freezer (-15 °C) until further treatment. The parameters of the experiments can be found in Table 5-7.

Table 5-6. Parameters of the gas phase encapsulation of $M(CO)_6$ and I_2 or $M(CO)_6$ into CNTs.

Experiment	Precursor		m precursor / mg		Nanotube		Product	Atmosphere, pressure / bar	Reaction temp. / °C	Reaction time / h
	1.	2.	1.	2.	type	m / mg				
5-1	$Mo(CO)_6$	I_2	15	30	MWNT	5	$(Mo(CO)_6, I_2)$@MWNT	Vacuum, 10^{-9}	120	72
5-2	$Mo(CO)_6$	I_2	40	80	SWNT	20	$(Mo(CO)_6, I_2)$@SWNT	Vacuum, 10^{-9}	120	120
5-3	$W(CO)_6$	I_2	80	160	SWNT	20	$(W(CO)_6, I_2)$@SWNT	Vacuum, 10^{-9}	120	72
5-4	$Mo(CO)_6$	N/A	100	N/A	SWNT	3	$Mo(CO)_6$@SWNT	Vacuum, 10^{-9}	120	72

Table 5-7. Parameters of the chemical transformation of $M(CO)_6$ and I_2 precursor molecules into metal iodide in CNTs.

Experiment	Starting material		Product	Atmosphere, pressure / bar	Reaction temp. / °C	Reaction time / h
		Formed in Experiment				
5-5	$(Mo(CO)_6, I_2)$@MWNT	**5-1**	$[Mo_6I^i_8I^a_2I^{a\text{-}a}_{4/2}]$@MWNTs	Argon, 0.7	500	1
5-6	$(Mo(CO)_6, I_2)$@SWNT	**5-2**	Mo_6I_{14}@SWNT	Argon, 0.7	500	1
5-7	$(W(CO)_6, I_2)$@SWNT	**5-4**	W_6I_{14}@SWNT	Argon, 0.7	500	1

Table 5-8. Parameters of the chemical transformation of $M(CO)_6$, $M(CO)_6$ and I_2 or metal iodide precursor molecules into MS_2 in CNTs.

Experiment	Starting material		Product	Atmosphere, pressure / bar	Reaction temp. / °C	Dwell time / h	Heating	Cooling
		Formed in Experiment					rate / °C min^{-1}	
5-8	$(Mo(CO)_6, I_2)$@MWNT	**5-1**	MoS_2@MWNT	H_2S, 1	550	2	25	25
5-9	$[Mo_6I^i_8I^a_2I^{a\text{-}a}{}_{4/2}]$@MWNTs	**5-5**	MoS_2@MWNT	H_2S, 1	550	2	25	25
5-10	$Mo(CO)_6$@SWNT	**5-4**	MoS_2@SWNT	H_2S, 1	550	2	25	25
5-11	Mo_6I14@SWNT	**5-6**	MoS_2@SWNT	H_2S, 1	550	2	25	25
5-12	W_6I_{14}@SWNT	**5-7**	WS_2@SWNT	H_2S, 1	550	2	25	25

Table 5-9. Parameters of the calcination of $[Mo_6I^i_8I^a_2I^{a\text{-}a}{}_{4/2}]$@MWNTs.

Experiment	Starting material		Atmosphere, pressure / bar	Reaction temp. / °C	Dwell time / h	Heating	Cooling
		Formed in Experiment				rate / °C min^{-1}	
5-13	$[Mo_6I^i_8I^a_2I^{a\text{-}a}{}_{4/2}]$@MWNTs	**5-5**	Argon, 0.4 bar	800	3	4.4	2.2

5.6.4 Reaction of the different precursors situated in CNTs with H_2S gas

The CNTs containing different precursor molecules, listed in Table 5-8, were transferred into a quartz boat and placed into a closed ceramic working tube (*d*=25 mm, *l*=60 cm) located within a tube furnace (Figure 5-54). In a typical experiment the system was purged at room temperature with Ar then H_2S for 1 hour each at ~15 mL/min. The furnace was heated up to the desired reaction temperature, typically 550 °C (25 °C/min), which was maintained along with a moderate (~15 mL/min) H_2S gas flow for the desired reaction time, typically for 2 hours, see Table 5-8.

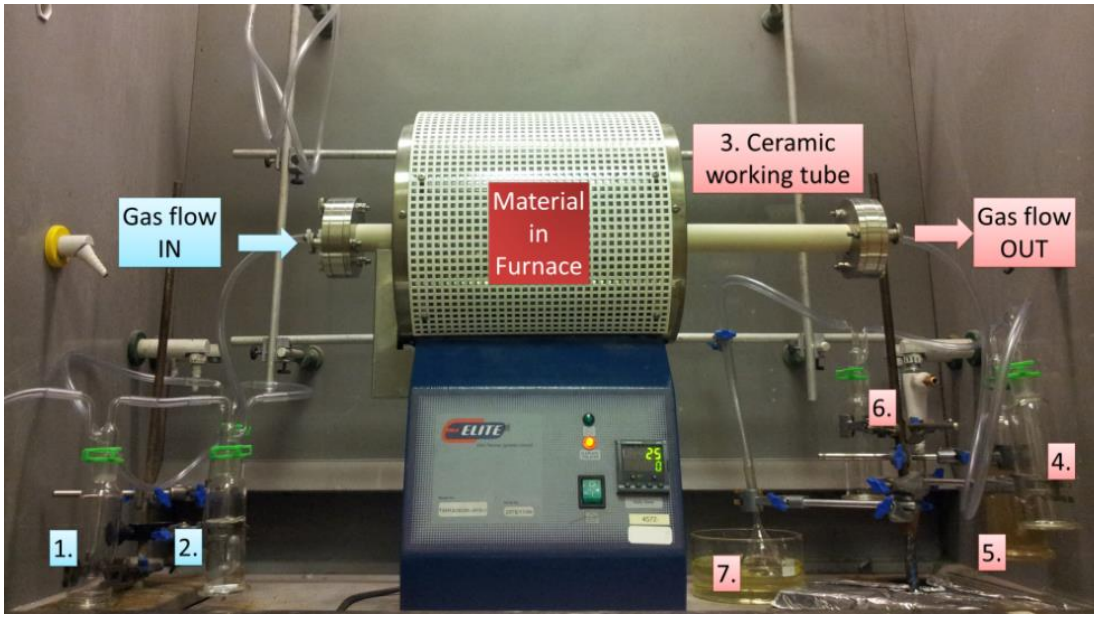


Figure 5-54. Experimental setup used for the reaction of H_2S gas with the different precursors situated in GNFs. The cold gas flow (Ar or H_2S) goes through an empty reversed gas bubbler (1.) and another one filled with paraffin oil (2.) before entering the ceramic working tube containing the sample (3.). The hot gas then flows through an empty reversed gas bubbler (4.), one filled with paraffin oil (5.) and another empty reversed gas bubbler (6.) and through a bleach bath (7.) before reaching the environment.

Then the furnace was cooled down (25 °C/min) to room temperature under Ar gas flow. The exhaust of the system was

released into the fume hood through a bleach bath in order to neutralise any excess H_2S.

5.6.5 Calcination under an Ar atmosphere

The material was sealed in a Pyrex glass vessel, which was first evacuated (10^{-6} mbar) then filled with Ar gas (0.4 bar). The sealed ampoule was placed into a box furnace and heated at 800 °C for 3 hours using 4.4 °C/min heating and 2.2 °C/min cooling rate, see Table 5-9.

5.6.6 Transmission electron microscopy and energy-dispersive X-ray spectroscopy

Prior to investigation, the carbon nanotube samples (~0.5 mg) were dispersed in isopropyl alcohol (2 mL) using an ultrasonic bath (~15 min). Subsequently, a few drops were dropcast onto a copper TEM grid coated with lacy carbon film (Agar Scientific) to support the carbon nanotubes.

TEM micrographs and EDX spectra were acquired with an emission gun JEOL 2100F microscope operated at 100 kV accelerating voltage at the Nottingham Nanotechnology and Nanoscience Centre, University of Nottingham.

High resolution TEM analysis was carried out on a C_S-corrected FEI Titan 80–300 TEM operated at 80 kV at the Central Facility of Electron Microscopy, Ulm University (Ulm 89081, Germany).

For filtering the FFT function built in Gatan DigitalMicrograph (V2.01) was used.

5.6.7 Transmission Electron Microscopy image simulation

Numerical image calculations were carried out using the MUSLI and QSTEM programs operating with the transfer properties listed in Table 5-10 and Figure 5-55, respectively.

Table 5-10. Summary of the transfer properties of the image forming system used for image simulation using the MUSLI program.

Cs (mm)	0.5
Defocus (Å)	-550 to -450
Apperture rad (nm^{-1})	0.3
Conv (mrad)	0.9
Focus spread (nm)	5

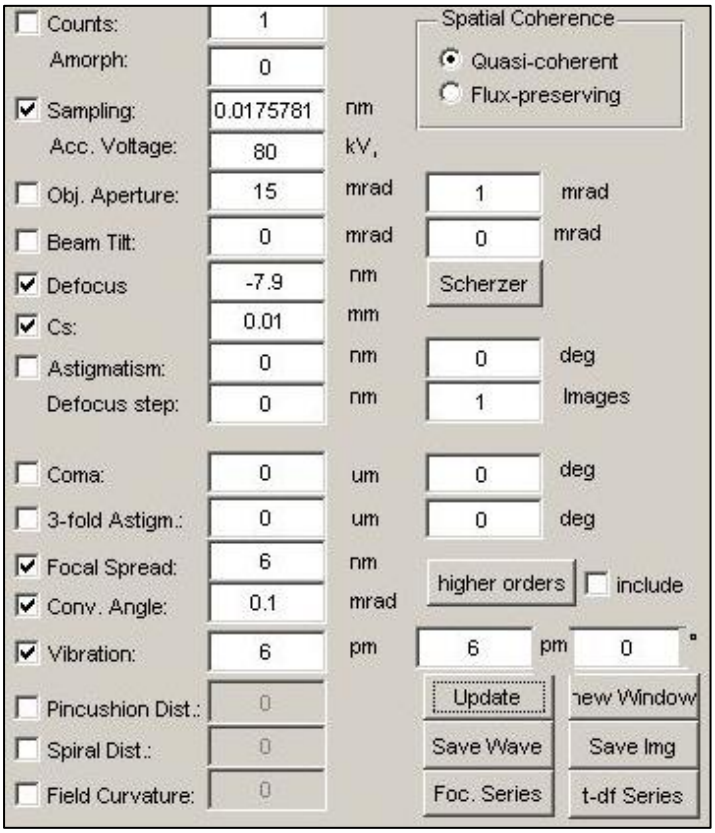


Figure 5-55. Summary of the transfer properties of the image forming system used for image simulation using the QSTEM program.

5.6.8 Raman spectroscopy

Prior to investigation, the carbon nanotube samples (~0.5 mg) were dispersed in isopropyl alcohol (2 mL) using an ultrasonic bath

(~15 min). Subsequently, the dispersion was drop-casted onto a Si(100) wafer to support the carbon nanotubes.

The Raman spectra were recorded on a Horiba–Jobin–Yvon LabRAM HR confocal Raman Microscope equipped with a Synapse CCD detector at the Nottingham Nanotechnology and Nanoscience Centre, University of Nottingham. The Raman measurements were performed at room temperature using an excitation laser wavelength of 532 nm operating at a power of *ca.* 4 mW (10%) and a 600 lines/mm grating. The Raman shift was calibrated using the Raleigh peak and the 520.7 cm^{-1} silicon line from an Si(100) reference sample.

5.6.9 MADLI-ToF mass spectrometry

Prior to investigation, the carbon nanotube samples (~0.5 mg) were dispersed in isopropyl alcohol (2 mL) using an ultrasonic bath (~15 min). Subsequently, the dispersion was mixed with trans-2-[3-(4-tert-Butylphenyl)-2-methyl-2-propenylidene]malononitrile (DCTB) then it was dropcasted onto a metallic sample holder plate and dried on room temperature.

The measurements were performed using a Bruker Ultraflex III MALDI-ToF mass spectrometer operated in positive ionisation mode and a laser power of 30%.

5.7 References

1. A. N. Khlobystov, D. A. Britz, and G. A. D. Briggs, *Acc. Chem. Res.*, 2005, **38**, 901–909.

2. L. Guan, K. Suenaga, Z. Shi, Z. Gu, and S. Iijima, *Nano Lett.*, 2007, **7**, 1532–1535.

3. X. Fan, E. Dickey, P. Eklund, K. Williams, L. Grigorian, R. Buczko, S. Pantelides, and S. Pennycook, *Phys. Rev. Lett.*, 2000, **84**, 4621–4624.

4. C. S. Allen, Y. Ito, A. W. Robertson, H. Shinohara, and J. H. Warner, *ACS Nano*, 2011, **5**, 10084–10089.

5. T. W. Chamberlain, J. Biskupek, G. A. Rance, A. Chuvilin, T. J. Alexander, E. Bichoutskaia, U. Kaiser, and A. N. Khlobystov, *ACS Nano*, 2012, **6**, 3943–3953.

6. Z. Wang, K. Zhao, H. Li, Z. Liu, Z. Shi, J. Lu, K. Suenaga, S.-K. Joung, T. Okazaki, Z. Jin, Z. Gu, Z. Gao, and S. Iijima, *J. Mater. Chem.*, 2011, **21**, 171–180.

7. H. Song, Y. Ishii, A. Al-Zubaidi, T. Sakai, and S. Kawasaki, *Phys. Chem. Chem. Phys.*, 2013, **15**, 5767–5770.

8. T. Fujimori, A. Morelos-Gómez, Z. Zhu, H. Muramatsu, R. Futamura, K. Urita, M. Terrones, T. Hayashi, M. Endo, S. Young Hong, Y. Chul Choi, D. Tománek, and K. Kaneko, *Nat. Commun.*, 2013, **4**, 2162–2170.

9. L. V. Yashina, A. A. Eliseev, M. V. Kharlamova, A. A. Volykhov, A. V. Egorov, S. V. Savilov, A. V. Lukashin, R. Püttner, and A. I. Belogorokhov, *J. Phys. Chem. C*, 2011, **115**, 3578–3586.

10. X. Pan and X. Bao, *Acc. Chem. Res.*, 2011, **44**, 553–62.

11. P. Serp and B. Machado, *Nanostructured Carbon Materials for Catalysis*, Royal Society of Chemistry, Cambridge, 2015.

12. S. a Miners, G. a Rance, and A. N. Khlobystov, *Chem. Commun. (Camb).*, 2013, **49**, 5586–5588.

13. D. A. Britz, A. N. Khlobystov, K. Porfyrakis, A. Ardavan, and G. A. D. Briggs, *Chem. Commun.*, 2005, 37–39.

14. A. Chuvilin, E. Bichoutskaia, M. C. Gimenez-Lopez, T. W. Chamberlain, G. A. Rance, N. Kuganathan, J. Biskupek, U. Kaiser, and A. N. Khlobystov, *Nat. Mater.*, 2011, **10**, 687–692.

15. Z. Wang, H. Li, Z. Liu, Z. Shi, J. Lu, K. Suenaga, S.-K. Joung, T. Okazaki, Z. Gu, J. Zhou, Z. Gao, G. Li, S. Sanvito, E. Wang, and S. Iijima, *J. Am. Chem. Soc.*, 2010, **132**, 13840–13847.

16. L. Grigorian, K. Williams, S. Fang, G. Sumanasekera, A. Loper, E. Dickey, S. Pennycook, and P. Eklund, *Phys. Rev. Lett.*, 1998, **80**, 5560–5563.

17. J. R. Schoonover, T. C. Zietlow, D. L. Clark, J. a. Heppert, M. H. Chisholm, H. B. Gray, A. P. Sattelberger, and W. H. Woodruff, *Inorg. Chem.*, 1996, **35**, 6606–6613.

18. E. J. Welch and J. R. Long, in *Progress in Inorganic Chemistry*, ed. K. D. Karlin, John Wiley & Sons, Inc., Hoboken, NJ, USA., 2005, vol. 54, pp. 1–46.

19. R. Tenne, *Adv. Mater.*, 1995, **7**, 965–995.

20. J. D. Franolic, J. R. Long, and R. H. Holm, *J. Am. Chem. Soc.*, 1995, **117**, 8139–8153.

21. K. S. Subrahmanyam, A. K. Manna, S. K. Pati, and C. N. R. Rao, *Chem. Phys. Lett.*, 2010, **497**, 70–75.

22. H. Valencia, A. Gil, and G. Frapper, *J. Phys. Chem. C*, 2010, **114**, 14141–14153.

23. R. Voggu, S. Pal, S. K. Pati, and C. N. R. Rao, *J. Phys. Condens. Matter*, 2008, **20**, 215211.

24. J. Etzkorn, H. a. Therese, F. Rocker, N. Zink, U. Kolb, and W. Tremel, *Adv. Mater.*, 2005, **17**, 2372–2375.

25. N. Zink, J. Pansiot, J. Kieffe, H. A. Therse, M. Panthöfer, F. Rocker, U. Kolb, and W. Tremel, *Chem. Mater.*, 2007, **19**, 6391–6400.

26. V. Fedorov, A. Mishchenko, and V. Fedin, *Russ. Chem. Rev.*, 1985, **54**, 408–423.

27. K. Kirakci, S. Cordier, A. Shames, B. Fontaine, O. Hernandez, E. Furet, J.-F. Halet, R. Gautier, and C. Perrin, *Chemistry*, 2007, **13**, 9608–9616.

28. A. Yella, M. Panthöfer, M. Kappl, and W. Tremel, *Angew. Chem. Int. Ed. Engl.*, 2010, **49**, 2575–80.

29. Y. Ma, Y. Dai, M. Guo, C. Niu, and B. Huang, *Nanoscale*, 2011, **3**, 3883–3887.

30. S. Bertolazzi, D. Krasnozhon, and A. Kis, *ACS Nano*, 2013, **7**, 3246–3252.

31. M. V. Kharlamova, L. V. Yashina, and A. V. Lukashin, *Appl. Phys. A*, 2013, **112**, 297–304.

32. A. Y. Shamrai, V.F.;Leitus, G.M.;Musatenko, *Kristallografiya*, 1988, **33**, 1289–1291.

33. M. Sergent, Ø. Fischer, M. Decroux, C. Perrin, and R. Chevrel, *J. Solid State Chem.*, 1977, **22**, 87–92.

34. T. W. Chamberlain, J. Biskupek, S. T. Skowron, P. a. Bayliss, E. Bichoutskaia, U. Kaiser, and A. N. Khlobystov, *Small*, 2015, **11**, 622–629.

6 Conclusions

As hybrid nanomaterials have become extremely important over the past two decades, they are at the forefront of both applied and fundamental research. Key current challenges are to find building units suitable for a particular hybrid nanomaterial and to combine them together in a controlled bottom-up assembly to achieve the desired physicochemical properties. However, first the fundamental interactions between the building units and their effects on the physicochemical properties of resultant nanomaterials have to be systematically studied at the atomic scale. Therefore, the main motivation of this research project was to understand how confinement on the nanoscale alters the properties of matter leading to new inorganic nanomaterials with potentially functional and exploitable properties.

In Chapter II of this thesis Group VI hexacarbonyl complexes ($M(CO)_6$, M=Cr, Mo and W) were encapsulated in single-walled carbon nanotubes (SWNT) as demonstrated by transmission electron microscopy (TEM), energy dispersive X-ray spectroscopy (EDX); and the host-guest interactions between $M(CO)_6$ complexes and SWNTs were investigated using vibrational spectroscopy and theoretical calculations.

The gas phase insertion of $M(CO)_6$ complexes into SWNTs was successfully developed and optimised to achieve good filling of carbon nanotubes with the guest-molecule which have been studied by IR spectroscopy inside nanotubes. It was found that in order to entrap the $M(CO)_6$ molecules in SWNTs the reaction temperature has to exceed a certain threshold (~120 °C), and at the end of the encapsulation the reaction mixture has to be quenched rapidly to ensure retention of the guest-molecules. These observations strongly suggest that the encapsulation of $M(CO)_6$ complexes takes place *via* a pre-adsorption mechanism similar to C_{60},[1–3] however the energy gained due to encapsulation is expected to be close to zero thus making the encapsulation of $M(CO)_6$ molecules in SWNTs reversible. Systematic TEM investigation of the as-synthesised $M(CO)_6$@SWNTs confirmed the deposition of $M(CO)_6$ complexes inside as well as on the surface of carbon nanotubes. As the IR response of encapsulated molecules can be masked by the response of surface adsorbed molecules, a cleaning procedure was developed for their removal.

Raman spectroscopy showed that no charge transfer takes place in $M(CO)_6$@SWNT systems, as no significant change was observed in the shape of the RBM and G mode of SWNTs. In contrast, Hartree-Fock (HF) calculations, including a dispersion component (HF+D), predicted partial electron transfer from the SWNTs to the $M(CO)_6$ molecules resulting in a partial negative charge

(0.04-0.06 ē) on M centre, which is too small to be detected by Raman spectroscopy. Analysis of $M(CO)_6$@SWNT systems by IR spectroscopy revealed the redshift of the stretching CO (ν_{CO}) IR band, which is attributed to van der Waals host-guest interactions in agreement with the earlier published observations.[4,5] Importantly, the shift of the CO stretching vibrations was found to increase from $Cr(CO)_6$ to $W(CO)_6$ (Cr<Mo<W) both experimentally and theoretically. The investigation of this trend showed that the strength of the van der Waals interactions between SWNTs and $M(CO)_6$ complexes depends on the electronegativity and polarisability of the metal centre as well as on the overall polarisability of the $M(CO)_6$ molecules. Thus, it has been demonstrated that in metal hexacarbonyl and carbon nanotube based host-guest systems greater overall polarisability of the guest molecule leads to greater van der Waals interactions between the host nanotube and the guest-molecules, manifested in the bigger redshift of the ν_{CO} IR band.

Using a range of analytical techniques, TEM, EDX and PXRD, Chapter III demonstrated that Group VI $M(CO)_6$ molecules can be encapsulated into graphitised carbon nanofibers (GNFs) using gas phase filling, and subsequently transformed into nanoparticles (NPs). Depending on the decomposition method, *i.e*. e-beam irradiation in TEM or heating, and the experimental conditions the

formation of amorphous/semicrystalline M-based NPs, MO_x NPs and MO nanorods were observed in GNFs by TEM imaging and X-ray powder diffraction. Thermal decomposition of $M(CO)_6$ in GNF was expected to provide metal NPs as reported for SWNT,[6,7] however, MO_x NPs and nanorods were surprisingly formed under various reaction conditions, even in the absence of oxygen. Systematic investigation of the chemical processes inside GNF indicated that the participation of CO ligands as a source of oxygen in the MO_x NP formation can be excluded, and suggested that GNFs can act as a source of oxygen during the thermal decomposition of $M(CO)_6$. Indeed, EDX investigation of GNFs revealed that a small amount of oxygen is present in their structure providing sufficient amount of oxygen atoms for the formation of MO_x NPs. Moreover, it was demonstrated that the presence of H_2O can dramatically alter the morphology of the nanostructure by aiding the formation of nanorods instead of spherical nanoparticles, which is in agreement with previous publications.[8–11] Overall, the synthesis of metal based nanoparticles inside GNFs by the encapsulation and *in situ* transformation of metal containing precursor molecules was successfully achieved.

Chapter IV showed that $Mo(CO)_6$ and other molecules, such as I_2, encapsulated into GNFs *via* gas phase filling, can serve as precursors for the formation of semiconductor MoS_2 nanostructures

using H_2S as a gas phase reactant. It was shown that the chemical nature and structure of the encapsulated precursor(s) *i.e.* $Mo(CO)_6$, $Mo(CO)_6$ and I_2, MoO_2, MoI_2 dramatically alter the morphology of the formed MoS_2 nanostructures, from flat layers of MoS_2 on the GNF step-edges, to small or large inorganic fullerene-like MoS_2 NPs, to large tightly packed particles built of 10 layers of MoS_2 or tubular structures, all of which were observed in GNFs. From all the tested precursors the mixture of $Mo(CO)_6$ and I_2 was found to be the most efficient at forming MoS_2 layers on the inner surface of GNFs resulting in uniform (MoS_2 nanotube)@GNF hybrid structures. It was shown that calcination of (MoS_2 nanotube)@GNF hetero-structures resulted in the collapse of the inner MoS_2 nanotube due to its larger than critical crystallite size.[12–14] The key achievement of this Chapter was the formation of hybrid van der Waals materials including a "tube inside a tube" structure, which was successfully implemented *via* the encapsulation and *in situ* transformation of the appropriate precursor molecules to a MoS_2 nanotube nesting inside the GNF.

Chapter V showed that multistep inorganic synthesis can be conducted within single- and multi-walled carbon nanotubes. Atomically thin SWNTs enabled the analysis of the resultant products at each step by conventional and aberration corrected (AC-)TEM, EDX, TEM image simulation and Raman spectroscopy. It

was demonstrated that single-chain arrays of individual M_6I_{14} clusters can be successfully synthesised by reacting encapsulated $M(CO)_6$ and I_2 precursors inside SWNTs. The reaction of the same precursors provided multilayers in MWNTs consisting of apparently interconnected molybdenum iodide clusters. Even more importantly, it was demonstrated that M_6I_{14} clusters, which reside inside CNTs can be completely converted into single and multi-layered MS_2 nanoribbons (NR) within SWNTs and MWNTs, respectively. Mechanisms of formation were postulated for the production of M_6I_{14} inside CNTs based on the sequential formation of binary metal iodide clusters, as well as for the formation of MS_2NRs, which involves the step-by-step conversion of M_6I_{14} through the formation of mixed metal chalcohalides. Raman spectroscopy and HRTEM have been used successfully to understand the fundamental chemical transformations in the multistep inorganic reactions leading to the formation of MI_2@CNTs and MS_2@CNTs, and to analyse the host-guest interactions between the encapsulated material and the CNTs. In summary, the encapsulation of $M(CO)_6$ and I_2 results in a material best described as $n[6M(CO)_6+2I_2+2I_5^-]@SWNT^{2n+}$ in which electrons are transferred from the SWNTs to the iodine atoms forming polyiodide anions. The subsequent formation of MoI_2 provides a material that can be described as $[M_6I_{14}^{2-}]_n@SWNT^{2n+}$ and in which, similarly to its precursor, electrons are transferred from the SWNTs to the

M_6I_{14} clusters, and the SWNTs acts as nanoscale counter-cations. The formation of MS_2NR from $[M_6I_{14}^{2-}]_n$@$SWNT^{2n+}$ was shown by Raman spectroscopy which also demonstrated moderate electron transfer from the SWNTs to the MS_2NRs. Therefore, these materials are best described as $[MS_2]^{\delta-}$@$SWNT^{\delta+}$. The dynamic behaviour, caused by thermal motion of M_6I_{14} clusters (translation and rotation) and MS_2NRs (twisting) in CNTs was demonstrated by time series AC-TEM imaging. The translation and rotation of M_6I_{14} clusters was found to be very similar to behaviour of tungsten polyoxometalate Linqvist ions *i.e.* $[W_6O_{19}]^{2-}$ either encapsulated in CNTs of deposited on graphene oxide.[15,16] Moreover, the twisting of MS_2NRs were found to be in good agreement with earlier publications showing identical behaviour in case of sulphur-terminated graphene nanoribbon and WS_2NR.[17,18,19] In addition, formation of 1D crystals confined in SWNTs from Mo_6I_{14} clusters, induced by the knock-on damage of the e-beam, was demonstrated *via* time series AC-TEM imaging. The careful analysis of high resolution TEM images coupled with TEM image simulation allowed the postulation of a mechanism of clusters polycondensation into 1D crystal and to reveal the structure and chemical composition of the formed crystal as $[(Mo_6I^i_8I^{i\text{-}a}{}_2I^a{}_2)_{n+2}I_2]^{2-}$ where n is the number of clusters added to the 1D crystal. The key achievement of this Chapter was the demonstration of multistep inorganic synthesis that can be conducted in CNTs *via* the *in situ*

transformation of the appropriate precursor molecules leading to novel inorganic hybrid nanomaterials.

6.1 References

1. B. W. Smith and D. E. Luzzi, *Chem. Phys. Lett.*, 2000, **321**, 169–174.

2. H. Ulbricht and T. Hertel, *J. Phys. Chem. B*, 2003, **107**, 14185–14190.

3. H. Ulbricht, G. Moos, and T. Hertel, *Phys. Rev. Lett.*, 2003, **90**, 7–10.

4. J. Wang, M. K. Kuimova, M. Poliakoff, G. A. D. Briggs, and A. N. Khlobystov, *Angew. Chem. Int. Ed. Engl.*, 2006, **45**, 5188–5191.

5. M. Yao, P. Stenmark, E. Abou-Hamad, F. Nitze, J. Qin, C. Goze-Bac, and T. Wagberg, *Carbon N. Y.*, 2010, **49**, 1159–1166.

6. T. W. Chamberlain, T. Zoberbier, J. Biskupek, A. Botos, U. Kaiser, and A. N. Khlobystov, *Chem. Sci.*, 2012, **3**, 1919–1924.

7. T. Zoberbier, T. W. Chamberlain, J. Biskupek, N. Kuganathan, S. Eyhusen, E. Bichoutskaia, U. Kaiser, and A. N. Khlobystov, *J. Am. Chem. Soc.*, 2012, **134**, 3073–3079.

8. G. L. Frey, A. Rothschild, J. Sloan, R. Rosentsveig, R. Popovitz-Biro, and R. Tenne, *J. Solid State Chem.*, 2001, **162**, 300–314.

9. V. K. Sarin, *J. Mater. Sci.*, 1975, **10**, 593–598.

10. A. Rothschild, J. Sloan, and R. Tenne, *J. Am. Chem. Soc.*, 2000, **122**, 5169–5179.

11. M. Homyonfer, B. Alperson, Y. Rosenberg, L. Sapir, S. R. Cohen, G. Hodes, and R. Tenne, *J. Am. Chem. Soc.*, 1997, **119**, 2693–2698.

12. F. Hoshyargar, A. Yella, M. Panthöfer, and W. Tremel, *Chem. Mater.*, 2011, **23**, 4716–4720.

13. N. Zink, J. Pansiot, J. Kieffe, H. A. Therse, M. Panthöfer, F. Rocker, U. Kolb, and W. Tremel, *Chem. Mater.*, 2007, **19**, 6391–6400.

14. R. Tenne, *Adv. Mater.*, 1995, **7**, 965–995.

15. J. Sloan, G. Matthewman, C. Dyer-Smith, A.-Y. Sung, Z. Liu, K. Suenaga, A. I. Kirkland, and E. Flahaut, *ACS Nano*, 2008, **2**, 966–976.

16. J. Sloan, Z. Liu, K. Suenaga, N. R. Wilson, P. a Pandey, L. M. Perkins, J. P. Rourke, and I. J. Shannon, *Nano Lett.*, 2010, **10**, 4600–4606.

17. T. W. Chamberlain, J. Biskupek, G. A. Rance, A. Chuvilin, T. J. Alexander, E. Bichoutskaia, U. Kaiser, and A. N. Khlobystov, *ACS Nano*, 2012, **6**, 3943–3953.

18. A. Chuvilin, E. Bichoutskaia, M. C. Gimenez-Lopez, T. W. Chamberlain, G. A. Rance, N. Kuganathan, J. Biskupek, U. Kaiser, and A. N. Khlobystov, *Nat. Mater.*, 2011, **10**, 687–692.

19. Z. Wang, K. Zhao, H. Li, Z. Liu, Z. Shi, J. Lu, K. Suenaga, S.-K. Joung, T. Okazaki, Z. Jin, Z. Gu, Z. Gao, and S. Iijima, *J. Mater. Chem.*, 2011, **21**, 171–180.